Development of Thermodynamically Integrated Processes for the Efficient Utilization of Energy Carriers (Hydrogen and Methanol)

by

Alireza KHATAMIJOUYBARI

THESIS BY ARTICLES PRESENTED TO ÉCOLE DE TECHNOLOGIE SUPÉRIEURE IN PARTIAL FULFILLEMENT OF THE REQUIREMENTS FOR THE DEGREE OF DOCTORATE IN ENGINEERING
Ph. D.

MONTREAL, 22 APRIL 2024

ÉCOLE DE TECHNOLOGIE SUPÉRIEURE
UNIVERSITÉ DU QUÉBEC

BOARD OF EXAMINERS

THIS THESIS HAS BEEN EVALUATED

BY THE FOLLOWING BOARD OF EXAMINERS:

M. Adrian Ilinca, Thesis Supervisor
Department of Mechanical Engineering, École de technologie supérieure

Mme Lyne Woodward, President of the Board of Examiners
Department of Electrical Engineering, École de technologie supérieure

M. Romain Lemaire, Member of the Jury
Department of Mechanical Engineering, École de technologie supérieure

M. Sohrab Zendehboudi, External Examiner
Faculty of Engineering and Applied Sciences, Memorial University Newfoundland

M. Ali Elkamel, External Examiner
Department of Chemical Engineering, University of Waterloo

IT WAS THE SUBJECT OF A DEFENSE BEFORE A JURY AND THE PUBLIC

10 APRIL 2024

AT ÉCOLE DE TECHNOLOGIE SUPÉRIEURE

DÉVELOPPEMENT DE PROCÉDÉS THERMODYNAMIQUEMENT INTÉGRÉS POUR LA UTILIZATION EFFICACE DE VECTEURS ÉNERGÉTIQUES (HYDROGÈNE ET MÉTHANOL)

Alireza KHATAMIJOUYBARI

RÉSUMÉ

Plusieurs systèmes intégrés, incorporant des technologies énergétiques propres, ont été proposés comme solutions potentielles aux défis posés par l'énergie à long terme. Une approche prometteuse consiste à utiliser des sous-produits industriels contenant de l'hydrogène et du dioxyde de carbone issus des gaz d'échappement industriels. Ces gaz peuvent être purifiés et convertis en hydrogène liquide ou en méthanol liquide, agissant ainsi comme des vecteurs énergétiques efficaces grâce à des méthodes de liquéfaction avancées. Cette approche contribue non seulement à la lutte contre la pollution de l'environnement, mais elle permet également de minimiser le gaspillage d'énergie. Cela s'inscrit parfaitement dans l'impératif mondial visant à atteindre des objectifs d'émissions nettes nulles. Cette étude présente trois structures intégrées innovantes pour le stockage d'énergie à base de combustible.

La première méthode propose une structure intégrée visant à liquéfier l'hydrogène en utilisant un cycle de réfrigération à éjecteur-compression, un cycle de réfrigérant multi-composants en cascade, ainsi que le cycle de génération d'énergie de Kalina. Pendant le processus de liquéfaction de l'hydrogène, l'excès de chaleur généré est efficacement utilisé par le cycle de production d'électricité de Kalina. Le système de réfrigération est intégré à la configuration du noyau principal à travers des courbes composites et grandes composites. Cela optimise les pourcentages de composition du réfrigérant et les pressions de fonctionnement du cycle de réfrigération afin d'obtenir la meilleure correspondance possible entre les courbes froides et chaudes.

L'étude présente également deux nouveaux procédés intégrés pour la production de méthanol. La première conception se focalise sur un processus générant des gaz combustibles à basse et haute pression, des composés aromatiques, de l'électricité, ainsi que de l'eau chaude en tant que produits secondaires, avec le méthanol liquide comme produit principal. Ce processus englobe le cycle de purification de l'hydrogène, le cycle de production de méthanol, le cycle de Rankine organique (ORC), le cycle d'absorption-compression (ACRC) et l'utilisation de capteurs solaires. La chaleur résiduelle du réacteur de méthanol est efficacement récupérée par l'ORC pour générer de l'énergie, tandis que l'ACRC assure le refroidissement du cycle de purification de l'hydrogène.

La deuxième conception pour la production de méthanol décrit un processus respectueux de l'environnement, utilisant l'hydrogène extrait du gaz de four à coke (COG) pour réagir avec le dioxyde de carbone dans un réacteur à méthanol. Les sous-systèmes de ce procédé comprennent une unité de capture de CO_2 pour séparer le dioxyde de carbone des gaz d'échappement, un procédé de purification et de liquéfaction du gaz naturel pour produire du

gaz naturel liquéfié (GNL), l'extraction d'hydrogène à partir de COG et un cycle de production de méthanol. Des panneaux photovoltaïques, adaptés à la situation géographique, sont utilisés pour fournir la puissance requise.

Dans les méthodes proposées pour la production de méthanol liquide, l'analyse économique est menée en utilisant le coût annualisé du système (ACS), et le processus est soumis à une optimisation multi-objectifs grâce à l'implémentation de l'algorithme génétique avancé NSGAII. Les méthodes de prise de décision floue, TOPSIS et LINMAP sont employées pour évaluer le taux de rendement optimal et le coût de revient du produit principal. Des analyses de sensibilité, d'énergie et d'exergie sont réalisées à l'aide du logiciel Aspen HYSYS V.10 et du code MATLAB afin d'évaluer de manière exhaustive les performances du procédé d'un point de vue thermodynamique.

Mots-clés : hydrogène liquide, synthèse de méthanol, analyse exergétique, analyse thermo-économique, optimisation multi-objectifs

DEVELOPMENT OF THERMODYNAMICALLY INTEGRATED PROCESSES FOR THE EFFICIENT PRODUCTION OF ENERGY CARRIERS (HYDROGEN AND METHANOL)

Alireza KHATAMIJOUYBARI

ABSTRACT

Several integrated systems incorporating clean energy technologies have been proposed as potential solutions for the challenges posed by long-term energy concerns. One promising approach involves using hydrogen-containing industrial by-products and carbon dioxide from industrial exhaust gases. These gases can be purified and converted into liquid hydrogen or liquid methanol, efficient energy carriers, through advanced liquefaction methods. This process not only helps address environmental pollution but also minimizes energy wastage. By employing hydrogen purification techniques or alternative processes to extract hydrogen from industrial by-products, clean energy carriers like liquid hydrogen and methanol can be produced, aligning with the global imperative of achieving net-zero emissions targets. This study introduces three innovative integrated structures for fuel-based energy storage.

The first method proposes an integrated structure to liquefy hydrogen using an ejector-compression refrigeration cycle, cascade multi-component refrigerant cycle, and the Kalina power generation cycle. The excess heat generated during the hydrogen liquefaction process is effectively utilized by the Kalina power generation cycle. The refrigeration system is integrated with the main core configuration through composite and grand composite curves, optimizing refrigerant composition percentages and refrigeration cycle operating pressures to achieve the best possible match between cold and hot curves.

The study also presents two novel integrated processes for methanol production. The first design focuses on a process that produces low-pressure and high-pressure fuel gases, aromatic compounds, electricity, and hot water as side products, with liquid methanol as the main product. This process includes hydrogen purification, methanol production, Organic Rankine (ORC), absorption-compression cycles (ACRC), and solar collectors. The ORC efficiently utilizes waste heat from the methanol reactor to generate power, while the ACRC provides cooling for the hydrogen purification cycle.

The second design for methanol production outlines an environmentally friendly process utilizing hydrogen extracted from coke oven gas (COG) to react with carbon dioxide in a methanol reactor. The subsystems of this process include a CO_2 capture unit for separating carbon dioxide from exhaust gases, a natural gas purification and liquefaction process to produce liquefied natural gas (LNG), hydrogen extraction from COG, and a methanol production cycle. Photovoltaic panels, customized to the geographical location, are employed to provide the required power.

In the proposed methods of liquid methanol production, economic analysis is conducted using the Annualized Cost of the System (ACS), and the process undergoes multi-objective

optimization through the implementation of the NSGAII algorithm. The decision-making methods, including fuzzy, TOPSIS, and LINMAP, are utilized to evaluate the optimum rate of return and prime cost of the main product. Sensitivity, energy, and exergy analysis are performed using Aspen HYSYS software V.10 and MATLAB code to comprehensively assess the process performance from a thermodynamic standpoint.

Keywords: liquid hydrogen, methanol synthesis, exergy analysis, thermo-economic analysis, multi-objective optimization

TABLE OF CONTENTS

LIST OF TABLES

Page

LIST OF FIGURES

Page

LIST OF ABBREVIATIONS

AB	Annual Benefit
AC	Alternating current
ACRC	Absorption–Compression Refrigeration Cycle
ACS	Annualized Cost of the System (USD)
ANN	Artificial Neural Network
AV	Additive value
BFD	Block Flow Diagram
BFG	Blast Furnace Gas
BIOU	Biogas upgrading
BOFG	Basic Oxygen Furnace Gas
C/ Comp	Compressor
CAES	Compressed Air Energy Storage
CC	Composite Curve
CCHP	Combined Cooling, Heating, and Power
CEPCI	Chemical Engineering Plant Cost Index
CES	Cryogenic Energy Storage
CH_4	Methane
CHG	Coal-based Hydrogen Gas
CO	Carbon monoxide
CO_2	Carbon dioxide
COG	Coke Oven Gas
COGH	COG-based Hydrogen
COP	Coefficient of Performance
CR	Conversion reactor
CRF	Capital recovery factor
CTMCR	COG-To-Methanol with CO2 Recycle
CTMWOSC	COG-To-Methanol Without Supplementary Carbon
CTMWSC	COG-To-Methanol with Supplementary Carbon
Cu-Cl	Copper-Chlorine
D/FD	Flash drum
DC	Direct current
DCFCs	Direct carbon fuel cells
DEA	Diethanolamine
DiffHor	Monthly average horizontal diffuse irradiation
ELCO	Energy Levelized Cost (USD)
ERC	Ejector Refrigeration Cycle
eSS	Enhanced Scatter Search
Fe-Cl	Iron-Chlorine
GA	Genetic algorithm

GCC	Grand Composite Curve
GHG	Greenhouse gas
GlobHor	Global horizontal irradiation
GlobInc	Global incident in collector plane
GMDH	Group method of data handling
GT-KC	Gas Turbine and Kalina Cycle
GTL	Gas to liquid
H_2	Hydrogen
H_2O	Water
H_2S	Hydrogen sulfide
HDH	Humidification-Dehumidification
HHV	High Heat Value (kJ/g)
HMEI	Hourly Maximum Energy Injected (kWh)
HX/HE	Heat exchanger
LCA	Life Cycle Assessment
LCOP	Levelized Cost of Product (USD)
LH_2	Liquid hydrogen
LHBO	Liquid hydrogen boil-off
LHV	Low Heat Value (kJ/g)
LINMAP	Linear programming approach for multidimensional analysis of preference
LMTD	Logarithmic Mean Temperature Difference (K)
LNG	Liquefied natural gas
LOHC	Liquid Organic Hydrogen Carriers
LPCOG	Liquefaction Process of Coke Oven Gas
LW	Lost Work (kW)
MCFC	Molten carbonate fuel cell
MDEA	Methyldiethanolamine
MED	Multi-Effect Desalination
Mg-Cl	Magnesium-Chloride
MINLP	Mixed Integer Nonlinear Programming
MIX	Mixer
MR	Methanol reactor
MRC	Multi-component Refrigerant Cycle
M-S	Multi-stream
NAB	Net Annual Benefit
NPV	Net Present Value
NSGA	Non-dominated Sorting Genetic Algorithm
OFC	Operating flow cost (USD)
ORC	Organic Rankine cycle
PC	Prime cost of product (USD)
PCCP	Post-Combustion Capture Process

PCM	Phase Change Materials
PFD	Process Flow Diagram
POR	Period of return (years)
PR	Performance Ratio
PSO	Particle Swarm Optimization
Pump/P	Pump
PV	Photovoltaic
R	Reactor
ROR	Rate of Return
SEC	Specific Energy Consumption (kWh/kg)
Sep	Separator
S-I	Sulphur-Iodine
SMR	Steam methane reforming
SOFC	Solid oxide fuel cell
SOPC	Summary of Product Cost (USD)
STC	Standard Test Conditions
SVD	Singular value decomposition
T/TB/ Turb	Turbine
Ti	Distillation tower/ Tower
TOPSIS	Technique for order of preference by similarity to ideal solution
V	Valve/Throttling valve
VATR	Value-added tax rate
V-Cl	Vanadium-Chlorine
VOP	Volume of product
VOP	Volume of Product
y	Actual value
$\hat{y}$	Computed value
Zn-S-I	Zink-Sulphur-Iodine

LIST OF SYMBOLS AND UNITS OF MEASUREMENT

A_a	Area of collector opening (m^2)
A_g	Glass coverage area (m^2)
A_r	Area of receiver (m^2)
C	Cost (USD)
C_p	Specific heat capacity (J/kg)
C_{rep}	Replacement cost (USD)
C_{ope}	Operating cost (USD)
C_{arep}	Annualized replacement cost (USD)
C_{aope}	Annualized operating cost (USD)
C_{amain}	Annualized maintenance cost (USD)
D_g	Diameter of glass coverage (m)
D_0	Outer diameter of tubular receiver (m)
E_x	Exergy (kJ)
$\dot{E}_x$	Exergy rate (kW)
f	Annual inflation rate
F_R	Thermal collection coefficient
G	Gibbs free energy ($kJ.kg^{-1}$)
Go	Array reference irradiance (kW/m^2)
h	Enthalpy ($kJ.kg^{-1}$)
$\bar{h}_0$	Enthalpy in ambient condition ($kJ.kg^{-1}$)
h_c	Heat transfer coefficient of the thermal convection (W/m^2K)
h_r	Heat transfer coefficient of the thermal radiation (W/m^2K)
H_t	In-plane solar radiation (kW/m^2)
I	Irreversibility (kJ/K)
i	Real interest rate
I_b	Direct of beam radiation (kW/m^2)
I_d	Sky diffuse irradiation (kW/m^2)
j	Nominal bank interest rate
L	Length of parabolic solar trough (m)
$\dot{m}$	Mass flow rate ($kg.s^{-1}$)
Nu	Nusselt number
P	Pressure (bar)
P_o	Nominal power in STC (kW)
$\dot{Q}$	Heat rate (kW)
Q_u	Useful absorbed energy (kJ)
Re	Reynolds number
s	Entropy ($kJ.kg^{-1}.K^{-1}$)
$\bar{s}_0$	Entropy in ambient condition ($kJ.kg^{-1}.K^{-1}$)

T	Temperature (K)
T_g	Temperature of glass coverage (K)
U_L	Total heat transfer coefficient of solar collector (W/m^2K)
W	Width of opening (m)
$\dot{W}$	Work rate (kW)
W_{sh}	Axial work (kJ)
η	Efficiency
η_s	Isentropic efficiency
ΔG^{mix}	Change of Gibbs free energy in the ambient temperature (kJ)

INTRODUCTION

With climate-friendly, low-cost, and socially acceptable energy sources becoming increasingly important, renewable energy sources have been considered a practical alternative to nuclear energy and fossil fuels. Clean energy sources should be managed to guarantee reliable access for consumers, a challenging objective to achieve. While direct utilization of energy products is often more straightforward and requires less advanced technology and infrastructure compared to indirect methods, it may not always represent the optimal choice (Kousksou et al., 2014).

Energy storage plays a significant role in transitioning into a neutral-emissions economy, helps balance demand and supply, and remarkably decreases wasted power. It can facilitate flexible renewable or clean energy production and guarantee integration into the power grid supplied by different means of power generation. Moreover, the stored energy can be transported and consumed in an area deprived of adequate resources or infrastructures like crude oil or natural gas (Montazeri & Niknam, 2017).

There are varied types of energy storage, each with benefits and drawbacks (Chauhan & Chauhan, 2019). Gas storage systems store energy by using energy produced in renewable power plants or off-peak grid power to compress gases like air, hydrogen, and nitrogen and store them in vessels. These cost-effective systems are suitable for long-lasting energy storage. Converting pressured gases into liquids makes them considerably high-density energy carriers and lowers the costs and carbon footprints associated with energy transportation. In this regard, researchers have been studying diverse liquids, such as liquid hydrogen (LH_2), liquid methanol, liquid carbon dioxide, and liquid ammonia, with hydrogen having a remarkable feature as a fuel (Amirante et al., 2017).

Electricity production from green energy resources has been growing exponentially in North American countries (Schmalensee, 2010). These resources, such as wind, tidal, and solar energies, are directly or indirectly related to the sun and its relative movement. Their

intermittent nature leads to semi-periodic electricity production in power plants (Perez-Arriaga & Batlle, 2012). Energy storage can handle these predictable imbalances between supply and demand to ensure a reliable power supply for consumers. Hydrogen storage is one of the applicable methods (Michalski, 2017). Using excess electricity, hydrogen from water electrolysis is employed in a reverse process in fuel cells to produce power when needed (Tamalouzt et al., 2016); (L. Zhang & Xiang, 2014). This is another reason for efficient hydrogen storage.

Hydrogen is the main or side product of many renewable power plants and industrial processes. Hydrogen is used in diverse industries, including petroleum, petrochemical, aerospace, and military (Dunn, 2002); (Ramachandran & Menon, 1998). It can be used as a refrigerant, a fuel, a feed gas in several sectors, or electricity generation in fuel cells (Cormos, 2011); (Sarbu & Sebarchievici, 2017). The development of hydrogen storage methods plays a significant role in the progress of the hydrogen economy (Abe et al., 2019); (Taljan et al., 2008).

Hydrogen is mainly produced from fossil sources of oil, natural gas, coal, and methane (Dufour et al., 2011) through the steam methane reforming (SMR) process (Boyano et al., 2011). However, this method has the drawbacks of using natural gas, which is not easily accessible in all countries. Besides, SMR methods release CO_2 with an emission rate of more than 13 (kg CO_2 eq/kg H_2) (Timmerberg et al., 2020). Water electrolysis is a popular method for hydrogen production. Although electrolyzers produce hydrogen in high purity and lead to almost zero carbon emissions, their hydrogen production capacity is lower than other methods. It is unsuitable for large-scale production due to the limited capacity of membranes used for water splitting in electrolyzers. The high cost of membranes is another disadvantage of this process. What is more, exergy efficiencies of electrolysis processes are nearly 35%, approximately half of that of SMR cycles, and their energy efficiency is 30% lower than that of SMR methods (Safari & Dincer, 2020).

Hydrogen production units are usually constructed in areas with easy access to fossil fuel resources (Aitani, 1996). These areas are not necessarily near the end users' location. Thus, hydrogen transfer using underground pipelines may be impossible (Züttel, 2007). Water electrolysis and thermo-electrochemical processes are also utilized for the hydrogen production from electrical and thermal power of nuclear power plants and renewable sources of solar, wind, biomass, and geothermal energy (Christopher & Dimitrios, 2012); (Malerød-Fjeld et al., 2017); (Ursua et al., 2012). Similarly, suitable construction sites for renewable or nuclear power plants may be possibly situated in areas far from hydrogen distribution sites (Wu et al., 2021). Besides, there may be unbalances between the production rate of hydrogen and its consumption in chemical or petrochemical industries. These reasons necessitate the construction of hydrogen storage facilities.

Produced gaseous hydrogen usually cannot be used directly. It should be transferred to target locations for utilization because suitable areas for its cost-effective production (based on renewable energy potentials and feed gas availability) may differ from the end-user's location. Not integrating the hydrogen liquefaction process in those suitable areas can lead to high risk and high carbon emissions in the transportation of gaseous hydrogen (Züttel, 2004). Therefore, integrating the gaseous hydrogen production process through novel thermochemical processes and hydrogen liquefaction will lead to a step-change in economic cost and energy efficiency.

Due to the low density of hydrogen, it cannot be considered an energy carrier unless its pressure is increased (Felderhoff et al., 2007). Storing gaseous hydrogen in pressure vessels (at a pressure up to 700 bar and ambient temperature) is the most conventional storage method (Lemmon et al.). This is because of its simplicity, especially in low to moderate pressure ranges; the technology is the same as other storage vessels used for gas storage. However, material embrittlement due to hydrogen diffusion into the metal should be considered. Therefore, minor development is required for technology adjustment as charge/discharge speed in pressured vessels is comparatively faster than other methods (Ni, 2006).

Gaseous hydrogen can be compressed or liquefied for long-term storage or transportation. When compressed, hydrogen has a density of approximately 23 kg/m^3 at 350 bar, almost three times higher than the volume required for liquid hydrogen storage (Sheffield et al., 2014). Besides, the higher the pressure is, the higher the risks are due to hydrogen penetration into the container material and explosion. Hydrogen liquefaction has received positive worldwide attention to such an extent that its capacity in 2020 in the United States, Canada, Asia, Europe, and South America are evaluated at 241, 51, 33.5, 20, and 2.3 tons/day, respectively. A rise of 5.3 tons/day in Europe is expected by the end of 2021, with Germany, France, and the Netherlands leading the way.

Besides, in combination with carbon dioxide, hydrogen can be converted into methanol, which has several advantages over hydrogen. Methanol is safer than hydrogen and is liquid in ambient conditions. Besides, producing methanol can help reduce carbon dioxide emissions, the main contributors to global warming. Methanol has more hydrogen by mass in one liter than in a liter of pure liquid hydrogen (98.8 g of hydrogen in 1 L of methanol at room temperature compared to 70.8 g in liquid hydrogen at − 253°C) (Gumber & Gurumoorthy, 2018). Methanol does not need advanced technologies to be stored and transported and can be used as a vehicle fuel. However, the heating value of methanol is six times lower than hydrogen's.

The reaction between hydrogen and carbon dioxide produces methanol. Plug flow reactor at the temperature of 200 ^{0}C (Y. Zhang et al., 2009) and a pressure of 50-100 bar is considered for methanol production (Nieminen et al., 2019). Carbon dioxide can be supplied from CO_2 absorption processes. These processes, commonly based on thermochemical reactions, can absorb carbon dioxide from the exhaust of industrial plants (Shahbaz et al., 2021).

Based on the literature review the research gaps can be stated as follows:

- Hydrogen liquefaction, despite its energy storage potential, faces challenges due to its capital and energy intensity, leading to high Specific Energy Consumption (SEC). To improve its viability, measures must focus on reducing SEC, enhancing efficiency, and cutting total energy usage. Solutions include adopting advanced liquefaction technology, optimizing process parameters, integrating renewable energy sources, and developing innovative storage and distribution methods. Through these efforts, hydrogen liquefaction can become a more competitive option for energy storage, supporting the transition to sustainable energy practices.
- The multi-component refrigerant cycle used in hydrogen precooling faces challenges in maintenance and control. Managing the proportion of each component becomes complex, especially in the event of a leak. This complexity can hinder system efficiency and increase maintenance requirements, highlighting the need for more robust and controllable refrigeration solutions. Innovative approaches to refrigerant management could alleviate these issues, improving the reliability and performance of hydrogen precooling systems.
- External utilities play a pivotal role in the cooling of hydrogen liquefaction and methanol production processes. Yet, the absence of robust thermal integration measures can detrimentally impact process efficiency and escalate overall energy consumption. Efforts directed towards integrating these utilities efficiently hold the promise of optimizing energy usage and bolstering process performance, thereby potentially yielding significant benefits in terms of cost savings and sustainability. Thus, the pursuit of effective thermal integration emerges as a cornerstone in the quest to maximize the efficiency and viability of these critical industrial processes.

As a result, the research objectives can be defined as:

- Introducing some novel integrated structure for efficient storage of hydrogen as liquid hydrogen or methanol
- Decreasing the energy consumption of hydrogen liquefaction or methanol production processes and increasing the energy and exergy efficiencies by process integration

- Design optimization of hydrogen liquefaction and methanol production processes by sensitivity analysis and the implementation of artificial intelligence

Until now, multiple integrated systems incorporating clean energy technologies have been suggested to address the challenges of long-term energy storage and efficient transportation to remote areas. One promising approach involves harnessing hydrogen-containing industrial by-products and carbon dioxide from industrial exhaust gases. These gases can be purified and transformed into liquid hydrogen, an effective energy carrier, using advanced liquefaction methods. Using hydrogen-containing industrial by-products, such as coke oven gas (COG) and ammonia synthesis flue gases, mitigates environmental pollution and reduces energy wastage. By employing hydrogen purification techniques or alternative processes to extract hydrogen from industrial side products, clean energy carriers can be produced in liquid hydrogen and methanol, which align with the global imperative of achieving net-zero emissions targets. Integrating cogeneration systems within unified structures enhances overall efficiency and minimizes equipment requirements compared to individual subsystem operations. This study proposes three innovative integrated structures for energy storage in the form of fuel.

The first storage method described in Chapter 2 proposes an integrated structure to liquefy hydrogen using an ejector-compression refrigeration cycle, cascade multi-component refrigerant cycle, and the Kalina power generation cycle. High economic costs, low efficiency, and high losses, along with the lack of development of new technologies, are among the significant problems facing hydrogen liquefaction technologies. Determined attempts have been made to optimize efficiency, minimize total costs, and reduce the structural complexity of the hydrogen liquefaction processes, such as utilizing the multi-component refrigerant cycle. Employing a multi-component refrigerant can lower energy consumption; however, it introduces challenges, such as heightened maintenance costs due to reduced controllability of the refrigerant cycle. Also, maintaining constant refrigerant components becomes challenging in the event of a leak in a multi-component refrigerant cycle. An ejector-compression refrigeration cycle is incorporated into the process to address

this issue. The surplus heat from the hydrogen liquefaction process is utilized in the Kalina power generation cycle. The integration of the refrigeration system into the main core configuration is illustrated through composite and grand composite curves. Refrigerant composition percentages and refrigeration cycle operating pressures are employed to match the cold and hot curves best. In all studies, sensitivity, energy, and exergy analyses are implemented to evaluate the performance of the process from a thermodynamic point of view.

In the second and third processes, described in chapters three, four, and five, methanol production is studied by proposing two innovative integrated processes. In Chapter 3, the novel process is designed to produce low-pressure and high-pressure fuel gases, aromatic compounds, electricity, and hot water, which are side products. At the same time, liquid methanol is considered the main product. The process includes the hydrogen purification cycle, the methanol production cycle, the Organic Rankin cycle (ORC), the absorption-compression cycle (ACRC), and solar collectors. The ORC absorbs the wasted heat in the methanol reactor to produce power, and the ACRC supplies cooling for the hydrogen purification cycle. For this process in Chapter 4, the Annualized Cost of the System (ACS) is applied for the economic analysis, and the NSGAII algorithm is implemented for multi-objective optimization of the process, with fuzzy, TOPSIS, and LINMAP being the decision-making methods to evaluate the optimum period of return, thermal efficiency, and exergy efficiency.

In Chapter 5, an environmentally friendly process is designed to produce methanol, which utilizes hydrogen extracted from coke oven gas to react with carbon dioxide in a methanol reactor. The subsystems include a CO_2 capture unit to separate carbon dioxide from exhaust gases, a natural gas purification and liquefaction process to produce liquefied natural gas (LNG), hydrogen from COG, and a methanol production cycle. Photovoltaic panels, according to geographical locations, are used to provide the required power. Annualized Cost of the System (ACS) is applied for the economic analysis, and the NSGAII algorithm is implemented for multi-objective optimization of the process, with TOPSIS and LINMAP

being the decision-making methods to evaluate the optimum rate of return and prime cost of the main product.

CHAPTER 1

METHODOLOGY

1.1 Research Methodology

This study aims to offer some efficient methods and facilitate energy transfer by converting hydrogen into liquid methanol and liquid hydrogen. The methodology used in the presented study can be categorized into five steps:

- Data collection
- Modeling
- Validation
- Analyses
- Optimization

In the first step, data related to the equipment and stream characteristics of processes associated with the production and liquefaction of hydrogen and methanol, including scientific articles, industrial patents, and records, is collected. Besides, renewable energy potentials of the target location (if applicable) are assessed using data collected from meteorological stations or analysis results extracted from related software such as PVsyst.

In the modeling phase, HYSYS and Aspen Plus software are implemented. They are powerful tools for modeling energy systems and are used in various studies related to the process and thermal integration (Haydary, 2019). The above software can be easily linked with programming software, including MATLAB and Fortran. Thus, data processing and analyses can be applied to the designed structures.

Regarding the equations of state used in this research, the adoption of the Peng-Robinson equation of state within Aspen HYSYS represents a pivotal choice, driven by its unmatched adaptability across a wide range of temperature and pressure conditions, extensive database

of binary interaction parameters, computational efficiency, and user-friendly implementation. This equation serves as the backbone of the software, offering engineers a reliable toolset for process analysis and design. While its role proves indispensable in localized examinations and the sizing of critical equipment such as compressors and expanders, its significance wanes in broader process evaluations. Nonetheless, within the acid gas package of Aspen HYSYS, the Peng-Robinson equation governs the vapor phase, complemented by the electrolyte non-random two-liquid activity coefficient model for electrolyte thermodynamics in the liquid phase. This integrated package facilitates the simulation of acid gas removal processes, particularly targeting contaminants like CO_2, thus enabling engineers to optimize system performance with precision. Through meticulous calibration against extensive datasets and thorough investigation into chemical absorption processes, rate-based simulations, and molecular thermodynamic models for amine solutions, Aspen HYSYS empowers engineers with a comprehensive toolkit to accurately predict and optimize the behavior of complex industrial systems (Shirmohammadi et al., 2020); (Aasadnia et al., 2021).

At the validation stage, the modeling result of each subsection is compared with the actual industrial data or other scientific data to be sure that the modeling is done with acceptable accuracy (within ±1%).

After modeling, analyses should be done to assess the performance of the developed integrated structures. These analyses include:

- Energy analysis is used to calculate the thermodynamic efficiency of the total process and each subsystem.
- Exergy analyses assess the reversibility of each equipment and stream used in the design of the whole structure by calculating exergy efficiencies and the share of each piece of equipment in the total exergy destruction.
- Sensitivity analysis determines the most influential variables (temperature, pressure, flow rate, etc.) in the designed process, which changes in their value significantly influence the

performance of the whole process. By this analysis, the structure's reaction to the changes in the values of these critical elements can be analyzed.

- Economic analysis determines production costs based on the quality of the energy conversion processes by using each product's thermodynamic value or its exergy.
- Optimization can be done to enhance the whole structure's efficiency by implementing artificial intelligence feed by data extracted from the sensitivity analysis results.

The analyses above are described in more detail in the following sections.

1.2 Sensitivity and pinch Analyses

One of the most straightforward and essential process optimization techniques is to adjust the operating conditions of the different parts of the system, also known as operational optimization. To improve optimization results, one of the tasks can be done by analyzing the sensitivity of essential system indicators to some critical and practical operational variables (e.g., pressure, flow rate, and percentage of flow components), which can be applied as a real-world basis for further optimization of the energy system (Saltelli et al., 2005). When there are a lot of design variables in the process, it is crucial to know the main parameters of the system to understand how the system reacts to changes in these variables. In this research, parametric sensitivity analysis by Aspen, HYSYS software, and Matlab programming determines the effects of significant parameters on the response variables to analyze the system performance under different conditions. It serves to select the appropriate design, operation, and optimization strategies for the integrated processes. Monitoring the feedback between the structure and the changes in operating variables makes it possible to analyze the integrated structure's response and sensitivity to each change.

Pinch analysis is a powerful method for minimizing energy consumption in thermodynamic processes and heat recovery systems, creating an optimal design for the heat exchanger that reduces the need for heating and cooling (Linnhoff, 1993). There are always temperature gaps between cold and hot streams in multi-stream heat exchangers. The closer the hot and

cold diagrams in multi-flow heat exchangers are, the lower the power consumption of the refrigeration cycle and the higher the efficiency of the whole system. The pinch technology can modify the energy consumption and determine the required utility by using its critical tools of composite curves (CC) and grand composite curves (GCC). The intersection points of the grand composite curve (GCC) diagram to the vertical axis are used to determine the pinch point (Schlosser et al., 2019). In this study, Aspen HYSYS V10.0 software is used to determine the pinch point, and MATLAB V10.0 software, in connection with Aspen HYSYS V10.0, is used to draw the composite and grand composite curves.

1.3 Energy analysis

Energy analysis is the quantitative measurement of energy entering and leaving a system. Energy analysis is based on thermodynamics' first law (Goel & Manik, 2021). The steady-state control volume energy and mass balance equation based on the thermodynamic first law is (Yousefizadeh Dibazar et al., 2020):

$$\dot{Q}_{Cv} - \dot{W}_{Cv} + \sum \dot{m}_i \left(h_i + \frac{1}{2} v_i^2 + g z_i \right) - \sum \dot{m}_o \left(h_o + \frac{1}{2} v_o^2 + g z_o \right) = 0$$
$$\sum \dot{m}_{in} = \sum \dot{m}_{out} \tag{1.1}$$

In Eq. (1-1), $\dot{Q}_{Cv}$, $\dot{m}$, h, $\dot{W}_{Cv}$, v, g and $z$are net heat transfer rate, mass flow rate, specific enthalpy, net or total work, the stream velocity of the working fluid, the gravitational acceleration, and the elevation from a reference position, respectively. The equations defining the energy balance in heat exchangers are provided in Eq. (1-2):

$$\dot{m}_{in,i}(h_{in1,i} - h_{in2,i}) = \dot{m}_{out,i}(h_{out1,i} - h_{out2,i})$$
$$T_{in1,i} = T_{out1,i} + \Delta\ T_{in,HXi} \tag{1.2}$$

Isentropic efficiency is assumed in the energy balance equations of compressors, turbines, and pumps, and heat loss is ignored. So, the energy balance in these types of equipment is considered as follows:

$$h_{out} = \frac{h_{out}^{S} - h_{in}}{\eta_s} + h_{in} \tag{1.3}$$

$$h_{out} = (h_{out}^{S} - h_{in})\eta_s + h_{in} \tag{1.4}$$

In the mixer, the energy balance and the mass conservation equations are defined as follows (Cao et al., 2020):

$$\dot{m}_{in,1}h_{in,1} + \dot{m}_{in,2}h_{in,2} = \dot{m}_{out}h_{out} \tag{1.5}$$

$$\dot{m}_{in,1} + \dot{m}_{in,2} = \dot{m}_{out} \tag{1.6}$$

$$h_{out} = \frac{\dot{m}_{in,1}h_{in,1} + \dot{m}_{in,2}h_{in,2}}{\dot{m}_{in,1} + \dot{m}_{in,2}} \tag{1.7}$$

Similarly, in the flash drums and separators, we have:

$$\dot{m}_{in}h_{in} = \dot{m}_{out,1}h_{out,1} + \dot{m}_{out,2}h_{out,2} \tag{1.8}$$

$$\dot{m}_{in} = \dot{m}_{out,1} + \dot{m}_{out,2} \tag{1.9}$$

Based on the first law of thermodynamics, the enthalpy remains constant in the throttling process in valves. Thus:

$$h_{in} = h_{out} \tag{1.10}$$

Coefficient of performance (COP) and specific energy consumption (SEC) are key factors of design for evaluating the quality of systems (Alimoradiyan & Ratlamwala, 2018). The COP represents amounts of produced cooling on system power consumption, which is expressed as follows:

$$COP = \frac{\dot{m}_{feed}.h_{feed} - \dot{m}_{product}.h_{product}}{Wnet} \quad (1.11)$$

Where $\dot{m}_{feed}$, $\dot{m}_{product}$, h_{feed},$h_{product}$ and $Wnet$ are feed gas mass flow rate, produced liquid hydrogen mass flow rate, feed gas hydrogen mass enthalpy, produced liquid hydrogen mass enthalpy, and total system power consumption. The SEC of the system is calculated as follows:

$$SEC = \frac{W_{net}(kW)}{\dot{m}(kg/h)} \quad (1.12)$$

1.4 Exergy analysis

Exergy shows the potential of a unit or equipment for useful work generation and provides valuable insights into the system efficiency enhancement. It is applied to measure how much equipment/stream's energy input is converted to useful work and how much is consumed. Exergy is the amount of work that is achieved by changing the state of a system from a specific state to ambient conditions, which is usually considered to be a temperature of 25 °C and a pressure of 1 atm in a reversible process (Mohammad H Ahmadi et al., 2017).

Exergy can be regarded as equivalent to reversible work. In other words, reversible work is the highest amount of harness able work (the lowest amount of work consumed in power consumption equipment) when the system goes through a process between initial and final conditions. The calculation of the exergy destruction and spotting its locations are the main objectives of exergy analysis. The amount of consumed exergy is also called irreversibility or exergy destruction. Therefore, the exergy destruction rate is proportional to the entropy produced (Kotas, 2013).

$$Ex_{destroyed} = T_0 S_{gen} \geq 0 \quad (1.13)$$

It is worth noting that exergy destruction has a positive value for all real systems and is zero for reversible systems. In the absence of kinetic energies, potentials, nuclei, electrical, magnetic, and surface tension effects, the exergy rate of a whole system can be considered as the sum of the following components (Kotas, 2013):

$$\dot{E}x = \dot{E}x_{ph} + \dot{E}x_{ch} \tag{1.14}$$

$\dot{E}x$ ،$\dot{E}x_{ph}$ و $\dot{E}x_{ch}$ are the exergy rate of the fluid flow and the sum of the physical and chemical exergy rates, respectively. Physical exergy and chemical exergy rates are calculated from Equations (1.15, 1.16) (Kotas, 2013):

$$\dot{E}x_{ph} = \sum_i \dot{n}_i \left((\bar{h}_i - \bar{h}_0) - T_0(\bar{s}_i - \bar{s}_0) \right) \tag{1.15}$$

$$\dot{E}x_{ch} = \dot{n} \left(\sum_i x_i \, \overline{ex}_i^{ch,0} + \bar{R}T_0 \sum_i x_i \ln(x_i \gamma_i) \right) \tag{1.16}$$

where $\bar{h}_0$ and $\bar{s}_0$ are the enthalpy and entropy of the flow at ambient temperature and pressure. In Equation (1.16), γ_i is the activity coefficient of the i^{th} component, which can have a value greater than or less than one and zero for an ideal mixture of different compounds. Ideal mixture means that the interactions between different molecules are negligible, and the properties of the mixture can be calculated based solely on the properties of the individual components and their respective proportions in the mixture. Calculating the chemical exergy of this nonideal mixture of different compounds is not straightforward due to the activity coefficient. It can be shown that the second term of Equation (1.16) is the Gibbs free energy change due to the mixing of different compounds and the formation of a solution at ambient temperature and pressure. Finally, the chemical exergy equation is transformed as follows (Pourfayaz et al., 2019):

$$\dot{E}x_{ch} = \dot{n} \left(\sum_i x_i \, \overline{ex}_i^{ch,0} \right) + \Delta G^{mix} \tag{1.17}$$

ΔGmix is the Gibbs free energy change of the mixture at ambient temperature and pressure. Knowing the location and amount of irreversibility of various processes in a thermodynamic system is the primary purpose of performing exergy analysis, which can determine the extent and how to improve the performance of that system. The exergy balance can be written as follows (Ebrahimi & Ziabasharhagh, 2017):

$$Ex_i + Ex_{Qi} = Ex_o + Ex_{Qo} + W_{sh} + I \tag{1.18}$$

The latter equation is used to calculate irreversibility or exergy destruction, in which Ex_i and Ex_o are input and output exergies of the flows, Ex_{Qi} and Ex_{Qo} input and output exergies of energy flows, W_{sh} shaft work on or by the system, and I denotes the irreversibly or exergy destruction. (Ebrahimi & Ziabasharhagh, 2017):

$$I_{p,c} = Ex_i - Ex_o = \sum (\dot{m}ex)_i + W - \sum (\dot{m}ex)_o \tag{1.19}$$

The exergy efficiency and destruction equation of some main equipment are shown in Table 1.1. The first step in the exergy analysis is the exergy calculation of streams in the processes, including the exergy of each stream and its exergy loss. Using the exergy balance for each piece of equipment, its destruction and efficiency can be calculated.

Table 1.1. The exergy efficiency and exergy destruction equations of equipment (Cao et al., 2020); (Mousavi & Mehrpooya, 2020); (Pourfayaz et al., 2019)

Equipment	Exergy efficiency	Exergy destruction
Heat Exchangers	$\eta_{ex} = \frac{\sum(\dot{m}ex)_o}{\sum(\dot{m}ex)_i}$	$ex_{des} = \sum(\dot{m}ex)_i - \sum(\dot{m}ex)_o$
Comp./ Pumps	$\eta_{ex} = \frac{\sum(\dot{m}ex)_i - \sum(\dot{m}ex)_o}{\dot{W}}$	$ex_{des} = \dot{W} + \sum(\dot{m}ex)_i - \sum(\dot{m}ex)_o$
Turbines	$\eta_{ex} = \frac{\dot{W}}{\sum(\dot{m}ex)_i - \sum(\dot{m}ex)_o}$	$ex_{des} = \sum(\dot{m}ex)_i - \sum(\dot{m}ex)_o - \dot{W}$
Expansion Valves	$\eta_{ex} = \frac{ex_o^{\Delta T} - ex_i^{\Delta T}}{ex_o^{\Delta P} - ex_i^{\Delta P}}$	$ex_{des} = \sum(\dot{m}ex)_i - \sum(\dot{m}ex)_o$
Ejector	$\eta_{ex} = \frac{\sum(\dot{m}ex)_o}{\sum(\dot{m}ex)_i}$	$ex_{des} = \sum(\dot{m}ex)_i - \sum(\dot{m}ex)_o$
Drums/ Reactors	$\eta_{ex} = \frac{\sum(\dot{m}ex)_o}{\sum(\dot{m}ex)_i}$	$ex_{des} = \sum(\dot{m}ex)_i - \sum(\dot{m}ex)_o$
Cycle	$\eta_{ex} = \frac{\sum(\dot{m}ex)_{prod} - \sum(\dot{m}ex)_{feed}}{\dot{W}}$	$ex_{des} = \sum(\dot{m}ex)_i - \sum(\dot{m}ex)_o$

Exergy destruction and efficiency of the distillation tower are obtained from equations (1.20) and (1.21).

$$Ex_{Column} = Ex_i - Ex_o = \sum(\dot{m}.ex)_i - \sum(\dot{m}.ex)_o \tag{1.20}$$

$$\eta_{ex} = \frac{Wmin}{Wmin + LW}, Wmin = \sum_{Out\ of\ stream} nb - \sum_{in\ to\ stream} nb \tag{1.21}$$

$$(b = h - T_0 s\ ,\ LW = T_0 \Delta S\mathrm{irr} = Lost\ Work)$$

$I_{Reactor}$ and η_{ex} are the exergy destruction and exergy efficiency of the methanol reactor achievable by Equations (1.22) and (1.23) (Ghorbani & Amidpour, 2021):

$$I_{Reactor} = Ex_i - Ex_o = \sum(\dot{m}.ex)_i - Ex_{out}^{Q} - \sum(\dot{m}.ex)_o \quad (1.22)$$

$$\eta_{ex} = \frac{Ex_{out}^{Q}}{\sum(\dot{m}.ex)_i - \sum(\dot{m}.ex)_o} \quad (1.23)$$

For parabolic solar troughs, exergy efficiency and exergy destruction are calculated as follows (Ghorbani & Amidpour, 2021):

$$I_{Collector} = Ex_i - Ex_o = \sum(\dot{m}.ex)_i - Ex_{out}^{Q} - \sum(\dot{m}.ex)_o \quad (1.24)$$

$$Ex_{out}^{Q} = \left[1 - \frac{4}{3}\frac{T_a}{T_s}(1 - 0.28\,ln\,f)\right] \times \dot{Q}_{in} \quad (1.25)$$

$$\eta_{ex} = \frac{\sum(\dot{m}.ex)_i - \sum(\dot{m}.ex)_o}{Ex_{out}^{Q}} \quad (1.26)$$

To calculate the physical and chemical exergy of the non-ideal mixtures in this study, Aspen HYSYS software V.10 and MATLAB code are used. Exergy is a state function that can be obtained for a control volume based on the exergy balance. Applying the exergy balance, the system efficiency and other required data (e.g., input, output, and destruction exergy) are determined for the exergy analysis.

The functions used to link HYSYS software and MATLAB programming are presented in Table 1.2.

Table 1.2. The functions used to link HYSYS software and MATLAB programming

Function	Description
hyconnect	- Connect to Hysys application as an activeX controller.
hyspread	- Connect to Hysys spreadsheet.
hycell	- Connect to Hysys spreadsheet cell.
hyvalue	- Get the value of Hysys spreadsheet cell.
hyunits	- Get the string specifying the units of a spreadsheet cell.
hyset	- Change the value of a cell in Hysys spreadsheet.
hyhold	- Set Hysys solver in hold mode.
hystart	- Set Hysys solver in solve mode.
hyissolving	- Check if the solver is running.
hysolvertoggle	- Toggle solver on/off
hyintegtoggle	- Toggle integrator on/off (dynamics mode).
hyisintegrating	- Check if the integrator is running (dynamics mode).
hyintegtime	- Get current integrator time in seconds (dynamics mode).

1.5 Economic analysis

The method chosen for the economic evaluation is the Annualized Cost of the System (ACS). The parameters of return on investment, product cost, and initial investment are the most influential in selecting the appropriate structure among all possible process designs. In this method, all system costs during the estimated technical life of the whole process are calculated, which consists of the Annualized Capital Cost (C_{acap}), Annualized Replacement Cost (C_{arep}), the Annualized Maintenance Cost (C_{amain}), and the Annualized Operating Cost of the system (C_{aope}). The cost of part replacement is neglected since the project's useful life is assumed to be twenty years. The existing relationships from recent references are used for the economic analysis of equipment used in the proposed process. Thus, the equations are updated using the Marshal and Swift Cost Index (Marshall et al., 2009).

$$Cost_{reference\ year} = Cost_{original\ year} \frac{Cost\ index_{reference\ cost\ year}}{Cost\ index_{original\ cost\ year}} \quad (1.27)$$

The value of ACS is obtained from the following equation (Afrouzy & Taghavi, 2021):

$$\begin{aligned} ACS = {} & C_{acap}(Components) + C_{arep}(Components) \\ & + C_{amain}(Components) + C_{aope}(Labor\ Cost \\ & + Fuel\ Cost + Insurance\ Cost) \end{aligned} \quad (1.28)$$

The annualized capital cost includes purchasing the equipment, which has been levelized throughout the useful life of the studied process. The following equation identifies this levelized cost (Afrouzy & Taghavi, 2021):

$$C_{acap} = C_{Cap}.CRF(i, Y_p) = C_{Cap}.\frac{i.(1+i)^{Y_p}}{(1+i)^{Y_p} - 1} \quad (1.29)$$

where C_{cap} is the total cost of the equipment purchased, i is the actual interest rate, Y_{proj} is equal to the useful life of the project, and CRF is the recoverable amount of the initial costs. To calculate the real interest rate (i), the annual inflation rate (f) and the nominal bank interest rate (j) are utilized as shown in the following equation (Afrouzy & Taghavi, 2021):

$$i = \frac{j - f}{1 + f} \quad (1.30)$$

In calculating the economic analysis of the proposed integrated structures, the project's useful life is 20 years. The fixed capital investment and other outlays are considered to calculate the equipment price. The fixed capital investment includes direct and indirect costs.

1.6 Optimization

NSGAII algorithm is implemented for multi-objective optimization of the processes, with TOPSIS, LINMAP, and fuzzy Bellman-Zadeh being the decision-making methods. A multi-objective optimization strategy has two or more objective functions that must be minimized or maximized. Like a single-objective optimization, it usually has several constraints that the optimal solutions must satisfy (Ahmadi & Ahmadi, 2016); (Ahmadi et al., 2015). In general, a multi-objective optimization problem is defined as follows:

$$Min\{f_1(X), f_2(X), \dots, f_K(X)\} \tag{1.31}$$

$$h_i(X) = 0\ , i = 1,2, \dots, p \tag{1.32}$$

$$g_i(X) \leq 0\ , j = 1,2, \dots, m \tag{1.33}$$

where $X = [x_1, x_1, \dots, x_n]^T$is the vector of the design variables, f represents the objective function, and g and h represent the constraints of the optimization problem that must be satisfied. In this study, the thermodynamic-economic objective functions are the efficiency of the whole hybrid developed system and the product's prime cost (PC).

Genetic algorithms are a powerful tool for solving a multi-objective optimization problem. The multi-objective genetic algorithm used in this paper is the NSGAII algorithm. A decision must be made to choose the optimal point for the developed structure. TOPSIS, LINMAP, and fuzzy Bellman-Zadeh methods have been chosen among several decision-making methods. In multi-objective optimization, the ideal point is associated with the Pareto-optimal front, which represents the set of solutions that cannot be improved in any criterion without worsening at least one other criterion. In the LINMAP method, the optimal endpoint is determined as the point on the Pareto front with the shortest distance to the ideal point. In LINMAP, the ideal point signifies the best possible position, strategically located with a non-ideal point on the opposite side. This non-ideal point indicates an area outside the Pareto front, considered an infeasible or impossible region. In the TOPSIS method, the optimal endpoint is the point with the lowest C_L value, defined in the following equation:

$$C_L = \frac{d_{i-}}{d_{i+} + d_{i-}} \tag{1.34}$$

Where d_{i-} and d_{i+} are the distances of each point from the non-ideal and ideal points, respectively.

The Bellman-Zadeh method, also known as the Bellman-Zadeh decision-making process, which involves converting linguistic variables into precise numerical values using fuzzy set theory. It then applies techniques such as fuzzy arithmetic, aggregation, and defuzzification to determine the best course of action or decision based on the given criteria and their associated linguistic descriptions. The Bellman-Zadeh method provides a systematic approach to decision-making in situations where imprecise or qualitative information is present. It allows decision-makers to handle uncertainty and vagueness in a structured manner when evaluating alternatives and making choices.

CHAPTER 2

THERMODYNAMIC AND EXERGY EVALUATION OF AN INNOVATIVE HYDROGEN LIQUEFACTION STRUCTURE BASED ON EJECTOR-COMPRESSION REFRIGERATION UNIT, CASCADE MULTI-COMPONENT REFRIGERANT SYSTEM, AND KALINA POWER PLANT

Alireza Khatami Jouybari [a], Adrian Ilinca [b], Bahram Ghorbani [c], Sajedeh Rooholamini[d]

[a, b] Department of Mathematics, Computer Science and Engineering, University of Quebec at Rimouski (UQAR), 300 All. des Ursulines, Rimouski, QC G5L 3A1, Canada
[c,d] Faculty of Engineering Modern Technologies, Amol University of Special Modern Technologies, Amol 4615664616, Iran

Paper published in *International Journal of Hydrogen Energy,* February 2022[1]
(Alireza Khatami Jouybari et al., 2022).

Abstract

Considerable recent ecological and energy concerns have aroused the exploitation of sustainable resources and cost-effective production of green energy carriers such as liquid hydrogen. Despite the remarkable merits of the multi-component refrigerant cycle in enhancing the hydrogen liquefaction process efficiency, it contributes to problematic controllability, increasing investment costs. Moreover, it is not easily possible to keep the composition share of refrigerants in case of leakage. This paper develops an innovative integrated structure for liquid hydrogen production, which benefits from the compression-ejector unit and six cascade multi-component refrigerant cycles in the pre-cooling and liquefaction stages. The Kalina power generation uses wasted heat in the integrated system. A power of 595.6 MW is necessary to produce 22.34 kg/s liquid hydrogen, resulting in specific energy consumption (SEC) of 7.405 kWh/kg LH_2 and a coefficient of performance (COP) of 0.103. Besides, the COP of the compression-ejector refrigeration cycle is 0.8682, and the thermal efficiency of the Kalina cycle is 0.1228. The exergy efficiencies of the

[1] Khatami Jouybari, A., Ilinca, A., Ghorbani, B., Rooholamini, S. – « Thermodynamic and Exergy Evaluation of an Innovative Hydrogen Liquefaction Structure Based on Ejector-Compression Refrigeration Unit, Cascade Multi-Component Refrigerant System, and Kalina Power Plant," International Journal of Hydrogen Energy, https://doi.org/10.1016/j.ijhydene.2022.01.190, 2022

proposed structure and the ejector-compression refrigeration cycles are 0.2359 and 0.6462, respectively. Heat exchangers take the lion's share of exergy destruction with 39.55%, followed by gas turbines (27.92%) and compressors (21.81%). Based on sensitivity analysis, with the pressure increase in the secondary stream of Ejector1, the SEC increases by 7.435 kWh/kgLH_2, and the COP of the ejector-compression refrigeration cycle decreases by 0.8242. As the pressure rises in the Kalina cycle, the SEC declines to a low of 7.4135 kWh/kg LH_2 at 26 bar, then increases with pressure.

Keywords: Hydrogen liquefaction structure, ejector-compression refrigeration system, multi-component refrigerant cycle, Kalina power plant, exergy and pinch analyzes

2.1 Introduction

With the unprecedented growth in the world population and people's living standards in the past decades, the global energy demand has been exponentially escalating, resulting in conventional energy sources being extravagantly consumed and diminished. The upward fluctuation in fuel prices resulting from an unbalanced energy market equilibrium and environmental concerns resulting from the considerably high carbon footprints of burning fossil fuels necessitates the use of sustainable resources and eco-friendly fuels like hydrogen (Y. Wang et al., 2012). The versatility of hydrogen makes it the fuel of the future. It is carbon-free, efficient, storable, the principal or side product of many renewable power plants, and the feed of various industries. Hydrogen has a lower heating value (LHV) of 120 kJ/g and a higher heating value (HHV) of 141 kJ/g, an energy density of approximately three times more than gasoline or diesel (Abdin et al., 2020). Liquefied hydrogen has been considered a high-density energy carrier (Berstad et al., 2017) and a substitute for compressed gaseous hydrogen to reduce its transportation expenses. Besides, thanks to its low boiling point, liquid hydrogen is used in the aerospace and rocket industries and high-density cryogenic energy storage (CES) systems (Edeskuty, 1964); (Hamdy et al., 2017).

Several methods have been developed for hydrogen liquefaction to enhance efficiency and lower the total costs, each using a different combination of renewable energy sources, precooling, liquefaction, and power generation cycles. Kanoglu et al. (Kanoglu et al., 2007) proposed a geothermal-energy-based liquid hydrogen production structure. They considered the absorption refrigeration cycle (ARC) for the precooling of hydrogen and the Linde-Hampson refrigeration cycle for the final hydrogen liquefaction, leading to performance improvement and a remarkable decrease in power consumption. Ratlamwala et al. (Ratlamwala, Dincer, Gadalla, et al., 2012) proposed a method for hydrogen liquefaction with a geothermal power generation system, triple-effect ARC for hydrogen precooling, and the Linde-Hampson liquefaction process. The heat required for the precooling of hydrogen in the absorption refrigeration cycle was provided by photovoltaic panels, heated air, and geothermal water. Cooled hydrogen entered the Linde-Hampson liquefaction cycle at -16.4 °C and liquefied. The geothermal power generation system produced the liquefaction required power. The results indicated that the increase in the mass flow rate of air decreases the production capacity of liquid hydrogen and precooled hydrogen. To precool hydrogen to 30 °C, Yilmaz et al. (Yilmaz, 2018) utilized the water-ammonia absorption refrigeration cycle, with the required heat which was supplied by high-temperature geothermal water. This water left the absorption refrigeration cycle and entered the isobutane-turbine to supply the heat for power generation and the power for the Claude liquefaction cycle, resulting in a decline in the specific energy consumption (SEC) to 10.06 kWh/kgLH_2. Hammad et al. (Hammad & Dincer, 2018) utilized liquid nitrogen to precool hydrogen to 81 K and expansion of high-pressure hydrogen gas in three expanders seated in a series to liquefy hydrogen and reduce the temperature to 30 K. The total energy and exergy efficiencies were 15.1% and 11.58%, respectively. Sadaghiani et al. (Sadaghiani & Mehrpooya, 2017) developed a novel liquid hydrogen production structure and analyzed it from energy and exergy points of view. Primary and secondary mixed refrigerant cycles with SECs of 1.10 kWh/kg.LH_2 and 3.26 kWh/kg.LH_2 reduced the hydrogen temperature to -195 °C and -253 °C, respectively. This novel structure was capable of producing 3.45 kg/s liquid hydrogen. The system exergy efficiency and COP were 55.47% and 0.179, respectively. Ratlamwala et al. (Ratlamwala, Dincer, & Gadalla, 2012) developed an innovative hybrid structure for the

tri-generation of power, cooling, and liquefied hydrogen using an absorption unit, Hampson–Linde system, binary power system, and geothermal sources. The impact of geothermal, environment temperature, and concentration of ammonia-water on the main parameters and efficiencies were examined via energy and exergy assessments. Ebrahimi et al. did pinch and sensitivity analyses in a developed hydrogen liquefaction structure fed by biomass to produce hydrogen from rice-husk gasification (Ebrahimi et al., 2020). Biomass was gasified, then compounds such as H_2S, COS, and CO_2 were separated from it. In the end, 0.5540 kg/s hydrogen was produced as syngas. Approximately one-third of this amount went to the liquefaction cycle, and the rest fed the combined steam and gas turbines cycle. This structure could produce 0.166 kg/s, and 5.81 kg/s liquid hydrogen and compressed CO_2, respectively, and has a power generation potential of nearly 8.1 MW. The COP and combined efficiency were 4.360 and 62.10%, respectively. The sensitivity analysis results indicated that with a 50% increase in hydrogen production rate, the total system heat and power efficiency increases to 50.4%. Yin et al. (Yin & Ju, 2020) proved that using the nitrogen precooling cycle and the helium expansion refrigeration cycle can produce 63 kg/h liquid hydrogen at -252.8 °C, with SEC and COP of 7.133 kWh/kg.LH_2 and 0.170. A hydrogen liquefaction structure with a production capacity of 335 ton/d liquid hydrogen and 130 MW power using geothermal energy was proposed by Seyam et al. (Seyam et al., 2020a). The nitrogen precooling cycle was used for precooling and the Claude cycle for the liquefaction of H_2. The exergy efficiency, energy efficiency, and SEC were 63.4%, 19.8%, and 6.41 kWh/kg.LH_2, respectively. The parametric study performed on the hydrogen liquefaction system shows that by reducing the flow rate of hydrogen to 9 kg/s and enhancing the pressure to 20 bar, the system SEC reduces to 4.7%. A liquid hydrogen production system with a capacity of 300 ton/d has been proposed by Cho et al. (Cho et al., 2021). Two mixed-refrigerant refrigeration cycles were used to supply the hydrogen liquefaction process required cooling. The results presented that the total system SEC was 4.07 kWh/kg.LH_2. Chang et al. (Chang et al., 2020) proposed a hydrogen liquefaction structure with a production capacity of 0.5 ton/d liquid hydrogen using liquefied natural gas (LNG) cold energy. LNG prepared required cooling for hydrogen precooling, and the closed Bryton cycle was used for final liquefaction. The system SEC was reported as 14.3 kWh/kg.LH_2. Taghavi et al. (Taghavi et al., 2021) developed an

innovative combined structure for the production of liquid hydrogen using the liquid air cold energy recovery, solid oxide fuel cell, CO_2 power unit, and photovoltaic panels. Six mixed refrigeration systems based on hydrogen/helium refrigerants were employed to liquefy the hydrogen. The SEC and exergy efficiency of the hybrid structure were 5.955 kWh/kgLH_2 & 53.22%, respectively. Seyam et al. (Seyam et al., 2020b) designed a renewable structure for the production of power, liquid hydrogen, and freshwater consisting of six subsystems: solar collectors, ORC, gas turbine power cycle, electrolyzer, multi-effect desalination (MED), and hydrogen liquefaction cycle. Seawater and solar energy were renewable sources used in this structure. The system could produce 355 ton/d liquid hydrogen, 201.3 MW power, and 684 kg/s fresh water. 32.09 kg/s freshwater enters the electrolyzer to produce hydrogen gas. The thermodynamical evaluation proved exergy, thermal efficiencies, and SEC of 23.05%, 88.12%, and 5.24 kWh/kg.LH_2, respectively. Yuksel et al. (Yuksel et al., 2018) proposed an innovative hybrid hydrogen production and liquefaction including a hybrid geothermal power system, a PEM electrolyzer, and hydrogen liquefaction. The results illustrated that as electrolyzer temperature grows from 60 °C to 85 °C, the efficiency of the hydrogen generation system rose from 39% to 44%.

Ejector refrigeration cycle (ERC) has a simple design, is reliable, and requires little maintenance, thanks to not having moving parts in their mechanism. In general, depending on the nozzle outlet location of the primary high-pressure stream, the design of the ejector is divided into two categories. When the nozzle output is front than the fixed area section, it is known as a constant pressure ejector. The constant pressure ejector performs better than the fixed area ejector (Alexis, 2004). It is named fixed-area mixing ejector when the nozzle output is in the fixed area section. Because in the case of constant area ejector, the mixing of the primary high-pressure stream with secondary low-pressure stream leads to a sudden increase in pressure, which forms a series of areas with separation or the return stream at the ejector inlet. This leads to a loss of total stream pressure. While creating a convergent path in constant pressure ejector design accelerates the secondary stream and reduces its pressure. Therefore, the mixing of two streams occurs at almost the same pressure. This reduces the total pressure loss in the two-stream mixing process (Hewedy et al., 2008). The exergy and

energy analysis of a high-capacity liquid carbon dioxide thermal-electrical energy storage system using the ejector refrigeration cycle and the trans critical CO_2 (T-CO_2) Bryton cycle was proposed by Liu et al. (Z. Liu et al., 2020). Al-Nimr et al. (Al-Nimr et al., 2020) developed an integrated structure including an ejector refrigeration cycle, a thermoelectric module system, and solar collectors. The system's COP and exergy efficiency were 0.3095 and 12.5%, respectively. The COP with the integration of thermoelectric modules improved to 13.3%. Two combined systems of power, heating, and cooling based on geothermal were introduced by Zare et al. (Zare & Takleh, 2020). The T-CO_2 ejector refrigeration cycle was used to produce cooling and the Rankine power cycle to produce power. By replacing the gas-coolers with internal heat exchangers, the output heat was reduced to 39.1%; nevertheless, the output refrigeration, exergy efficiency, and net output power were improved to 75.8%, 30.9%, and 49.1%, respectively. Thermodynamic and parametric analyses of a geothermal-combined power and cooling structure using ejector refrigeration and organic Rankine power cycles to generate cooling and power were performed by Wang et al. (N. Wang et al., 2020). The obtained results showed that the exergy efficiency, thermal efficiency, COP, and cooling capacity are 59.16 %, 18.16 %, 0.1224, and 93.74 kW, respectively. Al-Mahmoud et al. (Al-Mahmoud et al., 2020) introduced a novel combined desalination and cooling structure using the ejector refrigeration cycle and humidification-dehumidification (HDH) unit. A temperature increase in the generator and evaporator led to a growth in the COP and entrainment ratio of the system. As condenser temperature increased, these two factors decreased. Sadeghi et al. (Sadeghi & Ahmadi, 2021) thermodynamically and thermo-economically assessed a proposed compressed air energy storage (CAES) structure that used a combined cooling, heating, and power cycle (CCHP). It utilized a carbon dioxide ejector refrigeration cycle and a carbon dioxide gas turbine power generation cycle. In the charging phase, 72.02 kW power was used for air compression. While in the discharging phase, 136.56 kW power was generated by carbon dioxide gas turbines. The CCHP system was capable of generating 1.96 MW cooling and 65.8 MW heat. The results showed a system exergy efficiency of 68.19%.

The ORC and Kalina are two eco-friendly cycles for low-grade heat source efficient usage for system excess heat conversion to useful work or power. Kalina is modified ORC, which uses a mixture of ammonia-water instead of pure organic matter as the working fluid. Reliability, simplicity, and flexibility is the advantage of ORC power cycle, while despite having low overall efficiency. The Kalina uses energy sources more efficiently, has better thermodynamic second law performance, and has higher exergy efficiency (Nemati et al., 2017). Due to the non-constant evaporation temperature of Kalina working fluid, the heat source thermal match with the ammonia-water temperature profiles is good. On the other hand, ammonia concentration can improve the reversibility of the excess heat recovery step (Zare & Mahmoudi, 2015). Ebrahimi-Moghadam et al. (Ebrahimi-Moghadam et al., 2021) introduced the power and cooling co-generation system and evaluated it exergoeconomically and exergoenvironmentally. Air and fuel streams were consumed in the gas turbine power cycle. The heat output from the gas turbine cycle entered the Kalina power cycle and provided the power for the ejector refrigeration cycle. The exergy and exergoeconomic analyses showed that the largest share and the highest cost of exergy destruction belonged to the combustion chamber. In addition, the Kalina cycle had the least amount of energy destruction by water-ammonia working fluid. A novel integrated cooling and power generation structure, including a two-phase ejector refrigeration cycle, Kalina power generation cycle, and photovoltaic power system, was developed by Ghorbani et al. (Ghorbani, Ebrahimi, et al., 2021) for continuous cooling production at 171 K. The ERC with propane working fluid, provided cooling at 233 K. The second cycle with ethylene working fluid provides cooling at 171 K. Excess output heat utilized by the refrigeration cycle to supply the required heat of the Kalina cycle to produce 2753 kW power which improved the COP of the system from 0.7821 to 0.8277. Sensitivity analysis presented that increasing the operating pressure of the Kalina power cycle up to 1500 kPa reduces the structure power consumption to 12.37%. The exergy efficiency of the proposed system was reported to be 28.97%. Rooholamini et al. (Rooholamini et al., 2021) employed an ERC and multi-component refrigeration system using a low-temperature organic Rankine unit to cool the LNG cycle. The COP of the two steps cascade ejector refrigeration unit obtained 0.8635. Du et al. (Y. Du et al., 2021) showed using the ejector refrigeration cycle in the conventional

integrated gas turbine and Kalina power system (GT-KC) can increase the energy efficiency to 5.347% and decrease the minimum energy levelized cost (ELCO) to 0.802%.

So far, several integrated structures have been developed for hydrogen liquefaction. The main focus of many researchers has been on reducing specific energy consumption and using multi-component refrigerant cycles to provide pre-cooling. Using the mixed refrigerant cycle for pre-cooling of hydrogen leads to increased investment costs to control the cycle. Also, keeping the composition constant is not easily possible in case of leakage in the multi-component refrigerants. According to literature research, most articles focus on the use of absorption refrigeration cycles and regasification operations to pre-cool the hydrogen liquefaction cycle instead of the multi-component refrigerants unit. This paper develops an innovative hybrid system of hydrogen liquefaction using the pre-cooling compression-ejector and the cascade multi-component refrigerant cycle. It utilizes a two-stage propane-ethylene ejector refrigeration cycle for hydrogen pre-cooling, the six Linde-Hampson liquefaction cycles as cascade multi-component refrigerant cycle for hydrogen liquefaction, and Kalina power unit to supply part of the power required by the hybrid system. The structure is designed and analyzed in terms of exergy, pinch, and sensitivity. The novelty of the proposed integrated liquid hydrogen production structure is using the compression-ejector refrigeration cycle for pre-cooling of hydrogen rather than conventional refrigerant cycles with multi-component refrigerants.

2.2 System conceptual design

The main objective is to design and analyze a cryogenic hydrogen production structure consisting of the compression-ejector refrigeration, the cascade multi-component refrigerant, and the Kalina power generation cycles. A systematic and powerful method based on thermodynamic characteristics and mathematical approaches has optimized the designed refrigeration process. The block flow diagram (BFD) is illustrated in Figure 2.1. In this process, the compression-ejector refrigeration cycle is chosen to provide the cooling for hydrogen from 298.1 K to 173.1 K, and the cascade multi-component refrigerant cycle

liquefies hydrogen at 17.64 K. The output heat from the Linde-Hampson cycle enters the Kalina power generation cycle for energy recovery. Figure 2.2 depicts the process flow diagram (PFD) of the innovative hybrid system capable of producing liquid hydrogen with a rate of 22.34 kg/s. The Peng-Robinson equation of state is chosen to determine the thermodynamic characteristics of the working fluids and the initial design of the desired structure, as it proves to be highly accurate and applicable for a broad range of temperature and pressure. HYSYS software, which is the appropriate software for steady-state processes simulation and MATLAB m-file are employed to simulate the LH_2 production structure.

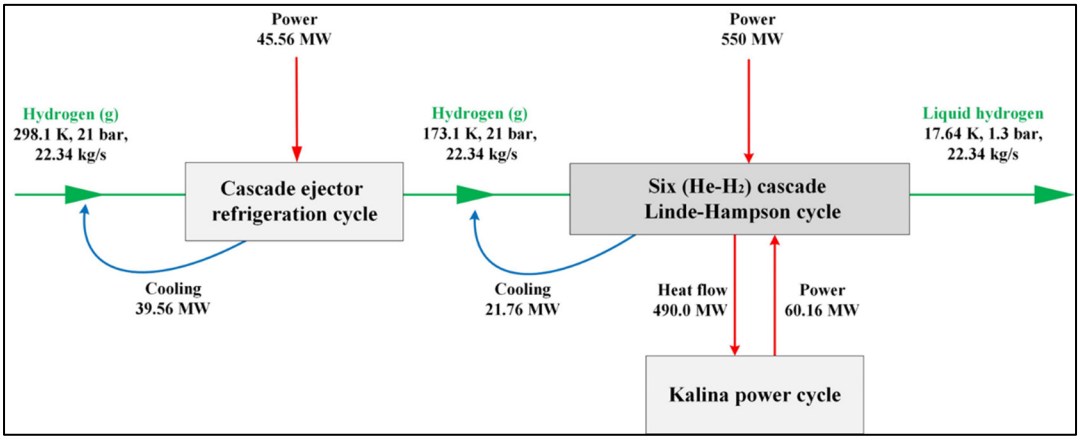

Figure 2.1. The BFD of the novel integrated structure
for the generation of liquid hydrogen

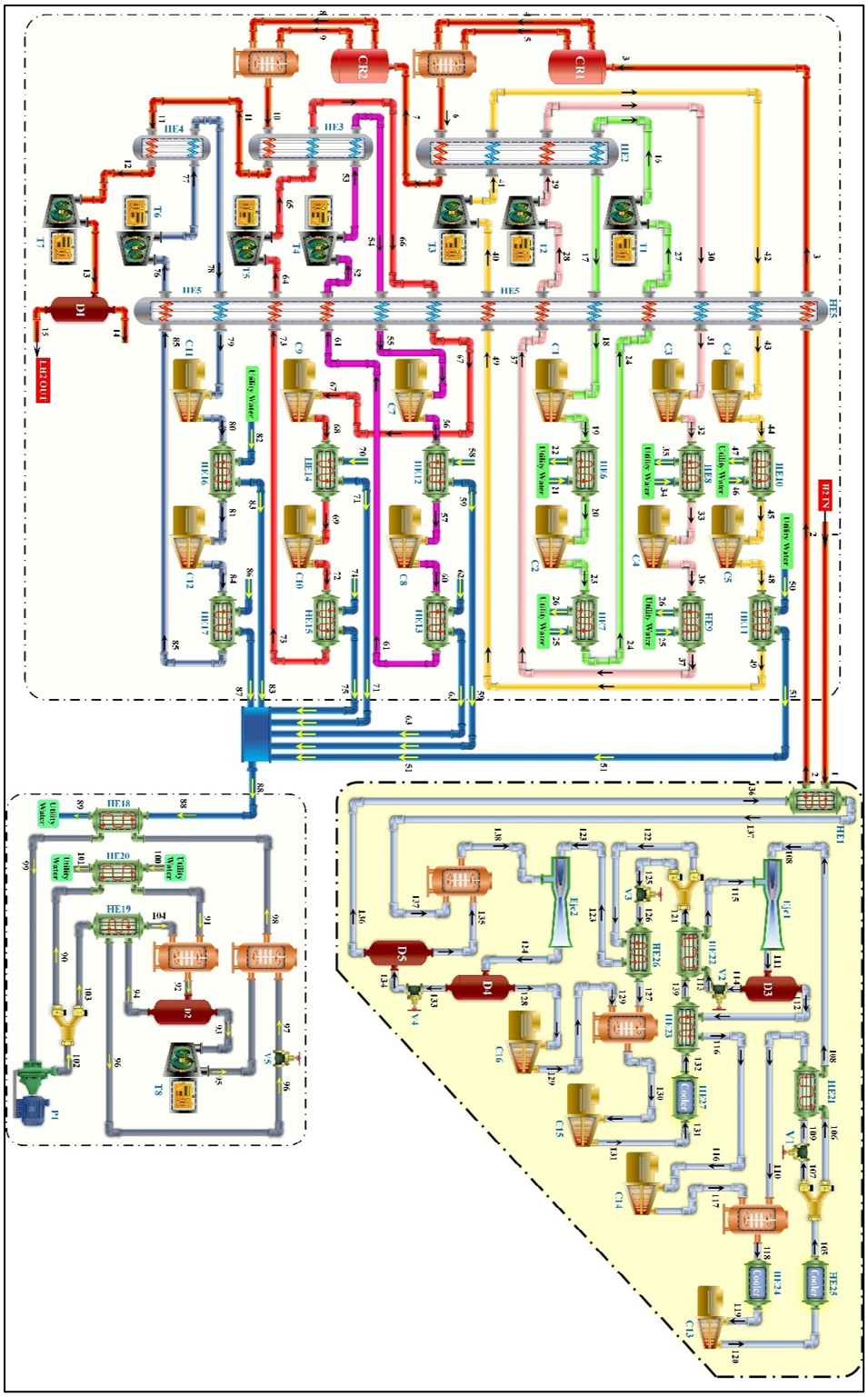

Figure 2.2. PFD of the innovative hybrid system
for the generation of liquid hydrogen

The following assumptions are considered for the process modeling:

1. In heat exchangers, pressure drops and heat leaks are ignored.
2. Kinetic and potential energies are ignored, and steady-state is assumed for heat transfers and streams.
3. In the ejector mixer chamber, the pressure is constant.
4. The isentropic efficiencies of the nozzle, mixing chamber, and diffuser are set to be 85%, 95%, and 85%, respectively, for ejector modeling.

The feed hydrogen temperature is 298.1 K, and the hydrogen liquefaction capacity of the desired integrated novel structure is 1930 ton/d. The 100 ton/d production capacity of the reference paper is used to simulate the Linde-Hampson liquefaction cycle (Sadeghi & Ahmadi, 2021). It was designed to supply liquid hydrogen for a city with up to two thousand vehicles fueled by H_2 (Kramer et al., 2006). Firstly, the hydrogen gas is cooled from 298.1 K to 173.1 K. Then, this precooled gas is converted to liquid hydrogen at 18.15 K in the isobaric cryogenic process. The COP of the compression-ejector and cascade multi-component refrigerant cycles are 0.8683 and 0.035, respectively, which include the power consumption required by the pumps and compressors. Hydrogen reaches a stable equilibrium by passing through the conversion reactors in the cascade multi-component refrigerant cycle by ortho-para conversion. Finally, liquid hydrogen at 18.15 K reaches 17.64 K by an isothermal turbine with a 21 bar to 1.3 bar pressure reduction. In the power generation unit, the structure excess heat is used to power recovery. The Kalina power cycle with the absorption of 489.9 MW heat produces 60.16 MW power.

2.3 System description

As Figure 2.2 depicts, the integrated generation system of liquid hydrogen consists of three units: the propane-ethylene compression-ejector precooling section, the cascade multi-component refrigerant liquefaction section, and the Kalina power generation unit.

22.34 kg/s hydrogen gas (stream 1) enters the HE1 heat exchanger at 298.1 K and is cooled to 173.1 K. In the cryogenic isobaric unit, the outgoing stream from the precooling stage (stream 2) is cooled through the HE5 heat exchanger to 78.55 K and enters the CR1 and then CR2 conversion reactors for ortho-para conversion. In 25 degrees centigrade and atmospheric pressure, the hydrogen equilibrium consists of nearly 75% of ortho hydrogen having a higher energy level than 25% remaining para hydrogen. This higher energy level makes liquid hydrogen more prone to evaporation because the released energy in ortho- para conversion is higher than the required energy for liquid hydrogen evaporation. Thus, the ortho-para conversion is essential for long-term storage of liquefied hydrogen and minimizing the losses of evaporation and vent in a storage tank. Therefore, most of the hydrogen liquefaction processes are designed, so that part of the structure is devoted to ortho-para transformation. Orthohydrogen converts to parahydrogen as the temperature decreases. Two ortho-para converters (CR1 and CR2) are considered in this structure to provide liquid hydrogen with a parahydrogen concentration of almost 50 percent in the first reactor and 100% in the second one. The parahydrogen-enriched stream passing HE2, 3, 4 loses their temperature being ready to enter the turbo-expander T7 at 18.15 K and 21 bar. At the final stage, liquid hydrogen is ready for storage or shipment by a pressure decrease to 1.3 bar in T7 and producing approximately 390 kW power. A separator is designed here to separate the possible vapor phase of the product.

Using an ejector instead of a throttle valve in conventional refrigeration systems improves the refrigeration system's performance (Sarkar, 2012). The main reason for using the ejector is that the expansion in the nozzle of the ejector is more efficient than the expansion in the throttle valve. Moreover, the pressure increase in the ejector output stream reduces the power consumption comparatively lower than that of the conventional compression refrigeration cycle. Two separate ejector refrigeration cycles with the working fluids of propane in the upstream and ethylene in the downstream processes are designed to supply cooling for hydrogen entered hydrogen. Stream 105 contains 168.1 kg/s of liquid propane in 298.1 K and 10.75 bar. While passage through Tee, it divides into 106 and 107 streams. Stream 107, after a pressure reduction of up to 4.1 bar in the throttle valve V1, enters the HE21 heat exchanger

to provides the cooling to reduce the temperature of stream 106. The output high-pressure stream 108 from the HE21 heat exchanger enters the Ejector1 as the primary stream along with the low-pressure secondary stream 115. The liquid and gas phases of the ejector outlet stream are separated by the D3 separator. The gas stream (stream 112) cools the stream 132 (ethylene) into the HE23 heat exchanger up to 243.1 K. After passing V2, the liquid part of the D3 separator with a temperature of 232.4 K (stream 113) provides cooling for the ethylene stream 139 in the downstream cycle. In the downstream ethylene cycle, stream 136 outlet of the D5 separator precools H_2 in the HE1. The excess heat (stream 88) from the cascade multi-component refrigerant cycle enters the water/ammonia Kalina power generation cycle and provides the heat for 60.16 MW of power generation.

2.3.1 Ejector-compression refrigeration cycle modeling

The design of the ejector in this paper is done with the method of mixing two fluids at constant pressure. More theory and background information on the ejector-compressor refrigeration system can be observed in the reference (Tan et al., 2017). The entrainment ratio (ε_r) is considered as Eq. (2-1):

$$\varepsilon_r = \frac{\dot{m}_2}{\dot{m}_1} \tag{2.1}$$

Where $\dot{m}_1$ and $\dot{m}_2$ represent the mass flow rates of high-pressure primary and low-pressure secondary streams, respectively. Expanders are considered to simulate the ejector nozzles in HYSYS software. The expansion of the high-pressure primary stream in the nozzle takes place at point K (Figure 2.3). As it expands, the initial stream pressure decreases to point $\acute{K}$. In Figure 2.3, pressure level in each section of the ejector is illustrated.

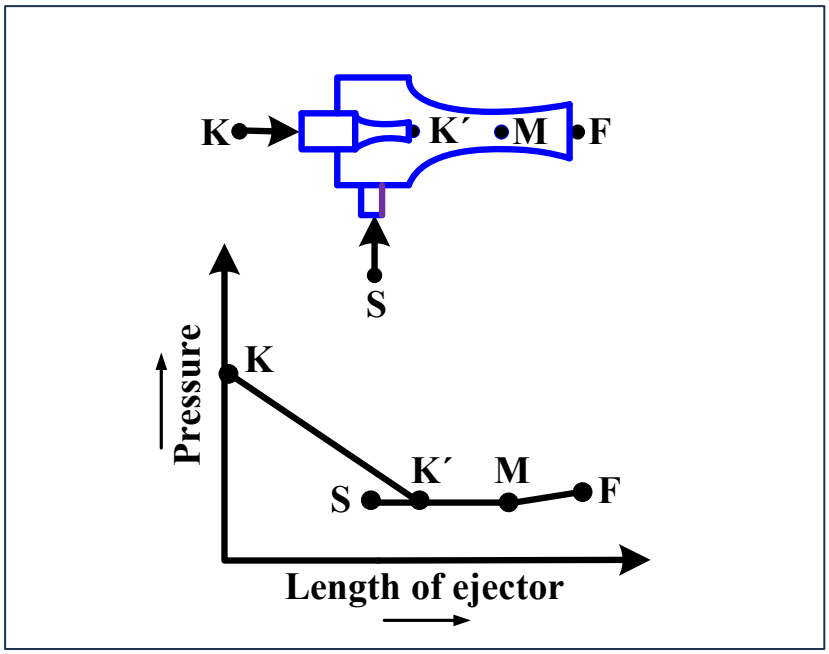

Figure 2.3. The schematic of the ejector modified from:
(Rooholamini et al., 2021); (Tan et al., 2017))

2.3.1.1 Nozzle modeling

The isentropic efficiency of the nozzle (M_N) is the difference of enthalpies of the nozzle input (h_K) and output ($h_{K'}$) to the difference of the enthalpy of the nozzle input and the enthalpy of the ideal nozzle output ($h_{K'}^S$) which is the enthalpy that the fluid would have at the exit of the nozzle if the process were isentropic (Tan et al., 2017); (Tan et al., 2016):

$$M_N = \frac{h_K - h_{K'}}{h_K - h_{K'}^S} \tag{2.2}$$

The pressure of the outlet stream from the nozzle (K') is assumed to be the same as the pressure of the secondary inlet stream to the mixing unit (point S, in Figure 2.3). The point K entropy is equal to the specific entropy of the output of an ideal isentropic nozzle ($S_{K'}^S$). The stream velocity at the nozzle output ($V_{K'}$) without considering the initial stream velocity is defined as follows (Tan et al., 2017); (Tan et al., 2016):

$$V_{K'} = \sqrt{2(h_{K'} - h_K) \times 1000} \tag{2.3}$$

2.3.1.2 Mixing unit modeling

For the ejector mixing unit simulation, a mixer and a tube are used in HYSYS (from point K′ to point M in Figure 2.3). The specific enthalpy of the mixture leaving the mixer unit is (Tan et al., 2017); (Tan et al., 2016):

$$h_M = \frac{1}{1+\varepsilon_r}.h_K + \frac{\varepsilon_r}{\varepsilon_r+1}.h_S - \frac{V_m^2}{2000} \tag{2.4}$$

V_M (the output stream velocity of the mixer unit) and $V_{M,i}$ (the ideal output velocity of the mixer unit) are obtained from equations (2-5) and (2-6) (Moghimi et al., 2018):

$$V_M = V_{M,I}\sqrt{\eta_M} = \frac{V_{K'}}{1+\varepsilon_r}.\sqrt{\eta_M} \tag{2.5}$$

$$V_{M,i} = \frac{1}{1+\varepsilon_r}.V_{K'} \tag{2.6}$$

Where η_M represents the efficiency of the mixture.

2.3.1.3 Diffuser modeling

Due to the similarity of the compressor and diffuser stream equations, the compressor is used in the ejector diffuser unit simulation. A low-pressure two-phase stream enters the diffuser and exits at a higher pressure. The ideal enthalpy of the diffuser output stream (h_F) is calculated as follows:

$$h_F = \frac{1}{1+\varepsilon_r}.h_K + \frac{\varepsilon_r}{\varepsilon_r+1}.h_S \tag{2.7}$$

$$h_{F,i} = h_M + \eta_d(h_F - h_M) \tag{2.8}$$

Next, the diffuser outlet pressure and its quality can determine using the state equation of the model in HYSYS software (Tan et al., 2017).

$$P_F = f(h_{F,i}, s_{F,i}) \tag{2.9}$$

$$x_F = f(h_F, p_F) \tag{2.10}$$

Based on the data extracted from the references (Tan et al., 2017); (Tan et al., 2016), the relation between the entrainment ratio and the quality of the outlet stream is defined as:

$$x_F = \frac{1}{1 + \varepsilon_r} \tag{2.11}$$

The entrainment ratio should be chosen to equal the output stream's quality from relations (2-10) and (2-11). Figure 2.4 shows the innovative integrated structure simulation algorithm of the hydrogen liquefaction cycle using the ejector-compression refrigeration unit and six cascade multi-component refrigerant cycle.

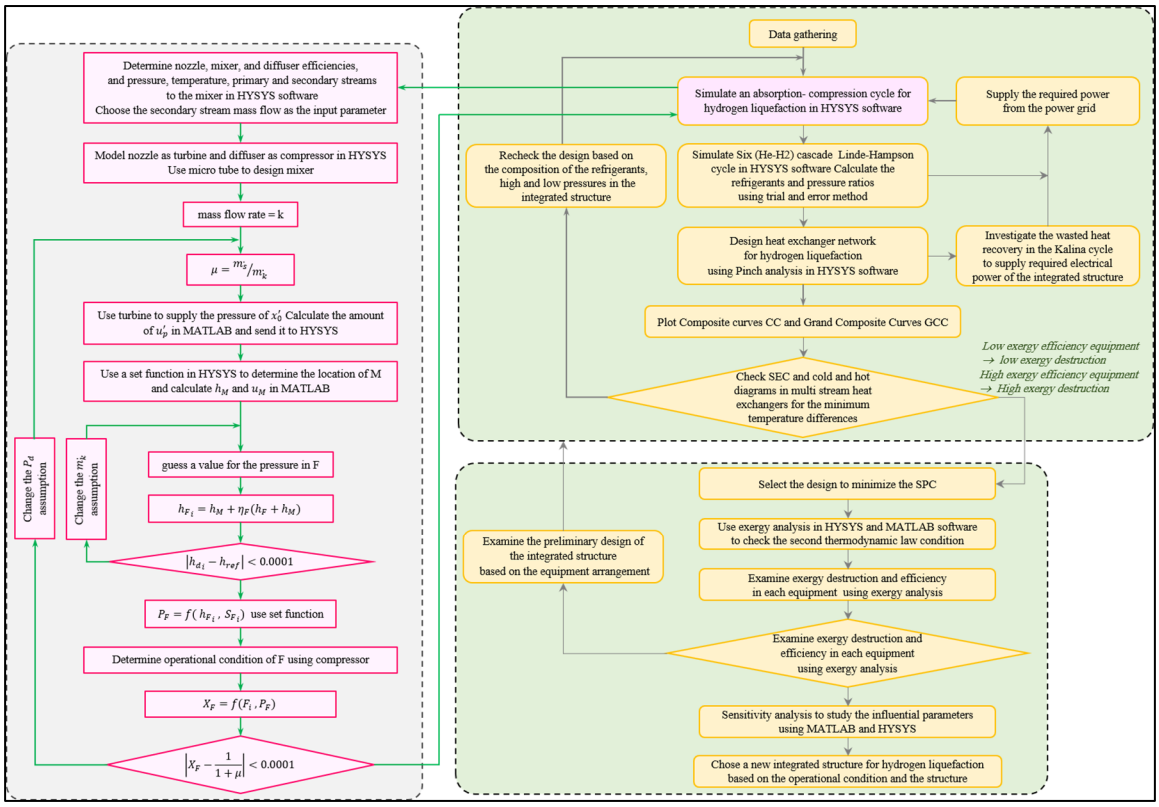

Figure 2.4. The simulation algorithm of the hydrogen liquefaction cycle

2.4 Energy and exergy analyses

Energy. The steady-state control volume energy and mass balance equation based on the thermodynamic first law is (Yousefizadeh Dibazar et al., 2020):

$$\dot{Q}_{Cv} - \dot{W}_{Cv} + \sum \dot{m}_i \left(h_i + \frac{1}{2}v_i^2 + gz_i\right) - \sum \dot{m}_o \left(h_o + \frac{1}{2}v_o^2 + gz_o\right) = 0$$
$$\sum \dot{m}_{in} = \sum \dot{m}_{out} \tag{2.12}$$

In Eq. (2-12), $\dot{Q}_{Cv}$, $\dot{m}$, h, $\dot{W}_{Cv}$, v, z and g are heat transfer rate, mass flow rate, specific enthalpy, work, the stream velocity of the working fluid, the gravitational acceleration and the elevation from a reference situation, respectively. The equations defining the energy balance in heat exchangers are provided in Eq. (2-13):

$$\dot{m}_{in,i}(h_{in1,i} - h_{in2,i}) = \dot{m}_{out,i}(h_{out1,i} - h_{out2,i})$$
$$T_{in1,i} = T_{out1,i} + \Delta\ T_{in,HXi} \tag{2.13}$$

Isentropic efficiency is assumed in the energy balance equations of compressors, turbines, and pumps, and heat loss is ignored. So, the energy balance in these types of equipment is considered as:

$$h_{out} = \frac{h_{out}^{S} - h_{in}}{\eta_s} + h_{in} \tag{2.14}$$

$$h_{out} = (h_{out}^{S} - h_{in})\eta_s + h_{in} \tag{2.15}$$

In the mixer, the energy balance and the mass conservation equations are defined as follows (Cao et al., 2020):

$$\dot{m}_{in,1}h_{in,1} + \dot{m}_{in,2}h_{in,2} = \dot{m}_{out}h_{out} \tag{2.16}$$

$$\dot{m}_{in,1} + \dot{m}_{in,2} = \dot{m}_{out} \tag{2.17}$$

$$h_{out} = \frac{\dot{m}_{in,1}h_{in,1} + \dot{m}_{in,2}h_{in,2}}{\dot{m}_{in,1} + \dot{m}_{in,2}} \tag{2.18}$$

Similarly, in the flash drums and separators, we have:

$$\dot{m}_{in}h_{in} = \dot{m}_{out,1}h_{out,1} + \dot{m}_{out,2}h_{out,2} \tag{2.19}$$

$$\dot{m}_{in} = \dot{m}_{out,1} + \dot{m}_{out,2} \tag{2.20}$$

Based on the first law of thermodynamics, the enthalpy remains constant in the throttling process in valves. Thus:

$$h_{in} = h_{out} \tag{2.21}$$

COP and SEC are key factors of design for evaluating the quality of systems (Alimoradiyan & Ratlamwala, 2018). The COP represents amounts of produced cooling on system power consumption, which is expressed as follows:

$$COP = \frac{\dot{m}_{feed}.h_{feed} - \dot{m}_{product}.h_{product}}{Wnet} \tag{2.22}$$

Where $\dot{m}_{feed}$, $\dot{m}_{product}$, h_{feed},$h_{product}$ and $Wnet$ are feed gas mass flow rate, produced liquid hydrogen mass flow rate, feed gas hydrogen mass enthalpy, produced liquid hydrogen mass enthalpy, and total system power consumption. The SEC of the system is calculated as follows:

$$SEC = \frac{W_{net}(kW)}{\dot{m}_{LH_2}(kg/h)} \tag{2.23}$$

Exergy. The structure distance from the dead state (the temperature of 298.1 K and the pressure of 101 kPa) is measured by exergy analysis. Exergy shows the potential of a unit or equipment for useful work generation and provides valuables insights into the system efficiency enhancement. It is applied to measure how much equipment/stream's energy input is converted to useful work and how much is consumed. The amount of consumed exergy is also called irreversibility or exergy destruction. The calculation of the exergy destruction and spotting its locations are the main objectives of exergy analysis. The irreversibility is defined as Eq. (2-24).

$$I = |W_{rev} - W_{real}| \tag{2.24}$$

The exergy destruction is equal to entropy generation as Eq. (2-25).

$$ex_{des,K} = T_0.S \tag{2.25}$$

Where $ex_{des,K}$, T_0 and $S$are the exergy destruction, ambient temperature, and generated entropy (Cao et al., 2020).

$$ex_{total,K} = ex_{Ph,K} + ex_{Ch,K} \tag{2.26}$$

In Eq. (2-26), the $ex_{total,K}$, $ex_{Ch,K}$, and $ex_{Ph,K}$ are the total, chemical, and physical exergies. The total exergy is defined as the sum of physical and chemical exergies in a stream (Pourfayaz et al., 2019):

$$ex_{Ph,K} = (h - h_0) - T_0(S - S_0) \tag{2.27}$$

$$ex_{Ch,K} = \sum \left(X_i ex_o^i\right) + G - \sum X_i\, G_i \tag{2.28}$$

In Eq. (2-27) and (2-28), the h_0, S_0, T_0 ,X_i, ex_o^i, G and G_i are the enthalpy and entropy at ambient condition, ambient temperature, the mole fraction of component i, standard chemical exergy of ith stream (in the ideal mixture), Gibbs free energy of a mix, and Gibbs free energy of ith stream, respectively. The irreversibility in the structure (I) is calculated as follows (Mehrpooya & Pakzad, 2020):

$$I = Ex_{out} + Ex_{Qout} + W_{shaft} - (Ex_{in} + Ex_{Qi}) \tag{2.29}$$

Ex_{in} and Ex_{out}indicate the input exergy and the output exergy. Ex_{Qi} and Ex_{Qout} refer to the exergy due to the inlet heat and heat loss.

2.5 Result and discussion

The simulation results, exergy, pinch, and sensitivity analyzes are presented in this section. The composition of major streams and their thermodynamic properties are tabulated in Table 2.1 and Table-A I.1 (see Annex I) , respectively. As the main product of the integrated structure, 22.34 kg/s of liquid hydrogen is produced at the temperature of 17.64 K. To

precool hydrogen gas, a compression-ejector refrigeration cycle with 39.56 MW of cooling capacity is employed. The cascade multi-component refrigerant cycle provides 21.76 kW cooling for the hydrogen liquefaction process. The 489.9 MW excess heat in the six Linde-Hampson refrigeration cycles is utilized for 60.16 MW power generation in the Kalina power cycle. COP and SEC of the integrated system are 0.103 and 7.405 kWh/kg LH_2, respectively. The equipment specification is accessible from Table 2.2. The exergy, pinch, and sensitivity analyses results are presented below.

Figures 2.5 to 2.7 illustrate T-S and P-H plots for two precooling ejector-compression refrigeration cycles and the Kalina power generation cycle. These figures provide information regarding the variation of entropy and enthalpy of refrigerant(s) with changes in temperature and pressure. Besides, the phase state of the refrigerant in each step of the cycle is accessible. As the efficiency of equipment like pumps, turbines and compressors are not assumed to be 100 % and deviations from the ideal state occur, places prone to irreversibility can be deduced from figures 2.5, 2.6, and 2.7. The stream pressure increase in the pumps and compressors of the integrated structure is presented as a vertical line in the P-H plot. It is accompanied by increasing the entropy slightly in the T-S diagram (see lines 99-102, 116-17, 130-131, 119-120). Also, increasing the temperature of heat exchangers at constant pressure is associated with increasing entropy in the T-S plot. On the other hand, the reduction of flow pressure in the gas turbines and the throttle valves is the form of a vertical line in the P-H diagram and is followed by increasing the entropy slightly in the T-S diagram (see lines 93-95, 96-97, 107-109, 113-114, 125-126, 133-134).

Table 2.1. The composition of streams in the integrated structure (mole fraction)

Stream	Hydrogen	Helium	Propane	Ethylene	H_2O	Ammonia
1	100	0	0	0	0	0
16	0	100	0	0	0	0
21	0	0	0	0	100	0
25	0	0	0	0	100	0
28	52.8	47.2	0	0	0	0
34	0	0	0	0	100	0
38	0	0	0	0	100	0
40	31.04	68.96	0	0	0	0
46	0	0	0	0	100	0
50	0	0	0	0	100	0
52	36	64	0	0	0	0
58	0	0	0	0	100	0
62	0	0	0	0	100	0
64	47.2	52.8	0	0	0	0
70	0	0	0	0	100	0
74	0	0	0	0	100	0
76	36	64	0	0	0	0
82	0	0	0	0	100	0
86	0	0	0	0	100	0
90	0	0	0	0	17.81	82.19
100	0	0	0	0	100	0
105	0	0	100	0	0	0
121	0	0	0	100	0	0

Table 2.2. The equipment specifications used in the novel integrated structure

Pump						
Parameter	Adiabatic efficiency	Power	ΔP	P ratio	Pressure head	Capacity
Unit	%	kW	bar	-	m	m^3/h
P1	80	1489	1860	5.227	278.8	2305.5
Turbine						
Parameter	Isentropic efficiency	Power	ΔP	P ratio	Polytropic efficiency	Outlet Temp.
Unit	%	kW	bar	-	%	K
T1	80	3440	1600	0.467	77.39	51.31
T2	80	8168	439	0.532	78.19	148.7
T3	80	22380	946	0.185	74.8	44.29
T4	77	9149	324	0.179	71.01	33.09
T5	80	4823	209	0.251	75.82	27.09
T6	80	5348	321	0.03	67.74	17.08
T7	85	390.5	1970	0.062	84.84	17.64
T8	90	61650	1830	0.197	88.82	296.5
Compressor						
Parameter	Adiabatic efficiency	Power	ΔP	P ratio	Polytropic efficiency	Outlet Press.
Unit	%	kW	bar	-	%	bar
C1	80	16990	700	1.5	81.52	21
C2	80	14851	900	1.429	81.35	30
C3	80	10498	151	1.303	80.87	6.5
C4	80	14883	288	1.443	81.19	9.38
C5	80	114519	275	2.279	82.52	4.9
C6	80	121289	671	2.369	82.63	11.61
C7	80	69384	99	2.394	82.75	1.7
C8	80	66870	225	2.324	82.66	3.95
C9	80	41581	70	2	82.16	1.4
C10	80	41489	139	1.993	82.15	2.79
C11	80	77566	50	6	85.04	0.6
C12	80	73992	271	5.517	84.85	3.31
C13	85	10218	665	2.622	85.87	10.75
C14	85	11416	292.9	3.5	85.97	4.1
C15	85	15194	1240	3.885	86.86	16.7
C16	85	8736.4	313.8	3.702	86.97	4.3

Table 2.2. The equipment specifications used in the novel integrated structure (continued)

Heat exchanger					
Parameter	Min. approach	LMTD	UA	Heat duty	Cold pinch Temp.
Unit	K	K	MJ/h°C	kW	K
HE1	2.662	32.28	4.411	39560	170.4
HE2	8.758	32.21	3.192	28570	44.29
HE3	1.057	1.979	18.68	10270	27.09
HE4	1.071	1.622	5.073	2286	17.09
HE5	1	1.598	1452	644300	297.1
HE6	1	2.234	26.99	16750	297.1
HE7	1	1.734	140.5	14880	355.1
HE8	1	2.164	16.96	10200	297.1
HE9	1	5.069	10.57	14880	297.1
HE10	1	7.118	57.43	113600	297.1
HE11	1	12.89	33.87	121300	297.1
HE12	1	10.01	24.76	68870	297.1
HE13	1	11.28	21.34	66870	297.1
HE14	1	1.528	96.96	41160	297.1
HE15	1	1.804	82.77	41490	297.1
HE16	1	41.16	6.679	76370	297.1
HE17	1	39.63	6.721	73990	297.1
HE18	12.81	14.74	120	489900	373.1
HE19	19.23	43.02	0.615	7345	353.1
HE20	1.3	5.246	295	429800	278.6
HE21	5	14.07	2.283	8919	268.5
HE22	3.8	5.066	31.74	44660	232.8
HE23	6.23	6.741	6.479	12130	269.9
HE24	5	15.74	2.134	9330	198.5

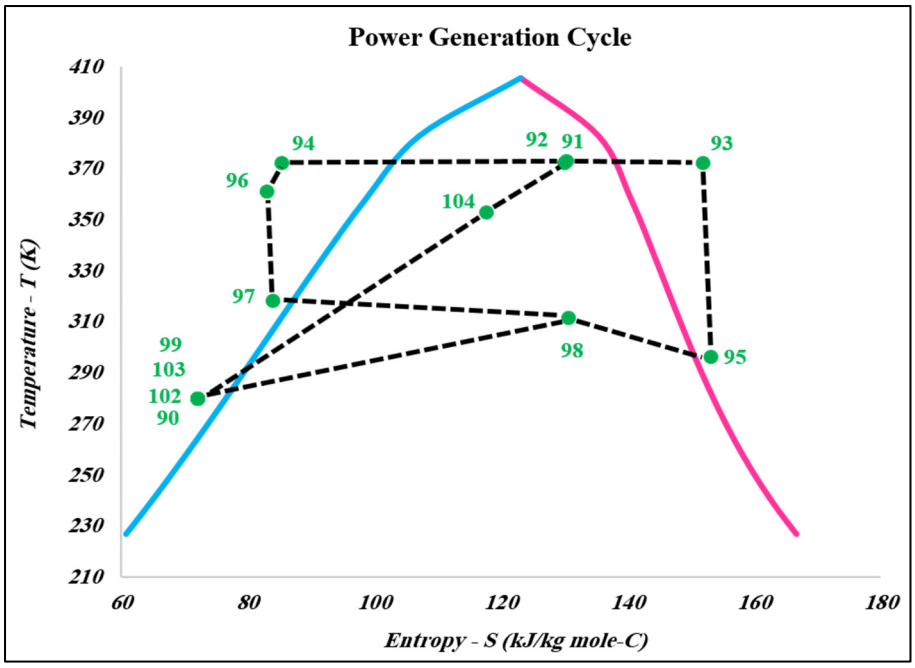

(a) T-S diagram

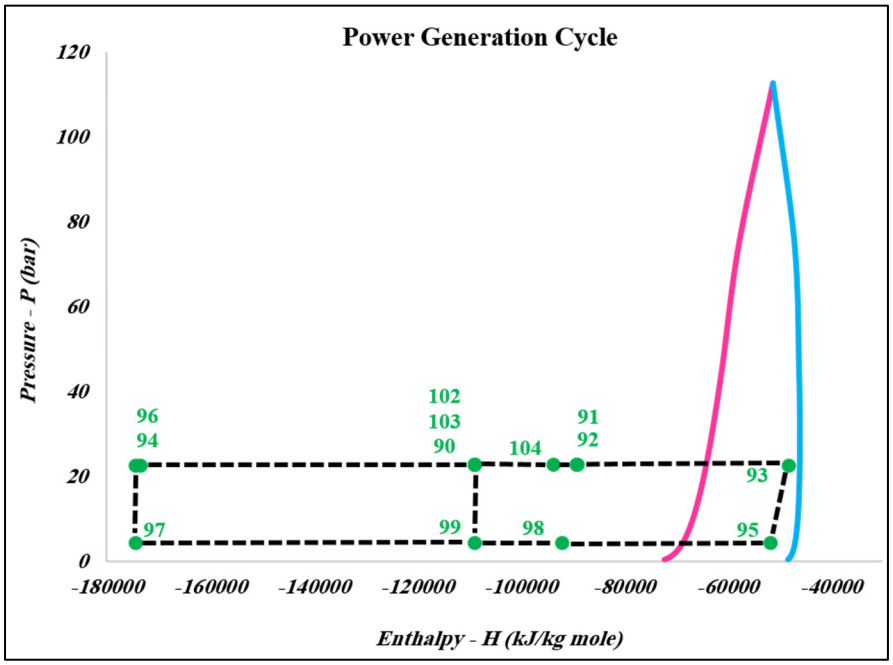

(b) P-H diagram

Figure 2.5. P-H and T-S diagrams of refrigerant in the Kalina power generation cycle

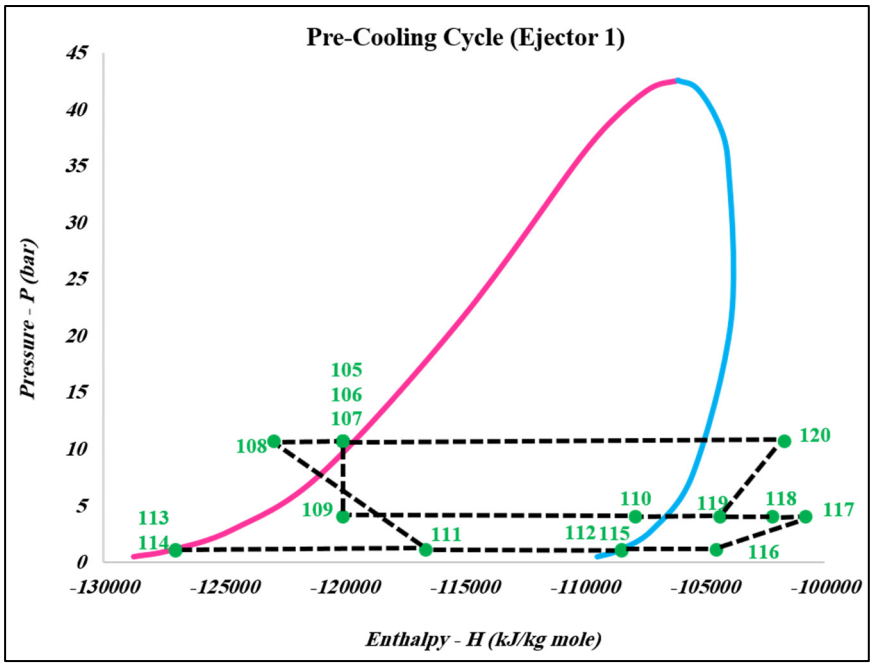

(a) P-H diagram

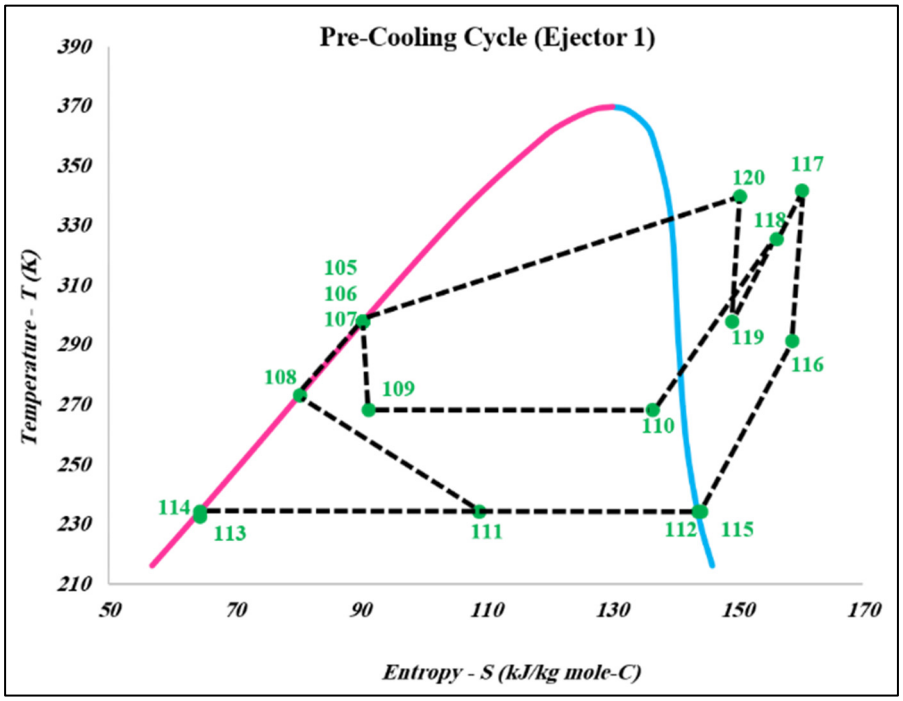

(b) T-S diagram

Figure 2.6. P-H and T-S diagrams of
the first ejector-compression refrigeration cycle

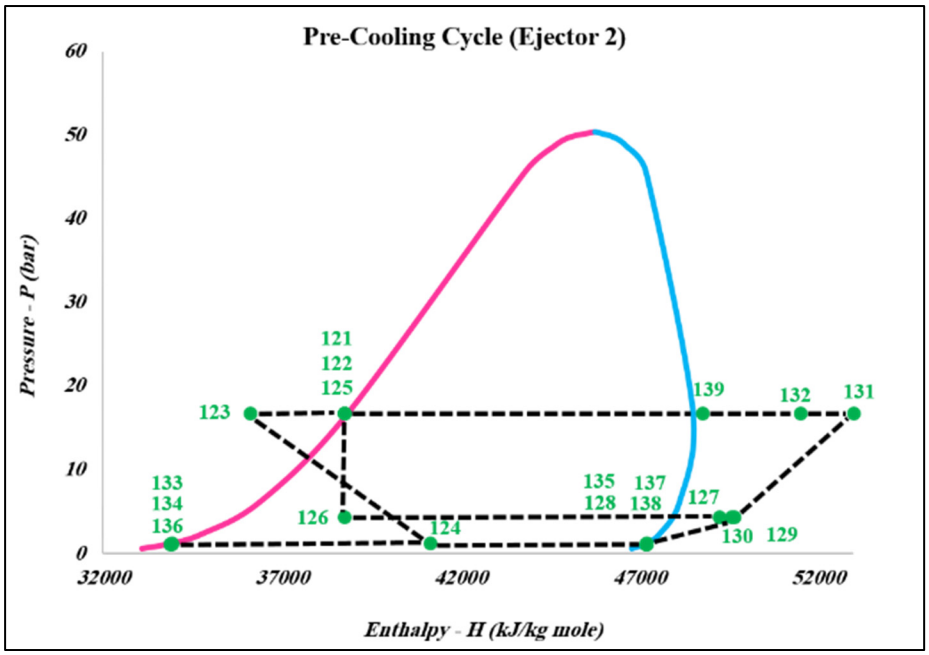

(a) P-H diagram

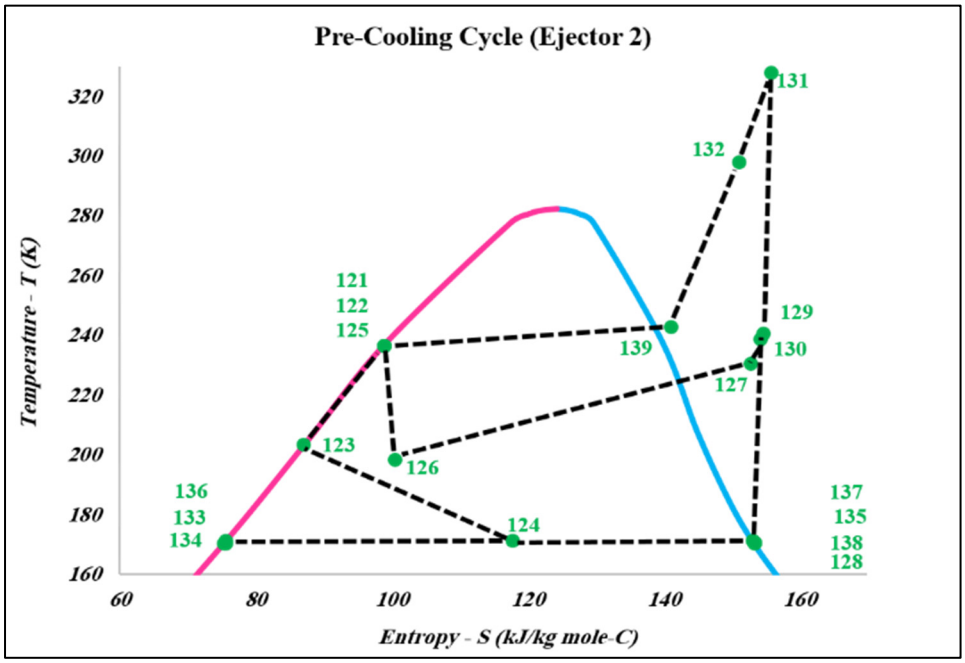

(b) T-S diagram

Figure 2.7. P-H and T-S diagrams of
the second ejector-compression refrigeration cycle

2.5.1 Exergy analysis results

Table 2.3 demonstrates the exergy characteristics of some streams used in the process. Table 2.4 represents the exergy efficiency and exergy destruction equations of equipment in the proposed structure. Exergy balance equations for components used in the hybrid structure are shown in Appendix A. Exergy analysis shows the quantity and the location of exergy destruction produced by each piece of equipment during the process. Based on each stream's exergy flow, exergy efficiency and exergy destruction in equipment (Table-A I.2 in Annex I) are calculated. Figure 2.8 illustrates each piece of equipment shared in the total exergy destruction. In this regard, heat exchangers, turbines and compressors have the highest percentage of exergy destruction with 0.3956%, 0.2793%, and 0.2181%. The total system exergy efficiency is 23.59%. The number of low- temperature heat exchangers in the developed system is more than other equipment; also a large part of the heat in these systems is wasted on the surrounding environment, so the amount of exergy destruction in this equipment is more than other equipment. Also, low-temperature turboexpanders don't have good performance and as a result, have high exergy destruction.

2.5.2 Validation phase results

Partial communication is utilized to validate the combined process. The parts of the hydrogen liquefaction system and the ejector-compression refrigeration unit are compared separately with similar processes in the industry or in the sources in which the process data is reported, and its accuracy is validated. Reference data (Asadnia & Mehrpooya, 2017) is used to simulate the cascade multi-refrigerant cycle for final hydrogen liquefaction. The comparison between data obtained from the integrated co-generation structure of liquid hydrogen, power, and cooling and the reference data (Asadnia & Mehrpooya, 2017) shows the SEC of the novel structure is relatively lower (Figure 2.9). To simulate the ejector-refrigeration cycle, Ref. (Tan et al., 2017) is used. The validation of the simulated ejector-compressor cycle in this paper compared to the reference (Tan et al., 2017) is presented in Table 2.5. To apply the ejector-compression refrigeration cycle in the integrated structure of hydrogen liquefaction, changes have been made in its operational characteristics. The results of refrigeration cycle

simulations show that the exergy efficiency and performance coefficient of the developed combined structure are higher than the reference (Tan et al., 2017).

Table 2.3. The exergy flow of some streams in the novel integrated structure (kW)

	Physical exergy	Chemical exergy	Total exergy		Physical exergy	Chemical exergy	Total exergy
1	83473.1	2642994.9	2726468	71	5409.8	63960.4	69370.2
2	95213.7	2642994.9	2738208.7	72	48895.2	2184876	2233771.2
3	141340.4	2642994.9	2784335.3	73	43253.3	2184876	2228129.3
7	150112.2	2623953.9	2774066.1	77	77867.5	1056791.8	1134659.2
11	198455.7	2642994.9	2841450.7	81	-13242.9	1056791.8	1043548.8
12	225601.2	2642994.9	2868596.1	82	22.56	118669.3	118691.9
13	224034.06	2642994.9	2867028.9	83	10037.1	118669.3	128706.4
16	154240.3	379350.0	533590.3	86	21.9	114980.0	115001.9
17	140655.6	379350.0	520005.6	87	9725.0	114980.0	124705.1
18	81318	379350.0	460668.0	88	60228.3	824338.1	884566.5
23	106195.7	379350.0	485545.7	93	128815.7	5692702.4	5821518.1
26	1250.1	38521.5	39771.5	96	8928.8	1455966	1464894.8
27	162841.5	379350.0	542191.5	97	6438.6	1455966	1462404.6
28	78192.7	1557056.5	1635249.3	98	65983.4	7148668.4	7214651.8
29	65833.0	1557056.5	1622889.6	99	78886.4	7148668.4	7227554.8
32	57119.9	1557056.5	1614176.5	102	80160.6	7148668.4	7228828.9
33	56579.7	1557056.5	1613636.2	103	1533.2	136729.4	138262.6
36	68872.9	1557056.5	1625929.5	106	15991.2	6188942.8	6204934
37	67758.2	1557056.5	1624814.8	107	3816.6	1477110.5	1480927.1
40	433941.5	4944719.4	5378660.9	110	2642.4	1477110.5	1479752.9
41	371120.4	4944719.4	5315839.8	111	17042.2	11019676	11036718
42	262821.6	4944719.4	5207540.9	112	2748.6	6189858.5	6192607
43	72703.4	4944719.4	5017422.8	113	14296.9	4830732.8	4845029.8

Table 2.3. The exergy flow of some streams in the novel integrated structure (kW) (continued)

	Physical exergy	Chemical exergy	Total exergy		Physical exergy	Chemical exergy	Total exergy
45	152344.7	4944719.4	5097064.1	115	1769.1	4830732.8	4832502
48	256093.9	4944719.4	5200813.3	118	13086.1	7666969	7680055.1
49	235835.5	4944719.4	5180554.9	119	12720.2	7666969	7679689.2
52	217731.4	2277474.0	2495205.5	122	33912.2	4868602	4902514.2
53	181733.9	2277474.0	2459207.9	123	37207.1	4868602	4905809.1
56	40102.4	2277474.0	2317576.4	126	8025.2	1214326.9	1222352.1
57	28187.3	2277474.0	2305661.4	127	3473.9	1214326.9	1217800.7
61	74124.2	2277474.0	2351598.3	131	30090.6	6082928.8	6113019.4
62	22.1	116245.0	116267.14	132	29777.3	6082928.8	6112706.1
63	7992.2	116245.0	124237.22	133	34679.1	4077180.1	4111859.2
66	135798.3	2184876.0	2320674.3	136	34649.1	4057827.9	4092476.9
67	-15789.1	2184876.0	2169086.9	137	5022.9	4057827.9	4062850.8
68	19366.2	2184876.0	2204242.2	138	5044.5	4076624.8	4081669.3
69	13804.5	2184876.0	2198680.5	139	31068.9	6082928.8	6113997.7

Table 2.4. The exergy efficiency and exergy destruction equation of equipment (Cao et al., 2020); (Mousavi & Mehrpooya, 2020); (Pourfayaz et al., 2019)

	Exergy efficiency	Exergy destruction
Heat Exchanger	$\eta_{ex} = \frac{\sum(\dot{m}ex)_o}{\sum(\dot{m}ex)_i}$	$ex_{des} = \sum(\dot{m}ex)_i - \sum(\dot{m}ex)_o$
Comp./ Pump	$\eta_{ex} = \frac{\sum(\dot{m}ex)_i - \sum(\dot{m}ex)_o}{\dot{W}}$	$ex_{des} = \dot{W} + \sum(\dot{m}ex)_i - \sum(\dot{m}ex)_o$
Turbine	$\eta_{ex} = \frac{\dot{W}}{\sum(\dot{m}ex)_i - \sum(\dot{m}ex)_o}$	$ex_{des} = \sum(\dot{m}ex)_i - \sum(\dot{m}ex)_o - \dot{W}$
Expansion Valve	$\eta_{ex} = \frac{ex_o^{\Delta T} - ex_i^{\Delta T}}{ex_o^{\Delta P} - ex_i^{\Delta P}}$	$ex_{des} = \sum(\dot{m}ex)_i - \sum(\dot{m}ex)_o$
Ejector	$\eta_{ex} = \frac{\sum(\dot{m}ex)_o}{\sum(\dot{m}ex)_i}$	$ex_{des} = \sum(\dot{m}ex)_i - \sum(\dot{m}ex)_o$
Drums/ Reactor	$\eta_{ex} = \frac{\sum(\dot{m}ex)_o}{\sum(\dot{m}ex)_i}$	$ex_{des} = \sum(\dot{m}ex)_i - \sum(\dot{m}ex)_o$
Cycle	$\eta_{ex} = \frac{\sum(\dot{m}ex)_{product} - \sum(\dot{m}ex)_{feed}}{\dot{W}}$	$ex_{des} = \sum(\dot{m}ex)_i - \sum(\dot{m}ex)_o$

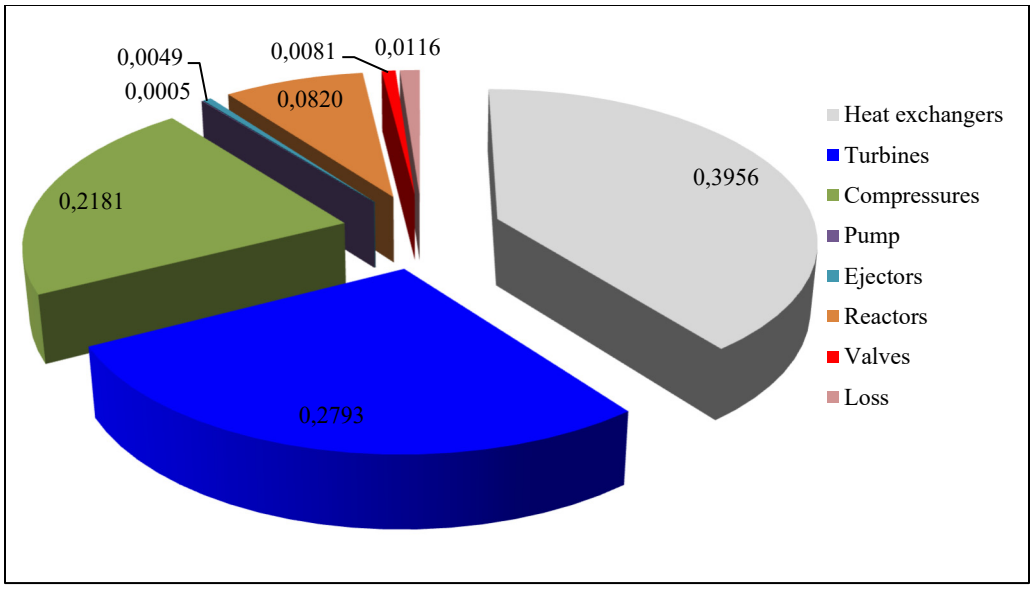

Figure 2.8. The share of each equipment's exergy destruction

Table 2.5. Validation of the ejector-compressor refrigeration cycle compared to reference
(Tan et al., 2017)

The main parameters	Unit	Tan et al.	In this paper
Performance coefficient of ejector-compression refrigeration cycle	-	0.76	0.868
Exergy efficiency of ejector-compression refrigeration cycle	%	60.4	64.62
The output stream pressure of the ejector 1	kPa	119.6	117.1
The output stream pressure of the ejector 2	kPa	118.4	116.2

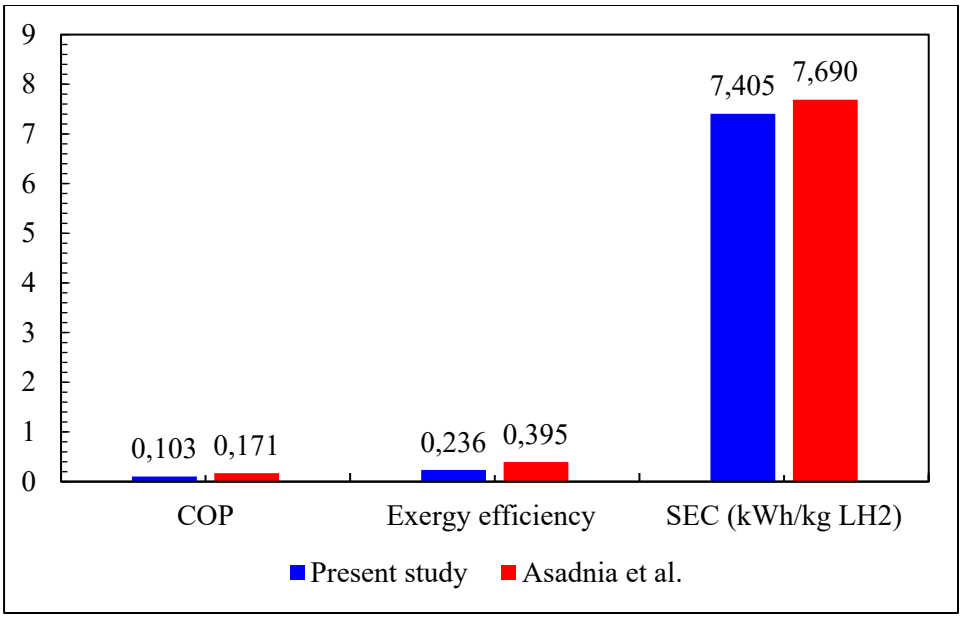

Figure 2.9. The compression data between
the present study and reference:
(Asadnia & Mehrpooya, 2017)

2.5.3 Pinch analysis results

Pinch analysis is a powerful method for minimizing energy consumption in thermodynamic processes and heat recovery systems, creating an optimal design for the heat exchanger that reduces the need for heating and cooling. The integration of the refrigeration cycles developed in this paper is provided by the process core in the form of hot and cold composite curves. Since in the multi-component refrigeration cycles, the minimum temperature difference between cold and hot currents is minimal (about 1 to 3 ˚C), the most suitable option for heat exchangers in this type of cycle is multi-current exchangers. Reducing the area between hot and cold diagrams minimizes the power consumption and degradation of exergy in the multi-stream heat exchangers. The operating pressures of the multi-component refrigerant cycle in the refrigeration system and the molar percentage of the refrigerant component composition must be selected so that the multi-stream heat exchangers establish the maximum agreement between the cold and hot composite curves. The design is performed using composite and grand composite diagrams that reflect a complete visual understanding of how the refrigeration cycle is arranged and its distance from the optimal

arrangement. By changing the structure and layout of equipment in the refrigeration cycle, using composite and grand composite diagrams, it moves to the optimal configuration. In this structure, pinch analysis is applied to design three multi-stream heat exchangers of HE2, HE3, and HE5 in the integrated structure for liquid hydrogen. Figure 2.10 shows the cold and hot composite (CC) curve HE2, HE3, and HE5 heat exchangers.

The hot streams in multi-stream heat exchangers HE2 and HE3 have a single component (hydrogen), so there is a gap between the hot and cold streams. In multi-stream heat exchangers HE5, hot and cold streams are multi-component, so there is a good match between them. The grand composite curve (GCC) of HE2, HE3, and HE5 heat exchangers is shown in Figure 2.11, respectively. The grand composition curve of heat exchangers shows that the amount of hot and cold utilization in the HE2, HE3, and HE5 heat exchangers are zero. The intersection points of the diagram to the vertical axis are used to determine the pinch point.

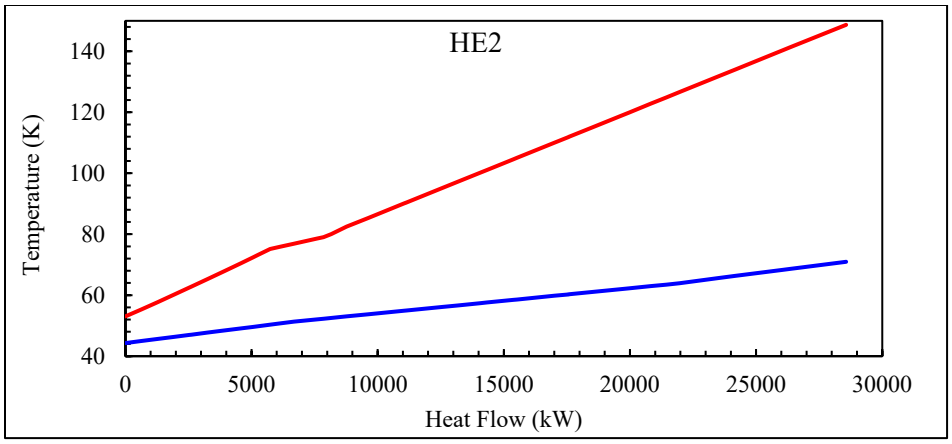

(a) heat exchanger HE2

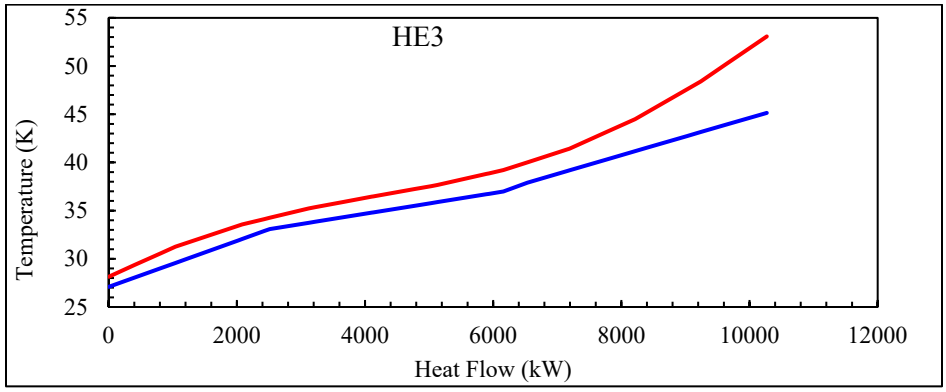

(b) heat exchanger HE3

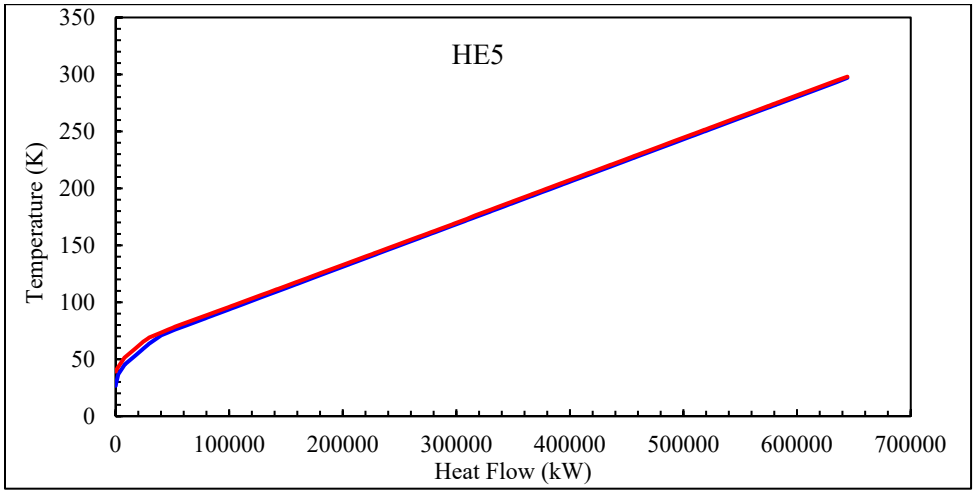

(c) heat exchanger HE5

Figure 2.10. The hot and cold composite curves of the multi-stream heat exchangers

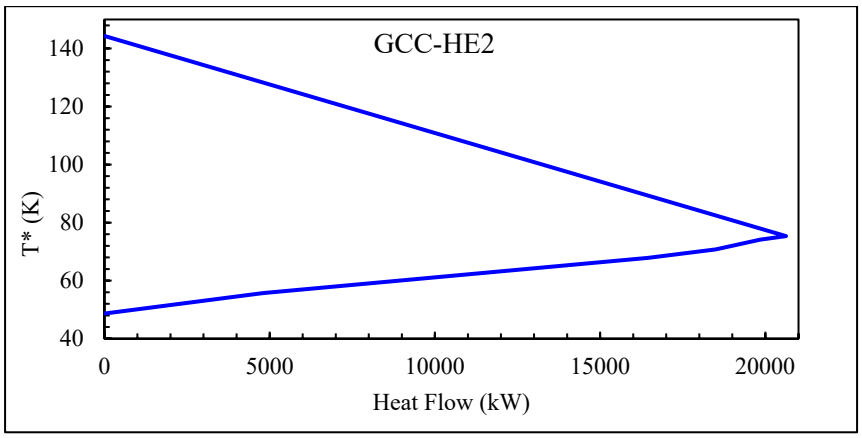

(a) Heat exchanger HE2

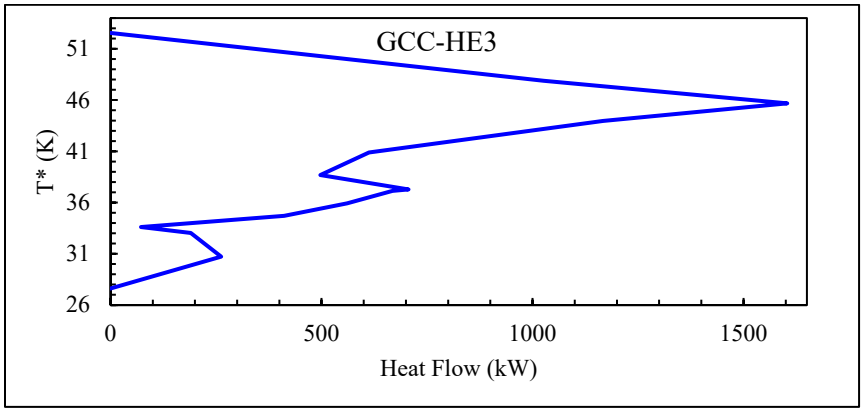

(b) Heat exchanger HE3

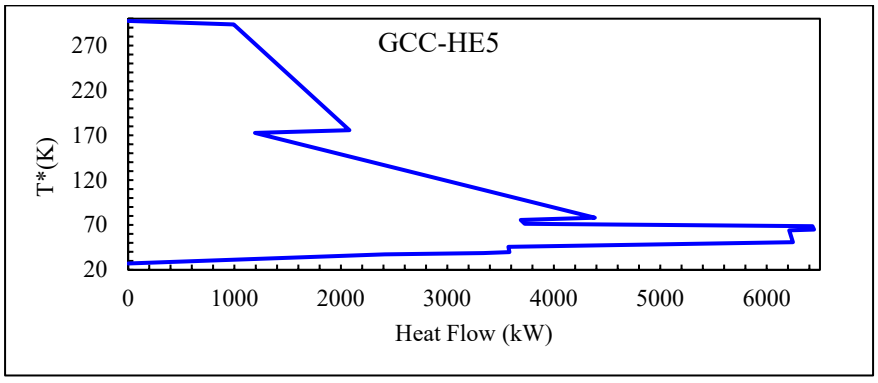

(c) Heat exchanger HE 5

Figure 2.11. The grand composite curve of
the multi-stream heat exchangers

2.5.4 Sensitivity analyses results

Sensitivity analysis or parametric study effectively evaluates the influential variables in a thermodynamic process design by assessing responses under different operating conditions. In this regard, the effect of critical parameter changes on system performance is assessed. Pressure pumped in the Kalina unit, the pressure of stream 130 in the pre-cooling system and the secondary stream pressure in Ejector 1 are considered key factors in the sensitivity analysis.

2.5.4.1 Pressure pumped in the Kalina unit

One of the essential parameters of the integrated structure performance is the pump pressure in the Kalina unit. As the pump's output pressure increases with the condition that the ratio of the compositions in the stream remains constant, the value of the vapor quality decreases and the flow rate of steam entering the gas turbine is reduced. As a result, a contraction occurs between decreasing the inlet flow rate and increasing the inlet flow pressure to the gas turbine. The influence of pressure pumped change on specific energy consumption and exergy efficiency of the integrated structure and the thermal efficiency of the Kalina power cycle is illustrated. Figure 2.12 indicates that by raising the pressure pumped from 10 bar to 30 bar, thermal efficiency increases to its peak of 0.1288 and subsequently declines with pressure increase. After experiencing a minimum of 7.413 kWh/kgLH_2 at 26 bar, the SEC of the integrated structure takes an upward trend with pressure enhancement. Likewise, the exergy efficiency rises to 0.2357 and declines with pumped pressure increases.

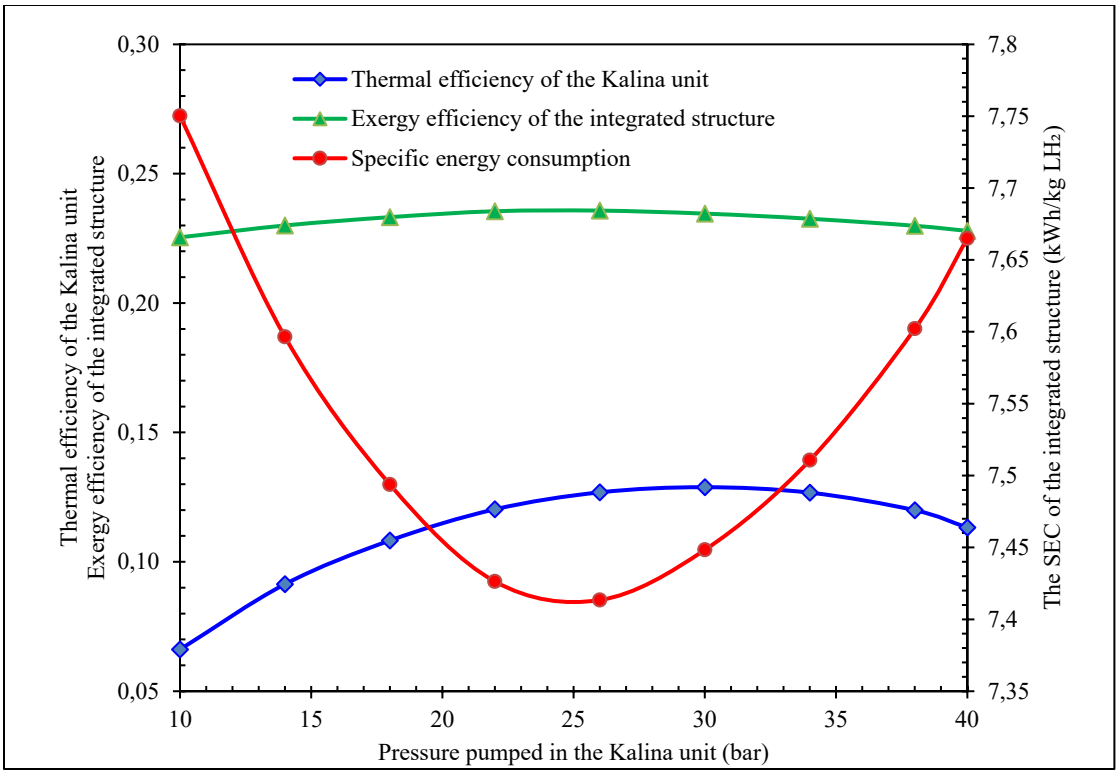

Figure 2.12. The effect of pressure pumped change on the SEC and exergy efficiency of the process, and the thermal efficiency of the Kalina power cycle

2.5.4.2 Pressure of stream 130 (kPa)

Another determining parameter in the integrated system quality is the pressure of stream 130, which directly relates to the system performance. Figure 2.13 provides the effects of pressure of stream 130 on the ejector-refrigeration cycle exergy efficiency and the SEC of the integrated structure. With the increase of stream 130 pressure and the constant pinch temperature in the HE26 heat exchanger, the inlet primary stream temperature to the ejector 2 increases. As a result, it increases the kinetic energy of the inlet stream to the nozzle in ejector 2. The amount of vapor in the two-phase mixture of the output stream from the ejector increases. The value of the entrainment ratio and the power consumption in the compressors decreases. According to this figure, by increasing pressure from 400 to 700 bar, exergy efficiency of ejector-refrigeration cycle increases up to 0.6641.

In contrast, the SEC of the integrated structure decreases to 7.389 kWh/kg LH_2. The effect of the pressure of stream 130 changes on exergy efficiency of integrated structure and rate of total exergy destruction is shown in Figure 2.14. The results show that as the pressure of stream 130 increases from 400 bar to 700 bar, the exergy efficiency of the integrated structure increase up to 0.2364. In contrast, the rate of total exergy destruction declines to 453813 kW. The effects of pressure of stream 130 on COP and power consumption of ejector-refrigeration cycle are provided in Figure 2.15. The results show that with increasing pressure stream 130 from 400 bar to 700 bar, COP and power consumption of ejector-refrigeration cycle rises to 0.8924 and decreases to 44329.8 kW, respectively. The trend of sensitivity analysis changes in this paper is similar to the sensitivity analysis results in the reference (Tan et al., 2017)

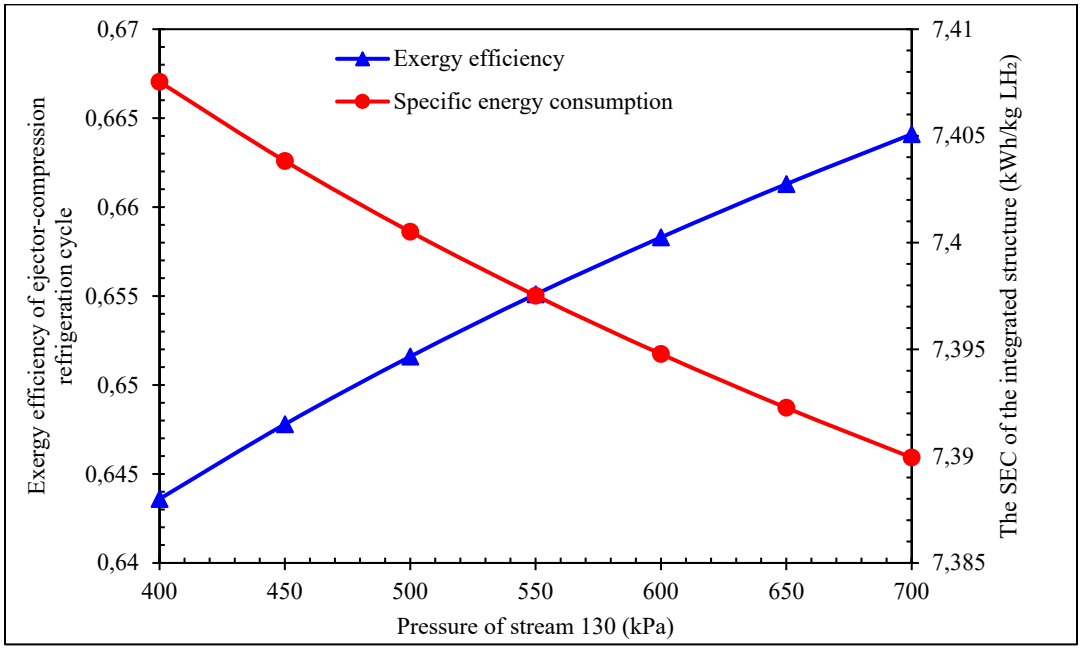

Figure 2.13. The effect of stream 130 pressure changes on the exergy efficiency of the ejector-compression refrigeration cycle and the SEC of the process

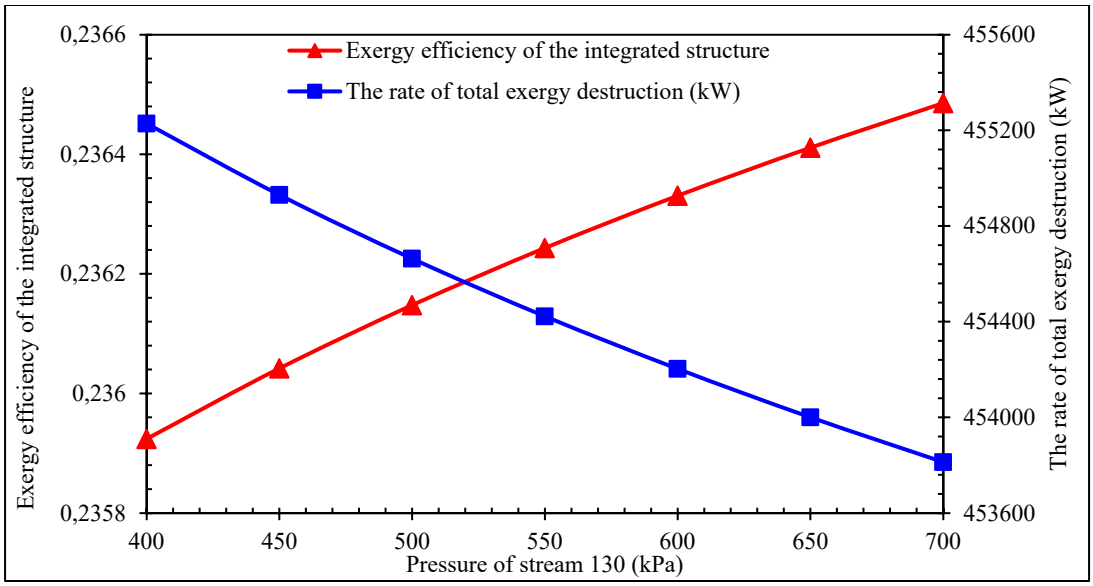

Figure 2.14. The effect of stream 130 pressure changes on the rate of total exergy destruction and the exergy efficiency of the integrated structure

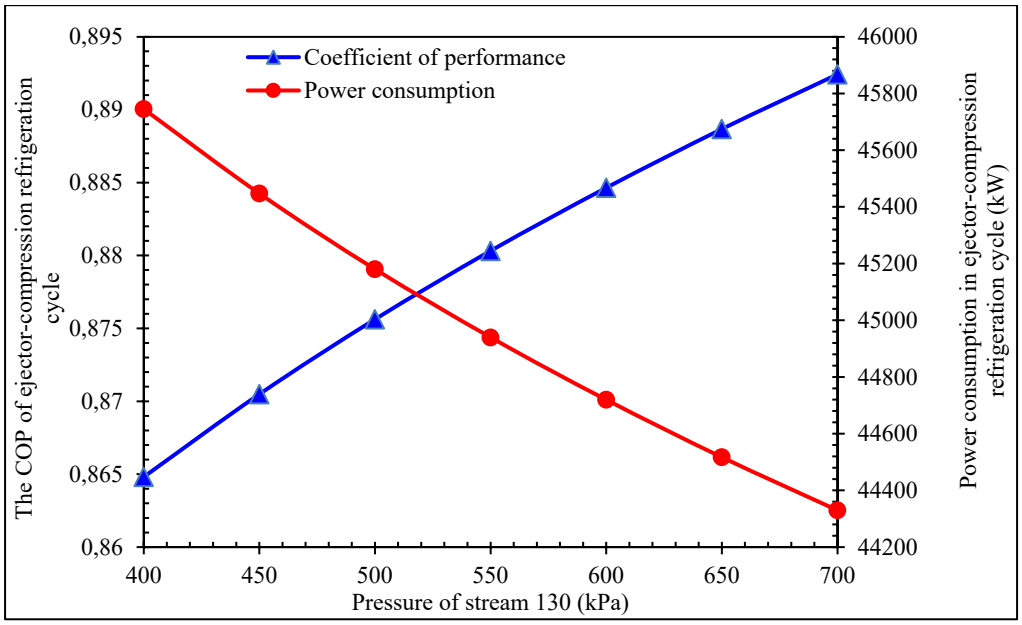

Figure 2.15. The effect of stream 130 pressure changes on the COP and power consumption of the ejector-compression refrigeration cycle

2.5.4.3 Secondary stream pressure in Ejector 1

The increase in the secondary stream pressure in Ejector1 has an adverse effect on the system's critical parameters. Figure 2.16 illustrates the impact of changes in secondary stream pressure in Ejector1 on the SEC of integrated structure and exergy efficiency of the ejector-refrigeration cycle. As the secondary stream pressure in Ejector1 increases, the propane temperature also increases. As a result, it increases the power consumption of the C15 compressor and decreases the power consumption of the C14 compressor. Finally, the power consumption of the ejector-compression refrigeration unit increases. By a pressure increase in the secondary stream in Ejector1 from 100 kPa to 200 kPa, the SEC of the structure and the exergy efficiency of the ejector-compression refrigeration cycle increases up to 7.435 kWh/kgLH_2 and decreases to 0.6159, respectively. Figure 2.17 indicates the effect of changing pressure in the secondary stream in Ejector1 on the COP and the power consumption of the ejector-compression refrigeration cycle. According to Figure 2.17, as the secondary stream pressure in Ejector1 raises from 100 kPa to 200 kPa, the COP and the power consumption of the ejector-compression refrigeration cycle declines to 0.8242 and increases up to 48007.2 kW, respectively. The trend of sensitivity analysis changes in this paper is similar to the sensitivity analysis results in the reference (Tan et al., 2017).

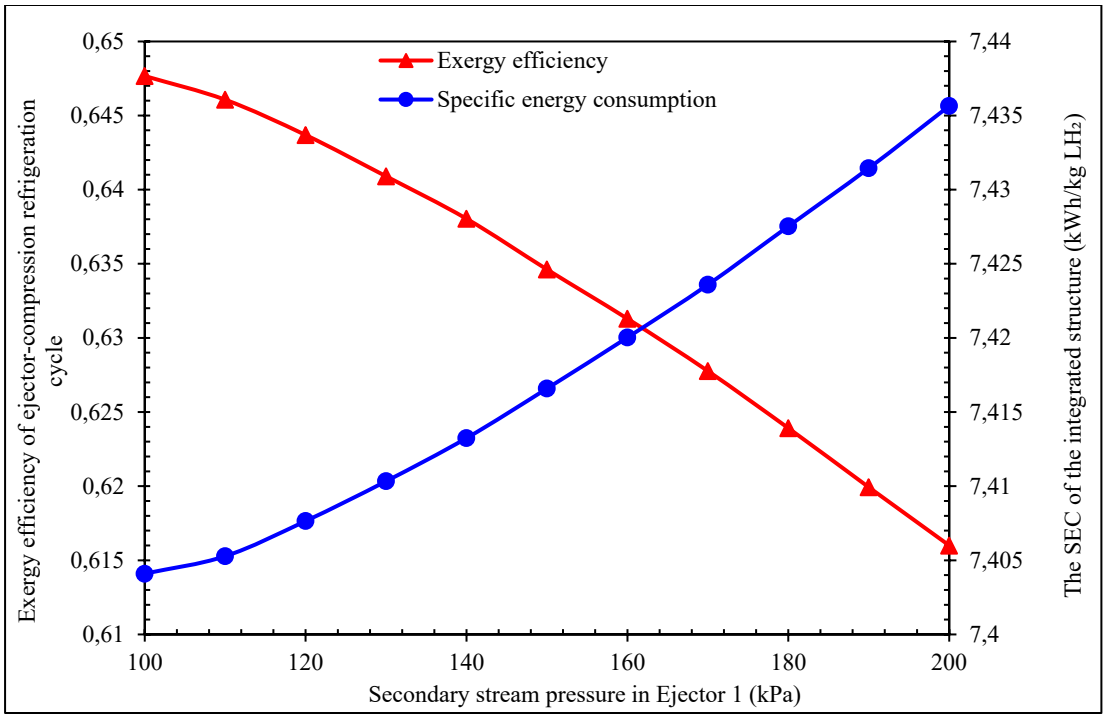

Figure 2.16. The effect of secondary stream pressure in Ejector1 on the SEC of the process and exergy efficiency of the ejector-compression refrigeration cycle

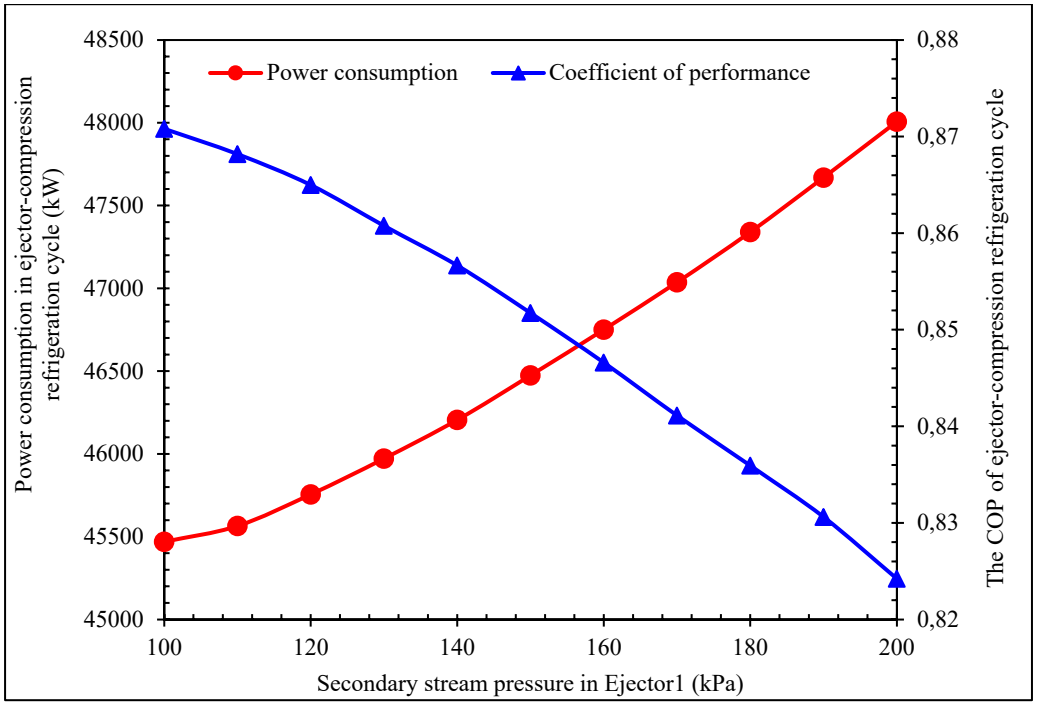

Figure 2.17. The effect of secondary stream pressure in Ejector1 on the COP and power consumption of the ejector-compression refrigeration cycle

2.6 Conclusion

High economic costs, low efficiency, high losses, and the lack of new technologies are among the significant problems facing hydrogen liquefaction technologies. Numerous attempts have been made to optimize the efficiency, minimize total costs, and reduce the structural complexity of the hydrogen liquefaction processes, such as utilizing the multi-component refrigerant cycle. However, using a multi-component refrigerant reduces energy consumption but results in additional maintenance costs associated with the controllability of the multi-component refrigerant cycle. Also, keeping the components in the refrigerant constant is not easy when leaking in a multi-component refrigerant cycle. This paper develops an integrated structure of hydrogen liquefaction using an ejector-compression refrigeration cycle, cascade multi-component refrigerant cycle, and the Kalina power generation cycle. Thermodynamic, pinch, exergy, and sensitivity analyses evaluate the developed structure, respectively. The outstanding results are as follows:

1. The developed integrated structure with consumption of 45.56 MW power in the ejector-compression refrigeration cycle and 550 MW of power in the cascade multi-component refrigerant cycle delivers 22.34 kg/s of liquid hydrogen. An ejector-compression refrigeration cycle pre-cools the hydrogen liquefaction structure, which transfers 39.56 MW cooling to hydrogen gas. Also, a cascade multi-component refrigerant cycle liquefies the pre-cooled hydrogen, producing 21.76MW cooling. The COP of the hydrogen liquefaction structure and the ejector-compression refrigeration cycle are 0.1030 and 0.8682, respectively. The Kalina power generation cycle consumes the excess heat of the hydrogen liquefaction process. The integration of the refrigeration system with the main configuration core is done in the form of composite and grand composite curves. Refrigerant composition percentages and refrigeration cycle operating pressures are employed to best match the cold and hot curves. As the difference between the area of the hot and cold graphs decreases, the total energy consumption and exergy degradation in the equipment decrease. The results demonstrate that the thermal efficiency of the Kalina cycle and SEC of the integrated structure are 0.1228 and 7.405 kWh/kg LH_2, respectively.

2. The two indicators of equipment's exergy destruction and exergy efficiency are examined to better compare the performance of different equipment in the developed process. Exergy analysis shows that the exergy destruction and the exergy efficiency of the hydrogen liquefaction cycle are 455 MW and 0.2359. The highest efficiency belongs to heat reactors, heat exchangers, and compressors. The results show that the throttle valves have low exergy efficiency and destruction rate of exergy. Also, the heat exchangers have high exergy efficiency and exergy destruction rate. Compressors, turbines, and heat exchangers also have high exergy efficiency despite their high exergy destruction. Therefore, modifying the integrated structure is not recommended by observing the above, and the developed system can be approved.

3. Effective parameters are determined to select a suitable integrated structure in the developed hydrogen liquefaction system. The sensitivity analysis results show that the pressure increase of stream 130 from 400 to 700 kPa leads to an increase in exergy efficiency and COP of the ejector-compression refrigeration cycle by 0.6641 and 0.8924, respectively. Also, when this pressure increases, the exergy efficiency of the integrated structure will increase by 0.2364, and the exergy destruction will decrease by 453.8 MW. Moreover, by enhancing the pressure pumped in the Kalina cycle from 10 to 26 bar, the Kalina cycle thermal efficiency and its total exergy efficiency increase by 0.1268 and 0.2357, respectively.

4. Economic and risk analyses can be completed for the integrated framework to continue this research. Also, the primary solution to increase exergy efficiency and reduce energy consumption is the operational optimization of the refrigerant composition percentage and refrigeration cycle operating pressure using meta-heuristic algorithms to be considered in future studies.

CHAPTER 3

NEW INTEGRATED PROCESS FOR THE EFFICIENT PRODUCTION OF METHANOL, ELECTRICAL POWER, AND HEATING

Alireza Khatami Jouybari [a], Adrian Ilinca [b], Bahram Ghorbani [c]

[a, b] Department of Mathematics, Computer Science and Engineering, University of Quebec at Rimouski (UQAR), 300 All. des Ursulines, Rimouski, QC G5L 3A1, Canada
[c] Faculty of Engineering Modern Technologies, Amol University of Special Modern Technologies, Amol 4615664616, Iran

Paper published in *MDPI-Energies*, January 2022[2]
(Alireza Khatami Jouybari et al., 2022a).

Abstract

In this paper, a novel process is developed to cogenerate 4741 kg/h of methanol, 297.7 kW of electricity, and 35.73 ton/h of hot water, including a hydrogen purification system, an absorption–compression refrigeration cycle (ACRC), an Organic Rankine Cycle (ORC), and parabolic solar troughs. The heat produced in the methanol reactor is recovered in the ORC and ACRC. Parabolic solar troughs provide thermal power to the methanol distillation tower. Thermal efficiencies of the integrated structure and the liquid methanol production cycle are 78.14% and 60.91%, respectively. The process's total exergy efficiency and irreversibility are 89.45% and 16.89 MW. The solar thermal collectors take the largest share of exergy destruction (34%), followed by heat exchangers (30%) and mixers (19%). Based on the sensitivity analysis, D17 (mixture of H_2 and low-pressure fuel gas before separation) was the most influential stream affecting the performance of the process. With the temperature decline of stream D17 from −139 to −149 °C, the methanol production rate and the total thermal efficiency rose to 4741.2 kg/h and 61.02%, respectively. Moreover, the growth in the hydrogen content from 55% to 80% molar of the feed gas, the flow rate of liquid methanol, and the total exergy efficiency declined to 4487 kg/h and 86.05%.

---

[2] Khatami Jouybari, A., Ilinca, A.; Ghorbani, B. – "New Integrated Process for the Efficient Production of Methanol, Electrical Power, and Heating. Energies, 15, 1054. https://doi.org/10.3390/en15031054, 2022

Keywords: integrated structure; hydrogen purification; methanol production; absorption–compression refrigeration unit; parabolic solar trough; Organic Rankine cycle

3.1 Introduction

The increasing rate of fossil fuel consumption has led to a global environmental crisis and depletion of conventional energy resources. These issues required the exploitation of renewable energy sources to produce alternative fuels (Dehghani Madvar et al., 2018). Hydrogen, as a green fuel and the most abundant element of the periodic table in the world, has absorbed researchers' attention in this regard. It can produce a comparatively high heat of combustion, leaving just water vapor (Abdin et al., 2021). As hydrogen has a remarkably low atomic mass, its storage and transportation are not cost-effective. A proper solution for this problem is hydrogen liquefaction, which optimizes its energy density (Rezaie Azizabadi et al., 2021). However, the liquefaction process has high investment costs and heat loss, low efficiency, and the need for state-of-the-art technologies (Sherif et al., 1997). Instead of hydrogen liquefaction for energy transportation, by adding CO_2 into hydrogen, it can be converted into liquid methanol, which has a higher liquefaction temperature and safety and the merit of decreasing the CO_2 concentration in the atmosphere.

The source of hydrogen for methanol production should have an acceptable range of purification. Extensive studies have been separately carried out on hydrogen purification and methanol production. The method for extracting impurities from hydrogen can be divided into three main categories: membrane separation, pressure swing absorption, and cryogenic absorption methods. Absorption and cryogenic techniques are employed for purification at high-capacity rates. The cryogenic process has the maximum recovery rate but provides hydrogen at minimum purity. As the energy consumption and purification cost in the cryogenic method are high, most studies have focused on optimizing its energy consumption (Muin et al., 2020).

The exergy and exergoeconomic analyses of a structure for hydrogen purification were carried out by Mehrpooya et al. (Mehrpooya et al., 2021). They utilized a water–ammonia diffusion–absorption refrigeration cycle to precool hydrogen at −32.61 °C and liquefied nitrogen for its cooling in the final stage. The total exergy efficiency of the structure, the outlet hydrogen purity, and the coefficient of performance of the refrigeration cycle were reported to be 93.82%, 88% molar, and 0.424, respectively. Aasadnia et al. (Aasadnia et al., 2021) applied the propane cryogenic cycle at −40 °C and the liquid nitrogen cycle at −155 °C to supply required cooling for the hydrogen purification process designed to provide 88% molar H_2, having the total exergy efficiency and hydrogen recovery rate of 91.73% and 25.1%, respectively. Hamedi et al. (Hamedi et al., 2018) studied the optimization of energy consumption in extracting nitrogen from natural gas using the Particle Swarm Optimization (PSO) algorithm. In this study, the nitrogen content of feed gas in single- or multi-column units is considered between 5% and 70%.

A stream with the main components of hydrogen and methane is the side product of many industrial processes. In this regard, Xu et al. (Xu & Lin, 2021b) proposed four different processes for the cogeneration of Liquid Hydrogen (LH_2) and Liquid Natural Gas (LNG) from the mentioned compound. Results showed that the purities of LNG in these systems were over 99.99%, and the Specific Energy Consumptions (SEC) were between 18.01 and 41.72 kWh/kmol. In another study, Xu et al. (Xu & Lin, 2021a) developed three integrated structures for the simultaneous generation of LH_2 and LNG using the helium reverse Brayton cycle from the feed containing hydrogen and methane gases. These systems' energy consumption and exergy efficiencies were 21.94–54.78 kWh/kmol (feedstock gas) and 13–66.5%. The multi-stage helium expansion refrigeration cycle is used in an integrated structure for the cogeneration of LH_2 and LNG by Xu et al. (Xu et al., 2018). The outlet stream from the coke oven gas containing methane and hydrogen fed the integrated structure. This system recovered hydrogen and methane with the rates of 99.68% and 97.92%, respectively.

Carbon dioxide, the primary greenhouse gas emitted through human activities, can be absorbed or recovered by some processes, producing methanol, methane, or formic acid to decrease its atmospheric concentration. Amongst all, methanol is the most favorable due to its application in internal combustion engines and fuel cells and easing hydrogen storage (Stiles, 1977)–(Bertau et al., 2014). Hosseini et al. (Hosseini et al., 2019) proposed an integrated structure for the tri-generation of methanol, power, and heat, including subsystems of natural gas reforming units, methanol production process, MCFC fuel cells, and combined heat and power (CHP) systems, resulting in the total energy and exergy efficiencies of 58.4% and 83.7% for the integrated structure and of 80.4% and 54.1% for methanol production. In addition, as the methanol production reaction is exothermic, the heat can serve in the CHP systems to keep the temperature of the process constant.

Mosaffa et al. (Mosaffa et al., 2019) developed an integrated structure with energy and exergy efficiencies of 48.8% and 32.7%, respectively, for the cogeneration of hydrogen, methanol, and power. Ishaq et al. (Ishaq & Dincer, 2020) employed wind turbines to supply the necessary power in a PEM electrolyzer for hydrogen production, subsequently combined with CO_2 in a methanol reactor. Carbon dioxide in this study was provided from the power plant's flue gas. Their integrated structure's energy and exergy efficiencies were calculated to be 40.5% and 42.3%, respectively. Nami et al. (Nami et al., 2018) proposed an integrated structure for the simultaneous production of methanol, carbon dioxide, and hydrogen, including the PEM electrolyzer, the oxyfuel power plant, and the ORC. The geothermal power was used to supply the ORC to convert thermal power into electricity. This structure's energy and exergy efficiencies and sustainability index were 14.7%, 42.43%, and 1.737, respectively.

Monnerie et al. (Monnerie et al., 2020) modeled a methanol production system including concentrating solar energy and a thermochemical cycle using Aspen Plus software. The price for methanol production was estimated at 1.14 Euro/Liter. An integrated structure including the alkaline electrolyzer, the ORC, the absorption refrigeration cycle, and the methanol production cycle was developed by Ghorbani et al. (Ghorbani, Mehrpooya, et al., 2021) to

simultaneously produce biomethane and biomethanol. Parabolic solar troughs supply the necessary thermal power of the ORC. The required CO_2 in this structure was provided by biogas upgrading. This integrated structure's energy and exergy efficiencies were 92.47% and 45.92%.

In another study, Ghorbani et al. (Ghorbani & Amidpour, 2021) developed an integrated structure for cogeneration of methanol, LNG, and helium by using the separation unit to extract helium from natural, methanol synthesis process, and solar dish collectors to supply the required heat of the natural gas reforming process for hydrogen production. This structure's energy and exergy efficiencies were 88.48% and 93.79%, respectively.

The compressor in the evaporation compression cycle is replaced by an absorber and a generator in absorption refrigeration cycles. The generator, pump, and absorber set in an absorption process are named thermal compressors. In fact, in the absorption system, the thermal power in generators is converted into cooling. The water–ammonia absorption cycles are suitable for providing cooling at temperatures around −30 °C and atmospheric pressure. For lower temperature ranges, the compression–absorption cycle can be used. Mehrpooya et al. (Mehrpooya et al., 2020) utilized a compression–absorption refrigeration cycle for the precooling stage of a natural gas liquefaction cycle at −54.62 °C. The refrigeration capacity per mass flow of flue gas and the coefficient of performance of the compression–absorption cycle were 0.0606 and 0.2539 MJ/kg, respectively. Chen et al. (Y. Chen et al., 2016) developed a refrigeration cycle including subsystems of a single-stage absorption cycle and an absorption–refrigeration cycle. The hot and cold temperatures sources were 200 and −15 °C. Exergy, economic, and environmental analyses of an ACRC at −54.62 °C were done by Mousavi et al. (Mousavi & Mehrpooya, 2020). The ORC supplied the electrical power. The flue gas heat provided the necessary thermal power in the compression–absorption refrigeration cycle and the ORC at 350 °C. The coefficient of performance in this process was 0.268.

Several studies have been carried out to develop the extraction from fuels and purification of hydrogen or methanol production. The main goals of the studies have been the optimization of the required heat, power generation and consumption, economic costs, and environmental friendliness. In some studies, the combined pinch and exergy analyses were applied to assess the cryogenic hydrogen purification systems. However, based on the literature review, not a lot of studies have been performed to develop an integrated structure for hydrogen purification and methanol production using renewable energies. This study aims to fill the gap of recent studies, offer an efficient method, and facilitate energy transfer by converting hydrogen into liquid methanol. The proposed integrated structure contains the hydrogen purification cycle, the liquid methanol production structure, the ORC, the ACRC, and parabolic solar troughs designed to simultaneously produce liquid methanol, electrical power, and heat. Parabolic solar troughs are designed based on the environmental condition of Bushehr city, Iran. Thermodynamic, exergy, and sensitivity analyses are completed to assess the integrated structure.

3.2 Description and Modeling

Hydrogen is considered an ideal fuel thanks to its merits of eco-friendliness and having a higher heating value compared to fossil fuels. However, the produced hydrogen in most processes is not pure, limiting its miscellaneous utilization. For example, except helium, nearly every impurity of H_2 converts into a solid state, choking heat exchangers and valves in the hydrogen liquefaction process. Several methods have been developed for hydrogen purification, with the cryogenic method known as the best option on a large recovery scale. Besides, hydrogen storage and transportation are challenging, whether as a compressed gas or liquefied. Purified hydrogen can be converted into liquid methanol and transported as a safe energy carrier to avoid the high costs of hydrogen liquefaction. This paper proposes a brand-new integrated structure for the simultaneous production of liquid methanol, electrical power, and heat, including subsystems of parabolic solar troughs and cryogenic purification, liquid methanol production, absorption–compression refrigeration, and the ORC. Figure 3.1 illustrates the block flow diagram (BFD) of the integrated structure with the production

capacity of 4741 kg/h of liquid methanol, 297.7 kW of electricity, and 35.73 ton/h of hot water. Hydrogen from the cryogenic purification cycle and carbon dioxide enter the methanol production cycle. Solar thermal collectors supply the heating required in the methanol distillation column. The ORC and the absorption–compression refrigeration cycle absorb the excess heat from the methanol production cycle to produce power and provide cooling for the purification cycle. Figure 3.2 depicts the integrated structure's process flow diagram (PFD). The Peng–Robinson equation of state and Aspen HYSYS V10.0 software are used for the simulation of the system consisting of these subsystems:

1- The cryogenic hydrogen purification cycle was developed in Aspen HYSYS V10.0 software. Pinch analysis in the forms of cold and hot composite curves was applied to integrate the process core and refrigeration cycle.
2- The liquid methanol production cycle was modeled in Aspen HYSYS V10.0 software and fed by hydrogen with 88.05% purity and CO_2.
3- An ORC was developed in Aspen HYSYS V10.0 software and fed by the excess heat of the liquid methanol production cycle.
4- The absorption–compression refrigeration cycle was modeled in Aspen HYSYS V10.0 software and employed to precool the hydrogen purification cycle.
5- Parabolic solar collectors were modeled using MATLAB V10.0 m-file. They are used to supply thermal power in the methanol distillation tower.

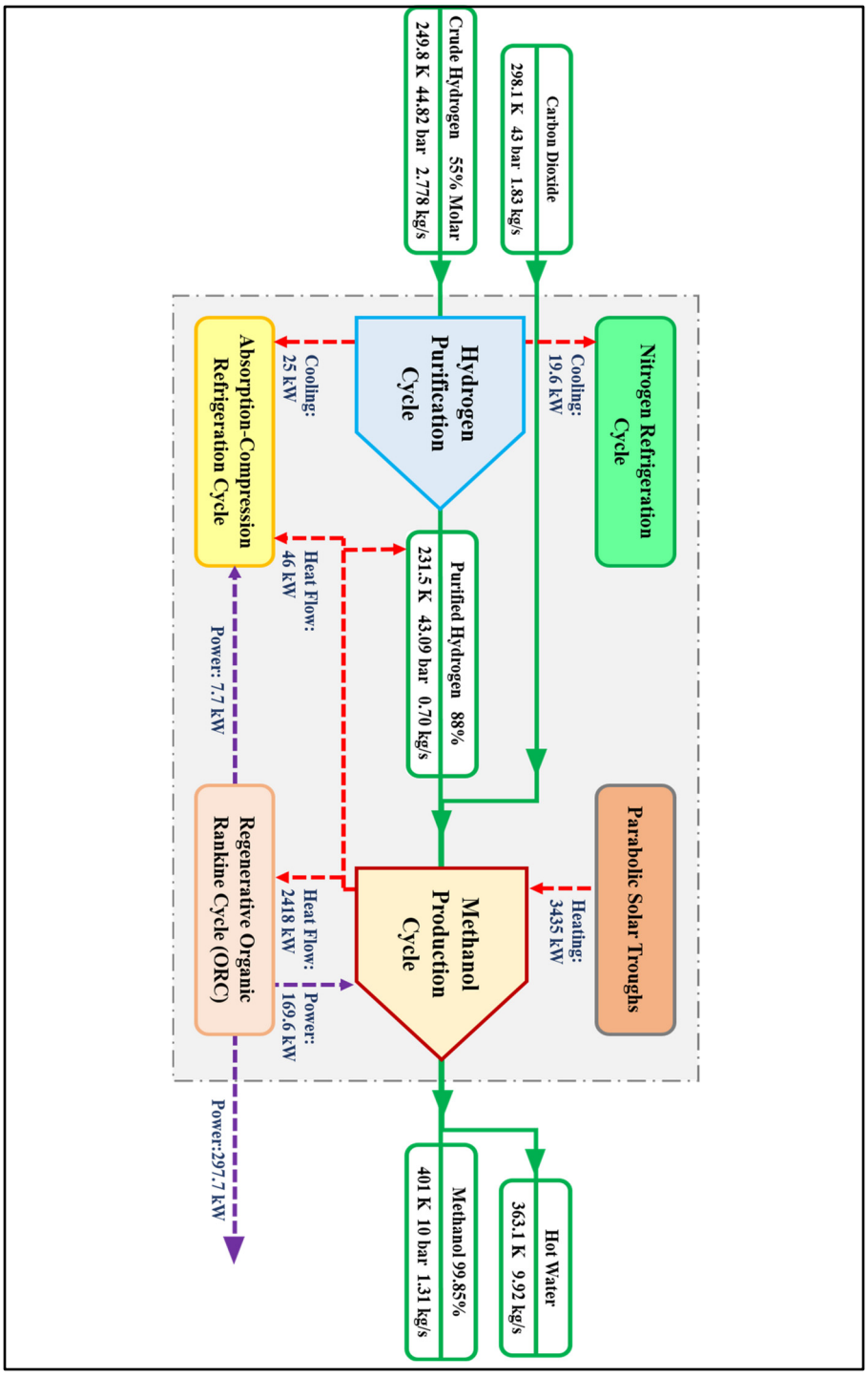

Figure 3.1. The block flow diagram (BFD) of the process

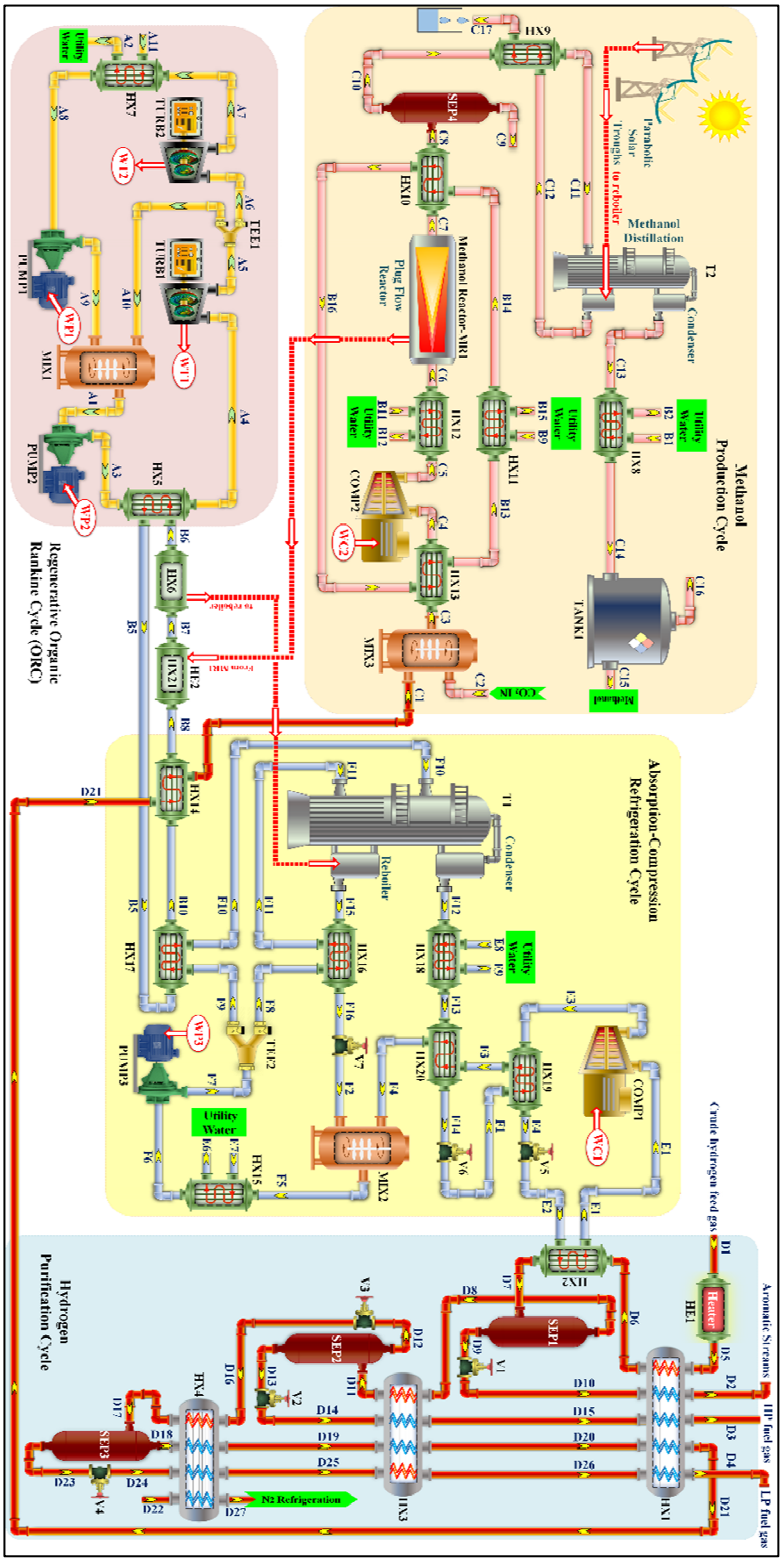

Figure 3.2. The process flow diagram (PFD)
of the integrated structure

The algorithm for the design and development of the novel integrated structure is illustrated in Figure 3.3.

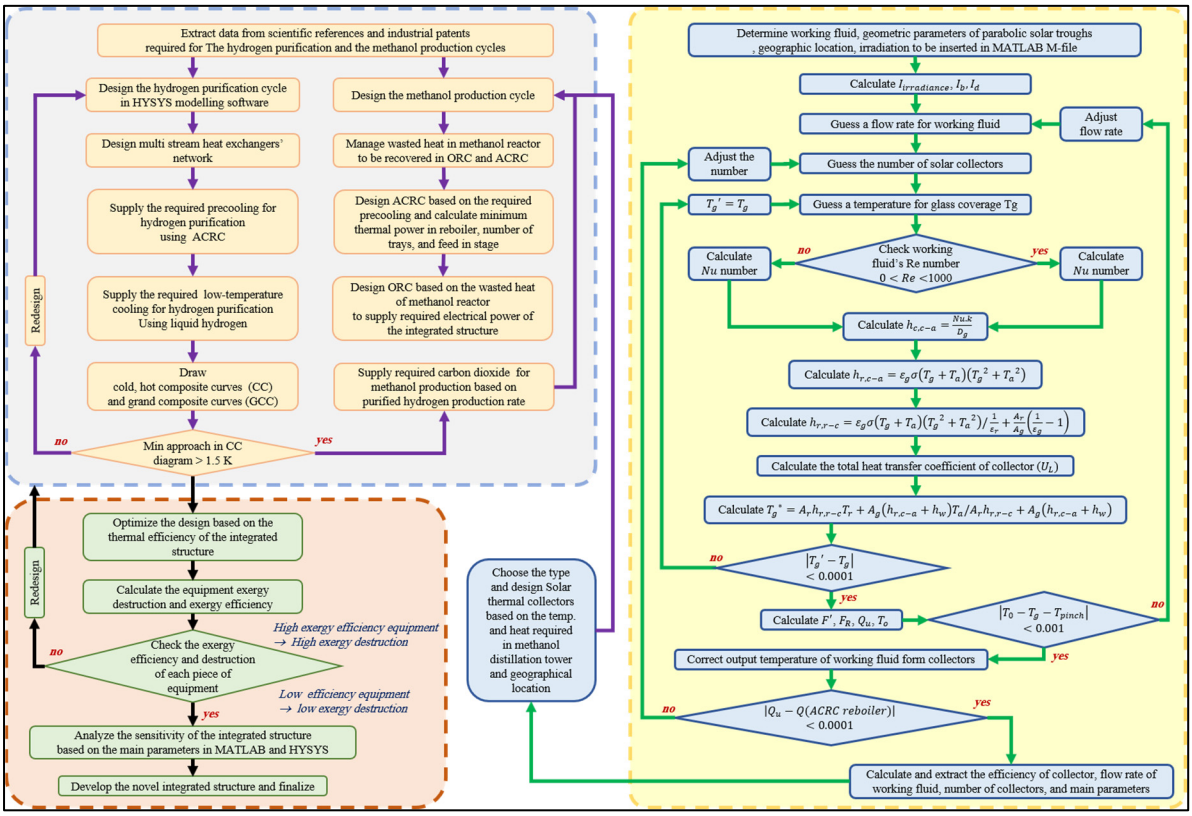

Figure 3.3. The algorithm of the design and development of the process

3.2.1 Cryogenic Hydrogen Purification Cycle

Methods for hydrogen purification can be categorized into three main groups: membrane separation, pressure swing absorption, and cryogenic absorption. Here, the cryogenic absorption method is chosen because of its applicability in the large-scale purification. Besides, cryogenic process has a higher recovery rate than pressure swing absorption method. This technology is based on the fact that each component in the feed gas has a different boiling point from other components, helping it to be liquefied and extracted from the mixture in a separator. Table 3.1 provides information regarding the component molar

fractions of streams in the integrated structure. The feed gas stream of crude hydrogen (stream D1) contains 55% hydrogen, 39% methane, 2% ethane, 1% propane, 2% nitrogen, and 1% benzene (molar). Stream D1, after preheating in the HE1 exchanger, enters the HX1 exchanger in 44.82 bar and −23.33 °C to be cooled to −34.44 °C. To provide required precooling in the purification cycle, the ACRC was employed. Two-phase stream D7 enters the flash drum (Sep1) to separate most of its liquid benzene and propane contents. After a pressure drop in the V1 throttling valve, these liquids first enter the HX1 exchanger (stream D10) in −33.5 °C and 17.24 bar to pro-vide cooling for the internal stream D5 and finally leave the cycle as D2 (aromatic stream). Gaseous stream D8 from the Sep1 flash drum enters the HX3 exchanger and its tempera-ture drops to −134.4 °C. The output stream D11 enters the next Sep2 flash drum. In this stage, the liquid stream D13 containing 86% molar methane, after passing through the V2 throttling valve, enters the HX3 and HX1 exchangers, respectively, to help with the pre-cooling of feed gas and leaves the cycle as stream D3 (high-pressure fuel gas). The outlet stream D12 from the above Sep2 flash drum enters the V3 throttling valve and, after a pressure drop to 43.09 bar, passes through the HX4 exchanger, and its temperature drops to −148.9 °C. The liquid and gaseous parts of stream D17 separate in the Sep3 flash drum into liquid stream D23 of 95.08% molar methane and stream D18 of 88.5% molar hydro-gen. Stream D23 firstly loses its pressure from 74 to 3.447 bar in the V4 throttling valve. Then, it provides cooling for the inlet stream in the HX4, HX3, and HX1 exchangers, and finally, leaves the cycle as stream D4 (low-pressure fuel gas). The reason for using the V1 to V4 valves is to decrease the temperature of streams by pressure drop to maximize their potential in supplying cooling for the inlet stream. The remaining required low-temperature cooling is designed to be provided by liquid nitrogen (stream D22). Stream D18 supplies cooling in the HX4, HX3, and HX1 exchangers and then goes to the methanol production cycle at 43.09 bar and −41.64 °C.

Table 3.1. Compositions of some important streams (molar%)

Stream	H_2	CH_4	C_2H_6	$C3H_8$	N_2	C_6H_6	CO_2	H_2O	NH_3	R-113	CH_3OH
A1	0	0	0	0	0	0	0	0	0	1	0
C3	0.71	0.08	0.00	0.00	0.02	0.00	0.19	0.00	0.00	0.00	0.00
C7	0.22	0.12	0.00	0.00	0.03	0.00	0.00	0.31	0.00	0.00	0.31
C9	0.57	0.33	0.00	0.00	0.09	0.00	0.00	0.00	0.00	0.00	0.01
C11	0.00	0.00	0.00	0.00	0.00	0.00	0.00	0.50	0.00	0.00	0.50
C12	0.00	0.00	0.00	0.00	0.00	0.00	0.00	1.00	0.00	0.00	0.00
C13	0.00	0.00	0.00	0.00	0.00	0.00	0.00	0.00	0.00	0.00	1.00
D1	0.55	0.39	0.02	0.01	0.02	0.01	0	0	0	0	0
D8	0.56	0.39	0.02	0.01	0.02	0.00	0	0	0	0	0
D9	0.01	0.07	0.04	0.10	0.00	0.78	0	0	0	0	0
D12	0.79	0.18	0.00	0.00	0.02	0.00	0	0	0	0	0
D13	0.03	0.87	0.06	0.03	0.01	0.00	0	0	0	0	0
D18	0.88	0.09	0.00	0.00	0.02	0.00	0	0	0	0	0
D22	0.00	0.00	0.00	0.00	1.00	0.00	0	0	0	0	0
D23	0.03	0.95	0.00	0.00	0.02	0.00	0	0	0	0	0
E1	0	0	0	0	0	0	1	0	0	0	0
F5	0	0	0	0	0	0	0	0.66	0.34	0	0
F8	0	0	0	0	0	0	0	0.65	0.35	0	0
F9	0	0	0	0	0	0	0	0.65	0.35	0	0
F12	0	0	0	0	0	0	0	0.00	1.00	0	0
F15	0	0	0	0	0	0	0	0.80	0.20	0	0

3.2.2 Absorption–Compression Refrigeration Cycle

Ammonia–water absorption refrigeration cycles are widely employed in industrial and commercial sectors where the temperature of the evaporator is close to the water freezing point. As the freezing point of ammonia is −77 °C, the absorption refrigeration cycles of water–ammonia are used in low-temperature processes in industries with the ability to

provide cooling at −30 °C. Absorption and compression cycles need to be combined to provide cooling in lower temperatures. In the present paper, the absorption–compression refrigeration cycle provides precooling for the cryogenic hydrogen purification cycle. ACRC includes the generator or desorber for water–ammonia separation in the distillation tower and reboiler, the purifier for the extraction of remaining water droplets from ammonia in the condenser of the distillation tower, the condenser for the liquefaction of purified ammonia (the HX18 exchanger), the evaporator to supply required cooling of the cycle by CO_2 evaporation (the HX2 exchanger), the absorbent for the absorption of water in ammonia (the HX15 exchanger), and the CO_2 compression refrigeration cycle to provide cooling at −42.07 °C.

In ACRC, stream F6, containing ammonia and water at 35 °C, enters Pump3 to in-crease its pressure from 270 to 1356 kPa, the required pressure of the generator. Stream F7 with 64.73% molar water and 35.27% molar ammonia is divided into streams F8 and F9 before entering the generator. Stream F8 enters the HX16 exchanger and, after a temperature increase to 114.2 °C, enters the distillation tower as stream F11. Stream F9 enters the HX17 exchanger and, after warming to 113.8 °C, enters the fourth tray of the distillation tower as stream F10. The required thermal power in this step is supplied by the wasted heat of the methanol reactor.

Part of the ammonia of the mixture entering the distillation tower (T1) evaporates by receiving the heat from the methanol reactor. This ammonia stream contains a low fraction of water distractable by the condenser situated at the top of the T1 tower. The generator and purifier are modeled in Aspen HYSYS V10.0 software as a distillation tower. The low ammonia content mixture leaves the reboiler of the tower with 79.33% molar water and 20.67% molar ammonia. The utility water at 25 °C supplies the required cooling in the purifier (condenser). The purified gaseous ammonia at 59.19 °C (stream F12) enters the HX18 exchanger to be liquefied and, after heat recovery in the HX20 exchanger, enters the V6 throttling valve to provide required cooling for the CO_2 compression refrigeration cycle.

After being combined with the outlet stream of the reboiler, the returning stream loses its temperature in the HX15 exchanger and enters Pump3.

The CO_2 compression refrigeration cycle after a pressure increase in the Comp1 compressor enters the HX19 exchanger and its temperature drops to −15.41 °C. Then, the outlet stream from the HX19 exchanger enters the V5 throttling valve to decrease its pressure to 900 kPa. The pressure drop leads to the temperature decrease of the CO_2 to −42.07 °C, helping the HX2 exchanger provide the required precooling in the hydrogen purification cycle. Subsequently, the CO_2 stream enters the compressor to increase its pressure at 4000 kPa.

3.2.3 Liquid Methanol Production Cycle

Due to the low boiling point of hydrogen and safety hazards associated with its storage and transport, hydrogen conversion into methanol for long-distance energy transportation is recommended. In the methanol production cycle, the purified hydrogen stream from the hydrogen purification cycle is mixed with stream C2 (CO_2) to enter the Comp2 compressor and the HX12 exchanger, and its pressure and temperature rise to 50 bar and 200 °C. Finally, the outlet stream (C6) enters the methanol production reactor, modeled as a plug flow reactor in Aspen HYSYS V10.0 software. In this kinetic model, two independent reactions (hydrogenation of carbon dioxide and reverse water–gas shift reaction) out of the three following dependent reactions are considered (L. Chen et al., 2011):

$$CO + 2H_2 \rightleftarrows CH_3OH \tag{3.1}$$

$$CO_2 + 3H_2 \rightleftarrows CH_3OH + H_2O \tag{3.2}$$

$$CO_2 + H_2 \rightleftarrows CO + H_2O \tag{3.3}$$

Methanol production is an exothermic reaction. Its wasted heat is recovered in ACRC to provide thermal power and in ORC for electrical power production. Stream C7 enters the HX10 exchanger and, after dropping its temperature to 44 °C, enters the Sep4 flash drum (as a two-phase flow). The gaseous mixture of hydrogen and hydrocarbons (stream C10) leaves

the Sep4 flash drum from above to enter the HX9 exchanger and increase its temperature to 95 °C. The liquid mixture of methanol and water from the Sep4 flash drum enters the T2 methanol distillation tower, the water content is extracted, and gaseous methanol (stream C13) leaves the tower from above. Stream C13 enters the HX8 exchanger to be liquefied and stored at 127.8 °C and 10 bar. Parabolic solar troughs are employed to provide thermal heating required in the boiler of the methanol distillation tower.

3.2.4 Organic Rankine Cycle

The excess heat from the methanol reactor could be recovered in the ORC, enhancing the efficiency of the integrated structure. Considering the inlet temperature of the HX5 exchanger (199 °C), the power generation cycle is chosen to be a ORC. First, stream A1 at 138 °C enters Pump2 and, after a pressure increase from 10 to 25 bar, passes through the HX5 exchanger to be heated at 192.5 °C, ready to enter the Turb1 turbine. The outlet stream from the Turb1 turbine (stream A5) with a pressure of 10 bar divides into two streams, A10 and A6. Stream A6, with a 0.8 bar pressure drop in the Turb2 turbine, provides 319.4 kW of power, and subsequently enters the HX7 condenser to cool at 28 °C using utility water at 25 °C. Next, the condenser's outlet stream enters Pump1 to retrieve its primary pressure of 10 bar. Then, after being mixed, streams A9 and A10 create stream A1 in the first step of the cycle.

3.2.5 Parabolic Solar Troughs

Parabolic solar troughs are employed as solar thermal collectors to provide 3435 kW of thermal power for the methanol production cycle. This type of collector can deliver heat at the temperature range required in the methanol distillation tower. The climatic condition of Bushehr city (with geographic coordinates of 28.92° N, 50.82° E, and 10 m height above the sea level) serves for the design of solar collectors. The following equations are used to determine the amount of absorbed radiation in parabolic solar troughs (L. Chen et al., 2011):

$$I_{irradiance} = I_b + I_d = I_{bn}\cos\theta + I_d \quad (3.4)$$

$$I_{bn} = A\,exp\left[-\frac{B}{\cos\theta}\right] \quad (3.5)$$

$$I_d = C \times I_{bn} \quad (3.6)$$

Where I_b, I_{bn}, I_d, and θ are beam radiation, beam radiation in direction of rays , sky diffuse radiation, and angle of incidence, respectively. A, B, and C are constants which change throughout the year due to seasonal changing of water vapor and dust content in the earth's atmosphere. The area of the receiver (A_r), glass coverage area (A_g), and the area of collector opening (A_a) are calculated as follows:

$$A_r = \pi D_o L \quad (3.7)$$

$$A_g = \pi D_g L \quad (3.8)$$

$$A_a = (W - D_g)L \quad (3.9)$$

D_0, Dg, W, and L are the outer diameter of the tubular receiver, the diameter of glass coverage, the width of the opening, and the length of the parabolic solar trough, respectively. For the modeling of the collector, in the beginning, a temperature for the glass coverage is guessed (T_g) to determine the heat transfers performed by thermal convection and radiation. The temperature of the glass coverage is calculated using the trial-and-error method, ignoring the heat transfer with the reflector. The heat transfer coefficient of the thermal convection due to the wind stream ($h_{c,c-a} = h_w$) is calculated as follows (k is air thermal conductivity) :

$$Nu = 0.4 + 0.54(Re)^{0.52} \quad 0.1 < Re < 1000 \quad (3.10)$$

$$Nu = 0.3(Re)^{0.6} \quad 1000 < Re < 50{,}000 \quad (3.11)$$

$$h_{c,c-a} = h_w = \frac{Nu.k}{D_g} \quad (3.12)$$

The heat transfer coefficient of the thermal radiation from the glass coverage to its surrounding area ($h_{r,c-a}$) is determined using Equation (3-13):

$$h_{r,c-a} = \varepsilon_g \sigma \left(T_g + T_a\right)\left({T_g}^2 + {T_a}^2\right) \tag{3.13}$$

The heat transfer coefficient of the thermal radiation between the receiver tube and glass coverage ($h_{r,r\text{-}c}$) is given by Equation (3-14) :

$$h_{r,r-c} = \frac{\varepsilon_g \sigma \left(T_g + T_a\right)\left({T_g}^2 + {T_a}^2\right)}{\frac{1}{\varepsilon_r} + \frac{A_r}{A_g}\left(\frac{1}{\varepsilon_g} - 1\right)} \tag{3.14}$$

The thermal convection heat transfer between the receiver tube and glass coverage is ignored because the tube is evacuated. Considering the area of the receiver as A_r, the total heat transfer coefficient of the solar collector can be calculated as follows:

$$U_L = \left[\frac{A_r}{\left(h_w + h_{r,c-a}\right)A_c} + \frac{1}{h_{r,r-c}}\right]^{-1} \tag{3.15}$$

As the U_L is calculated based on an estimated temperature for T_g, the result needs to be validated. At first, T_g is calculated from Equation (3-16):

$$T_g = \frac{A_r h_{r,r-c} T_r + A_g\left(h_{r,c-a} + h_w\right)T_a}{A_r h_{r,r-c} + A_g\left(h_{r,c-a} + h_w\right)} \tag{3.16}$$

Then, the difference between the estimated value and the calculated value of T_g is minimized. Having T_g, the efficiency coefficient of solar collectors is calculated by Equation (3-17) (Kalogirou, 2013):

$$F' = \frac{\frac{1}{U_L}}{\frac{1}{U_L} + \frac{D_o}{h_{fi} D_i} + \left(\frac{D_o}{2k} ln \frac{D_o}{D_i}\right)} \tag{3.17}$$

The thermal collection coefficient (F_R) is calculated as follows (Kalogirou, 2013):

$$F_R = \frac{\dot{m}c_p}{A_r U_L}\left[1 - exp(-\frac{U_L F' A_r}{\dot{m}c_p})\right] \quad (3.18)$$

The calculation of useful absorbed energy is performed based on the concept of absorbed radiation as follows (Kalogirou, 2013):

$$Q_u = [SA_a - A_r U_r(T_i - T_a)] \quad (3.19)$$

Finally, the output temperature of the stream (T_o) is:

$$T_o = T_i + \frac{Q_u}{\dot{m}c_p} \quad (3.20)$$

The average hourly changes, which are important factors contributing to the performance of solar thermal collectors, are shown in Figure 3.4.

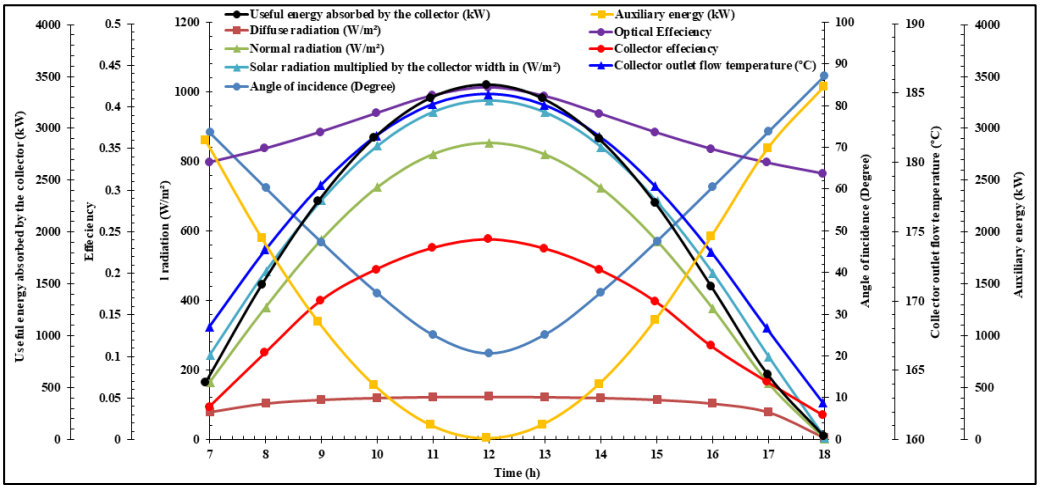

Figure 3.4. The average hourly changes in important values contribute to the performance of solar thermal collectors

3.3 Energy Analysis

The energy balance equation for each piece of equipment is calculated using specific enthalpy, as follows (Noroozian et al., 2017):

$$\sum_{in} \dot{m}_{in}\, h_{in} - \sum_{out} \dot{m}_{out}\, h_{out} - \dot{W} + \dot{Q} = 0 \tag{3.21}$$

Energy balance equations for each heat exchanger by considering the heat loss equal to zero are:

$$\dot{m}_{in,i}(h_{in1,i} - h_{in2,i}) = \dot{m}_{out,i}(h_{out1,i} - h_{out2,i}) \tag{3.22}$$

$$T_{in1,i} = T_{out1,i} + \Delta\ T_{in,HXi} \tag{3.23}$$

For the energy balance, Equations (3-23) and (3-24) related to pumps' and turbines' isentropic efficiency are used (Noroozian et al., 2017):

$$h_{out} = \frac{h_{out}^{S} - h_{in}}{\eta_s} + h_{in} \tag{3.24}$$

$$h_{out} = (h_{out}^{S} - h_{in})\eta_s + h_{in} \tag{3.25}$$

The energy balance and the mass conservation equations in mixers are as follows:

$$\dot{m}_{in,1}h_{in,1} + \dot{m}_{in,2}h_{in,2} = \dot{m}_{out}h_{out} \tag{3.26}$$

$$\dot{m}_{in,1} + \dot{m}_{in,2} = \dot{m}_{out} \tag{3.27}$$

By combining Equations (3-26) and (3-27), the refrigerant enthalpy in the outlet stream of mixers, h_{out}, is calculated as:

$$h_{out} = \frac{\dot{m}_{in,1}h_{in,1} + \dot{m}_{in,2}h_{in,2}}{\dot{m}_{in,1} + \dot{m}_{in,2}} \tag{3.28}$$

In separators and flash drums, the energy balance and the mass conservation equations are calculated as follows:

$$\dot{m}_{in}h_{in} = \dot{m}_{out,1}h_{out,1} + \dot{m}_{out,2}h_{out,2} \tag{3.29}$$

$$\dot{m}_{in} = \dot{m}_{out,1} + \dot{m}_{out,2} \tag{3.30}$$

Based on the first law of thermodynamics, the throttling process in valves is enthalpy constant. Therefore (Ebrahimi & Ziabasharhagh, 2017):

$$h_{in} = h_{out} \tag{3.31}$$

For modeling the distillation tower, Figure 3.5 is used, showing the overall balance in one of its stages, which is applicable for many of its design options. A vapor stream and a liquid stream enter each tray and leave it. In each tray, a vapor, liquid, or a two-phase stream goes out at the side outlet, feed enters, and products leave the tray. This helps to model towers with multiple feeds and products and with auxiliary heat exchangers.

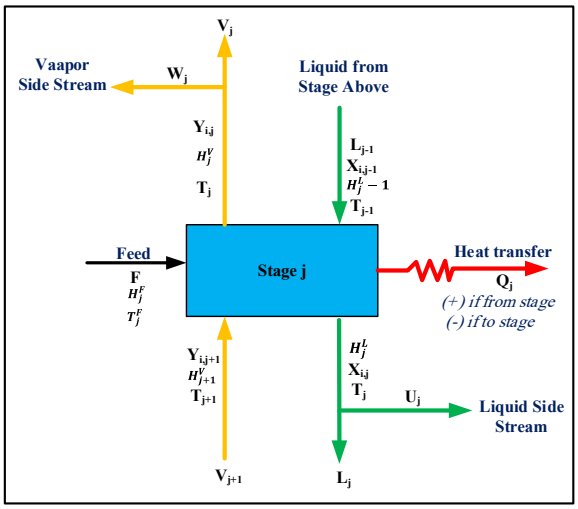

Figure 3.5. The overall balance in one of the stages of tower, modified from: (Ebrahimi & Ziabasharhagh, 2017)

Regarding Figure 3.5, MESH equations can be written as follows (Ebrahimi & Ziabasharhagh, 2017):

$$L_{j-1}\ x_{i,j-1} + V_{j+1}\ y_{i,j+1} + F_j\ Z_{i,j} - (L_j + U_j)\ x_{i,j} - (V_j + W_j)\ y_{i,j} = 0 \qquad (3.32)$$

Where, i is component number and j is tray number. F, W, V, L, and U represent feed, vapor side stream, vapor stream, liquid stream, and liquid side stream, respectively. x and y are liquid and vapor fraction, respectively. The balanced equation for each section in a tray of the tower is:

$$y_{i,j} - k_{i,j}x_{i,j} = 0 \qquad (3.33)$$

The sum equation for each tray is:

$$\sum_{i=1}^{NC} y_{i,j} - 1 = 0\ ,\sum_{i=1}^{NC} x_{i,j} - 1 = 0 \qquad (3.34)$$

The thermal energy balance equation for each tray is:

$$L_{j-1}\ H^L{}_{j-1} + V_{j+1}\ H^V{}_{j+1} + F_j\ H^F{}_j - (L_j + U_j)\ H^L{}_j - (V_j + W_j)\ H^V{}_j - Q_j = 0 \qquad (3.35)$$

In Equation (3-36), H represents enthalpy and Q_j is determined based on the heat source with a temperature of T_0.

3.3.1 Exergy Analysis

Exergy is the maximum power achievable from a system in its transition to the standard condition by a reversible process. Therefore, exergy can be defined as reversible work. Hence, exergy destruction has a direct relation with entropy production.

$$Ex_{destroyed} = T_0 S_{gen} \geq 0 \tag{3.36}$$

The exergy loss in all real systems has a positive value and is zero for reversible systems. By ignoring nuclear, electrical, potential, kinetic, surface tension, and magnetic energies, the total exergy rate of a system can be calculated as (Kotas, 2013):

$$\dot{Ex} = \dot{Ex}_{ph} + \dot{Ex}_{ch} \tag{3.37}$$

Where $\dot{Ex}$, $\dot{Ex}_{ph}$, and $\dot{Ex}_{ch}$ are the exergy rate of the stream, the sum of its physical exergies, and the sum of its chemical exergies, achievable by Equations (3-39) (Naeimi et al., 2019):

$$\dot{Ex}_{ph} = \sum_i \dot{n}_i \left((\bar{h}_i - \bar{h}_0) - T_0 (\bar{s}_i - \bar{s}_0) \right) \tag{3.38}$$

$$\dot{Ex}_{ch} = \dot{n} \left(\sum_i x_i \, \overline{ex}_i^{ch,0} + \bar{R} T_0 \sum_i x_i \, ln(x_i \gamma_i) \right) \tag{3.39}$$

$\bar{h}_0$ and $\bar{s}_0$ are enthalpy and entropy at the ambient pressure and temperature. In Equation (3-39), γ_i is the activity coefficient of the i^{th} component which can have a value greater than or less than one and zero for an ideal mixture of different compounds. Ideal mixture means that the interactions between different molecules are negligible, and the properties of the mixture can be calculated based solely on the properties of the individual components and their respective proportions in the mixture. The calculation of chemical exergies for nonideal mixtures using Equation (3-39) is problematic, as the second term in this equation is the

Gibbs free energy of different components when forming the mixture in the ambient condition which results equation (3.40)

Regarding the definition of chemical exergy, all the calculations are performed at ambient temperature. Therefore, G^E is the Gibbs free energy for the mixture in the ambient temperature can be written in the form of equation (3.41)

$$G^E = G - \sum x_i \, G_i - RT_\circ \sum x_i \, Lnx_i \tag{3.40}$$

$$G^E = RT_\circ \sum x_i \, Lny_i \tag{3.41}$$

Adding the same term in each side of Equation (3-41):

$$\begin{aligned} G^E + RT_\circ \sum x_i \, Lnx_i &= RT_\circ \sum x_i \, Ln\gamma_i + RT_\circ \sum x_i \, Lnx_i \\ &= RT_\circ \sum x_i \, (Lnx_i + Ln\gamma_i) = RT_\circ \sum x_i \, (Lnx_i\gamma_i) \end{aligned} \tag{3.42}$$

By inserting Equation (3-42) into Equation (3-40):

$$\begin{aligned} G - \sum x_i \, G_i - RT_\circ \sum x_i \, Lnx_i + RT_\circ \sum x_i \, Lnx_i = RT_\circ \sum x_i \, (Lnx_i\gamma_i \,) \\ \rightarrow \quad G - \sum x_i \, G_i = RT_\circ \sum x_i \, Lnx_i\gamma_i = \Delta G^{mix} \end{aligned} \tag{3.43}$$

ΔG^{mix} is the change in the Gibbs free energy at ambient temperature. Finally, the chemical exergy equation is converted into Equation (3-44) (Ghorbani & Amidpour, 2021):

$$\dot{E}x_{ch} = \dot{n}(\sum_i x_i \, \overline{ex}_i^{ch,0} + \Delta G^{mix}) \tag{3.44}$$

The main objective of the exergy analysis is to find the places in a thermodynamic system where irreversibility occurs and measure them. This analysis helps to promote the systems'

efficiency. The exergy balance equation is shown in Equation (3-45) (Ghorbani & Amidpour, 2021):

$$Ex_i + Ex_{Qi} = Ex_o + Ex_{Qo} + W_{sh} + I \tag{3.45}$$

Equation (3-45) is used to calculate the irreversibility or exergy losses. Ex_i, Ex_o, Ex_{Qi}, Ex_{Qo}, W_{sh}, and I are exergies of inlet and outlet flows, and exergies of inlet and outlet energy streams, axial work, and irreversibility (exergy loss), respectively.

$$I_{p,c} = Ex_i - Ex_o = \sum(\dot{m}ex)_i + W - \sum(\dot{m}ex)_o \tag{3.46}$$

Ex_i and Ex_o are the irreversibility of the inlet and outlet exergies. The efficiency of pumps and compressors is calculated as follows (Ghorbani & Amidpour, 2021):

$$\eta_{p,c} = \frac{\sum(\dot{m}ex)_i - \sum_i(\dot{m}ex)_o}{W} \tag{3.47}$$

The exergy destruction and the efficiency of turbines can be calculated by Equations (3-48) and (3-49) (Ghorbani & Amidpour, 2021):

$$I_T = Ex_i - Ex_o = \sum(\dot{m}ex)_i - W - \sum_i(\dot{m}ex)_o \tag{3.48}$$

$$\eta_t = \frac{W}{\sum(\dot{m}ex)_i - \sum_i(\dot{m}ex)_o} \tag{3.49}$$

For heat exchangers, I_{HX} and η_{HX} are calculated by (Ghorbani & Amidpour, 2021):

$$I_{HX} = Ex_i - Ex_o = \sum(\dot{m}ex)_i - \sum(\dot{m}ex)_o \tag{3.50}$$

$$\eta_{HX} = 1 - \left\{ \left[\frac{\sum_1^n(\dot{m}\Delta ex)}{\sum_1^n(\dot{m}\Delta eh)}\right]_h - \left[\frac{\sum_1^n(\dot{m}\Delta ex)}{\sum_1^n(\dot{m}\Delta eh)}\right]_c \right\} \tag{3.51}$$

For the exergy destruction and its efficiency in throttling valves, Equations (3-52) and (3-53) are utilized (Ghorbani & Amidpour, 2021):

$$I_V = Ex_i - Ex_o = \sum(\dot{m}ex)_i - \sum(\dot{m}ex)_o \tag{3.52}$$

$$\eta_{ex} = \frac{ex_o^{\Delta T} - ex_i^{\Delta T}}{ex_i^{\Delta p} - ex_o^{\Delta p}}\ ,\ \ (ex^{\Delta T} = \int_T^{T_0} \frac{T - T_0}{T}\, dh,\ \ ex^{Ph} = ex^{\Delta T} + ex^{\Delta T}) \tag{3.53}$$

In distillation columns (towers) for the calculation of exergy destruction and exergy efficiency, the following equations are employed (Ghorbani & Amidpour, 2021):

$$\mathrm{I_{Column}} = \mathrm{Ex_i} - \mathrm{Ex_o} = \sum(\dot{\mathrm{m}}\mathrm{ex})_\mathrm{i} + \mathrm{Ex}_{\mathrm{Reb}}^{\mathrm{Q}} - \mathrm{Ex}_{\mathrm{Con}}^{\mathrm{Q}} - \sum(\dot{\mathrm{m}}\mathrm{ex})_\mathrm{o} \tag{3.54}$$

$$\eta_{\mathrm{ex}} = \frac{\mathrm{Ex}_{\mathrm{Con}}^{\mathrm{Q}} + \sum(\dot{\mathrm{m}}.\,\mathrm{ex})_\mathrm{o}}{\sum(\dot{\mathrm{m}}\mathrm{ex})_\mathrm{i} + \mathrm{Ex}_{\mathrm{Reb}}^{\mathrm{Q}}} \tag{3.55}$$

$\mathrm{I_{Reactor}}$ and η_{ex} are the exergy destruction and exergy efficiency of the methanol reactor achievable by Equations (3-56) and (3-57) (Ghorbani & Amidpour, 2021):

$$I_{Reactor} = Ex_i - Ex_o = \sum(\dot{m}.ex)_i - Ex_{out}^{Q} - \sum(\dot{m}.ex)_o \tag{3.56}$$

$$\eta_{ex} = \frac{Ex_{out}^{Q}}{\sum(\dot{m}ex)_i - \sum(\dot{m}ex)_o} \tag{3.57}$$

For parabolic solar troughs, exergy efficiency and exergy destruction are calculated as follows (Ghorbani & Amidpour, 2021):

$$I_{Collector} = Ex_i - Ex_o = \sum(\dot{m}ex)_i - Ex_{out}^{Q} - \sum(\dot{m}ex)_o \tag{3.58}$$

$$Ex_{out}^{Q} = \left[1 - \frac{4}{3}\frac{T_a}{T_s}(1 - 0.28\, ln\, f)\right] \times \dot{Q}_{in} \tag{3.59}$$

$$\eta_{ex} = \frac{\sum(\dot{m}ex)_i - \sum(\dot{m}ex)_o}{Ex^{Q}_{out}} \tag{3.60}$$

3.4 Results and Discussion

In this paper, an integrated structure for the cogeneration of liquid methanol, power, and heat is developed. The weather condition of Bushehr city is considered for the model of parabolic solar troughs. The cryogenic purification cycle provides 88.05% molar hydrogen from the 55% molar feed of crude hydrogen. This cycle receives 19.62 kW of low-temperature cooling from the absorption–compression refrigeration cycle and 19.62 kW of low-temperature cooling from liquid nitrogen to produce side products. These side products include 1123 kg/h of low-pressure fuel (86.81% molar methane) and 54.99 kg/h of high-pressure fuel (95.08% molar methane). The residual outlet of the cycle consists of 871.1 kg/h of aromatic compounds. The purified hydrogen and CO_2 enter the methanol production cycle to produce 4741 kg/h of liquid methanol, easy to store or transport to remote areas. For supplying thermal power in this cycle, parabolic solar troughs and auxiliary boilers are designed. The ACRC and ORC recover the heat of the exothermic reaction in the methanol reactor. The ACRC provides 29.97 kW of cooling at −42.07 °C for the hydrogen purification cycle by receiving 49.05 kW of heat. The ORC produces 475 kW of net electrical power from its 2418 kW input thermal power. Plots of P-H and T-S corresponding to the ORC are shown in Figure 3.6 a and b, providing information regarding the vapor fraction of the stream and places with irreversibility and entropy production.

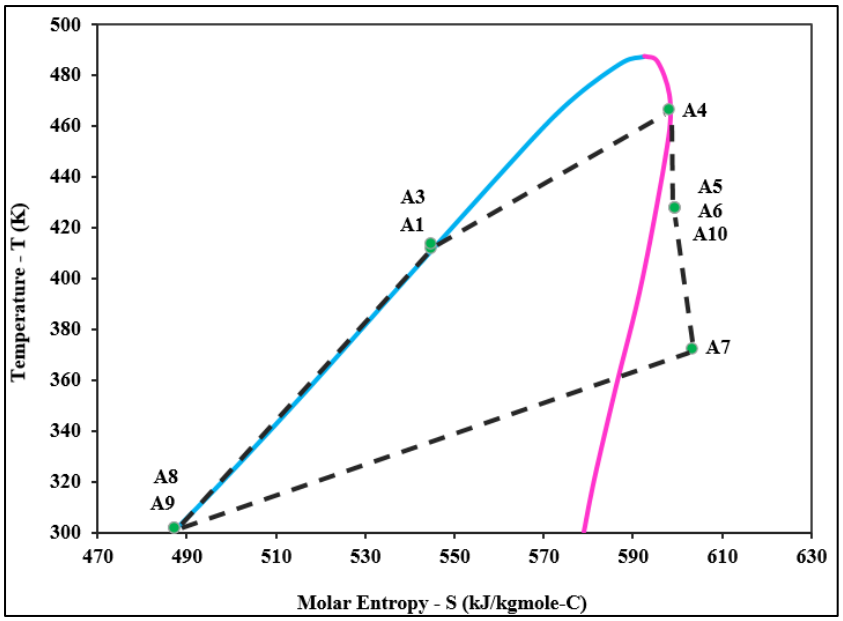

(a) T-S diagram

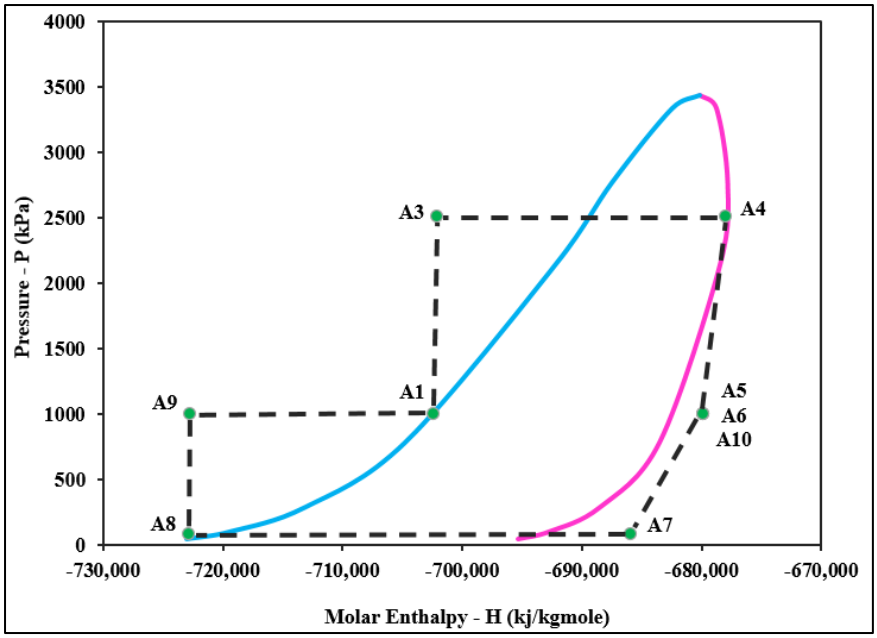

(b) P-H diagram

Figure 3.6. T-S diagram and P-H diagram for the organic Rankine power generation cycle

The plug flow reactor is used for methanol production modeled in Aspen HYSYS V10.0 software. This reactor produces 2493 kW of heat at 200 °C. Parabolic solar troughs are utilized to supply the required 3435 kW of thermal power in the methanol distillation tower for the separation of water and liquid methanol. As the intensity and direction of the sun are not stable, the periodic nature of the amount of the heat suppliable by the solar collectors necessitates the use of an auxiliary boiler to ensure the constant thermal power. Parabolic solar troughs are modeled using MATLAB V10.0 m-file code, each having a 6.1 m length and 2.3 m width. The oil stream containing 24.62% molar Biphenyl and 75.38% molar dipH-Ether is used for the heat transfer from the solar collectors to the distillation tower. The thermal and optic efficiencies, outlet temperature from the collectors, and useful thermal power at 12:00 O'clock are 42.37%, 24.08%, 184.9 °C, and 3422.8 kW, respectively. An auxiliary boiler supplies the remaining required heat (12.2 kW). The results show that the energy efficiencies of the ORC, the methanol production cycle, the total thermal efficiency of the integrated structure, and the COP of the ACRC are 19.46%, 60.91%, 78.014%, and 0.3031, respectively. The results of energy, exergy, and sensitivity analyses of the integrated structure are as follows. Validations of the developed integrated structure are available in Table 3.6. Thermodynamic characteristics of streams are provided in Table 3.7.

3.4.1 Energy Analysis Results

The required information for each subsystem and cycle is extracted from data in industrial patents and scientific references. Table 3.2 shows the operational condition of equipment used in the proposed integrated structure. The minimum temperature difference between the hot and cold curves in heat exchangers (ΔT_{min}) is considered as the output parameter. It is the main factor contributing to the heat transfer between hot and cold sections. The refrigeration cycles' integration in the present study is provided by the process core in the form of cold and hot composite curves. The pinch technology can modify the energy consumption and determine the required utility by using its key tools of composite curves (CC) and grand composite curves (GCC). Figures 3.7a–c show composite curves of three multi-stream heat exchangers of HX1, HX3, and HX4. In heat exchangers in which a single-component

refrigerant is used (CO_2 in the HX1 exchanger and N2 in the HX4 exchanger), the distance between hot and cold curves is more than that of the heat exchanger with a multi-component refrigerant. A good matching between hot and cold curves in the heat exchanger with the multi-component refrigerant is noticeable as the ΔT_{min} value decreases, utilities used in the structure decrease, and the area required for heat transfer increases.

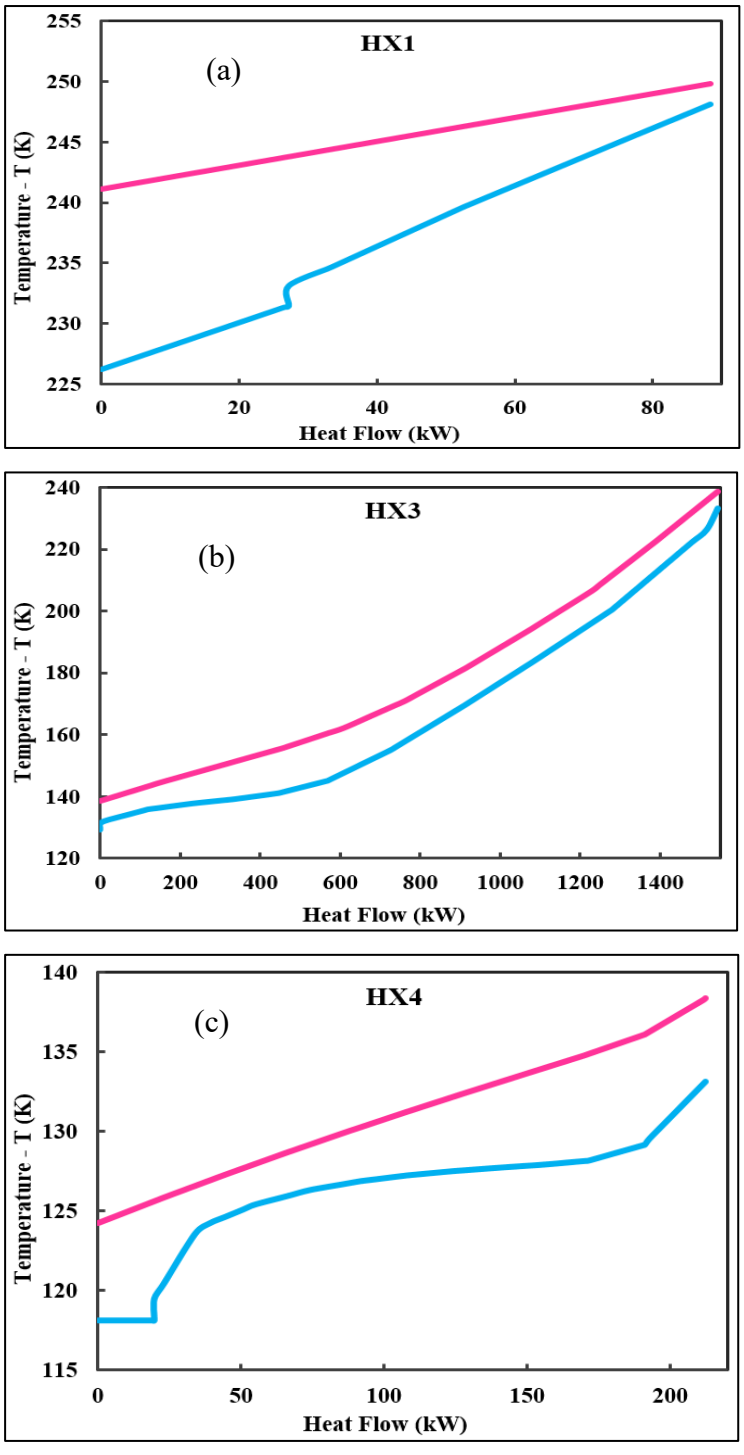

Figure 3.7. Hot (pink) and cold (blue) composite curves
(a) HX1, (b) HX3, and (c) HX4

Table 3.2. Equipment major specifications

Pump						
Parameter	Adiabatic efficiency	Power	ΔP	P ratio	Pressure head	Capacity
Unit	%	kW	bar	-	m	m^3/h
Pump1	85	6.85	9.2	12.5	60.17	10.0
Pump2	85	26.59	15.0	2.5	122.6	10.0
Pump3	75	0.36	11.39	6.25	175.3	10.0
Turbine						
Parameter	Isentropic efficiency	Power	ΔP	P ratio	Polytropic efficiency	Outlet Temp.
Unit	%	kW	bar	-	%	K
Turb1	80	189.0	15.0	0.40	79.45	427.1
Turb2	80	319.4	920.0	0.08	78.73	371.4
Compressor						
Parameter	Adiabatic efficiency	Power	ΔP	P ratio	Polytropic efficiency	Outlet Press.
Unit	%	kW	bar	-	%	bar
Comp1	80	7.3	31.0	4.45	87.37	40.0
Comp2	75	169.6	7.0	1.16	75.47	50.0
Column						
Parameter	No. of stages	Feed stage	Tray Space	Cond. duty	Reboiler duty	
Unit	-	-	m	kW	kW	
Column1	8	4	0.55	10.36	45.09	
Column2	53	26.5	-	411.7	453.5	

Table 3. 2. Equipment major specifications (continued)

Heat exchanger					
Parameter	Min. approach	LMTD	UA	Heat duty	Cold pinch Temp.
Unit	°C	°C	MJ/h°C	kW	K
HX1	1.67	5.91	53.82	88.33	248.15
HX2	2.90	8.65	10.39	24.97	238.25
HX3	5.56	11.10	500.85	1544.50	233.15
HX4	2.54	4.26	179.464	212.42	125.43
HX5	3.75	5.00	1739.95	2418.40	413.11
HX7	3.00	19.87	352.18	1943.40	298.15
HX8	102.82	105.6	4.56	1336.82	298.15
HX9	6.74	31.04	51.45	443.61	316.52
HX10	4.00	6.55	2259.26	4109.66	313.15
HX11	15.00	29.04	324.04	2613.87	298.15
HX12	173.68	174.30	0.54	26.39	303.15
HX13	10.00	57.61	93.47	1495.78	453.15
HX14	184.62	184.60	0.003	0.14	231.53
HX15	10.00	18.59	12.21	63.07	298.15
HX16	24.06	27.32	5.93	44.97	387.35
HX17	29.87	60.55	1.76	29.57	386.99
HX18	5.00	8.07	14.95	33.51	303.15
HX19	1.56	23.15	5.03	32.31	256.18
HX20	20.80	24.68	0.39	2.70	287.35
Reactor					
Parameter	Duty	ΔP	No. of Segments	Total volume	Number of tubes
Unit	kW	bar		m3	-
MR1	2493	20.0	20	14.26	1621

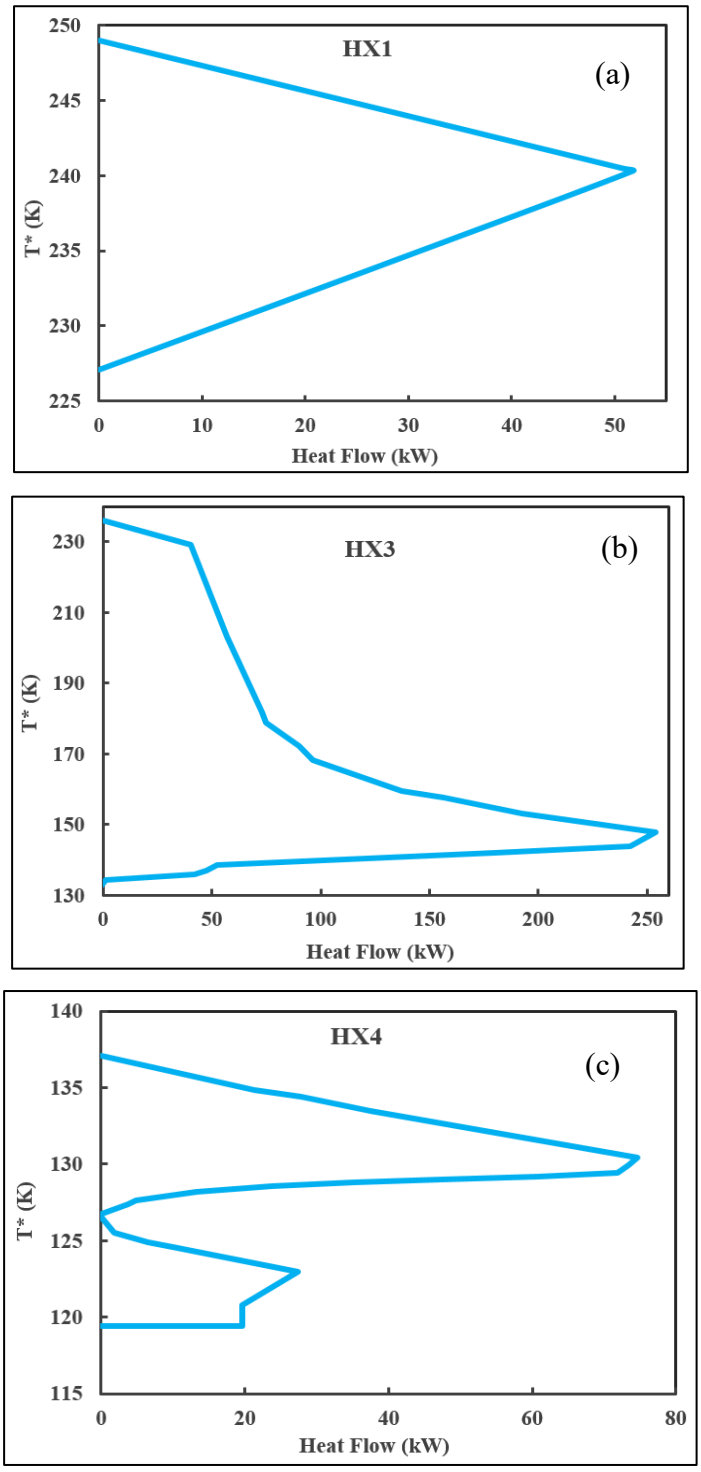

Figure 3.8. Grand composite curves (GCC) for
(a) HX1, (b) HX3, and (c) HX4

Figures 3.8a–c show the grand composite curves for the HX1, HX3, and HX4 exchangers. In this paper, Aspen HYSYS V10.0 software is used to determine the pinch point, and MATLAB V10.0 software in connection with Aspen HYSYS V10.0 is used for drawing the composite curves and grand composite curves.

3.4.2 Exergy Analysis Results

Exergy analysis is performed using Aspen HYSYS V10.0 software and MATLAB V10.0 m-file programming. The functions used to link HYSYS V10.0 software and MATLAB V10.0 programming are available in the Supplementary Document. The first step in the exergy analysis is the exergy calculation of streams in the processes, including the exergy of each stream and its exergy loss. Using exergy balance for each piece of equipment, its exergy destruction and exergy efficiency can be calculated. The inlet, outlet, and destructed exergies in each piece of equipment are shown in Table 3.3. It shows that throttling valves have lower exergy efficiencies than other equipment. The reason for using these valves in refrigeration processes is to decrease the refrigerant's temperature by lowering its pressure. The reduced temperature facilitates the cooling of hot sources in the process. Therefore, the exergy efficiency in throttling valves can be defined as the exergy difference related to providing cooling to the exergy difference related to the pressure decrease. As these valves have lower exergy destruction than other equipment, their contribution to the total exergy destruction is insignificant. Due to high levels of heat transfers in heat exchangers, they produce considerable irreversibility. However, as shown in Table 3.3, heat exchangers have higher exergy efficiencies than other equipment. Therefore, for the performance comparison of equipment used, both their irreversibility and exergy efficiency parameters are considered. Figure 3.9 illustrates the share of each piece of equipment in the total exergy destruction, with the parabolic solar trough taking the lion's share of 34%, followed by heat exchangers with 30% and mixers with 19% of the total share. Among heat exchangers, the maximum share of exergy destruction belongs to the HX6 and HX8 exchangers, with 50% and 11%, respectively. Based on the exergy analysis, the total exergy efficiency of the integrated structure and its irreversibility are 89.45% and 16.89 MW, respectively.

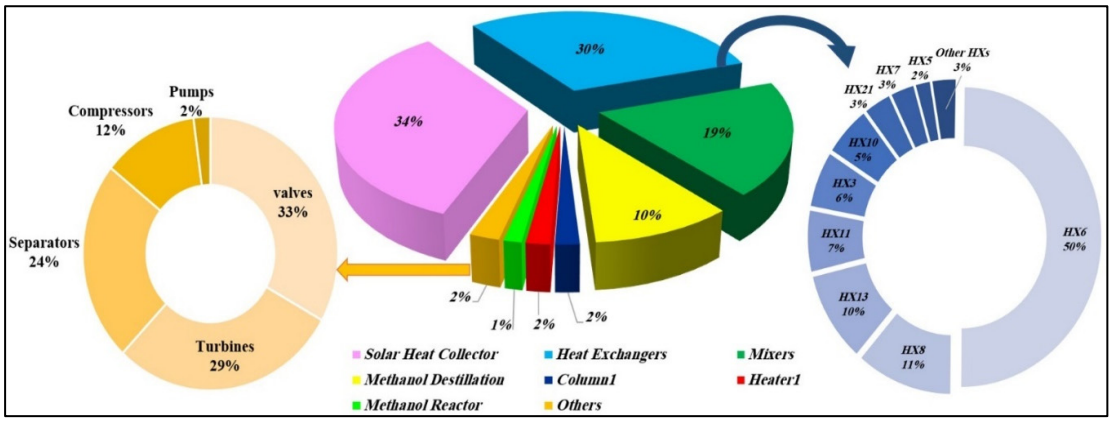

Figure 3.9. The share of each piece of equipment in the total exergy destruction

Table 3.3. Inlet exergy (IE), outlet exergy (OE), exergy efficiency (EEf) and exergy destruction (ED) of each equipment

Item	IE	OE	ED	EEf	Item	IE	OE	ED	EEf
	kW	kW	kW	kW		kW	kW	kW	kW
HX1	312,897	312,893	3.84	95.65	Pump2	16,415	16,411	3.43	87.11
HX2	156,642	156,641	1.17	95.33	Pump3	1121	1121	0.09	75.82
HX3	293,351	293,156	194.7	87.39	Sep1	156,589	156,589	0.00	100
HX4	136,878	136,860	18.11	91.48	Sep2	147,260	147,260	0.00	100
HX5	809,672	809,614.	57.37	97.63	Sep3	68,5211	68,521	0.00	100
HX6	795,551	793,967	1583	99.80	Sep4	49,070	49,016	54.12	100
HX7	37,832	37,742	89.95	95.37	Tank1	27,848	27,848	0.00	100
HX8	71,211	70,854	356.5	73.33	TEE1	17,013	17,013	0.00	100
HX9	28,754	28,710	43.79	90.13	TEE2	1121	1121	0.00	100
HX10	596,219	596,044	174.6	95.75	MIX1	16,512	16,388	123.8	99.25
HX11	552,948	552,734	213.7	91.82	MIX2	1126	1125	0.50	99.96
HX12	52,103	52,093	9.56	63.76	T1 *	1331	1146	184.2	86.16
HX13	597,921	597,608	313.2	79.06	T2 **	29,422	29,262	1076	99.45
HX14	844,348	844,348	0.08	43.03	V1	10,437	10,436	1.01	78.94
HX15	3026	30221	4.06	93.56	V3	68,267	68,250	17.73	73.69
HX16	1251	1249	2.21	95.09	V4	16,126	16,116	10.54	69.17
HX17	792,827	792,823	3.70	87.49	V5	59.47	58.82	0.65	64.89
HX18	1069	1069	0.08	99.77	V6	563.7	563.4	0.34	72.12
HX19	621	617	3.83	88.16	V7	568.6	568.4	0.19	75.24
HX20	1121	1121	0.27	89.91	MR1	51,244	51,108	135.9	87.16
Turb1	17,235	17,202	33.11	85.09	HE1	156,746	156,564	181.6	99.88
Turb2	17,235	17,202	33.11	85.09	HX21	793,294	793,191	102.2	99.99
Comp1	65.33	51.58	0.94	87.18	Collec.	3,098,312	3,094,735	3577	47.34
Comp2	51,281	51,254	26.75	84.23	MIX3	52,815	50,947	1868	96.46
Pump1	8432	8431	1.35	80.26	V2	78,992	78,947	45.16	77.20

* Ammonia–water distillation tower. ** Methanol distillation tower.

3.4.3 Sensitivity Analysis Results

One of the most effective methods for helping the optimization of a thermodynamic structure is sensitivity analysis. This method assesses the influence of operational variables on the structure's important parameters. Operational variables include temperature, pressure, flow rate, and composition of the streams. By tracing the feedback of the structure to the changes in operational variables, the reaction of the integrated structure and its sensitivity to each alteration could be analyzed. Here, the reaction of the structure to the changes in variables in the most influential streams are presented.

3.4.3.1 Changing the Temperature of Stream D17

The most important stream in the purification cycle is stream D17. The temperature increase in this stream directly relates to the amount of produced vapor (stream D18), resulting in a decline in hydrogen purity. Therefore, a temperature increase in stream D17 leads to an increase in the methane content of the feed stream C1 in the methanol production cycle. Considering that the flow rate of CO_2 remains unchanged, the methanol production capacity, the heat produced in the methanol reactor, and the thermal power required in the methanol distillation tower will decline. Similarly, the total efficiency and the efficiency of the methanol production cycle will decrease. Figure 3.10 demonstrates the changes in the main system parameters with the changes in stream D17's temperature. Figure 3.10 a,b show that by increasing the temperature of stream D17 from −149 to −139 °C, the produced heat in the methanol reactor, required heat in the distillation tower, the efficiency of the integrated structure, and the methanol production rate decrease to 2485 kW, 3420 kW, 70.45%, and 4719.6 kg/h, respectively. Based on the results from Figure 3.10 c, with a temperature decrease in stream D17, the wasted heat and produced methanol decrease, resulting in a decline in the thermal efficiency of the methanol production cycle to 49.77%. Besides, this temperature decrease leads to a growth in exergy destruction to 17.04 MW. The main reason for this phenomenon is the increase in the pinch temperature in the HX4 exchanger and the reduction in the production rate.

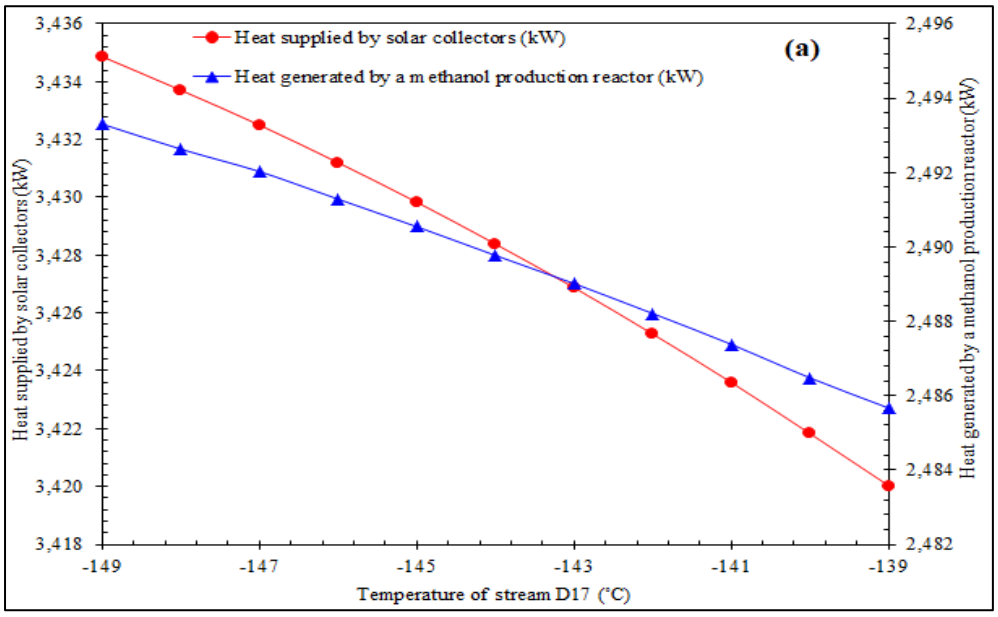

(a) The influence of changes in stream D17's temperature on heat supplied by parabolic solar troughs and heat produced by the methanol reactor

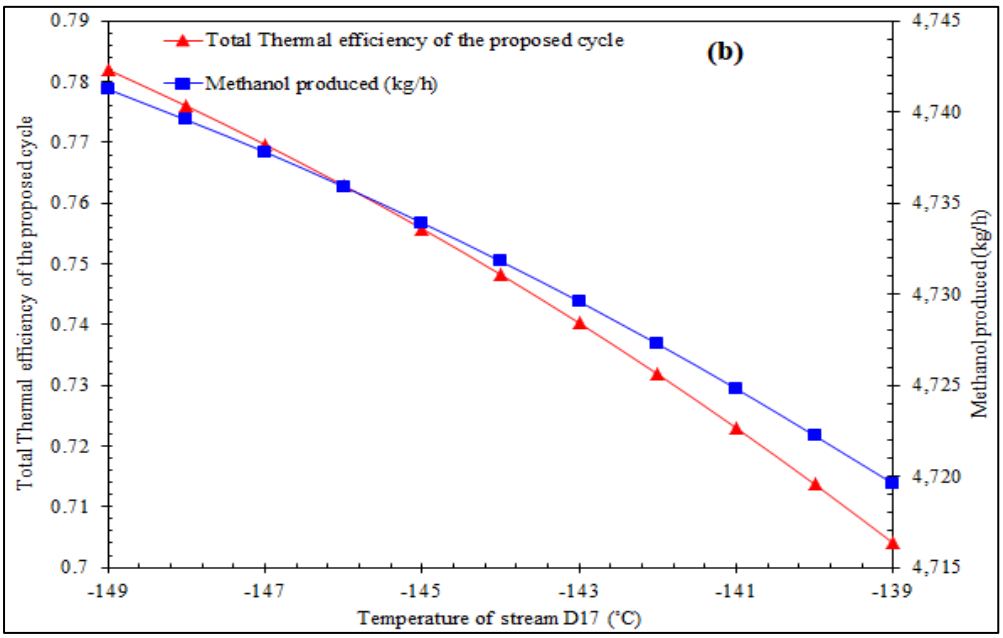

(b) The influence of changes in stream D17's temperature on total thermal efficiency and the methanol production rate

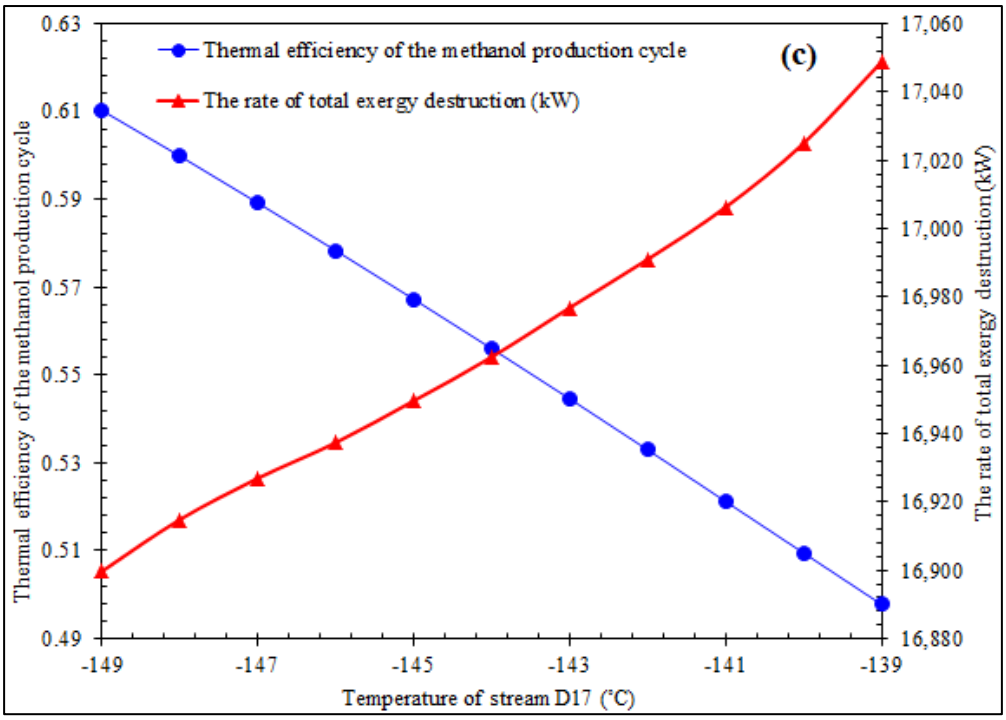

(c) The influence of changes in stream D17's temperature on the thermal efficiency of the methanol production cycle and total exergy destruction.

Figure 3.10. a, b, c. The influence of changes in stream D17's temperature on principal output parameters

3.4.3.2 Changing the Hydrogen Fraction of Inlet Feed in the Hydrogen Purification Cycle

The changes in the main parameters of the integrated structure with the changes in the hydrogen fraction of inlet feed in the hydrogen purification cycle are shown in Figure 3.11. The main parameters here include methanol production rate, exergy efficiency of the integrated structure, wasted heat in the methanol reactor, and solar collectors' thermal power production. A rise in the hydrogen fraction of crude feed gas leads to an increase in hydrogen purity entering the methanol production cycle. Considering that the cooling supplied by nitrogen refrigeration remains unchanged, the fractions of methane and nitrogen in the outlet stream increase, resulting in a decrease in the thermal value. Thus, considering that the flow rate of CO_2 is constant, the wasted heat in the methanol reactor and methanol production rate decline. Figure 3.11a,b show that when the hydrogen purity in the feed gas increases from

55% to 80% molar, the exergy efficiency, methanol production rate, wasted heat in the methanol reactor, and the thermal power production by solar collectors decrease to 86.05%, 4487 kg/h, 2431.7 kW, and 3261.8 kW, respectively. The increase in the hydrogen purity in the feed gas leads to decreases in the thermal efficiency of the integrated structure to 25.95% and total exergy destruction to 25.41 MW, as shown in Figure 3.11c.

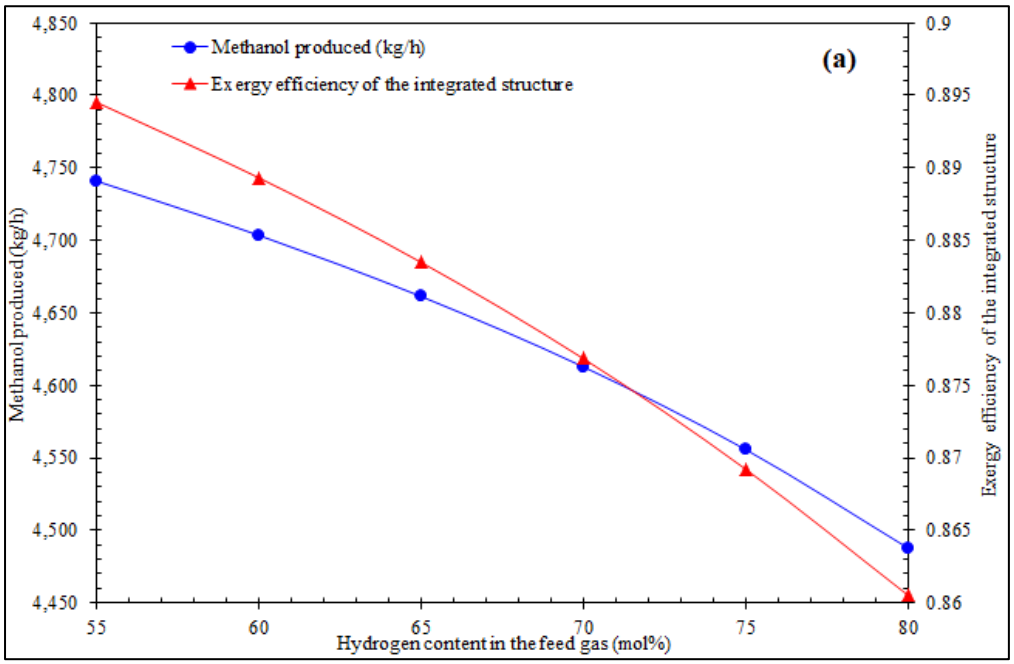

(a) The influence of the changes of the hydrogen content of crude feed gas on the methanol production rate and total exergy efficiency

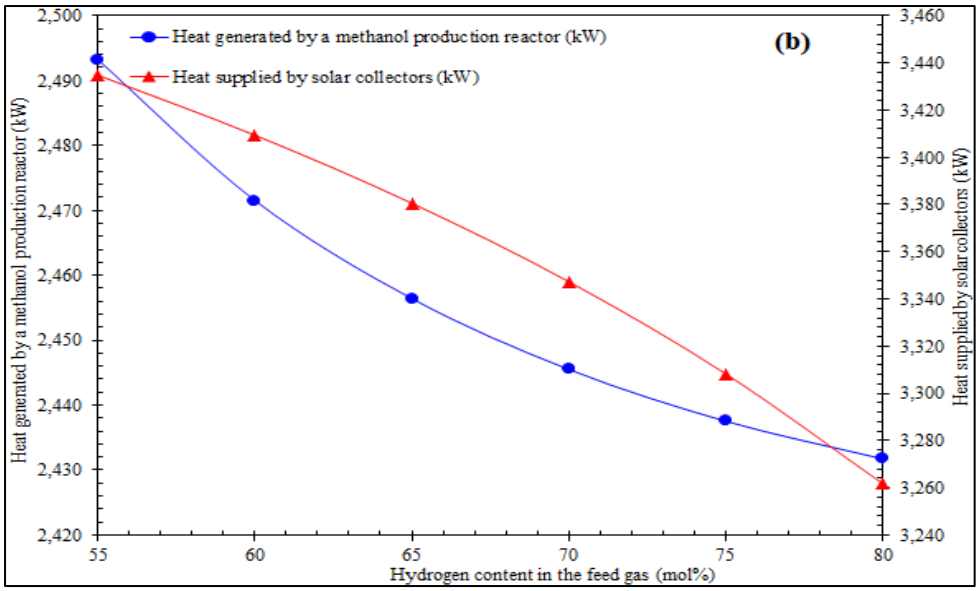

(b) The influence of the changes of the hydrogen content of crude feed gas on heat generated by the methanol production reactor and heat supplied by solar collectors

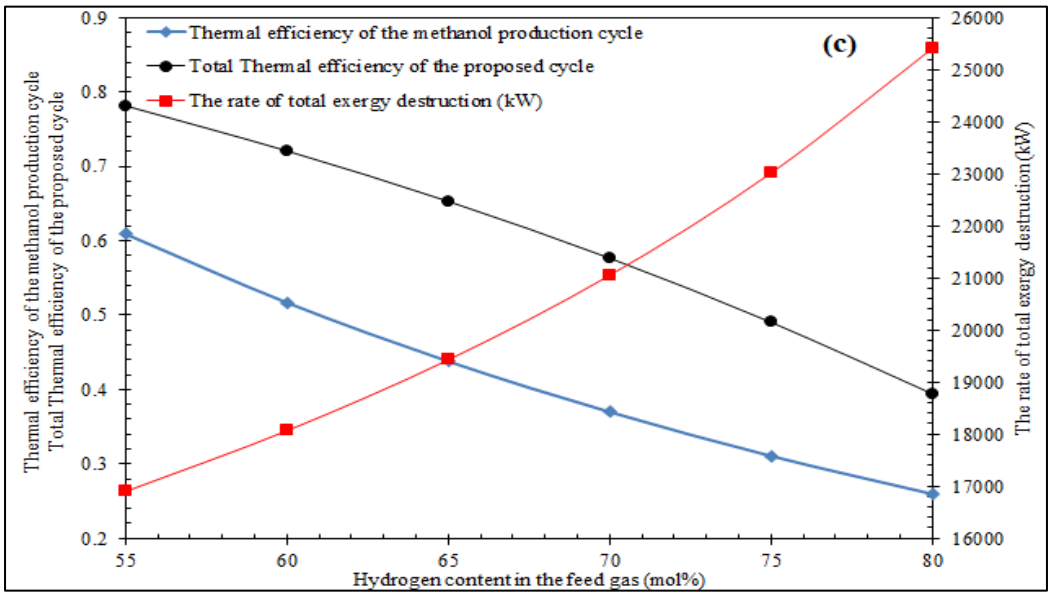

(c) The influence of the changes of the hydrogen content of crude feed gas on total thermal efficiency and thermal efficiency of the methanol production cycle, and the rate of total exergy destruction

Figure 3.11. The influence of the changes of the hydrogen content of crude feed gas on main outcome parameters

3.4.3.3 Changing the Flow Rate of CO_2 in the Methanol Production Cycle

Considering that the hydrogen fraction of the feed gas remains constant, with an increase in the flow rate of CO_2, the wasted heat in the methanol reactor and the methanol production rate increase. Figure 3.12 shows the influence of this change in the main parameters of the integrated structure. Figure 3.12a,b show that the growth in the CO_2 flow rate from 5000 to 9000 kg/h results in increases in the methanol production rate, the thermal efficiency of the integrated structure, the thermal efficiency of the methanol production cycle, and wasted heat in the methanol reactor to 5975.8 kg/h, 82.30%, 73.41%, and 3073 kW, respectively. As a considerable part of the total exergy destruction occurs in parabolic solar troughs, with the increase in the required thermal power in the reboiler of the methanol distillation tower, exergy efficiency declines, and exergy destruction increases.

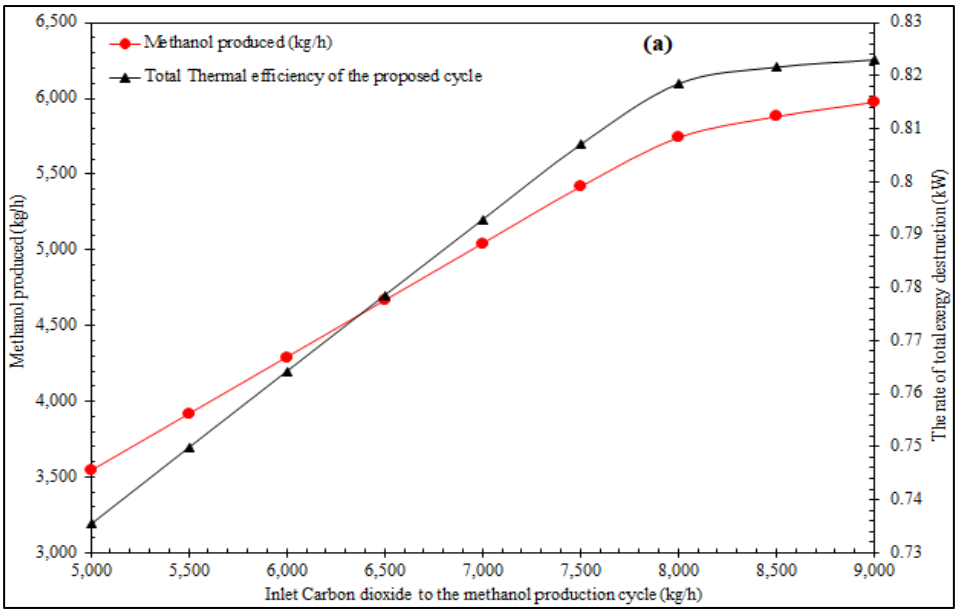

(a) The influence of the changes of the CO_2 flow rate on the methanol production rate and total exergy destruction

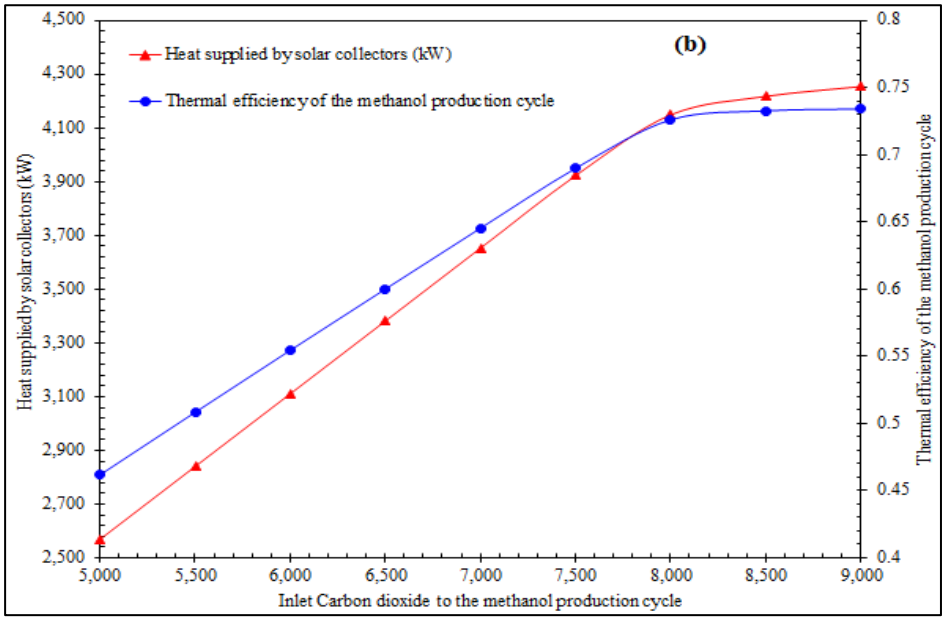

(c) The influence of the changes of the CO_2 flow rate on heat supplied by solar collectors and the thermal efficiency of the methanol production cycle

Figure 3.12. The effect of the changes of the CO_2 flow rate on main output parameters

The results show that decreasing the flow temperature of D17 and the hydrogen content in the feed gas and increasing the carbon dioxide content entering the methanol production system leads to an increase in the thermal efficiency of the proposed integrated structure and the heat supplied by solar collectors.

3.5 Validation of the developed integrated structure

Partial validation was used to validate the integrated structure for power, heat, and liquid methanol cogeneration. The cryogenic hydrogen purification and the absorption–compression refrigeration cycles of the integrated structure were compared with similar processes available in industries or resources in which related data are reported, and the accuracy of results is validated. In Table 3.4, the main parameters of the cryogenic hydrogen purification cycle are validated with the studies carried out by Asadnia et al. (Aasadnia et al., 2021) and Mehrpooya et al. (Mehrpooya et al., 2021), including the required precooling and low-temperature cooling, the hydrogen content in the purified outlet stream, and exergy efficiency. Mehrpooya et al. (Mehrpooya et al., 2021) used the absorption–diffusion refrigeration cycle, Asadnia et al. (Aasadnia et al., 2021) used the propane compression cycle, and the present paper used the absorption–compression refrigeration cycle to provide cooling.

Table 3.4. Validation of the main parameters of the cryogenic hydrogen purification cycle (Mehrpooya et al., 2021) , (Aasadnia et al., 2021)

Parameter	Present Study	Mehrpooya et al	Asadnia et al.	Unit
Type of refrigeration cycle	Absorption–compression	Diffusion–absorption	Propane compression	
Required refrigeration for precooling	0.0024	0.07125	0.00227	kWh/kg
Required N_2 for low-temperature cooling	0.001962	0.00196	0.001962	kWh/kg
Purity of the separated hydrogen	88% molar	88	88	% molar
Exergy efficiency	92.83%	93.825	91.73	%

Table 3.5. Validation of the main parameters of the developed integrated structure (Y. Chen et al., 2017); (Mehrpooya et al., 2020); (Mousavi & Mehrpooya, 2020)

Item	Mixture	COP	Refrigerant Temperature (Evaporator), °C
This study	$H_2O/N_2/CO_2$	0.3031	−42.07
Chen et al.	$H_2O/NH_3/CO_2$	0.277	−55
Mehrpooya et al.	$H_2O/NH_3/CO_2$	0.2539	−54.62
Mousavi et al.	$H_2O/NH_3/CO_2$	0.268	−54.62

The findings of our study indicate that the data derived from the integrated structure developed herein align well with the reference data outlined in Table 3.5, demonstrating an acceptable level of accordance. Notably, the implementation of cooling at a lower temperature (-42.07 °C) resulted in a marked improvement in the Coefficient of Performance

(COP) compared to the values documented in the aforementioned references. This enhancement underscores the efficacy and innovation of our approach, as it contributes to achieving greater energy efficiency and performance optimization within the system. These results not only validate the effectiveness of our methodology but also offer valuable insights for future research and practical applications in the field of cooling systems and energy conservation.

The result of the comparison between the liquid methanol production cycle in the present study and the work carried out by Hosseini et al. (Hosseini et al., 2019) is available in Table 3.6, showing appropriate accordance between the present and reference paper. The evaluation encompasses a range of parameters crucial to the efficiency and effectiveness of the system. These parameters include but are not limited to, the wasted heat generated by the methanol reactor, the requisite heat demanded by the reboiler, the inefficiencies in the solar thermal collectors, and the purity levels achieved in the resultant liquid methanol. Each of these aspects plays a pivotal role in determining the overall performance and viability of the process. By meticulously scrutinizing these parameters, we can gain deeper insights into the system's functionality, identify potential areas for optimization, and ultimately enhance its operational efficacy.

Table 3.6. Validation of the liquid methanol production cycle (Hosseini et al., 2019)

Parameters	Unit	This Study	Hosseini et al.	Relative Error
Pressure drop	kPa	2000	2000	0
Heat released from methanol reactor to methanol production	kWh/kmol	16.83	17.1	−1.604
Required heat of reboiler to methanol production	kWh/kmol	23.19	23.32	−0.5605
Wasted heat of the condenser to methanol production	kWh/kmol	11.2	11.2	0
Condenser temperature	°C	138.5	138.5	0
Reboiler temperature	°C	180.3	180.3	0
Methanol purity	%	99.8	99.8	0.0601
Reactor's inlet mixture rate to the methanol production	-	4.424	4.423	15.81
External reflux ratio		1.3	1.3	0

Thermodynamic characteristics of streams, including temperature, pressure, and flow rate, are provided in Table 3.7.

Table 3.7. The used streams thermodynamic characteristics

	Temp.	Press.	Flow		Temp.	Press.	Flow
	^{0}C	kPa	kmol/h		^{0}C	kPa	kmol/h
A1	138.06	1000	361.1	D3	-25	551.581	313.81
A2	35	100	9003.07	D4	-25	344.738	70.69
A3	139.96	2500	361.1	D5	-23.33	4481.59	1025.72
A4	192.5	2500	361.1	D6	-32	4481.59	1025.72
A5	153.95	1000	361.1	D7	-34.44	4481.59	1025.72
A6	153.95	1000	189.58	D8	-34.44	4481.59	1012.89
A9	28.42	1000	189.58	D11	-134.44	4481.59	1012.89
A10	153.95	1000	171.52	D12	-134.44	4481.59	699.08
B1	25	100	13,218.05	D13	-134.44	4481.59	313.81
B2	30	100	13,218.05	D14	-141.68	551.581	313.81
B3	165	100	1803.49	D15	-40	551.581	313.81
B6	199.01	100	461.93	D18	-148.89	4309.22	628.39
B7	200	100	461.93	D19	-140	4309.22	628.39
B8	143	100	461.93	D20	-46.9	4309.22	628.39
B9	25	100	1983.39	D21	-41.64	4309.22	628.39
B10	143	100	461.93	D22	-155	2294.85	25.82
B11	25	100	260.97	D23	-148.89	4309.22	70.69
B13	139.9	100	318.61	D25	-144	344.738	70.69
C1	-41.61	4309.22	628.39	E2	-42.07	900	7.21
C2	25	4300	149.92	E3	81.33	4000	7.21
C3	-33.92	4300	778.32	E4	-15.41	4000	7.21
C4	180	4300	778.32	E6	30	100	584.4
C6	200	5000	778.32	E8	30	100	155.22
C10	43.37	2000	297.4	F3	-14	217	5.86
C11	95	2000	297.4	F4	14.2	217	5.86
C12	180.32	1000	149.34	F5	61.08	217	31.78

Table 3.7. The used streams thermodynamic characteristics (continued)

	Temp.	Press.	Flow		Temp.	Press.	Flow
	^{0}C	kPa	kmol/h		^{0}C	kPa	kmol/h
C13	138.55	1000	148.06	F6	35	217	31.78
C14	127.82	1000	148.06	F7	35.24	1356	31.78
C15	127.82	1000	148.06	F8	35.24	1356	19.09
C16	127.82	1000	0	F9	35.24	1356	12.7
C17	50.11	1000	149.34	F10	113.85	1356	12.7
D1	-73.33	4481.59	1025.72	F15	138.26	1356	25.92
D2	-25	1723.69	12.82	F16	66.1	1356	25.92

3.6 Conclusions

Cogeneration systems in integrated structures increase the efficiency and decrease the equipment in energy systems compared to when each subsystem works separately. This paper proposed a novel system for the cogeneration of liquid methanol, electricity, and hot water. In this integrated structure, hydrogen purification, methanol production, Organic Rankine, absorption–compression cycles, and solar collectors were used. Energy, exergy, and sensitivity analyses were employed for the evaluation of the structure, leading to the following results:

1- This integrated structure received 10,000 kg/h of crude hydrogen, 6598 kg/h of carbon dioxide, and 19.62 kW of cooling from liquid nitrogen, 3435 kW of thermal power from parabolic solar troughs, and produced 4741 kg/h of liquid methanol, 35.73 ton/h of hot water, and 297.7 kW of net electrical power. The side products of this process include low-pressure and high-pressure fuel gases and aromatic compounds. The ORC absorbed the wasted heat in the methanol reactor to produce 475 kW power and the ACRC to supply 24.97 kW cooling for the hydrogen purification cycle. The thermal efficiencies of the integrated structure, the liquid methanol production cycle, and the ORC were 78.14%, 19.64%, and 60.91%,

respectively. The COP of the ACRC was calculated to be 78.14%. The results proved that 98.08% of the hydrogen was extracted from the crude feed in the purification cycle.

2- The exergy analysis showed that the integrated structure's exergy efficiency and exergy destructions were 89.45% and 16.89 MW, with 6.51 MW being considered as the total exergy loss. Despite the considerably high exergy losses in heat exchangers, their exergy efficiencies were higher than other equipment. Besides, throttling valves have low exergy efficiencies and a minor share in total exergy destruction. The previously mentioned design principles are the main reason for the integrated structure's high efficiency. Thus, no revision or correction is required for the structure.

3- The sensitivity investigation indicated that the thermal efficiency of the methanol production cycle and exergy efficiency of the integrated structure decreased by up to 25.95% and 86.05%, respectively, when the feed gas's hydrogen content increased from 55 mol% to 80 mol%. The thermal efficiency of the proposed cycle and productivity of the methanol increased by up to 82.30% and 5975 kg/h, respectively, with the increase of carbon dioxide composition in the methanol production cycle from 5000 to 9000 kg/h.

4- For future work, advanced exergoeconomic and environmental analyses can be implemented to decrease economic costs and carbon dioxide emissions. Additionally, it is possible to use multiple compositions instead of a carbon dioxide refrigerant in the refrigeration cycle and evaluate its effect on the main parameters of the integrated system.

CHAPTER 4

ECONOMIC APPRAISAL AND ENHANCED EFFICIENCY OPTIMIZATION FOR LIQUID METHANOL PRODUCTION PROCESS

Alireza Khatamijouybari [a], Adrian Ilinca [b]

[a, b] Department of Mechanical Engineering, École de Technologie Supérieure, 1100, Rue Notre-Dame Ouest, Montréal, QC H3C 1K3, Canada

Paper published in *MDPI-Sustainability*, February 2024[3]
(Khatamijouybari & Ilinca, 2024).

Abstract

The presented study examines the economic viability and optimization of a previously designed integrated process for producing liquid methanol. The annualized cost of the system method is applied for economic analysis. The optimization method includes a robust hybrid approach that combines the NSGA-II multi-objective optimization algorithm with artificial intelligence. Decision variables for the optimization are taken from a sensitivity analysis to optimize the exergy and energy efficiencies and the investment return period. Decision-making methodologies, including LINMAP, fuzzy, and TOPSIS, are utilized to identify the optimal outcomes, effectively identifying points along the Pareto-optimal front. Compared with the original design, the research outcomes demonstrate an over 38% reduction in the process's investment return period post optimization, as evaluated through the TOPSIS and LINMAP methodologies. Additionally, the highest level of thermal efficiency achieved through optimization stands at 79.9%, assessed using the LINMAP and TOPSIS methods, and 79.2% using the fuzzy Bellman–Zadeh method. The process optimization in the presented research, coupled with the improved economic feasibility, mitigates energy consumption through maximizing efficiency, thereby fostering sustainable and environmentally friendly development..

---

[3] Khatamijouybari, A.; Ilinca, A. Economic Appraisal and Enhanced Efficiency Optimization for Liquid Methanol Production Process. Sustainability, 16, 1993. https://doi.org/10.3390/su16051993, 2024

Keywords: Multi-objective optimization, economic analysis, sensitivity analysis, methanol production

4.1 Introduction

Hydrogen is widely regarded as an ideal fuel due to its environmentally friendly nature and heating value higher than conventional fuels (Chamousis, 2009). Hydrogen storage and transportation systems can be categorized into three primary groups: material-based, physical-based, and chemical-based methods. Material-based methods include physical absorption (physisorption) and chemical absorption (hydrides). Although considered safe, these methods lack the storage performance required for large-scale storage and transportation (Y. Li et al., 2021); (D. Wang et al., 2019). Physical-based methods involve storing hydrogen in its natural state without relying on chemical reactions or sorbent materials. This category encompasses hydrogen compression, hydrogen liquefaction, and two-phase storage systems of cryo-compression and slush hydrogen. Among all, compressed gas storage is the most widely used method globally, constituting 80% of all hydrogen refueling stations, followed by liquid storage (F. Zhang et al., 2016). Two prevalent chemical-based methods for hydrogen storage are methanol and ammonia. Methanol boasts a superior volumetric energy density and lower toxicity than ammonia. This positions methanol as a highly favorable choice as an energy carrier, complementing the use of liquid hydrogen (Ghorbani, et al., 2023).

Therefore, an alternative for hydrogen liquefaction for energy transportation is the reaction of purified hydrogen with CO_2 to convert it into liquid methanol (Ravikumar et al., 2020); (Wiesberg et al., 2019), which offers advantages such as a higher liquefaction temperature, enhanced safety, and the ability to reduce CO_2 concentrations in the atmosphere (Adamson & Pearson, 2000); (Ott et al., 2000). This makes methanol a safer and more cost-effective energy carrier, eliminating the need for expensive hydrogen liquefaction processes (Adamson & Pearson, 2000); (Sollai et al., 2023).

The hydrogen produced in many processes is not pure, limiting its diverse applications (Cheng et al., 2007); (Dawood et al., 2020). Several hydrogen purification methods have been developed to address this, with the cryogenic method being recognized as one of the most effective options for large-scale recovery (Z. Du et al., 2021).

In a recent study, which is the reference paper for the presented research (Alireza Khatami Jouybari et al., 2022a), a novel method was devised to simultaneously achieve multiple objectives: producing methanol at a rate of 4.74 tons per hour, generating 297.7 kW of electricity, and yielding 35.73 tons of hot water per hour. This comprehensive process involved components like a hydrogen purification system, an organic Rankine cycle (ORC), an absorption-compression refrigeration cycle (ACRC), and the integration of parabolic solar troughs.

The primary focus of the previous study was addressing safety concerns linked to hydrogen storage and transport by converting it to methanol for efficient long-distance energy transportation. The heat generated by the methanol reactor was effectively recovered using ORC and ACRC processes, with added thermal power from parabolic solar troughs in the methanol distillation tower. The integrated structure's thermal efficiency was 78.14%, while the liquid methanol production cycle exhibited 60.91% efficiency.

The thorough evaluation included energy, exergy, and sensitivity analyses. Notably, the mixture temperature of H_2 and LP fuel gas before separation emerged as a critical parameter affecting hydrogen purity in the methanol reactor, resulting from the sensitivity analysis in the reference paper.

The cryogenic process, with the highest recovery rate for hydrogen, offered lower purity than other methods. Efforts in the field have been geared toward minimizing the cryogenic method's energy consumption due to its high energy use and purification cost (Muin et al., 2020).

Research has been performed focusing on optimizing the required heat, power generation and consumption, economic costs, efficiencies, and environmental friendliness of industrial processes as one of the promising methods used in economic assessments of thermally-integrated processes (Ghorbani, et al., 2020); (Golchoobian et al., 2021); (Khatami Jouybari et al., 2022b). Multi-objective optimization using the combination of neural networks and genetic algorithms of Non-dominated Sorting Genetic Algorithm-II (NSGA-II) has been widely used in related studies, with decision-making methods (e.g., fuzzy, LINMAP, and TOPSIS) to find final optimal data from the analysis.

In recent research, a novel approach was introduced to produce portable and environmentally friendly liquid methanol from coke oven gas and exhaust gas emanating from power plants (Alireza Khatami Jouybari et al., 2022b). The method encompasses several components, including a CO_2 capture unit aimed at separating carbon dioxide from the exhaust gases, a process for purifying and liquefying natural gas to generate liquefied natural gas (LNG), and a cycle for methanol production. Utilizing the Annualized Cost of the Structure (ACS) methodology for economic assessment yielded noteworthy results for the payback period and a prime cost for the manufactured methanol. Integrating the non-dominated sorting genetic algorithm into the thermo-economic optimization of the hybrid system, accompanied by decision-making facilitated by the TOPSIS and LINMAP methods, led to the determination of optimal parameters.

Ghorbani et al. introduced an optimal thermally integrated process designed for hydrogen storage, aiming for net-zero CO_2 emissions (Ghorbani, Zendehboudi, & Afrouzi, 2023). Utilizing fuel cells to mitigate carbon dioxide emissions and simultaneously fulfill heat and power requisites for hydrogen production and liquefaction under elevated temperatures is a central facet of this approach. The enhancement of investment return periods and efficiencies was achieved through the synergistic amalgamation of genetic algorithms and artificial intelligence methodologies, ensuring optimal outcomes. Within multi-objective optimization, a trio of decision-making methodologies were harnessed to guide the process effectively.

In a previous research, an industrial methanol plant was modeled in Aspen Plus and optimized in Matlab to enhance carbon capture endeavors (Bonfim-Rocha et al., 2018). Considering design parameters and capital costs, aided by sensitivity analysis, led to generating response surfaces by varying bagasse for energy cogeneration. The objective was to boost the net present value while curbing CO_2 emissions across scenarios. Mathematically, chemical process synthesis becomes a multi-objective optimization task involving mixed integer nonlinear programming (moMINLP), encompassing economic and environmental factors. This study employed the ε-constraint method, translating one objective into an extra constraint and solving iteratively across epsilon values. The intricate optimization was successfully tackled with the enhanced scatter search (eSS) technique.

Taghdisian et al. introduced an eco-design approach for fostering the sustainable advancement of methanol production, executed by applying a multi-objective optimization model centered around CO_2 efficiency (Taghdisian et al., 2015). Upon conducting an inventory analysis via life cycle assessment, it became evident that carbon dioxide emerged as the primary emission from methanol production. Hence, the multi-objective model was structured to concurrently maximize methanol production and minimize CO_2 emissions, ultimately yielding a set of Pareto-optimal solutions. The multi-objective model was transformed into a singular objective optimization problem using the weighted product method to streamline the process into a single optimal solution. The ensuing task of identifying the optimal single point was successfully accomplished by employing a genetic algorithm.

Another study aimed to enhance bio-methanol production from sugar cane bagasse through pyrolysis, primarily focusing on maximizing output (Yousef et al., 2020). Employing experimental data, a robust model describing bio-methanol yield was developed using the fuzzy logic technique. Subsequently, the Particle Swarm Optimization (PSO) algorithm was applied to pinpoint optimal operating parameter values for maximizing bio-methanol output. The parameters under control encompassed reaction temperature, reaction time, and nitrogen

flow. The outcomes revealed a strong alignment between the fuzzy model and experimental data, surpassing predictions from an artificial neural network (ANN) model employed earlier. Building upon this model, the particle swarm optimizer achieved a notable enhancement of 20% in bio-methanol yield compared to the experimental baseline.

Dehghani et al. undertook an extensive investigation encompassing steady-state simulations of a Radial Flow Gas-Cooled Reactor and a Radial Flow Gas-Cooled Membrane Reactor (Dehghani et al., 2021). The central aim of their study was to enhance the process of CO_2 removal during methanol synthesis. By employing the NSGA-II, the research adopted a two-pronged optimization approach. The primary objectives were twofold: maximizing the methanol production rate while ensuring optimal selectivity. In order to identify the ultimate Pareto-optimal solution, the research employed decision-making techniques such as TOPSIS, LINMAP, and Shannon's Entropy. Of particular note, Shannon's Entropy emerged as the frontrunner with the lowest deviation index, resulting in impressive enhancements of 78.3% for CO_2 removal and 10.77% for methanol production rates.

In a particular investigation, a novel electro-thermochemical process leveraging industrial flue gas thermal energy and wind turbines was conceptualized for the dual purposes of CO_2 absorption and hydrogen storage via methanol, formic acid, and ammonium bicarbonate (Ghorbani, Zendehboudi, Monajati Saharkhiz, et al., 2023). The validity, verification, and exploration of sensitivities were supplemented by the integration of a multi-objective optimization methodology combining a hybrid neural network and a genetic algorithm, thereby facilitating an all-encompassing evaluation of the proposed system. The requisite objective functions, decision variables, and constraints for the optimization phase were elucidated through meticulous sensitivity analysis. Multiple multi-criteria decision assessment techniques were employed to prioritize and select the optimal point from the available Pareto set. Subsequently, energy and exergy efficiencies were computed using the TOPSIS/LINMAP methods, while power consumption, energy, and exergy efficiencies under optimal operating conditions were determined using the Bellman–Zadeh approach.

Ghahraloud et al. (Ghahraloud & Farsi, 2017) undertook an investigation centered around the modeling and optimization of the methanol oxidation process utilizing an iron-molybdenum oxide catalyst within a fixed bed reactor. With a focus on achieving both formaldehyde production capacity and selectivity, the study approached it as a multi-objective optimization challenge. The problem formulation involved considering feed and coolant temperatures, along with the air-to-methanol ratio, as pivotal decision variables. The non-dominated multi-objective genetic algorithm facilitated the derivation of a Pareto optimal front by integrating a developed mathematical process model and a multi-objective optimization model. Subsequently, the TOPSIS decision-making method was employed to select the singular optimal point from the comprehensive optimal Pareto front.

The primary objective of this study is to assess economically and optimize the initial design delineated in the reference paper (Alireza Khatami Jouybari et al., 2022a). While the reference paper primarily concentrated on the innovative design, energy, exergy, and sensitivity analyses, the present study seeks to appraise the economic viability of the design through economic analysis. Additionally, the study aims to optimize the integrated structure both thermodynamically and economically utilizing a multi-objective optimization method. This involves a comprehensive analysis of the key parameters that exert the most significant influence on the performance of the original design. It is aimed to focus on efficiency optimization and optimize return period of investment using data resulted from sensitivity analysis and within the context of economic implications.

In addressing the imperative of sustainable development, this study strives to significantly contribute to environmental stewardship by optimizing the economic viability and thermodynamic efficiencies of the integrated process for liquid methanol production aligning with the broader goals of sustainability in the energy storage.

4.2 A brief description of the process under study

In the referenced article, an integrated structure was developed to generate methanol, heating and power. The system included various sub cycles of organic Rankine cycle, solar troughs, liquid methanol generation system, cryogenic cycle to purify H_2, and an absorption-compression refrigeration cycle. The Block Flow Diagram (BFD) corresponding to the overall process is shown in Figure 4.1 (Alireza Khatami Jouybari et al., 2022a).

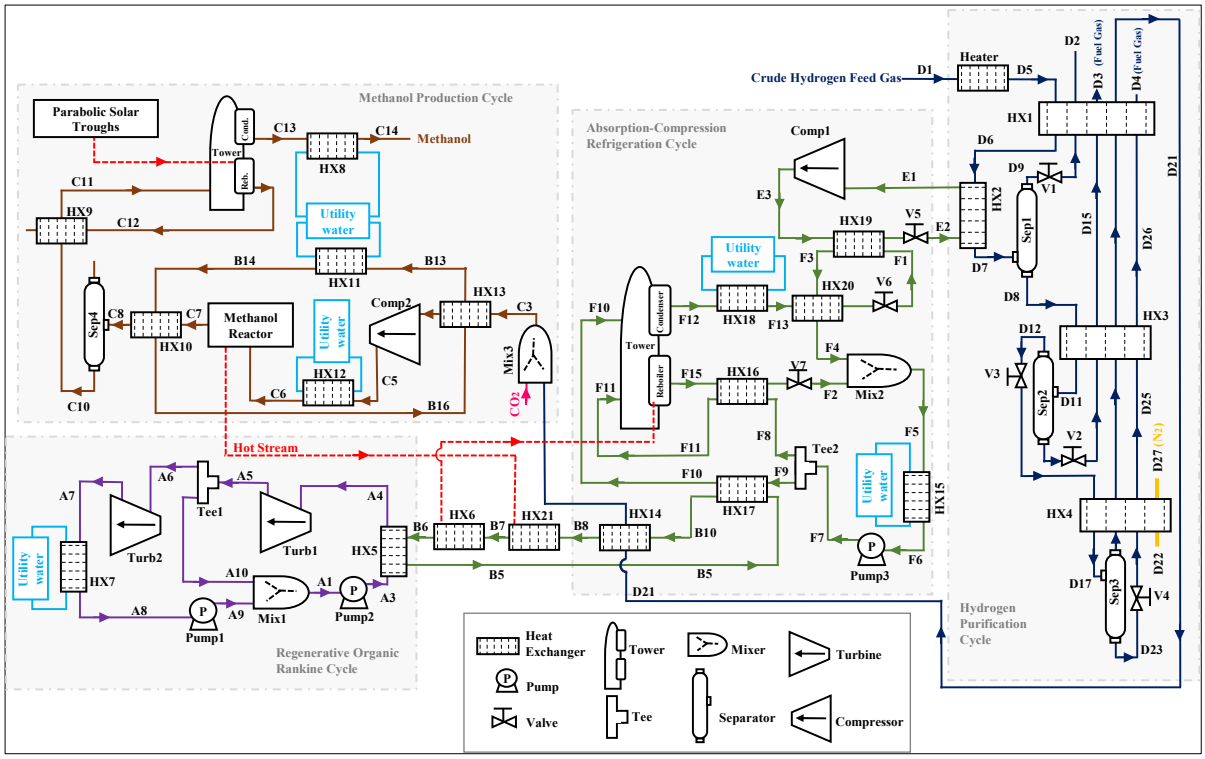

Figure 4.1. Block flow diagram of the process under study
(Alireza Khatami Jouybari et al., 2022a)

The process started with a crude hydrogen stream with 55% molar purity for hydrogen and 39% for methane. The absorption compression refrigeration cycle (ACRC) provided precooling in the purification cycle. In a flash drum, stream D17 separated into stream D23 with methane in a liquid phase (95.08% mol) and stream D18 of H_2 (88.5% mol).

The ACRC played a critical role in precooling the cryogenic hydrogen purification cycle. It consisted of various elements, including a generator to separate ammonia and water, a purifier to remove remaining water droplets from ammonia, a condenser for ammonia liquefaction, an evaporator for cycle cooling by CO_2 evaporation, and an absorbent for water absorption in ammonia. A CO_2 ACRC cycle also provided cooling for the process at -42 °C. In the methanol generation cycle, after mixing hydrogen with CO_2, their temperature and pressure are raised to 200 °C and 50 bar, respectively. Subsequently, the C6 stream entered the plug-flow methanol reactor. The methanol production process was exothermic, and its waste heat was recovered in two other cycles, including the ACRC cycle for thermal power generation and the ORC cycle to produce electricity. For harnessing solar energy, parabolic troughs were designed as thermal collectors, collecting 3,435 kW of thermal power from the sun to support the methanol reactor temperature, operating within the required temperature range of 200^0C. By incorporating cogeneration systems in this integrated structure, efficiency was improved, and equipment requirements were reduced compared to individual subsystems working independently. The consolidated system received a flow of 6,6 tons/h of carbon dioxide and 10 tons/h of crude hydrogen, 3,4 kW of thermal energy from parabolic troughs, and 19.6 kW of cooling via liquid nitrogen. The system yielded 4.7 tons/h of liquid methanol, 297.7 kW of net electricity, and 35.7 tons/h of heated water. Byproducts encompassed low-pressure and high-pressure fuel gases along with aromatic compounds. The ORC harnessed excess heat from the methanol reactor, resulting in 475 kW of power generation, while the ACRC cycle furnished 25 kW of cooling for hydrogen purification. The outcomes demonstrated a 98 percent efficiency in extracting hydrogen from the initial crude feed during the purification phase.

4.3 Economic analysis methodology

The economic evaluation of the process relies on the Annualized Cost of the Structure (ACS) approach. The essential factors for determining the optimal setup include the investment's returns period, the net annual benefit, and the electricity's prime cost. The ACS method involves calculating the total design costs depending on the technical lifespan of the entire

system. To find the values used in ACS of the designed process, the following equation is utilized (Ebrahimi et al., 2015):

$$\begin{aligned} ACS = {} & C_{acap}\,(Components) + C_{arep}\,(Components) \\ & + C_{amain}\,(Components) + C_{aope}(Fuel\ price \\ & + Insurance\ price + Other\ price) \end{aligned} \tag{4.1}$$

$\mathbb{C}_{amain}$ represents the cost of annualized maintenance and $\mathbb{C}_{arep}$ the cost for annualized replacement. $\mathbb{C}_{aope}$ and $\mathbb{C}_{acap}$ are annualized operating and capital prices of the process. The project's useful life is considered twenty years, and the replacement price for the components is omitted. For calculating the price of components, the chemical engineering plant cost index (CEPCI) can be implemented as (Shirmohammadi et al., 2021, 2022):

$$C_{reference\ year} = C_{original\ year}\frac{CI_{reference}}{CI_{original}} \tag{4.2}$$

Here CI and C are considered as cost index and component's cost. The following equation can achieve the annualized capital cost for components considered in the plant's lifespan (Yang et al., 2009):

$$C_{acap} = C_{Cap}\ CRF\big(i.y_p\big) = C_{Cap}\ \frac{i(1+i)^{y_p}}{(1+i)^{y_p}-1} \tag{4.3}$$

The real interest rate and the project's useful life are represented as i and y_p, respectively. The nominal interest rate can be calculated by the following relation (Ngan & Tan, 2012); (Reyhani et al., 2016):

$$i = \frac{j-f}{1+f} \tag{4.4}$$

Where, j representing the nominal interest rate, and f symbolizing the annual inflation rate, serve as pivotal factors in financial assessments. The calculation of the net present value in the prime year (NPV) follows a specific method (Reyhani et al., 2016):

$$NPV = \frac{ACS}{CRF(i\ .y_p)} = ACS\frac{(1+i)^{y_p}-1}{i(1+i)^{y_p}} \tag{4.5}$$

To calculate the product's prime cost (PC), the assessment of the operating flow costs (OFC), volume of product (VOP), and initial investment costs (CC) is needed using the equation provided below (Rahimi et al., 2014):

$$PC = \frac{OFC}{VOP} \tag{4.6}$$

The determination of the Summary of Product Cost (SOPC) in the market and the computation of the Net Annual Benefit (NAB) follow specific methodologies tailored to the intricate financial dynamics of each metric. By applying these calculated values, businesses gain insights into cost structures and annual financial gains, facilitating informed strategic planning. (Rahimi et al., 2014):

$$SOPC = VOP \times C_{\text{product in the market}} \tag{4.7}$$

$$NAB = (SOPC - OFC) \times (1 - VATR\ \%) \tag{4.8}$$

Within the net annual benefit framework, two significant elements, the value-added tax rate (VATR) and incomes generated from byproducts sales stemming from the referenced process, are incorporated. The economic landscape further unfolds through essential parameters like the rate of return (ROR), the investment period of return (POR), and additive value (AV), each of which finds attainable definition through specific methodologies. Engaging with these variables generates a comprehensive financial understanding, guiding decision-makers toward effective strategies and informed choices. (Rahimi et al., 2014):

$$ROR = \frac{NAB}{CC} \tag{4.9}$$

$$POR = \frac{CC}{NAB} \tag{4.10}$$

$$AV = C_{\text{product in the market}} - PC \tag{4.11}$$

The additive value represents the disparity between the product's cost and its prime price in the market. This figure has the potential to fluctuate based on the application of a range of up-to-date technologies during the manufacturing procedure.

4.4 Results of economic evaluation

An organized methodology is developed through mathematical and thermodynamic analyses aimed at optimizing the efficiency of the liquid methanol storage system. This involves the seamless integration of Aspen HYSYS V10 software, complemented by a MATLAB m-file code. The primary purpose of this integrated approach is to comprehensively evaluate the economic aspects pertaining to the studied process. The study examines the impact of methanol and crude hydrogen prices, as well as electricity and fuel gas costs, on key economic parameters. Through economic analysis, the objective is to evaluate the viability of the design, ensuring a satisfactory return on investment timeframe. Additionally, a sensitivity analysis on the economic facets of the design aims to ascertain that variations in market prices of feedstocks, utilities, and products maintain the profit margin within an acceptable range.

The successful integration of thermal processes among various subsystems leads to the elimination of external utility requirements, subsequently resulting in a notable enhancement of the system's overall efficiency. At the core of the economic assessment of this hybrid system lie critical determinants, including but not limited to the duration necessary for the return on investments, the primary cost associated with electricity, the net annual profits generated, and the initial expenditures required for investment. Within the domain of economic scrutiny, the analysis considers the economic backdrop, entailing factors such as an

annual inflation rate set at one percent, a nominal interest rate of 1.5 percent, and a foreseeable operational lifetime spanning twenty years. For a comprehensive understanding of calculating the equipment's costs utilized within the newly devised framework, valuable and in-depth insights can be sourced from dependable references (Couper et al., 2005); (Ghorbani et al., 2022); (Rustagi, 2019); (Sadeghi et al., 2020). The economic facets of the system are assessed through a meticulous consideration of the scale of the methanol production reactor. After this initial evaluation, an in-depth sensitivity analysis is executed to uncover the intricate ways various parameters exert influence over the system's size and its associated economic variables. Determining prices for essential elements such as methanol, hydrogen, electrical power, and components is a complex task, heavily swayed by factors ranging from geographic location to specific applications.

Consequently, the prevailing prices within analogous configurations are embraced as the foundation for reference to establish a solid baseline for economic scrutiny. Embedded within the ambit of this research is a comprehensive investigation into the repercussions of methanol and crude hydrogen price fluctuations, in conjunction with the fluctuations in electricity and fuel gas costs, meticulously undertaken to ascertain their impact on pivotal economic indicators. The comprehensive results of this intricate economic analysis are presented in Table 4.1, affording a lucid exposition of the outcomes yielded by the evaluation process. Based on the average market price of 0.4 USD/kg methanol (Chiou et al., 2023), the derived outcomes from the analysis provide notable insights: the calculated return period stands at 6.63 years, while the prime price of the product is determined to be 0.15 USD/kg, and a substantial annual net benefit of 9.34 MMUSD is observed. The levelized cost of methanol production for the different natural gas based methanol production processes ranges between 0.252 to 0.280 Euro/kg methanol (Arnaiz del Pozo et al., 2022), and a cost parity between renewable and conventional methanol production methods is anticipated in 2032 (Schorn et al., 2021). The levelized cost of the product resulting from the present study shows a competitive value compared to the conventional methods.

Table 4.1.The evaluation outcomes of the economic analysis

Factors	rate
Levelized cost of product (USD/kg methanol)	0.246
Annual benefit (MMUSD/years)	10.380
Net annual benefit (MMUSD/years)	9.341
Prime cost (USD/kg methanol)	0.150
Return period (Years)	6.637
Additive value (USD/kg methanol)	0.250
Rate of return (%)	15.066

4.4.1 Sensitivity Analysis

The sensitivity analysis encompasses an in-depth exploration and identification of operational parameters that hold significant sway over the economic efficiency of the evolving system. This analysis also encompasses a comprehensive study of how the designated objective function responds to alterations made to the chosen decision variables. A detailed examination is conducted to ascertain the impact of costs associated with liquid nitrogen, fuel gas, electricity, and methanol on many economic parameters embedded within the system. By extrapolating valuable insights from the results of this rigorous sensitivity assessment, it becomes possible to devise pragmatic strategies to enhance the process of designing and optimizing crucial parameters. This iterative approach enables a refined understanding of the intricate interplay between various elements, paving the way for improved decision-making and a more robust system configuration.

As illustrated in Figure 4.2. a,b, the produced methanol price in the market has a significant impact on the return period where an increase in the main product price (liquid methanol) from 0.35 to 0.8 USD/Kg the period of return exponentially decreases from 8.30 to 2.55 years. This change in the methanol market price has a direct and almost linear relationship with both additive value and annual net benefit. Quadrupling the price of methanol from 0.2

to 0.8 USD/Kg values related to added value and annual benefit will grow almost twelve times.

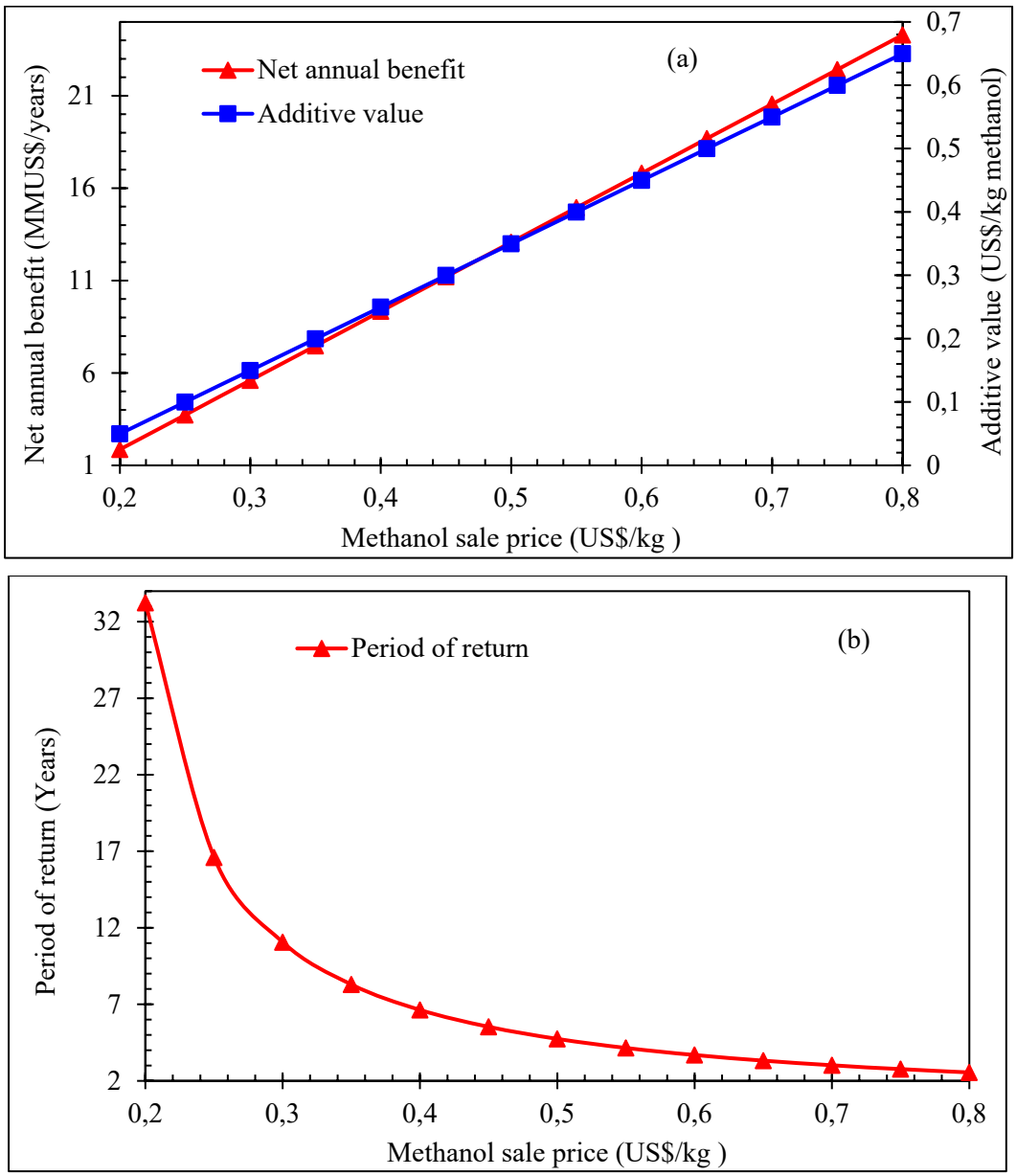

Figure 4.2. (a, b) The effect of changes in the methanol price on the key parameters of economic evaluation

Crude gas containing hydrogen is considered the process's main feed. Based on the sensitivity analysis result in Figure 4.3. a,b, a rise in the feed gas price from 0.8 to 3

USD/MMBTU grows the prime and levelized costs from 0.13 to 0.36 and 0.22 to 0.46 USD/kg methanol. However, it lowers the net annual benefits and additive value from 10.15 and 0.271 to 1.273 and 0.034, respectively. When the crude feed gas cost is more than 1.8 USD/MMBTU, the period of return in an exponential trend passes 10 years, questioning the whole project's cost-effectiveness.

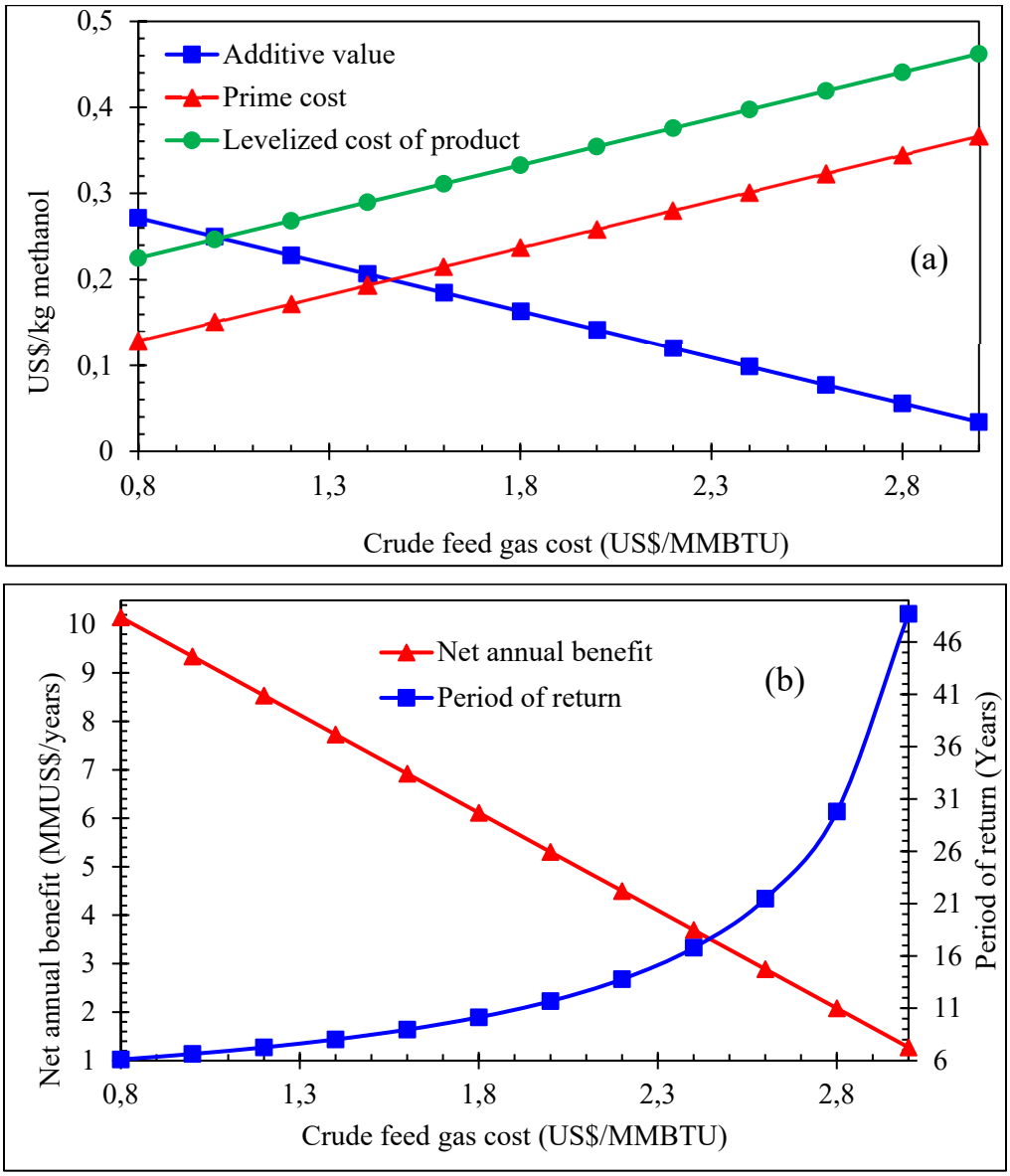

Figure 4.3. (a, b) The effect of changes in the crude feed gas cost on the key parameters of economic evaluation

As depicted in Figure 4.4. a,b, the price of fuel gas, as the side product of the process, affects the critical parameters of economic analysis in the same trends as the price of methanol. The fuel gas cost growth from 1.6 to 3 USD/MMBTU additive value and annual net benefits rise from 7.653 to 10.546 MMUSD/years and from 0.191 to 0.282 USD/kg methanol, respectively. Nevertheless, this increase in the fuel gas price lowers the prime and levelized product cost from 0.208 to 0.117 and 0.304 to 0.214 USD/kg methanol and the return period from 8.645 to 5.878 years. As shown, the changes in the methanol price have more significant effects on the main parameters of economic analysis compared to that of fuel gas prices.

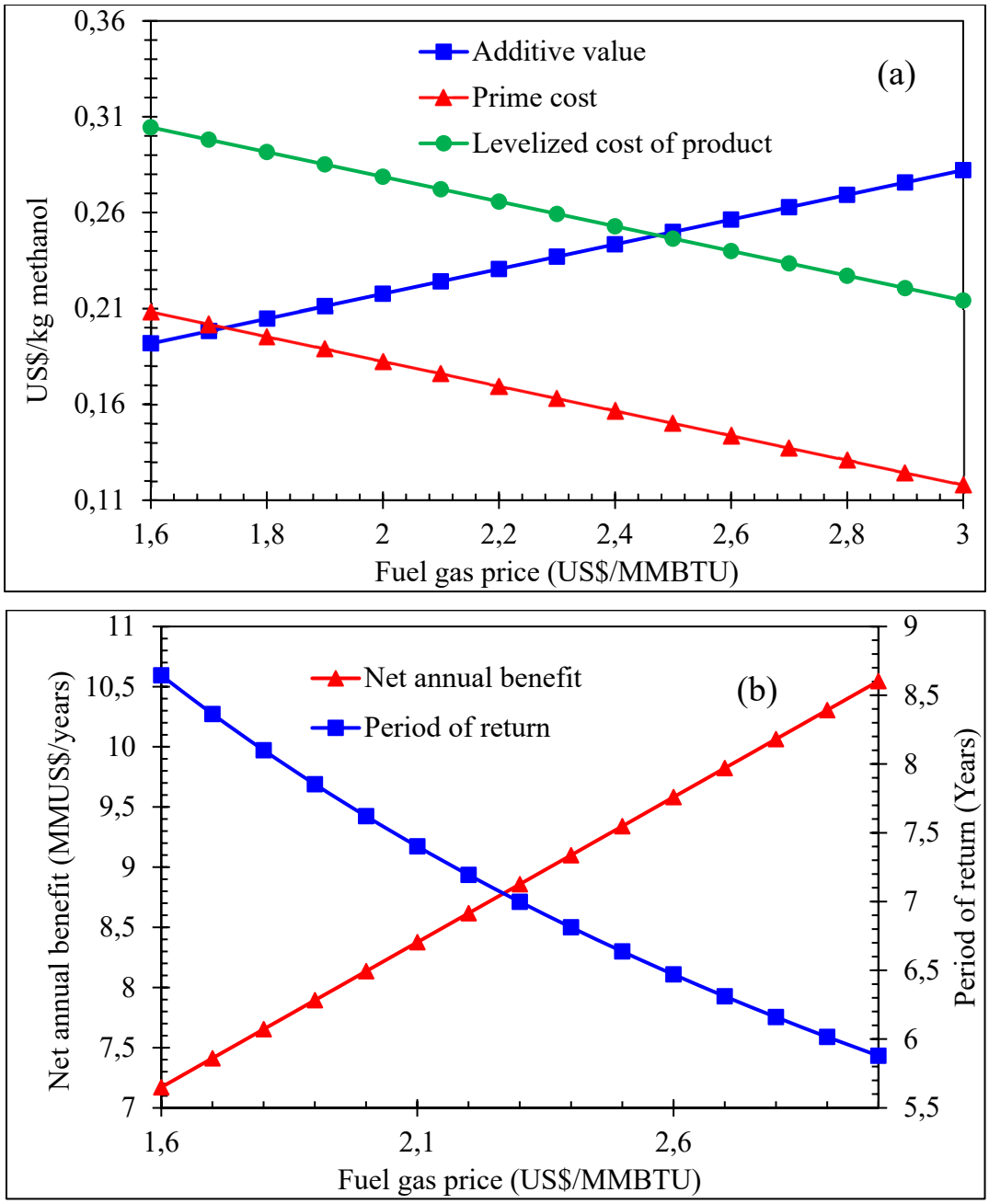

Figure 4.4. (a, b) The effect of fluctuation in the value of fuel gas price on the key parameters

As the thermally integrated process is almost self-sufficient, the changes in electricity price have a minor effect on costs, benefits, and return period. Based on the results illustrated in Figure 4.5. a,b, even by a noticeable change in the electricity price, from 0.05 to 0.4 USD/kWh, the period of return, additive value, net annual benefits, and levelized cost of the

product may experience marginal changes by less than 9 percent. In comparison, the product's prime cost will decrease by 14 percent from 0.156 to 0.134 USD/kg methanol.

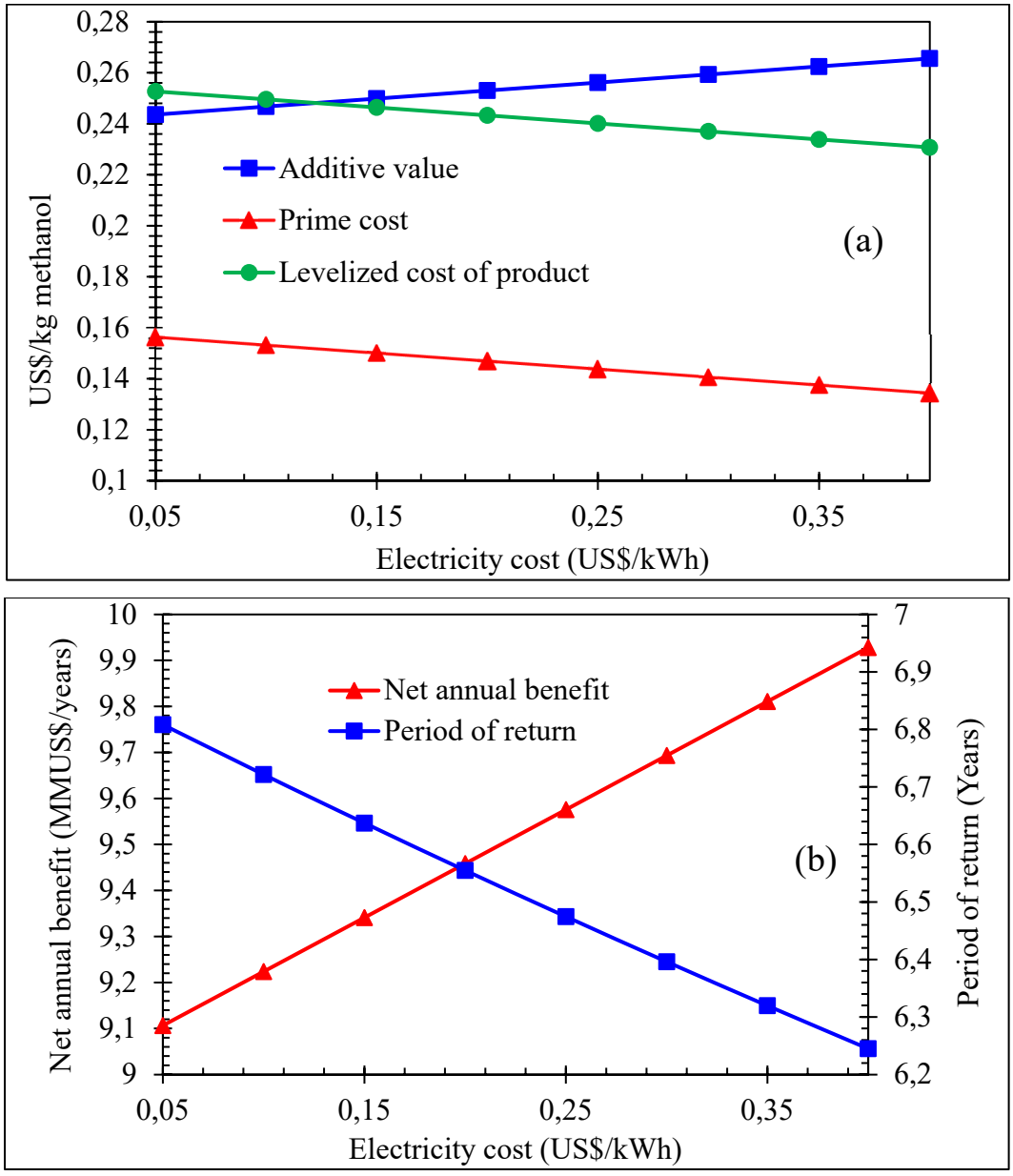

Figure 4.5. (a, b) The effect of changes in the electricity cost on the key parameters of economic evaluation

Liquid nitrogen is used in the hydrogen purification cycle (lines D22 and D27 in the heat exchanger HX4). The rise in the cost of liquid hydrogen from 0.1 to 0.5 USD/litre almost

doubles the return period from 6.286 to 11.99 years (see Figure 4.6. a,b). It also increases the prime and the product levelized cost by 0.125 USD/kg methanol from 0.136 and 0.232 USD/kg methanol, respectively.

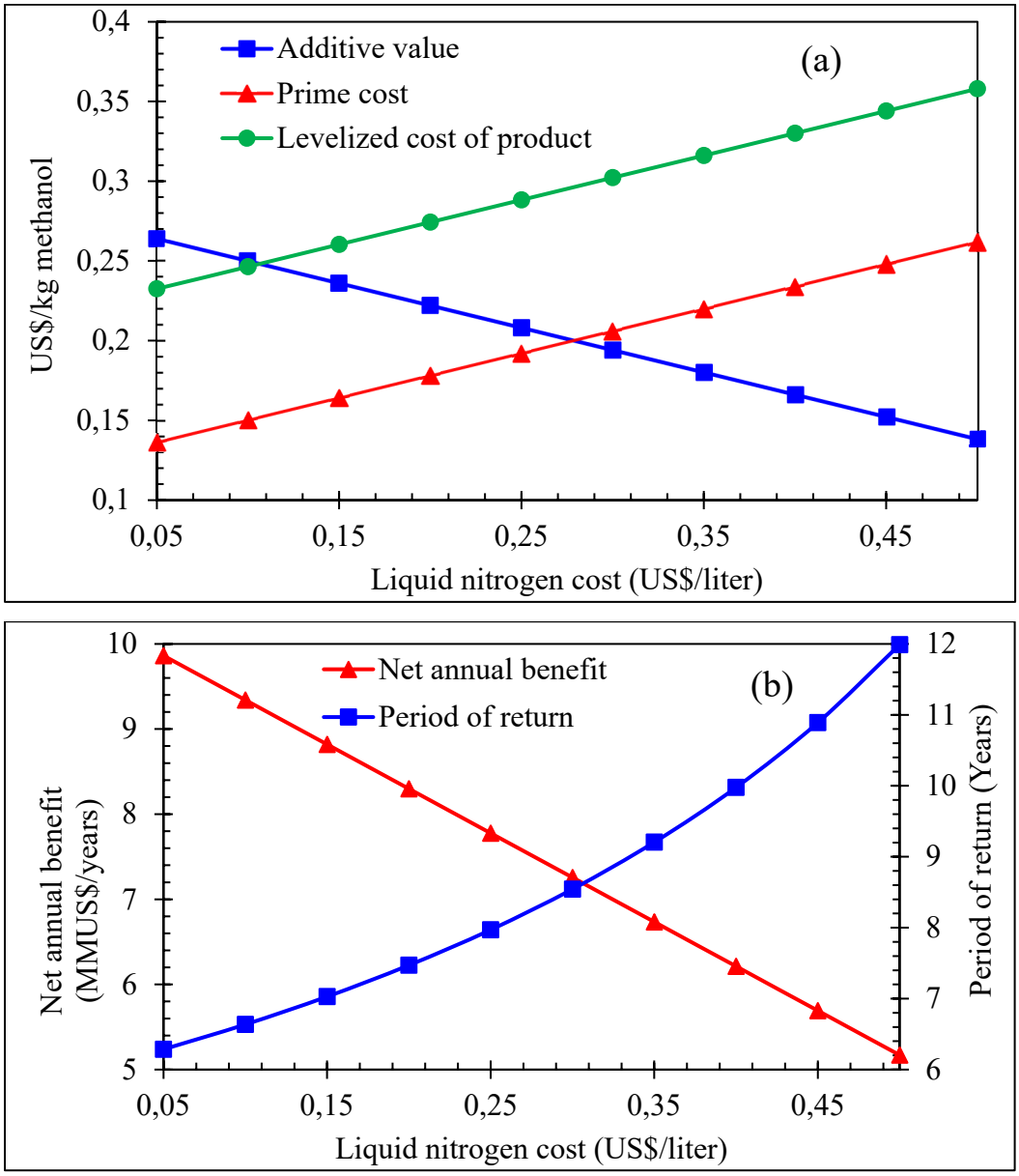

Figure 4.6. (a, b) The effect of changes in the liquid nitrogen cost on the key parameters of economic evaluation

4.5 Optimization methodology

Extracted from Hysys, the seamless communication between objective functions and decision variables is ingeniously achieved through integrating a hybrid approach. This innovative method harmonizes the capabilities of the Group Method of Data Handling (GMDH)-type polynomial neural network with the genetic algorithm's (GA) effectiveness. Within this algorithmic framework, multiple neurons in each layer establish intricate connections utilizing a polynomial equation in second order, effectively giving rise to the inception of fresh neurons in subsequent layers. The focal point of this hybridization is the training process of the GMDH network. The primary goal of this network training is the anticipation of the output $\hat{y}_i$ values nestled within intricate input vectors denoted as $X = (x_{i1}\ x_{i2}\ x_{i3}\ \dots x_{in})$. The progression of this training can be articulated in comprehensive detail as follows (Kalantary et al., 2009):

$$\hat{y}_i = \hat{f}(x_{i1}\ , x_{i2}\ , x_{i3}, \dots, x_{in})\ (i = 1, 2, \dots, M) \tag{4.12}$$

The objective is to reduce the squared disparities between the observed results and their associated anticipated values. This entails aiming for a closer alignment between actual outcomes and the values predicted for them (Ardalan et al., 2009):

$$\sum_{i=1}^{M}\left[\hat{f}(x_{i1}\ , x_{i2}\ , x_{i3}, \dots, x_{in}) - y_i\right]^2 \rightarrow min \tag{4.13}$$

One can employ an equation derived from the Volterra series to depict the interconnectedness between the inlet and outlet points. This expression encapsulates the relationship between these points, offering insights into their shared dynamics. (Ardalan et al., 2009):

$$y = a_0 + \sum_{1}^{n} a_i x_i + \sum_{1}^{n}\sum_{1}^{n} a_{ij} x_i x_j + \sum_{1}^{n}\sum_{1}^{n}\sum_{1}^{n} a_{ijk} x_i x_j x_k + \cdots \tag{4.14}$$

The equation mentioned above can be characterized as a bivariate polynomial comprising solely of two variables (neurons), as demonstrated below (Ardalan et al., 2009):

$$\hat{y} = G(x_i\ x_j) = a_0 + a_1 x_i + a_2 x_j + a_3 x_i x_j + a_4 x_i^2 + a_5 x_j^2 \tag{4.15}$$

The determination of the coefficients a_i involves employing regression techniques. It entails minimizing the discrepancy between the calculated value $(\hat{y})$ and the real value (y) for each set of input variables X_i and X_j. Furthermore, the coefficients of each second-order equation G_i are derived to achieve the optimal outlet alignment within the comprehensive input-output data pairs (Khayyam et al., 2020). The error function *(E)* is calculated as depicted below:

$$E = \frac{\sum_{i=1}^{M}(y_i - G_i)^2}{M} \rightarrow min \tag{4.16}$$

The input vectors encompass the hydrogen content within the feed gas, the temperature of stream D17, and the incoming carbon dioxide flow rate. As for the output vectors, they include the return period, exergy efficiency, and thermodynamic efficiency. The process employs multi-objective optimization with the dual objectives of minimizing the return period while simultaneously maximizing the thermodynamic and exergy efficiencies. The NSGAII genetic algorithm method is utilized to carry out this optimization. For each set of optimal operational parameters, the Pareto frontier is derived, and from among the points along this frontier, the ultimate optimal point is selected through techniques such as LINMAP, fuzzy Bellman-Zadeh and TOPSIS. The optimization model is presented in the following format (Alireza Khatami Jouybari et al., 2022b):

$$\frac{Min}{Max}: \mathcal{F}_t(X), \qquad t = 1, 2, 3, \dots, \mathcal{T} \tag{4.17}$$

$$h_k(X) = 0, \qquad k = 1, 2, 3, \dots, \mathcal{K} \tag{4.18}$$

$$g_j(X) \geq 0, \qquad j = 1, 2, \dots, \qquad \mathcal{J} \tag{4.19}$$

$$X_i(\mathcal{L}) \leq X_i \leq X_i(\mathcal{U}), \qquad i = 1\ 2\ \ldots\ \aleph \tag{4.20}$$

Here, $\mathcal{F}$ represents the objective function, $\mathrm{X} = [\mathrm{X}_1\ \mathrm{X}_2\ \ldots\ \mathrm{X}_\aleph]^{\mathrm{T}}$ $(\aleph \in \mathbb{R}_\aleph)$ denotes the n-dimensional variable vectors, and g and h signify the constraints inherent to the model that must be satisfied. Due to differing dimensions of objective functions, it becomes necessary to apply scaling and normalization to the target space before constructing a decision. Various normalization techniques are employed within the decision-making procedure, encompassing methods like non-dimensionalized fuzzy and Euclidean approaches. The non-dimensionalized objective utilizing the Euclidean method is delineated as (Mohammad H. Ahmadi, Sayyaadi, et al., 2013):

$$\mathcal{F}_{ij}^{\aleph} = \frac{\mathcal{F}_{ij}}{\sqrt{\sum_{i=1}^{\mathcal{M}} \left(\mathcal{F}_{ij}\right)^2}} \tag{4.21}$$

$\mathcal{F}_{ij}^{\aleph}$ represents a matrix for objectives corresponding to different points along the Pareto frontier, where *i* designates the routes index along the Pareto boundary, and *j* signifies the indicator for objectives across the objective space. The application of non-dimensionalization involves utilizing the Euclidean method in the TOPSIS/LINMAP approaches, and the Bellman–Zadeh approach relies on the fuzzy method. The non-dimensionalized objective using the fuzzy method is characterized as (Jokar et al., 2017):

- For objectives maximization

$$\mathcal{F}_{ij}^{\aleph} = \frac{\mathcal{F}_{ij} - \min\left(\mathcal{F}_{ij}\right)}{\max\left(\mathcal{F}_{ij}\right) - \min\left(\mathcal{F}_{ij}\right)} \tag{4.22}$$

- For objectives minimization

$$\mathcal{F}_{ij}^{\aleph} = \frac{\max(\mathcal{F}_{ij}) - \mathcal{F}_{ij}}{\max(\mathcal{F}_{ij}) - \min(\mathcal{F}_{ij})} \tag{4.23}$$

4.5.1 TOPSIS and LINMAP approaches

The point of optimality situated along the Pareto boundary signifies a circumstance in which each individual objective achieves its maximum value in isolation from the influences of the other objectives. In contrast, the non-ideal point denotes specific coordinates within the targeted space wherein each objective assumes its least advantageous condition. The TOPSIS technique involves computing the distances between the parameters residing along the Pareto frontier and both the most optimal and least favorable points. This computation is executed through the utilization of a specific formula, which encapsulates the essence of the calculation process in this method. By employing this formula, the TOPSIS technique establishes a structured approach to evaluating and quantifying the discrepancies between different parameter sets and their corresponding optimal and suboptimal benchmarks. (Toghyani et al., 2014):

$$\ell_{\aleph-} = \sqrt{\sum_{j=1}^{\aleph} \left(\mathcal{F}_{ij} - \mathcal{F}_{j}^{Non-ideal}\right)^2} \tag{4.24}$$

$\aleph$ denotes the objective index within the Pareto frontier, while i represents the solutions along the Pareto frontier *(i = 1, 2, ..., $\mathcal{M}$)*. Within the framework of the LINMAP methodology for making decisions, the notion of optimality takes on a distinct characterization: it pertains to the configuration that maintains the minimal distance conceivable from the ideal state. This method emphasizes the significance of minimizing the disparity between the achieved and theoretically perfect states, underscoring the importance of aligning outcomes as closely as possible with the optimal objective conditions (Mohammad H. Ahmadi, Mohammadi, et al., 2013).

$$\ell_{\aleph+} = \sqrt{\sum_{j=1}^{\aleph} \left(\mathcal{F}_{ij} - \mathcal{F}_j^{Ideal}\right)^2} \tag{4.25}$$

In the previously mentioned equations, $\ell_{\aleph-}$ and $\ell_{\aleph+}$ represent the parameters distances within the Pareto boundary from the least favorable and most optimal scenarios. Subsequently, the criterion of decision is derived from $\mathcal{H}_\ell$. The point characterized by the maximum $\mathcal{H}_\ell$ parameter is regarded as the optimal point according to the TOPSIS decision-making methodology. Within the equations mentioned earlier, the variables $\ell_{\aleph-}$ and $\ell_{\aleph+}$ assume roles that signify the extent of parameter deviations along the Pareto boundary concerning the least favorable and most optimal instances. Consequently, the decision criterion is extracted from the value of the parameter $\mathcal{H}_\ell$. Notably, within the context of this methodology, the point distinguished by the highest $\mathcal{H}_\ell$ parameter value is identified as the optimal point, serving as the pinnacle of decision-making in accordance with the TOPSIS approach. This strategic selection is driven by maximizing the calculated parameter, aligning to attain the most desirable outcome within the decision-making process (Toghyani et al., 2014).

$$\mathcal{H}_\ell = \frac{\ell_{\aleph-}}{\ell_{\aleph+} + \ell_{\aleph-}} \tag{4.26}$$

4.5.2 Bellman–Zadeh approach

Incorporating the Bellman and Zadeh methodology results in converting each individual objective into either a fuzzy objective function or a separate fuzzy group, representing a pivotal aspect of this approach. Central to this methodology is the introducing of membership matrix functions, a fundamental component of the process. In this framework, the columns of the matrix are dedicated to encapsulating the membership functions corresponding to the objectives, which are articulated in a fuzzy manner to account for uncertainty and imprecision. This matrix structure serves as a structural foundation for the transformation and manipulation of objective-related information within the context of the fuzzy framework

introduced by Bellman and Zadeh. (Mohammad H Ahmadi et al., 2015). The rows within the membership matrix are in direct correspondence with the values attributed to the membership function that specifically relate to the trajectory obtained through the process of deriving from the Pareto boundary. To provide further clarification, the exact count of objectives perfectly aligns with the number of columns currently present within the matrix representing the membership function. In a similar manner, the total quantity of solutions that are strategically positioned along the Pareto boundary effectively coincides with the precise number of rows that are encompassed within the aforementioned matrix. By effectively utilizing the Bellman–Zadeh methodology, the initial route originating from the Pareto frontier is systematically determined through the meticulous process of identifying the maximum value inherent within the membership function attributed to the lower-level objective.

4.6 Results of optimization approaches

In a departure from concentrating solely on a single optimal point, the methods discussed are implemented to unveil an array of optimal solutions. Genetic algorithms have gained prominence due to their effectiveness in optimizing various functions. In the specific framework of this study, the NSGAII technique is skillfully employed to discern the operational arrangement that offers the utmost advantages. Figure 4.7 serves as a visual guide, offering a comprehensive overview of the optimization process pertaining to the procedure under examination.

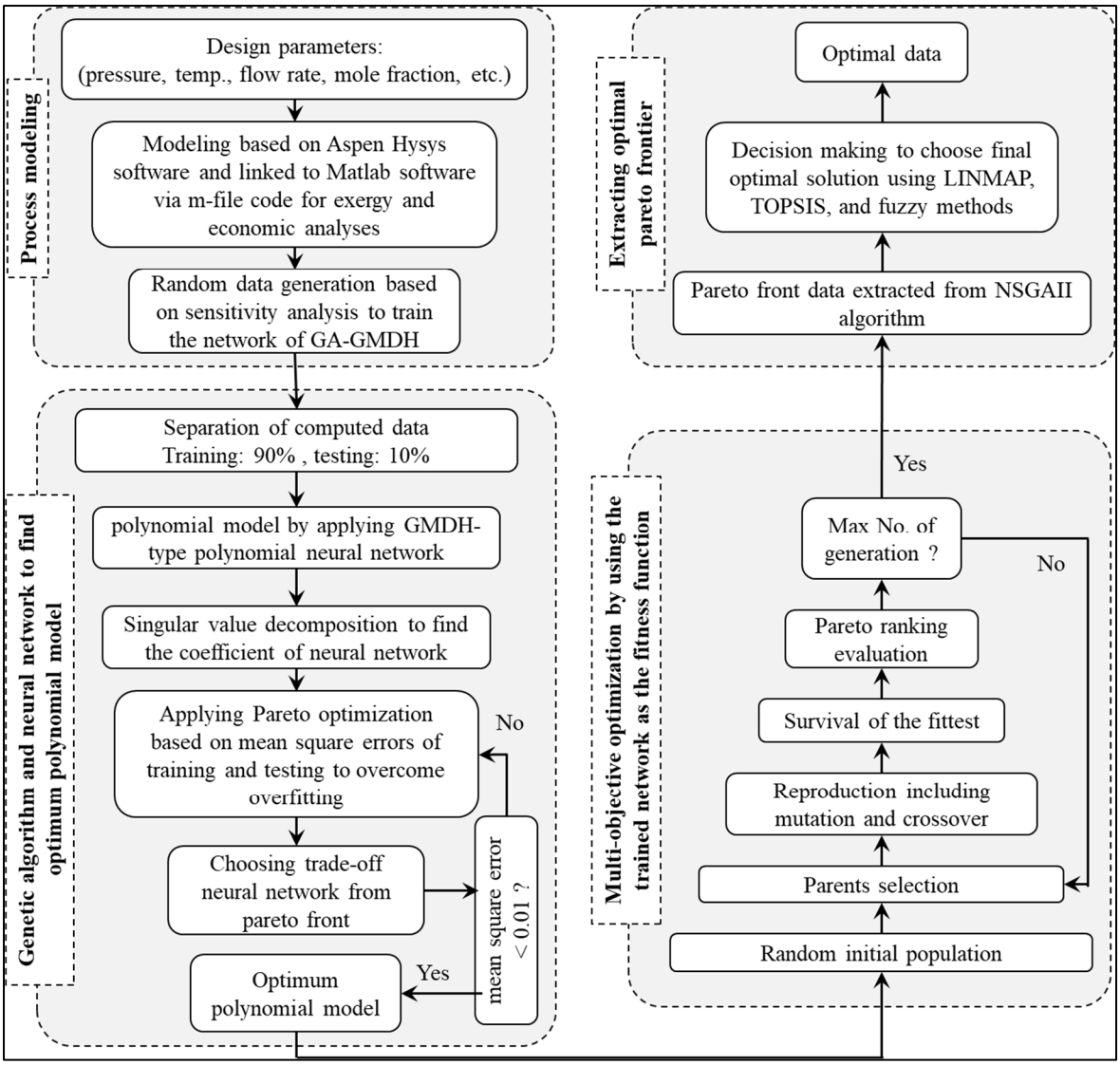

Figure 4.7. The optimization process considered to develop the design

The architectural arrangement of the network and the calculation of coefficients within the governing equations are both orchestrated through the concurrent application of the genetic algorithm and the Singular Value Decomposition (SVD) technique. The genetic algorithm's role in this context involves efficiently constraining the search range of the GMDH neural network, thereby facilitating the SVD method’s optimal integration to ascertain the 6 factors of communication that oversee interactions between the 2 neurons. Beyond this, the optimization process encompasses the critical task of determining the most appropriate count of neurons within each latent layer in conjunction with their intricate intercommunication

structure. These efforts are all directed towards the ultimate objective of extracting the most advantageous compilation of coefficients of the quadratic polynomial.

The Pareto optimal boundary is established, and the optimal points are identified by applying decision-making methods such as TOPSIS, LINMAP, and the fuzzy Bellman-Zadeh methods. Within this research, the objective functions during the thermodynamic and economic evaluation phase are the proposed system's overall thermal and exergy efficiencies, along with the return period. Table 4.2 enumerates the objective functions, decision variables, and constraints determined via sensitivity analysis for utilization within the optimization stage. Employing sensitivity analysis to scrutinize the design and its responsiveness to variations in diverse parameters, the identification of decision variables is undertaken. The criterion for selecting parameters for deliberation typically revolves around those wielding substantial influence over efficiency and cost implications. In this context, five parameters are designated as decision variables and constraints, encompassing the temperature of the D17 stream, hydrogen content in the feed gas, inlet CO_2 flow rate, minimum temperature approach of heat exchangers, and compressor pressure ratio. These parameters are strategically chosen for their discernible impact on the overall efficacy and economic considerations within the examined system. Through the application methodologies for decision-making, establishing the Pareto optimal boundary is achieved, concurrently identifying the most favourable points. Within the framework of this research endeavour, the objective functions employed throughout the evaluation stages span both thermodynamic and economic domains, specifically encompassing the comprehensive assessment of the system’s thermal and exergy efficiencies and determining the return period. The consequential outcomes derived from the sensitivity analysis, meticulously outlining the enumeration of constraints, objective functions and decision variables, as meticulously documented in Table 4.2, collectively play an indispensable role as pivotal inputs for the forthcoming optimization phase.

Table 4.2. Objective functions, considered constraints, and decision variables

Objective functions	Range
Max thermal efficiency $= \mathcal{F}_1(\mathrm{X})$ Max exergy efficiency $= \mathcal{F}_2(\mathrm{X})$ Min period of return $= \mathcal{F}_3(\mathrm{X})$	
Decision variables and constraints	
Temperature of D17 stream	Between -139 and -149 ˚C
Hydrogen content in the feed gas	Between 55 and 80 mol%
Inlet CO_2 flow rate	Between 5 and 9 ton/h
Min. temp. approach of heat exchangers	> 1 ℃
Compressor pressure ratio	> 1

Figure 4.8 presents the visualization of the Pareto frontier, resulting from the implementation of the NSGAII algorithm. Throughout the procedure, a diverse array of outcomes is produced by employing different decision-making strategies, with the findings from the TOPSIS/LINMAP approaches revealing a striking degree of similarity. Figure 4.9 serves as a platform to showcase the ultimate optimal results achieved via each distinct approach, further accentuated by the representation of non-ideal and ideal points within the study context.

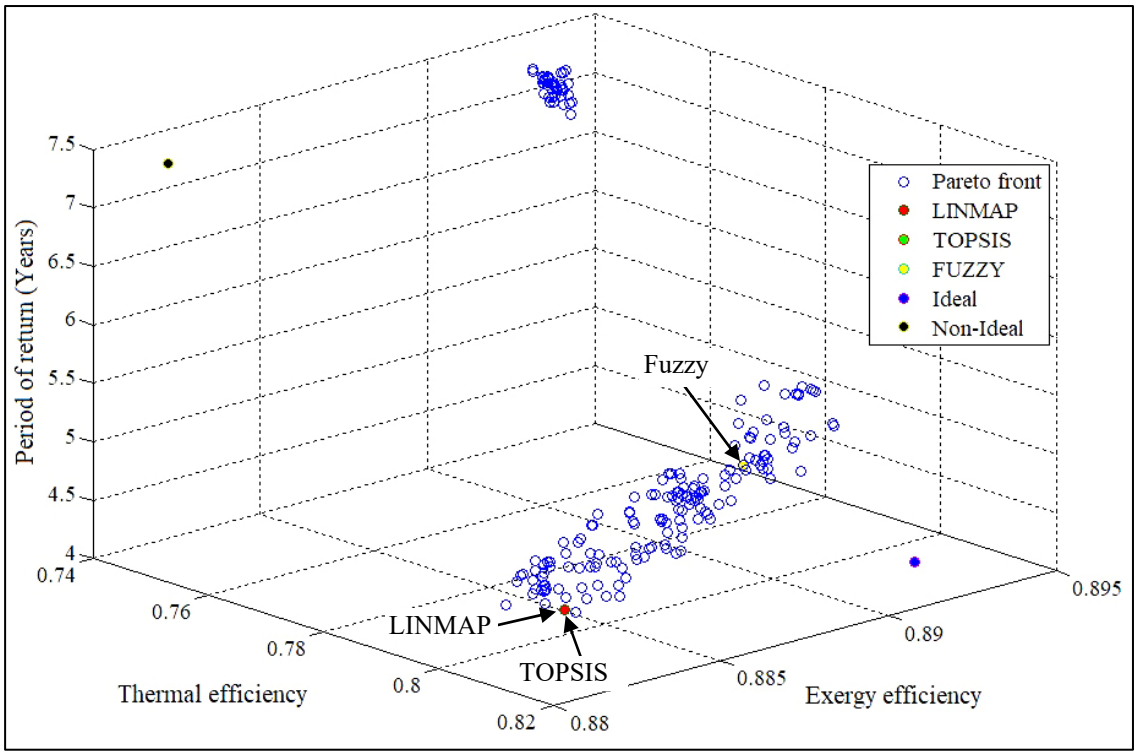

Figure 4.8. Pareto frontier resulting from utilizing the algorithm of NSGAII

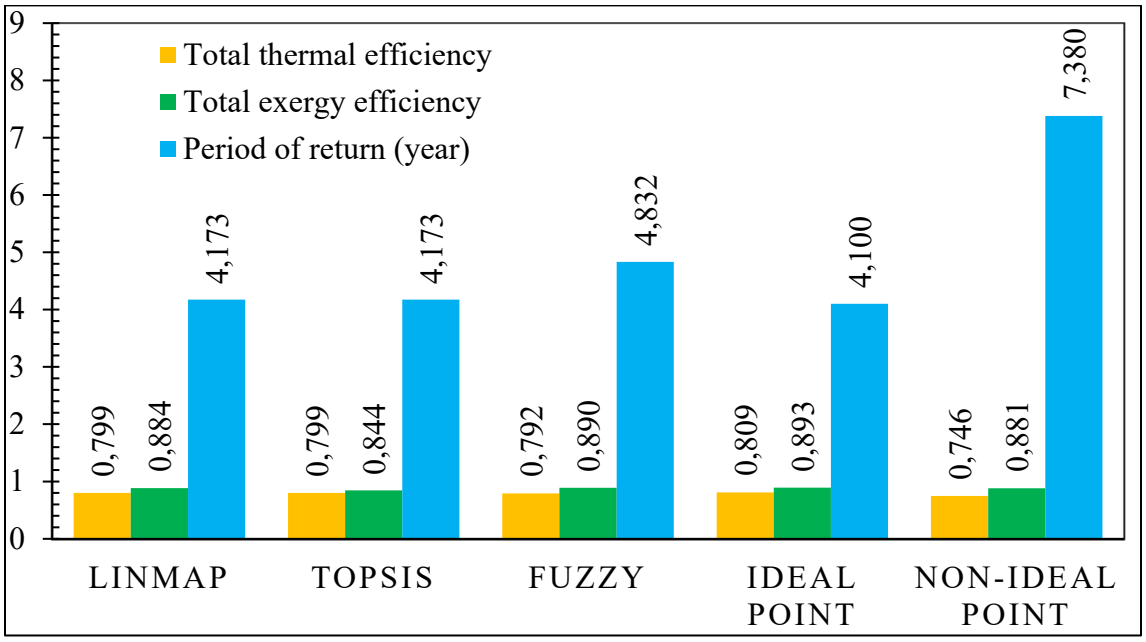

Figure 4.9. The ultimate optimal solution derived from each decision-making method

The outcomes demonstrate that the return period of the process after optimization is 38.16 percent lower than the base scenario by using the TOPSIS and LINAMP methods. The value for the return period in the fuzzy Bellman-Zadeh approach is 4.832 years, 15.8% higher than the two other decision-making methods. The optimum total thermal efficiency of the process calculated from all the methods is almost the same, with the result of fuzzy Bellman-Zadeh being 0.7 percent lower than LINAP and TOPSIS methods (79.9%). However, the integrated process from the fuzzy method has a higher exergy efficiency than the system chosen based on the other two approaches. The values of the ideal point for total thermal efficiency, total efficiency for exergy, and the return period are calculated to be 80.9%, 89.3%, and 4.1 years, respectively.

4.7 Conclusion

The findings of this research underscore a substantial contribution to sustainability within the realm of process engineering. Through the application of a robust hybrid optimization approach, our study not only achieves remarkable reductions in the investment return period but concurrently enhances thermal efficiency. These improvements directly translate to reduced energy consumption and a more sustainable operation, aligning with the global agenda for environmentally conscious industrial practices. To achieve the study goals, an economic assessment is used by employing the ACS methodology. This was done to investigate the economic viability of a combined system designed to produce liquid methanol. The effect of methanol and crude hydrogen prices, electricity, and fuel gas costs on effective economic parameters is investigated. By combining artificial intelligence with neural networks and GA, the results for the return period of investment and thermodynamic efficiencies are improved in the next step. Moreover, applying the three methodologies investigated plays a pivotal role in facilitating decision-making within the employment of optimization. The following are the primary outcomes of the study:

The results indicate that the return period, net annual benefit, and the prime cost of methanol are 6.63 years, 9.34 MMUSD/year and 0.15 USD/kg, respectively .

The methanol market price significantly impacts the return period. A rise in the main product price (liquid methanol) from 0.35 to 0.8 USD/Kg sharply cuts the return period from 8.30 to 2.55 years. This shift connects directly and almost linearly with additive value and net annual benefit and. Elevating the feed gas price from 0.8 to 3 USD/MMBTU increases prime and levelized costs for methanol production, reaching 0.13 to 0.36 and 0.22 to 0.46 USD/kg, respectively. Conversely, this raises costs and reduces net annual benefits and additive value, decreasing from 10.15 and 0.271 to 1.273 and 0.034, respectively. Additionally, if the crude feed gas cost exceeds 1.8 USD/MMBTU, the return period increases drastically beyond 10 years.

The optimized process showcases a remarkable 38.16% reduction in the return period compared to the base case, as indicated by the TOPSIS and LINMAP methods. However, within the fuzzy Bellman-Zadeh framework, the return period value computes 4.832, marking a 15.8% increase compared to the other decision-making methods. While the optimal total thermal efficiency remains nearly constant across all methods, the fuzzy Bellman-Zadeh approach records a mere 0.7% deviation, slightly lower than the LINMAP and TOPSIS methods (79.9%).

For the future research plan, analyses including uncertainty, flexibility, and sustainability analysis can be investigated for the developed process to assess the overall robustness, adaptability, and credibility of the design and evaluate the climatic and environmental impact of the project during its life cycle from an economic point of view.

CHAPTER 5

THERMO-ECONOMIC OPTIMIZATION OF A NEW SOLAR-DRIVEN SYSTEM FOR EFFICIENT PRODUCTION OF METHANOL AND LIQUEFIED NATURAL GAS USING THE LIQUEFACTION PROCESS OF COKE OVEN GAS AND POST-COMBUSTION CO_2 CAPTURE

Alireza Khatami Jouybari [a], Adrian Ilinca [b], Bahram Ghorbani [c]

[a, b] Department of Mathematics, Computer Science and Engineering, University of Quebec at Rimouski (UQAR), 300 All. des Ursulines, Rimouski, QC G5L 3A1, Canada
[c] Faculty of Engineering Modern Technologies, Amol University of Special Modern Technologies, Amol 4615664616, Iran

Paper published in *Energy Conversion and Management*, July 2022[4]
(Alireza Khatami Jouybari et al., 2022b).

Abstract

The utilization of hydrogen-containing industrial by-products such as coke oven gas (COG) and ammonia synthesis flue gases contributes to environmental pollution and energy waste. This paper develops a novel integrated structure for the simultaneous production of portable and relatively clean liquid fuels from COG and power plant exhaust gases. The subsystems include a CO_2 capture unit to separate carbon dioxide from exhaust gases, natural gas purification and liquefaction process to produce liquefied natural gas (LNG), hydrogen from COG, and a methanol production cycle. Photovoltaic panels with geographical location (30.75˚ N, 56.65˚ E – Zarand, Iran) are used to provide the required power. This process provides 144.7 kmol/h of methanol and 368 kmol/h of LNG as the main product and 9193 kmol/h of hot water as an industrial utility. The integrated structure's total energy and exergy efficiencies are 65.36% and 68.72%, respectively. The largest share of exergy degradation belongs to the photovoltaic panels (81.33%), heat exchangers (5.66%), and distillation towers

---

[4] Khatami Jouybari, A., Ilinca, A., Ghorbani, B. – « Thermo-economic optimization of a new solar-driven system for efficient production of methanol and liquefied natural gas using the liquefaction process of coke oven gas and post-combustion carbon dioxide capture," Energy Conversion and Management, https://doi.org/10.1016/j.enconman.2022.115733, 2022

(3.152%). The system's levelized annual cost method is applied for the economic analysis. The results show that the payback period and the product's final cost are 4.29 years and 396.7 USD/ton-methanol. The sensitivity analysis results show that the efficiency of the whole process and the cost of the product increase to 69.05% and 400.5 USD/ton-methanol when the hydrogen content of the coke oven gas decreases from 65% mol to 54% mol. Moreover, the decrease in COG flow rate, from 991.6 kmol/h to 901.6 kmol/h, reduces the cost of the product and the irreversibility of the whole system to 385.5 US $/ton-methanol and 55382 kW. NSGAII algorithm is implemented for multi-objective optimization of the process, with TOPSIS and LINMAP being the decision-making methods. From the optimization results, the optimum values for the efficiency of the whole hybrid system and the cost of the product are calculated to be 65.83% and 0.3611 USD/kg methanol.

Keywords: Coke oven gas, methanol synthesis, CO_2 capture, LNG production, thermo-economic analysis, multi-objective optimization

5.1 Introduction

Coke oven gas (COG) is considered a valuable by-product of coal carbonization in coke production used in the steel industry. Typically, one ton of coke produces approximately 360 m^3 of COG. Disposal of COG without efficient reuse is generally a waste of energy from this valuable source. COG can be utilized as a potential feedstock for the production of hydrogen, pure methane, synthesis gas, and methanol (Razzaq et al., 2013). This valuable intermediate product is widely employed in steel and other non-ferrous metals industries, including copper, lead, and zinc in blast furnaces. The integration of coke production systems with the COG purification process is implemented to increase energy efficiency and market competitiveness. Thus, the recovery of coke by-products is a standard methodology in most coke factories consisting of two stages of the coke production process and the COG process (X. Liu & Yuan, 2016). Li et al. systematically evaluated the environmental impact of the coke production life cycle by dividing it into several sub-processes and comparing the result with the base (without allocation) method. According to the life cycle assessment (LCA)

results, the coke production significantly reduces the environmental impact compared to the without allocation method. They showed that reducing the consumption of washed coal in the coking process and increasing the efficiency and ecological compatibility of coal mining and processing is beneficial for the sustainability of coke production. The raw COG process enters the gas collectors from the rising pipes above the coke oven and is sent for treatment. Four sub-processes include cooling system, sulfur recovery, ammonia recovery, and crude benzene recovery (Shirmohammadi et al., 2020). Lee et al. undertook the economic analysis of a methanol production (MEOH) system of gases emitted from a steel plant, particularly coke oven and oxygen furnace gases. Synthesis gas was produced with a specific ratio of hydrogen to monoxide and subsequently converted into methanol. Methanol's energy efficiency and production cost were calculated to be 54.6-55.9% and 0.57 $/kg, respectively. Economic and sensitivity analyses of the developed structure showed that the cost of the product is slightly higher than that of the market price. But in some cases, the production cost is reducible (Lee et al., 2019).

Advanced processes for synthesizing methanol from COG have limitations such as poor hydrogen utilization, low efficiency, and high energy consumption, leading to high production costs. Integrating methanol synthesis from COG with other liquid fuel production processes can be a practical solution to overcome these limitations (Uribe-Soto et al., 2017); (Zhen & Wang, 2015). The steel-making process consists of several sub-units, including coke oven gas (COG), blast furnace gas (BFG), and basic oxygen furnace gas (BOFG). These exhaust gases are commonly used as energy sources to generate heat and electricity in the iron and steel industries, which leads to a waste of energy as well as greenhouse gas emissions (Xiang et al., 2017). The prices of exhaust gases from the sub-units of coke oven gas, blast furnace gas, and oxygen furnace gas in the steel industry have been calculated to be 2.95 $/kmol, 0.46 $/kmol, 0.17 $/kmol, respectively (Bermúdez et al., 2013); (Ishioka et al., 1992); (Lundgren et al., 2013). Also, the volumetric composition of coke oven gas is 55-60% hydrogen, less than 2% carbon dioxide, 5-8% carbon monoxide, 23-27% methane, and 3-6% nitrogen (Bermúdez et al., 2012).

Generally, methanol production in such methods consists of four synthesis gas preparation stages, including H_2 and CO, synthesis gas purification, methanol gas synthesis, and distillation of crude methanol (Alireza Khatami Jouybari et al., 2022a). The main difference in methanol production processes is due to the different methods of synthesizing gas production. The results show that the average cost of methanol production through COG is 25.1 and 19.8% lower than its production from coal and natural gas, respectively (Jingying Li et al., 2018). Han et al. have studied different strategies for the utilization of carbon in end products. They identified the best strategy for producing a pure product including methane, methanol, hydrogen, and liquid fuels using carbon. The results showed that the product's cost price for the production of 8.23×104 ton/year of methanol from COG is 0.13 $/kg (Han et al., 2019). Yi et al. developed a new process for the production of methanol from COG using COG-to-methanol with CO_2 recycle (CTMCR), COG-to-methanol without supplementary carbon (CTMWOSC), and COG-to-methanol with supplementary carbon (CTMWSC). CTMRC, CTMWSC, and CTMWOSC cycle exergy efficiencies were 60.3%, 56%, and 57.3%, respectively. The costs of methanol for the integrated structures of CTMCR, CTMWOSC, and CTMWOSC were calculated to be 152.7 USD/ton, 212.9 USD/ton, and 174.7 USD/ton, respectively (Yi et al., 2016). Kim et al. developed two integrated structures for the simultaneous production of methanol, heat, and power. The energy efficiency of the developed processes was calculated between 53% and 71%, and the minimum methanol price of the developed processes was calculated to be 0.23-0.29 USD/kg (Kim et al., 2019).

Methanol synthesis to produce a potentially portable liquid fuel is promising for the utilization of coke oven gas. Zhao et al. developed a new and efficient method for converting COG and coke powder to methanol and ammonia using a chemical ring to produce hydrogen. Their integrated system has better energy efficiency and exergy than other COG to ammonia and methanol production technologies. The integrated structure's energy efficiency and exergy efficiency were calculated to be 60.7-78.7% and 54.4-70.1%, respectively (Zhao et al., 2021). Hao et al. developed an integrated system for the co-production of dimethyl ether (DME), methanol and electricity with coal-fired fuel and coke oven gas (COG). The simulation results showed that the exergy efficiency increased by 7.8%, and the cost of

exergy and CO_2 emission decreased by 0.88 US $/GJ and 0.023 kg/MJ, respectively, compared to the baseline state (Hao et al., 2015).

COG-based Hydrogen (COGH) production can be a potential alternative to coal-based hydrogen gas (CHG) production due to China's large-scale coke production industry. Results from reference (Junjie Li & Cheng, 2020) showed that energy consumption, carbon emissions, investment costs, and operating costs of COGH were 34.6%, 36.7%, 27.4%, and 8.7% lower than CGH, respectively. In contrast, the COGH profit and internal rate of return are 1.35 and 2.35 times of CGH, respectively. Deng et al. developed a process to convert coke oven gas and blast furnace gas (BFG) from steel refineries to methanol. Compared to current operating methods, the integrated process developed can increase the net value by up to $54 million. Moreover, the resulting carbon efficiency was calculated to be up to 72% (Deng & Adams II, 2020). Lin et al. developed an integrated structure to produce liquefied natural gas and hydrogen based on coke oven gas. The simulation results showed that by increasing the hydrogen content in the COG and increasing the methane recycling rate, the unit power consumption enhances (Lin et al., 2014). Xu et al. developed a new low-temperature refrigeration system to simultaneously produce liquid hydrogen and natural gas from coke ovens using Aspen HYSYS software. The results showed that the proposed system with acceptable energy consumption could achieve a methane recovery rate of 97.9% and a hydrogen recovery rate of 99.7% (Xu et al., 2018). Xu et al. introduced four processes for producing LNG and liquid hydrogen, including open-loop N_2, open-loop H_2, closed-loop N_2, and closed-loop H_2. The results showed that the purity of LNG and liquid hydrogen produced by the processes exceeded 99.99%, and the specific energy consumption of the systems (SEC) was 18.01-41.2 kWh/kmol (Xu & Lin, 2021b). Xu et al. studied three novel structures for the simultaneous production of liquid hydrogen and liquefied natural gas based on coke oven gas. The refrigeration required to liquefy hydrogen gas was provided by a two-stage helium expansion cycle, and the exergy efficiency of the developed structures was between 13 and 66.5% (Xu & Lin, 2021a).

Absorption and carbon utilization to convert valuable products such as chemicals and fuels can help reduce climate change (Daggash et al., 2018). Shirmohammadi et al. proposed a carbon dioxide removal unit based on mono-ethanolamine using Aspen HYSYS software. The outcomes were validated with real data from the petrochemical industries. They found that the highest specific heat consumption and purity of carbon dioxide were 4.78 MJ/kgCO_2 and 95.5 mol%, respectively (Shirmohammadi et al., 2020). Gervasi et al. simulated a post-combustion CO_2 capture plant in Aspen HYSYS software using the Kent-Eisenberg thermodynamic model. The specific heat consumption of the developed structure was proved to be 3.71 GJ/tonCO_2 with 85% purity of produced CO_2 (Gervasi et al., 2014). Morales-Mora et al. developed an MEA-based carbon dioxide separation system with Aspen Plus software. Isolation efficiency and CO_2 flow purity were calculated to be 95.4% and 95%, respectively. The specific heat consumption of their developed structure was 4.36 MJ/kgCO_2 (Morales-Mora et al., 2019). Li et al. modeled a carbon dioxide separation system with a purity of 99.1% in the Aspen Plus environment. Reboiler temperature and energy consumption in their developed structure were calculated to be 123.7 ^{0}C and 3.1 MJ/ kgCO_2, respectively (K. Li et al., 2016).

Numerous processes for hydrogen separation from coke oven gas have been proposed in recent years. In most cases, GOC gas has been used as a fuel in industry, power generation in boilers and turbines, synthesis gas production, and other applications. In recent studies, coke oven gas has been used in the simultaneous production systems of LNG and liquid hydrogen. Liquid hydrogen energy storage in the industry is expensive and sometimes costly. Therefore, in order to reduce environmental pollution and convert carbon dioxide extracted from industrial exhaust gases into valuable fuels, in this paper, a new integrated structure for the production of methanol and LNG using coke oven gas and carbon dioxide has been developed, which is a hybrid process including a carbon dioxide separation unit, a hydrogen purification and separation unit from coke oven gas, a nitrogen compression refrigeration cycle and a methanol production cycle. This process aims to produce LNG, methanol, and hot water. Thermodynamic, exergy, economic, and sensitivity analyzes are implemented to evaluate the performance of the developed integrated structure.

5.2 Process description

Methanol and LNG are both considered suitable fuels to be used as energy carriers. This paper proposes a brand-new integrated structure for the simultaneous production of these fuels and hot utility water, including subsystems of the liquefaction process of coke oven gas (LPCOG) for the production of purified LNG and hydrogen, the industrial post-combustion capture process (PCCP) based on monoethanolamine for the capture of carbon dioxide, and the methanol synthesis process for the production of methanol. Figure 5.1 demonstrates the proposed system's block flow diagram (BFD). To supply the electrical power of the whole process, a Photovoltaic solar panels system is designed by PVsyst software. Figure 5.2 shows the developed hybrid process's process flow diagram (PFD). For the modeling and analyses, pressure drops in heat exchangers and flash drums and heat loss in equipment are ignored. Peng-Robinson equation of state is employed to model the whole process in HYSYS software. Equipment and streams characteristics, including compositions of important streams and their pressure, temperature, flow rates, enthalpy, entropy, and exergy, are available in Tables 5.1, and Table-A II-1, 2 (see Annex II).

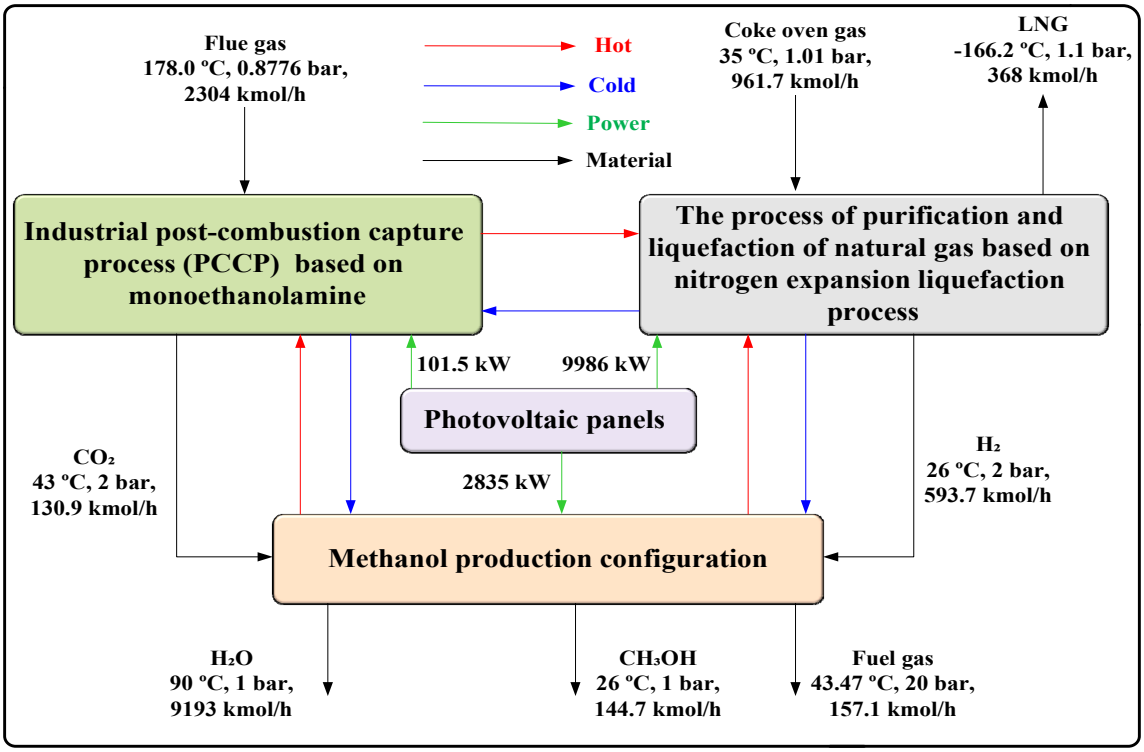

Figure 5.1. Block flow diagram (BFD) of the proposed system

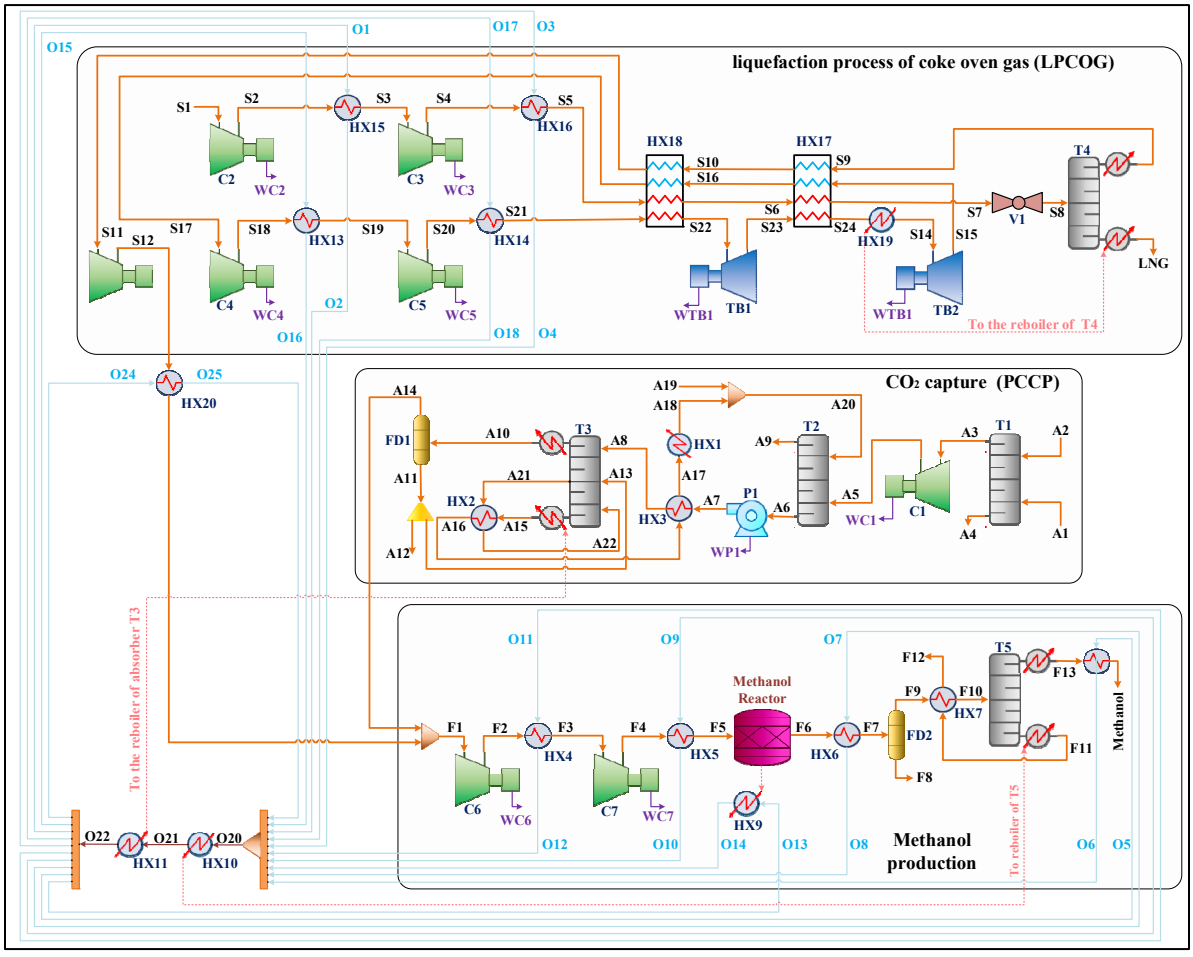

Figure 5.2. Process flow diagram (PFD) of the proposed system

Table 5.1. The molar composition of streams in the integrated structure

Stream	CO_2	N_2	H_2O	ME Amine	O_2
A1	0.0678	0.7240	0.1756	0	0.0326
A2	0	0	1	0	0
A6	0.0546	0	0.8309	0.1145	0
A9	0.0159	0.8205	0.1266	0.0001	0.0369
A10	0.7168	0.0003	0.2828	0.0001	0
A13	0.0013	0	0.9982	0.0005	0
A14	0.9556	0.0003	0.0440	0	0
A22	0.0535	0	0.8359	0.1106	0
S1	0	0.0300	0	0	0
LNG	0	0.0099	0	0	0
S9	0	0.0424	0	0	0
S22	0	1	0	0	0
F1	0.1726	0.0348	0.0080	0	0
F8	0	0.1597	0.0031	0	0
F9	0	0.0004	0.4740	0	0
F12	0		1	0	0
Methanol	0	0.0008		0	0
O23	0	0	0	0	0
O26	0	0	1	0	0

Table 5. 1. The molar composition of streams in the integrated structure (continued)

Stream	CO	CH_4	H_2	Methanol	Bi Phenyl	diPH-Ether
A1	0	0	0	0	0	0
A2	0	0	0	0	0	0
A6	0	0	0	0	0	0
A9	0	0	0	0	0	0
A10	0	0	0	0	0	0
A13	0	0	0	0	0	0
A14	0	0	0	0	0	0
A22	0	0	0	0	0	0
S1	0.0300	0.3900	0.5500	0	0	0
LNG	0.0209	0.9691	0	0	0	0
S9	0.0356	0.0311	0.8909	0	0	0
S22	0	0	0	0	0	0
F1	0.0292	0.0255	0.7300	0	0	0
F8	0	0.1173	0.7086	0.0113	0	0
F9	0	0.0001	0	0.5252	0	0
F12	0	0	0	0	0	0
Methanol	0	0.0003	0	0.9990	0	0
O23	0	0	0	0	0.2462	0.7538
O26	0	0	0	0	0	0

5.2.1 LPCOG process

Coke oven gas can be transformed into LNG by extracting its hydrogen contents, increasing its applicability and transportability. Besides, the extracted hydrogen can be used directly in petrochemical industries or be stored in the form of compressed, liquefied, or liquid organic hydrogen carriers (LOHC) such as methanol, which has the merit of absorbing carbon

dioxide helping the reduction of greenhouse gases. The composition of COG in different cases varies but can be considered as a combination of hydrogen, methane, carbon monoxide, carbon dioxide, nitrogen, and other minor contents. On average, H_2 has a share of 55% molar; however, it can vary from 45 to 65 percent. Here, it is assumed that the methane content of COG is 39% molar, and its CO_2 content is extracted before entering the LNG production process (Lin et al., 2014). The stream S1, after two steps of compression, increases its pressure from nearly atmospheric to 50 bar before entering HX17. To keep the temperature of COG constant at 35 ^{0}C, two heat exchangers of HX15 and HX16 are utilized after each compression step. HX17 and HX18 are multi-stream flows designed to super cool the stream S5 from 35 to -181.9 ^{0}C (stream S7). The nitrogen expansion liquefaction process is employed to provide cooling for the liquefaction of COG through multi-stream heat exchangers. The absorbed heat by the nitrogen in two steps enters turbines TB1 and TB2 via S22 and S14 streams to produce 977.6 kW and 566.1 kW of power, respectively. Besides, the heat required in the reboiler of the LNG Distillation tower (T4) is supplied by the nitrogen expansion liquefaction process (HX19). To decrease the temperature of S7 even further, a throttling valve V1 is designed to lower its temperature from -181.9 to -190 ^{0}C by losing the pressure from 50 bar to 1.2 bar. The two-phase flow of S8 enters distillation tower T4 to its LNG contents be separated. Gaseous hydrogen with approximately 89% purity leaves T4 to enter the methanol production process, and liquefied natural gas leaves the distillation tower at 166.2 ^{0}C temperature and 1.2 bar pressure to be stored or transported.

5.2.2 PCCP process

The required carbon dioxide for methanol production is assumed to be supplied by the absorption from flue gas of the industrial plants, which contains 6.78% CO_2, 72.4% N_2, 17.56% H_2O, and 3.26% oxygen (stream A1). The water vapor content of stream S1 is decreased through the absorber T1, to after a pressure increase by compressor C1, enters the next absorber T2 at 0.9 bar pressure. Here, MEA amine is utilized to absorb carbon dioxide in T2, making a CO_2-rich liquid stream A6. Stream A9, mainly containing nitrogen and

oxygen gases, leaves the absorber T2 from above. The overall MEA reactions are presented as follows (Shirmohammadi et al., 2020):

$$CO_{2(g)} + H_2O_{(l)} \leftrightarrow H_2CO_{3(l)} \quad (5.1)$$

$$MEA + CO_2 + H_2O \leftrightarrow MEA - H^+ - COO^- + H_2O \quad (5.2)$$

$$MEA - H^+ - COO^- + H_2O \leftrightarrow MEA - COO^- + H_3O^+ \quad (5.3)$$

$$2MEA + CO_2 \rightarrow MEA - COO^- + MEAH^+ \quad (5.4)$$

$$MEA - COO^- + H_2O \rightarrow {HCO_3}^- + MEA \quad (5.5)$$

$$MEA + H_3O^+ \rightarrow MEAH^+ + H_2O \quad (5.6)$$

$$H_2CO_3 + H_2O \rightarrow {HCO_3}^- + H_3O^+ \quad (5.7)$$

$${HCO_3}^- + H_2O \rightarrow {CO_3}^{2-} + H_3O^+ \quad (5.8)$$

The pressure and temperature of the A6 stream are adjusted to 87 ^{0}C and 4.4 bar by pump P1 and heat exchanger HX3 before entering desrober T3. Here, carbon dioxide is separated from MEA amine to leave T3 from above, and MEA rich streams of A15 and A21 leave T3 to enter T3 and T2 again after HX3 adjusts their temperature. A10 stream enters flash drum FD1, and after reducing its temperature from 89 to 43 ^{0}C, gaseous carbon dioxide is separated from water with 95.56% purity, ready to enter the methanol production cycle at 2 bar pressure.

5.2.3 Methanol synthesis process

In comparison with hydrogen, methanol is safer and easier to liquefy and transport. It also has the advantage of being used to absorb carbon dioxide. In the present paper, the purified and extracted hydrogen from COG is considered to react with the absorbed carbon dioxide from the flue gas to produce methanol. In this regard, streams S13 and A14 are collected to make stream F1. After two compression and temperature adjustment stages through compressors C6 and C7 and heat exchangers HX4 and HX5, it is ready to enter the reactor at 50 bar pressure and 200 ^{0}C temperature. For the simulation of methanol production reaction,

a plug flow reactor is considered in HYSYS software. This reaction is an exothermic reaction presented as follows (Ortiz et al., 2013); (Van-Dal & Bouallou, 2013):

$$CO_2 + 3H_2 \leftrightarrow CH_3OH + H_2O \tag{5.9}$$

The heat of the reaction is used to supply the required heat in the reboilers of methanol distillation tower T5 and reboiler absorber T3 as well as supplying 180.5 m^3/h hot water at 90 ^{0}C, rectifying the need for external utilities. Non-reacted hydrogen and impurities (mainly methane) are separated from methanol in flash drum FD2 at 43.44 ^{0}C to methanol/water mixture (stream F10) be ready to enter the distillation tower at 93 ^{0}C. After distillation, the water content of stream F10 leaves T4 from the lowest stage at 180.3 ^{0}C to preheat the inlet stream F9. Stream F13 with 99.85% purity leaves T4 from the upper stage at 10 bar and 138.5 ^{0}C and, after cooling to the ambient temperature, ready for storage or transportation.

5.2.4 Photovoltaic power supply system

To supply the necessary power of the designed system, an on-grid system of photovoltaic panels is designed. This is in line with the objective of diminishing greenhouse gas emissions of the study. The total required external power is 12.92 MW. 9.98 MW of this power is consumed by the purification and liquefaction of natural gas based on the nitrogen expansion liquefaction process. A portion equal to 2.83 MW supplies the required power of the Methanol production configuration, and the rest of 0.10 MW is sent to the Industrial post-combustion capture process (PCCP) based on monoethanolamine. Using the meteorological data of the selected location (Zarand city, Iran), PVsyst software is implemented to simulate the photovoltaic system. In order to do the performance assessment of the system, parameters recommended by International Energy Agency (IEA) are in action consisting of performance ratio (PR), inverter efficiency (η_{inv}), system's total energy loss (L_S), array capture loss (L_C), final system yield (Y_F), array yield (Y_A), and reference yield (Y_R). Following is the equation for the calculation of the final yield (Ayompe et al., 2011):

$$Y_F = \frac{P_{AC}}{P_{PV}} \tag{5.10}$$

E_{AC} represents the output power (AC) of inverters, and P_{PV} is the maximum produced power at standard test conditions (STC). Array yield (Y_A) can be calculated from the following equation (Ghorbani, Ebrahimi, et al., 2020):

$$Y_A = \frac{E_{DC}}{P_O} \tag{5.11}$$

Where, E_{DC} is the produced DC power, and (P_O) is the nominal power in STC. Reference yield can be achieved by dividing in-plane solar radiation (H_t) to array reference irradiance (G_o) (Ghorbani, Ebrahimi, et al., 2020):

$$Y_R = \frac{H_t}{G_o} \tag{5.12}$$

To calculated L_S (total energy loss) and L_C (Array Capture Loss) (Ghorbani, Ebrahimi, et al., 2020):

$$L_S = Y_R - Y_F \tag{5.13}$$

$$L_C = Y_R - Y_A \tag{5.14}$$

The performance ratio (PR) is the final system yield (Y_F) divided to reference yield, (Y_R) and is calculated as follows (Marion et al., 2005):

$$PR = \frac{Y_F}{Y_R} \tag{5.15}$$

It can be concluded that the efficiency of the inverter (η_{inv}) can be gained as follows (Ghorbani, Ebrahimi, et al., 2020):

$$\eta_{inv} = \frac{P_{AC}}{P_{DC}} \tag{5.16}$$

Finally, the efficiency of the photovoltaic module (η_{PV}) multiplied by the photovoltaic inverter efficiency results in the total system efficiency (η_{system}) (Ghorbani, Ebrahimi, et al., 2020):

$$\eta_{system} = \eta_{PV} \times \eta_{inv} \tag{5.17}$$

5.3 Considered analyses

5.3.1 Energy analysis

Considering the control volume for each of the equipment used in the integrated structure developed with the help of the special enthalpy value, the energy balance equations can be presented as follows (Ghaebi et al., 2017):

$$\sum_{in} \dot{m}_{in}\, h_{in} - \sum_{out} \dot{m}_{out}\, h_{out} - \dot{W} + \dot{Q} = 0 \tag{5.18}$$

Energy balance equations in heat exchangers are obtained from the following equation (Seyam et al., 2020a):

$$\begin{gathered} \dot{m}_{in,i}(h_{in1,i} - h_{in2,i}) = \dot{m}_{out,i}(h_{out1,i} - h_{out2,i}) \\ T_{in1,i} = T_{out1,i} + \Delta\, T_{in,HXi} \end{gathered} \tag{5.19}$$

Energy balance equations in pumps/compressors and turbines (considering the isentropic efficiency) are presented below (Seyam et al., 2020b):

$$h_{out} = \frac{h_{out}^{S} - h_{in}}{\eta_s} + h_{in} \tag{5.20}$$

$$h_{out} = (h_{out}^{S} - h_{in})\eta_s + h_{in} \tag{5.21}$$

Also, considering the energy and mass balance equations in mixtures, the energy equations is achieved as follows (Seyam et al., 2020b):

$$h_{out} = \frac{\dot{m}_{in,1}h_{in,1} + \dot{m}_{in,2}h_{in,2}}{\dot{m}_{in,1} + \dot{m}_{in,2}} \tag{5.22}$$

Equations (5.23) and (5.24) are used as the energy and mass balance equations in flash drums and separators (Seyam et al., 2020b):

$$\dot{m}_{in}h_{in} = \dot{m}_{out,1}h_{out,1} + \dot{m}_{out,2}h_{out,2} \tag{5.23}$$

$$\dot{m}_{in} = \dot{m}_{out,1} + \dot{m}_{out,2} \tag{5.24}$$

Considering the control volume for throttle valves according to the first law of thermodynamics (constant enthalpy process), the energy equation is (Seyam et al., 2020b):

$$h_{in} = h_{out} \tag{5.25}$$

For modeling, a stream of steam and a stream of liquid enter each tray, and a stream of steam and a stream of liquid leave. Besides, in each tray, a stream of steam or liquid or a combination of them can be extracted as lateral streams of steam or liquid, called flow mediation. The feed can enter the tray, and heat can also enter or leave the tray. With such modeling, multi-input feed towers, multi-product towers, and towers with side heat exchangers can be modeled. According to Figure 5.3, the MESH equations can be written as follows:

1- The mass conservation equation for tray j and article i can be written for each stage (tray) as follows (Ebrahimi & Ziabasharhagh, 2017):

$$L_{j-1}\ x_{i,j-1} + V_{j+1}\ y_{i,j+1} + F_j\ Z_{i,j} - (L_j + U_j)\ x_{i,j} - (V_j + W_j)\ y_{i,j} = 0 \qquad (5.26)$$

2- Equilibrium equation for each component in one stage (tray) of the tower (Ebrahimi & Ziabasharhagh, 2017):

$$y_{i,j} - k_{i,j}x_{i,j} = 0 \qquad (5.27)$$

3- Sum equations for each step (tray) (Ebrahimi & Ziabasharhagh, 2017):

$$\sum_{i=1}^{NC} x_{i,j} - 1 = 0 \qquad (5.28)$$

$$\sum_{i=1}^{NC} y_{i,j} - 1 = 0 \qquad (5.29)$$

4- Thermal equilibrium equation (energy) for each stage (tray) (Ebrahimi & Ziabasharhagh, 2017):

$$L_{j-1}\ H^L{}_{j-1} + V_{j+1}\ H^V{}_{j+1} + F_j\ H^F{}_j - (L_j + U_j)\ H^L{}_j - (V_j + W_j)\ H^V{}_j - Q_j = 0 \qquad (5.30)$$

In these equations, the symbol Q is determined according to the heat source and the temperature of the heat source.

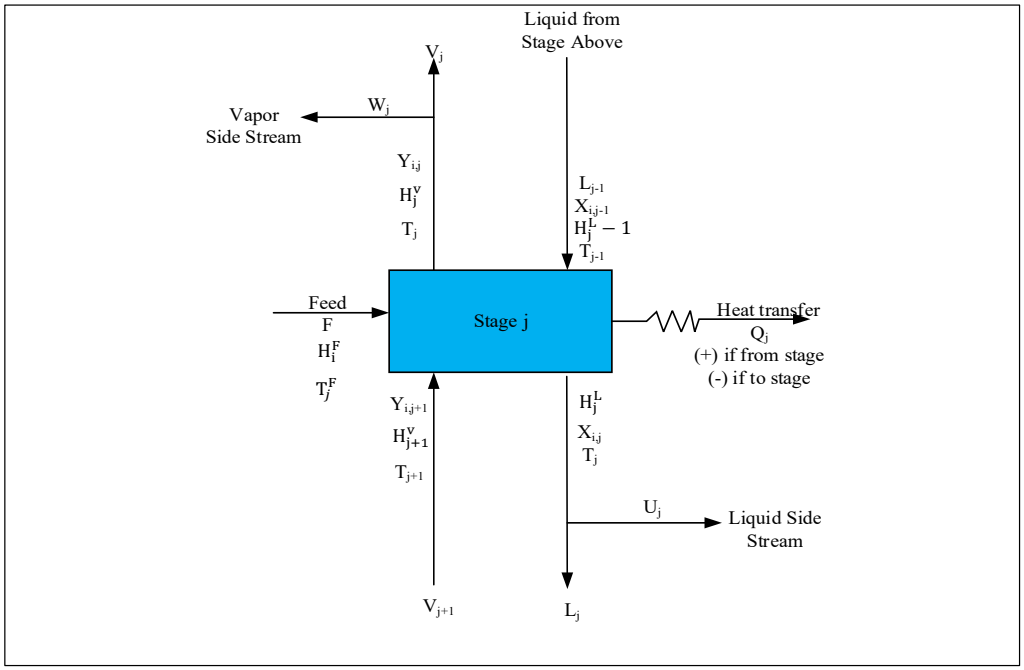

Figure 5.3. An overall equilibrium step of a distillation tower
modified from:
(Ebrahimi & Ziabasharhagh, 2017)

5.3.2 Exergy analysis

Exergy is the amount of work that is achieved by changing the state of a system from a specific state to ambient conditions, which is usually considered to be a temperature of 25 °C and a pressure of 1 atm, in a reversible process (Mohammad H Ahmadi et al., 2017). Exergy can be regarded as equivalent to reversible work. In other words, reversible work is the highest amount of harnessable work (the lowest amount of work consumed in power consumption equipment) when the system goes through a process between initial and final conditions. Therefore, the exergy destruction rate is proportional to the entropy produced (Kotas, 2013).

$$Ex_{destroyed} = T_0 S_{gen} \geq 0 \tag{5.31}$$

It is worth noting that exergy destruction has a positive value for all real systems and is zero for reversible systems. In the absence of kinetic energies, potentials, nuclei, electrical,

magnetic, and surface tension effects, the exergy rate of a whole system can be considered as the sum of the following components (Kotas, 2013):

$$\dot{E}x = \dot{E}x_{ph} + \dot{E}x_{ch} \tag{5.32}$$

$\dot{E}x$ ،$\dot{E}x_{ph}$ و $\dot{E}x_{ch}$ are the exergy rate of the fluid flow, and the sum of the physical and chemical exergy rates, respectively. Physical exergy and chemical exergy rates are calculated from Equations (5.33, 5.34) (Kotas, 2013):

$$\dot{E}x_{ph} = \sum_i \dot{n}_i \left((\bar{h}_i - \bar{h}_0) - T_0(\bar{s}_i - \bar{s}_0) \right) \tag{5.33}$$

$$\dot{E}x_{ch} = \dot{n} \left(\sum_i x_i \, \overline{ex}_i^{ch,0} + \bar{R} T_0 \sum_i x_i \ln(x_i \gamma_i) \right) \tag{5.34}$$

Where, $\bar{h}_0$ و $\bar{s}_0$ are the enthalpy and entropy of the flow at ambient temperature and pressure. In Equation (5.34), γi is the activity coefficient of component ith, which can have a value greater than or less than one. For an ideal solution, its value is zero. Calculating the chemical exergy of an ideal mixture of different compounds is not straightforward due to the coefficient of activity. It can be shown that the second sentence of Equation (5.34) is the Gibbs free energy change due to the mixing of different compounds and the formation of a solution at ambient temperature and pressure. Finally, the chemical exergy equation is transformed as follows (Alireza Khatami Jouybari et al., 2022a):

$$\dot{E}x_{ch} = \dot{n} \left(\sum_i x_i \, \overline{ex}_i^{ch,0} \right) + \Delta G^{mix} \tag{5.35}$$

ΔGmix is the Gibbs free energy change of the mixture at ambient temperature and pressure. Knowing the location and amount of irreversibility of various processes in a thermodynamic system is the primary purpose of performing exergy analysis, which can determine the extent

and how to improve the performance of that system. The exergy balance can be written as follows (Ebrahimi & Ziabasharhagh, 2017):

$$Ex_i + Ex_{Qi} = Ex_o + Ex_{Qo} + W_{sh} + I \tag{5.36}$$

The latter equation is used to calculate irreversibility or exergy destruction, in which Exi and Exo are input and output exergies of the flows, Ex_{Qi} and Ex_{Qo} input and output exergies of energy flows, W_{sh} shaft work on or by the system, and I denotes the irreversibly or exergy destruction. Equation (5.37) refers to the exergy balance of the pumps (Ebrahimi & Ziabasharhagh, 2017):

$$I_{p,c} = Ex_i - Ex_o = \sum(\dot{m}ex)_i + W - \sum(\dot{m}ex)_o \tag{5.37}$$

Where Ex_i , Ex_o represent irreversibility, input exergy, and output exergy, respectively. The exergy efficiency of the pumps is obtained from the following equation (Ebrahimi & Ziabasharhagh, 2017):

$$\eta_{p,c} = \frac{\sum(\dot{m}ex)_i - \sum_i(\dot{m}ex)_o}{W} \tag{5.38}$$

Reactions and exergy efficiencies of turbines are calculated based on the following equations:

$$I_T = Ex_i - Ex_o = \sum(\dot{m}ex)_i - W - \sum_i(\dot{m}ex)_o \tag{5.39}$$

$$\eta_t = \frac{W}{\sum(\dot{m}ex)_i - \sum_i(\dot{m}ex)_o} \tag{5.40}$$

Exergy destruction of a heat exchanger and its exergy efficiency are obtained from equations (5.41) and (5.42), respectively.

$$I_H = Ex_i - Ex_o = \sum(\dot{m}ex)_i - \sum(\dot{m}ex)_o \tag{5.41}$$

$$\eta_H = 1 - \left\{ \left[\frac{\sum_1^n(\dot{m}\Delta ex)}{\sum_1^n(\dot{m}\Delta eh)}\right]_h - \left[\frac{\sum_1^n(\dot{m}\Delta ex)}{\sum_1^n(\dot{m}\Delta eh)}\right]_c \right\} \tag{5.42}$$

Exergy destruction and exergy efficiency of throttling valves are obtained from Equations (5.43) and (5.44).

$$Ex_{D,HX} = Ex_i - Ex_o = \sum(\dot{m}.ex)_i - \sum(\dot{m}.ex)_o \tag{5.43}$$

$$\eta_{ex} = \frac{e_o^{\Delta T} - e_i^{\Delta T}}{e_i^{\Delta p} - e_o^{\Delta p}} \tag{5.44}$$

$$e^{\Delta T} = \int_T^{T_0} \frac{T - T_0}{T}\, dh, \qquad e^{Ph} = e^{\Delta T} + e^{\Delta T}$$

Exergy destruction and exergy efficiency of the distillation tower are obtained from equations (5.45) and (5.46).

$$Ex_{Column} = Ex_i - Ex_o = \sum(\dot{m}.ex)_i - \sum(\dot{m}.ex)_o \tag{5.45}$$

$$\eta_{ex} = \frac{Wmin}{Wmin + LW}$$

$$,Wmin = \sum_{Out\ of\ stream} nb - \sum_{in\ to\ stream} nb \tag{5.46}$$

$$(b = h - T_0 \mathrm{s}\ ,\ LW = T_0 \Delta S\mathrm{irr} = Lost\ Work)$$

5.3.3 Economic analysis

The method chosen for the economic evaluation is the Annualized Cost of the System (ACS). The parameters of return on investment, product cost, and initial investment are the most

influential in selecting the appropriate structure among all possible process designs. In this method, all system costs during the estimated technical life of the whole process are calculated (see Table 5.2), which consists of the Annualized Capital Cost (C_{acap}), Annualized Replacement Cost (C_{arep}), the Annualized Maintenance Cost (C_{amain}), and the Annualized Operating Cost of the system (C_{aope}). Since the project's useful life is assumed to be twenty years, parts replacement cost is neglected. For the economic analysis of equipment used in the proposed process, the existing relationships from the references are used, with many of them belonging to previous years. Thus, the equations are updated using Marshal and Swift Cost Index (Marshall et al., 2009).

$$C_{reference\ cost\ year} = Cost_{original\ year} \frac{CI_{reference\ cost\ year}}{CI_{original\ cost\ year}} \tag{5.47}$$

Table 5.3 shows the equations used to calculate the equipment price of the hybrid process (Bilal et al., 2013); (Couper et al., 2005); (Sameti & Haghighat, 2019); (Yang et al., 2008). The value of ACS is obtained from the following equation (Afrouzy & Taghavi, 2021):

$$\begin{aligned} ACS = {} & C_{acap}(Components) + C_{arep}(Components) \\ & + C_{amain}(Components) + C_{aope}(Labor\ Cost \\ & + Fuel\ Cost + Insurance\ Cost) \end{aligned} \tag{5.48}$$

The annualized capital cost includes purchasing the equipment, which has been levelized throughout the useful life of the studied process. The following equation identifies this levelized cost (Afrouzy & Taghavi, 2021):

$$C_{acap} = C_{Cap}.CRF(i, Y_{proj}) = C_{Cap}.\frac{i.(1+i)^{Y_{proj}}}{(1+i)^{Y_{proj}} - 1} \tag{5.49}$$

Where, C_{cap} is the total cost of the equipment purchased, i is the actual interest rate, Y_{proj} is equal to the useful life of the project, and CRF is the recoverable amount of the initial costs.

In order to calculate the real interest rate, the annual inflation rate and the nominal bank interest rate are utilized as shown in the following equation (Afrouzy & Taghavi, 2021):

$$i = \frac{j - f}{1 + f} \tag{5.50}$$

In calculating the economic analysis of the proposed integrated structures, the annual inflation rate is 17%, the bank nominal interest rate is 20%, and the project's useful life is 20 years. The fixed capital investment and other outlays are considered to calculate the equipment price. The fixed capital investment includes direct cost and indirect cost. The following equations are employed for the economic assessment (Ebrahimi & Ziabasharhagh, 2017); (Sameti & Haghighat, 2019):

$$C_{Cap} = \sum(C_k^{Com}) + \sum(C_k^{Con}) + \sum\left(C_k^{Pump}\right) + \sum_k(C_k^{HX}) + \sum(C_k^{TB}) + \sum_k(C_k^{FD}) + \sum_k(C_k^{Tower}) + \sum_k \sum_m(C_m^{PV}) + \left(C_m^{Batery}\right) + (C_m^{Inverter}) + \left(C_m^{Diesel}\right) + \sum_k \sum_m\left(C_m^{Onsite\ price}\right) + \sum_k \sum_m\left(C_m^{Offsite\ price}\right) + \sum_k \sum_m\left(C_m^{Indirect\ price}\right) + \sum_k \sum_m\left(C_m^{Other\ outlys}\right) \tag{5.51}$$

$$\sum_k \sum_m\left(C_m^{Onsite\ price}\right) = \sum_k\left(C_m^{\text{Purchased equipment installation}}\right) + \sum_k\left(C_m^{\text{Piping}}\right) + \sum_k\left(C_m^{\text{Instrumentation and control}}\right) + \sum_k\left(C_m^{\text{Electrical equipment and material}}\right) \tag{5.52}$$

$$\sum_k \sum_m\left(C_m^{Offsite\ price}\right) = \sum_k\left(C_m^{\text{Engineering and supervision}}\right) + \sum_k\left(C_m^{\text{Construction cost}}\right) + \sum_k\left(C_m^{\text{Icontingencies}}\right) \tag{5.53}$$

$$\sum_k \sum_m\left(C_m^{Other\ outlys}\right) = \sum_k\left(C_m^{Working\ Capital}\right) + \sum_k\left(C_m^{\text{Sturtup}}\right) \tag{5.54}$$

$$C_{Cap} = \sum_k \sum_m \left(C_{cap}.CRF\left(i, Y_{project}\right)\right)_m + \sum_k \sum_m \left(C_{rep}.SSF\left(i, Y_{project}\right)\right)_m + \sum_k \sum_m(C_{amain})_m + \sum_k \sum_m\left(C_{aope}\right)_m \tag{5.55}$$

Considered input prices and calculated data corresponding to the economic analysis are available in Table 5.4.

Table 5.2. Parameters used for the calculation of variables in the economic analysis (Ebrahimi & Ziabasharhagh, 2017); (Afrouzy & Taghavi, 2021)

Definition	Parameter
Annualized Cost of System	$ACS=C_{acap}$ (*Components*) + C_{arep} (*Components*) + C_{amain} (*Components*) + C_{aope} (*Labor Cost+ Fuel Cost + Insurance Cost*)
Annualized Capital Cost	C_{cap}= *1.1 of Total capital cost* $C_{acap} = C_{cap}.CRF(i,Y_p)= C_{cap}.\frac{i.(1+i)^{Yp}}{(1+i)^{Yp}-1}$
Annualized Replacement Cost	$Crap= C_{cap}(Base).\ (1+i)^{Yp}$ $Carep = C_{rap}.SFF(I,\ Y_p)= C_{rap}.\ \frac{j}{(1+i)^{Yp}-1}$
Annualized Maintenance Cost	*For* Y_p*=20 ,* C_{amain}*=0.05 of Capital Cost*
Annualized Operating Cost Operating Flow Cost	OFC= (*Labor cost+ Coking coal cost + Insurance cost*) *Number of labor = 50 , Labor cost =400 US$/Month* *Coke oven gas cost= 105 (US$/ton*) *Insurance cost=0.02 of Capital Cost*
Net Present Value	$NPV= ACS/ CRF(i,Y_p)$
C1= Cost of Total produced LNG (US$ per Year) NEW ACS = ACS-C1	*LNG cost= 7 US$/Million Btu*
Levelized cost of Product Total Product in one Year	*LCOP= New ACS/ Total Product in one Year* (Kg Methanol)
Prime Cost	*VOP= Volume of Product , PC=OFC/VOP*
Summary Of Product Cost	*COP= Cost Of Product, SOPC= VOP. COP*
Annual Benefit	*AB= SOPC*- OFC
Net Annual Benefit	*NAB= AB.*(*1-Tax percent*) *, Tax=0.1*(*AB*)
Period Of Return	$POR= C_{cap}/NAB$
Rate Of Return	$ROR= NAB/ C_{cap}$
Additive Value	*AV=COP-PC*

Table 5.3. Purchased equipment cost functions used in the economic analysis (Ebrahimi & Ziabasharhagh, 2017); (Afrouzy & Taghavi, 2021)

Component	Purchased equipment cost functions
Compressor	$C_{Com} = \left(\frac{39.5 \times \dot{m}}{\eta_C}\right)\left(\frac{p_{discharge}}{p_{suction}}\right) ln\left(\frac{p_{discharge}}{p_{suction}}\right)$ C_{Com} = Cost of compressor (k$)
Photovoltaic	C_{PV}=840 $/m^2 (PV array cost) $C_{Batery\ cost}$ =220 $/kWh $C_{Inverter\ cost}$ =750 $/kWh $C_{Diesel\ genset\ cost}$ =550 $/kWh
Heat exchanger	$C_E = a(V)^b + c$ C_E = Cost of heat exchanger ($)
Condenser	$C_C = 516.6 \times A_{Condenser} + 268.45$
Pump	$C_P = f_M f_T C_b$ C_P = Cost of Pump ($) $C_b = 1.39exp[8.833-0.6019(lnQ(H)^{0.5})+0.0519(lnQ(H)^{0.5})^2]$, Q in gpm, H in ft head f_M = Material Factor $f_T = exp[b_1+b_2(lnQ(H)^{0.5})+b_3(lnQ(H)^{0.5})^2]$ b_1 = 5.1029, b_2 = -1.2217, b_3= 0.0771
General heat exchanger	$C_{HX} = 8500 + 409 \times A_{HX}^{0.85}$
Flash Drum	$C_D = f_m C_b + C_a$ C_D = Cost of drum ($) $C_b = 1.218exp[9.1-0.2889(lnW)+0.04576(lnW)^2]$, 5000<W<226000 lb shell weight $C_a = 300D^{0.7396} L^{0.7066}$, 6<D<10, 12<L<20 ft f_m = Material Factor

Table 5. 3. Purchased equipment cost functions used in the economic analysis (continued)

Component	Purchased equipment cost functions
Column	$C_b=1.128exp(6.629+0.1826\ (logW)+0.02297*(logW)^2)$ $Cp1= 300\ (D^{0.7395})\ (L^{0.7068})$ $C_1=1.218\ [(1.7C_b+23.9V1+Cp1)\ ]$ C_2=Cost of installed manholes, trays and nozzles C_3= Cost of condenser C_4= Cost of reboiler $C_{Ab} = C_1+C_2+C_3+C_4$ C_{Ab}= Cost of Drum ($)
Cooler	$C_C =1.218k(1+fd+fp)Q^{0.86}$, $20<Q<200$ M BTU/hr C_C= Cost of cooler ($) f_m=Design Type f_P=Design Pressure (psi) $a=0.4692, b=0.1203, c=0.0931$

Table 5.4. Considered input prices and calculated data

Parameter	*Value*
Coke oven gas cost (MMUS$/Year)	8.026
Prime cost of product (US$/kg methanol)	0.3967
Net annual benefit (MMUS$/Year)	15.19
Annualized operating cost (MMUS$/Year)	16.09
Annualized cost of system (MMUS$/Year)	20.30
Net present value (MMUS$/Year)	314.6
Period of return (Year)	4.29
Rate of return (%)	23.29
Insurance cost (MMUS$/Year)	1.305
Levelized cost of product (US$/kg methanol)	0.0877

5.4 Results and discussion

Partial validation is chosen for the validation of each subsystem used in the presented article. For the liquefaction process of coke oven gas (LPCOG) validation, modeling results are compared to outcomes from the reference (Lin et al., 2014). Based on Figure 5.4, compared values of unit power consumption, hydrogen and methane contents of the products, and the ratio of the flowrate of LNG to COG show acceptable accordance. The PCCP process for the CO_2 absorption is validated with reference (Shirmohammadi et al., 2020), and the results are available in Figure 5.5. Except for the heat consumption rate of the cycle that shows a decrease of 0.863 MJ/kgCO_2 in this study (thanks to the thermal integration) other compared variables nearly matched. As shown in Figure 5.6, all parameters studied for validating the methanol production cycle are suitably in accordance with that of referenced paper (Hosseini et al., 2019). Reducing the area between hot and cold diagrams decreases heat exchangers' consumed power and exergy destruction. This is done by applying pinch analysis on two multi-stream heat exchangers of HX17 and HX18 in the LPCOG process. Figure 5.7 shows the cold and hot composite (CC) curves for these heat exchangers.

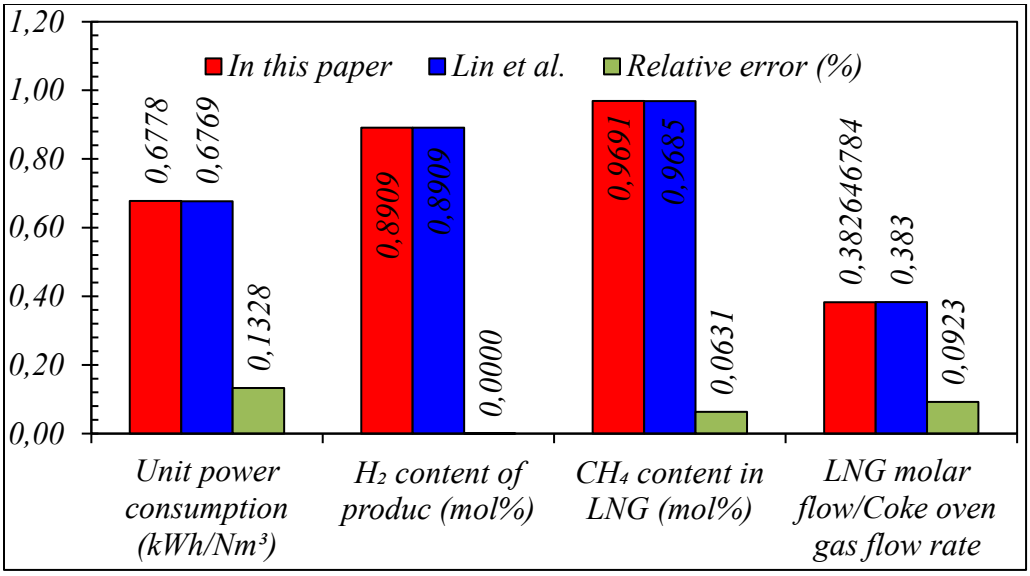

Figure 5.4. Validation results of the liquefaction process of coke oven gas

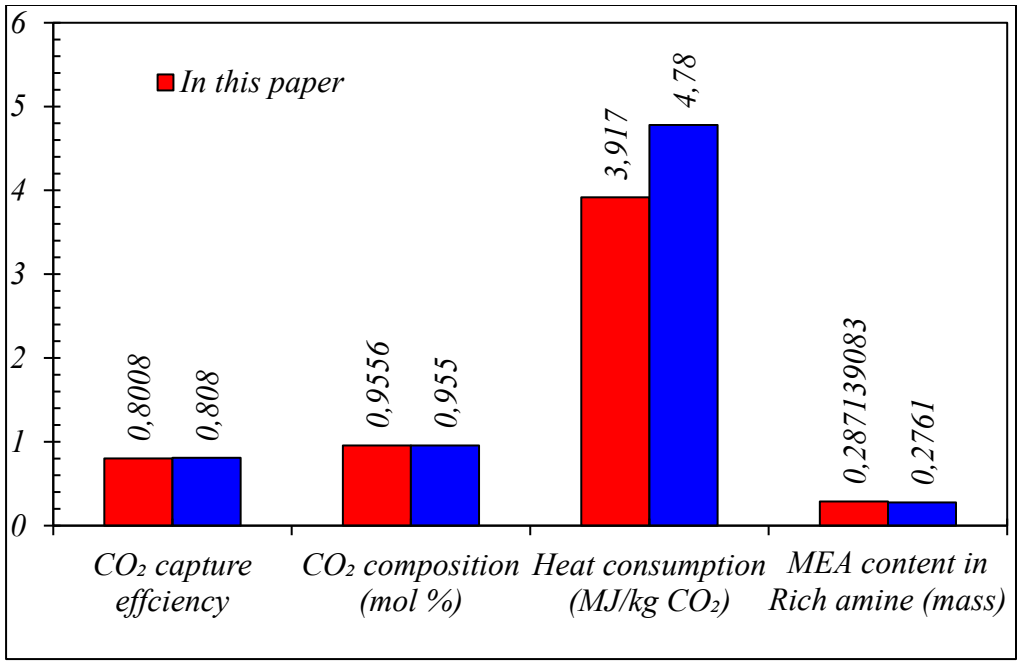

Figure 5.5. Validation results of the the CO_2 absorption process

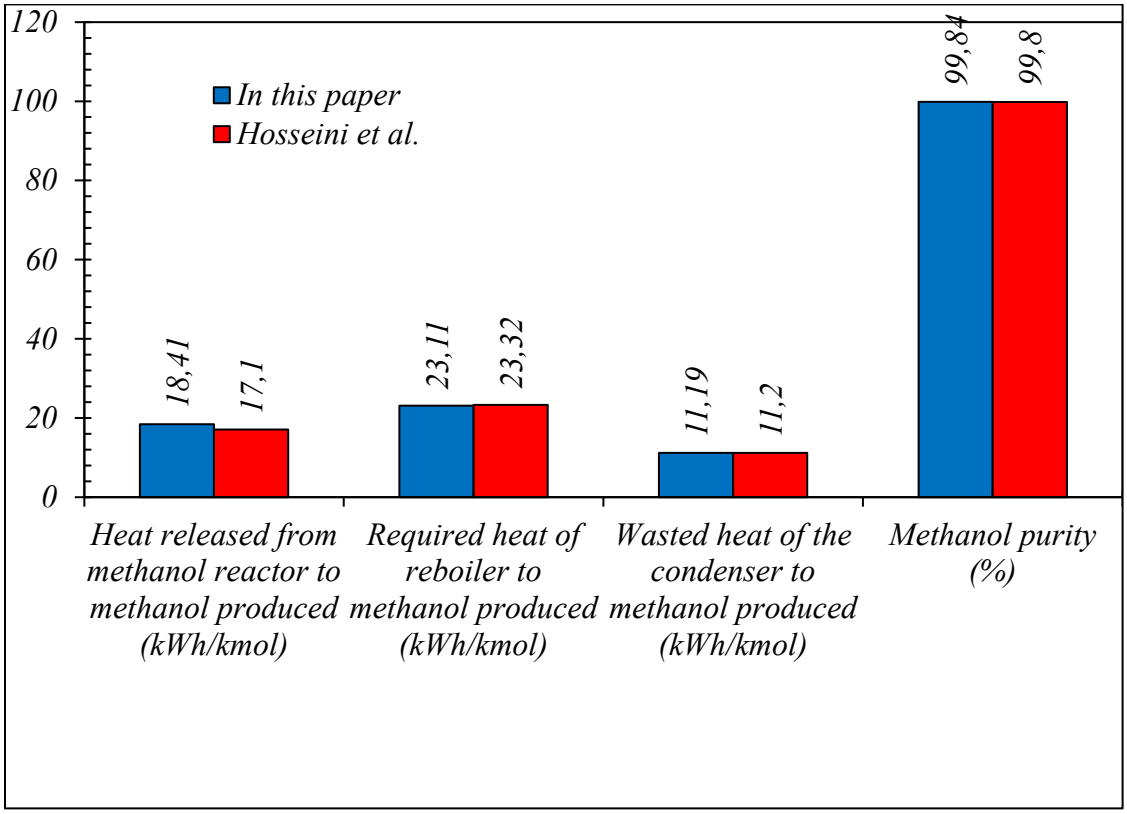

Figure 5.6. Validation results of the methanol production process

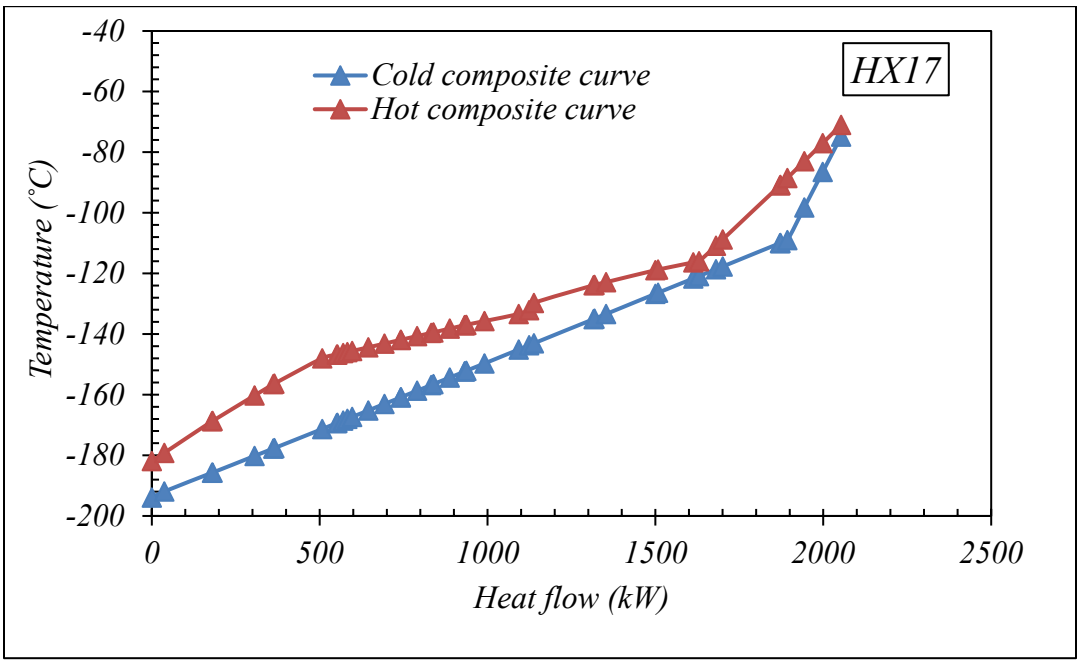

(a) Heat exchanger HX17

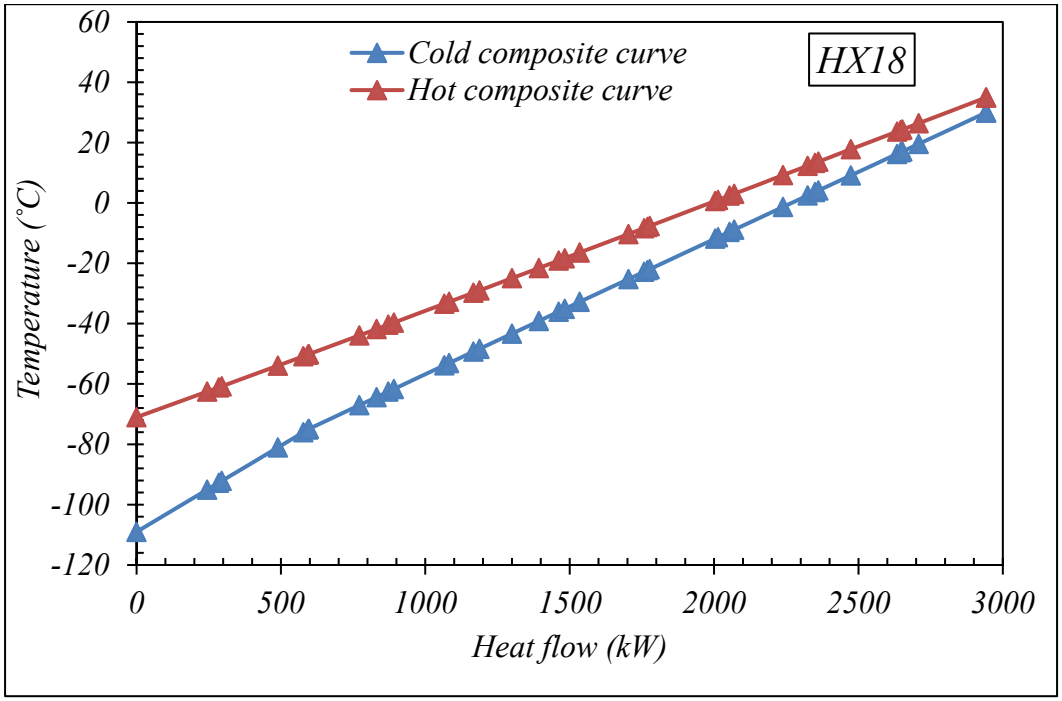

(b) Heat exchanger HX18

Figure 5.7. Hot and cold composite curves for multi-stream heat exchangers

To evaluate the performance of the whole process, each subsystem, as well as streams and equipment implemented in the development of the introduced integrated structure energy, exergy, sensitivity, and economic analyses are done. PV panels help turbines, powered by the recovered heat, supply the required electricity for the whole process. Analyses results are presented and discussed as follows. Calculated exergies, including inlet and outlet exergies, exergy destructions, and exergy efficiencies of the equipment used in the designed process are presented in Table 5.5. The amount and share of each group of equipment in the total exergy destruction are provided in Figures 5.8 and 5.9, respectively. In the heat exchanger network design, the share of each heat exchanger in the total amount of exergy destructed by this network is shown in Figure 5.10. From exergy analysis, it can be noticed that PV panels with 46570.1 kW, equal to 81.34% of the total exergy destruction (57257.0 kW), take the lion's share, followed by the heat exchangers network by 3245 kW. Among heat exchangers, HX12 and HX18, by 713.5 kW and 628.3 kW of exergy destruction showed the maximum shares of 22.31% and 19.38%, respectively.

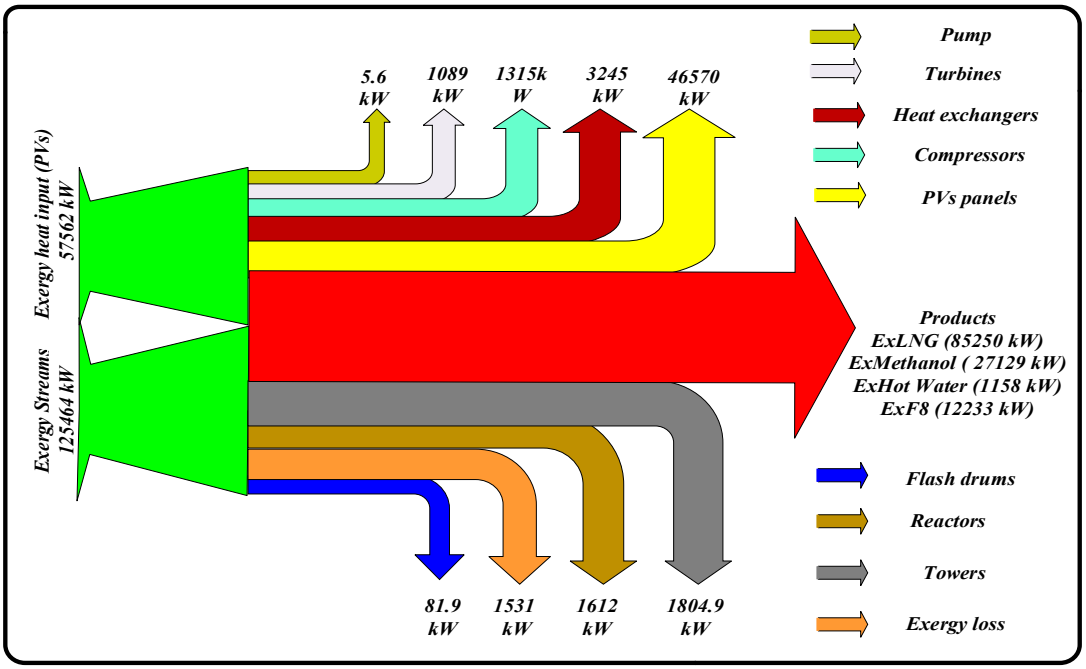

Figure 5.8. Input and output exergy streams of the designed process

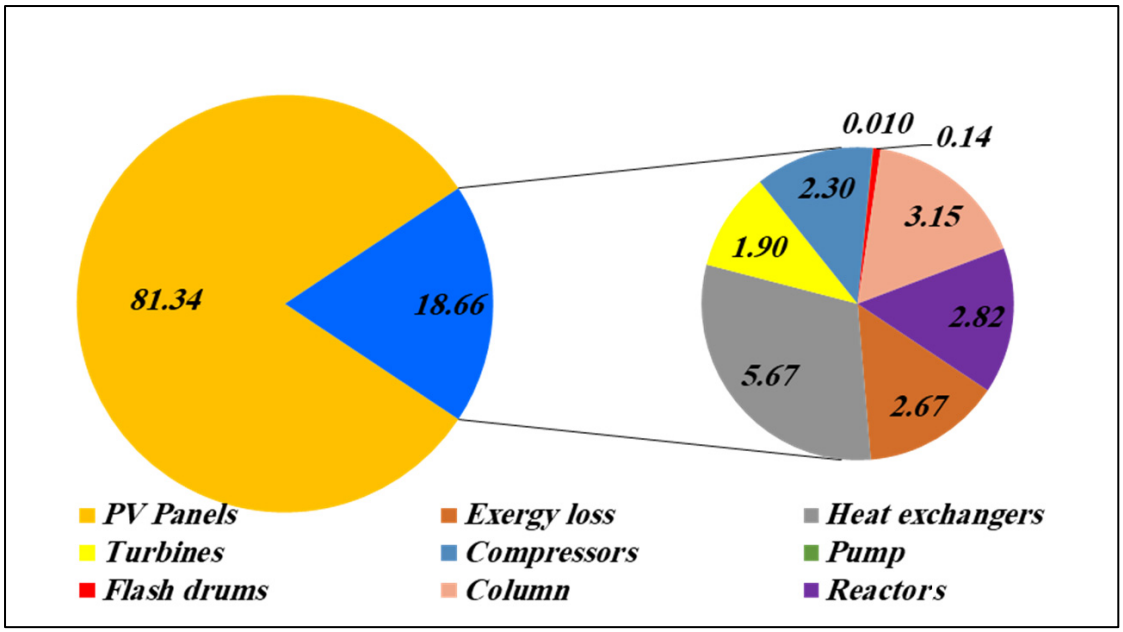

Figure 5.9. Exergy destruction shares of each group of equipment

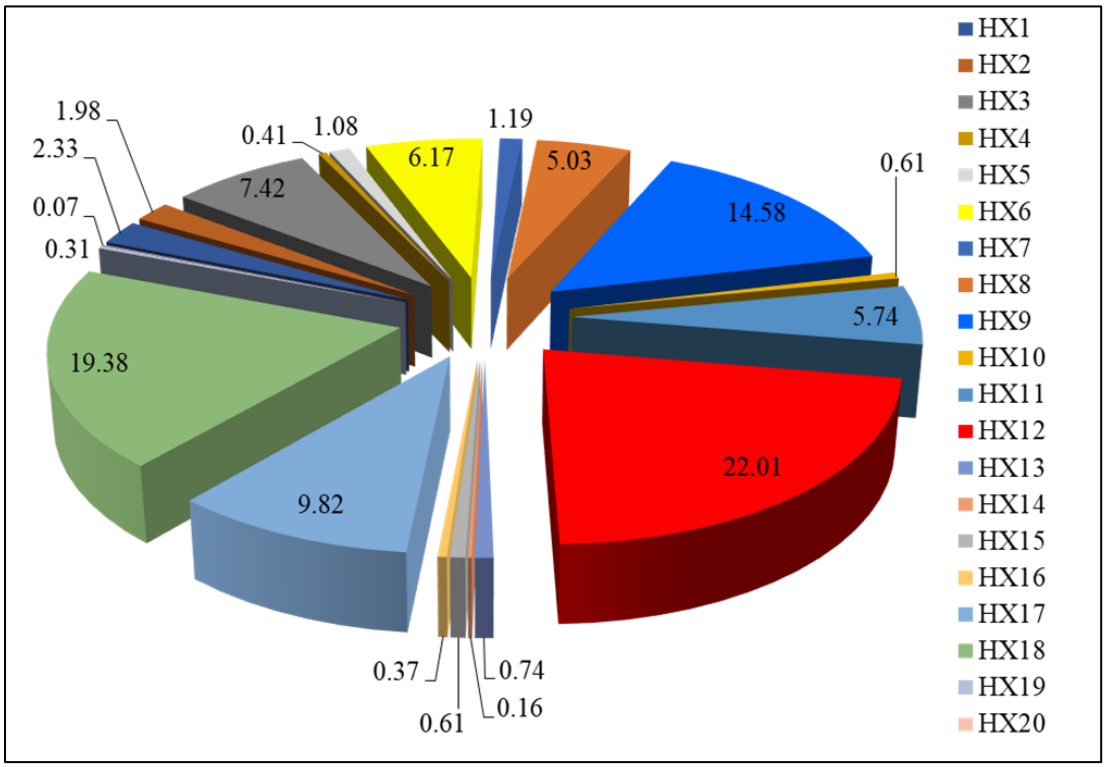

Figure 5.10. Exergy destruction shares among heat exchangers

Table 5.5. Input exergy, output exergy, and destroyed exergy (in kW), and exergy efficiency of each equipment of the integrated structure

Equipment	Inlet exergy	Outlet exergy	Exergy destruction	Exergy efficiency
HX1	275132.9	275057.4	75.5	0.8195
HX2	544831.7	544767.6	64.1	0.9666
HX3	551014.9	550774.5	240.4	0.9373
HX4	162290.9	162277.4	13.4	0.9882
HX5	67585.1	67550.0	35.1	0.8593
HX6	492156.2	491956.2	200.0	0.9469
HX7	27989.7	27951.1	38.6	0.9030
HX8	405754.4	405591.3	163.1	0.9107
HX9	318729.7	318257.2	472.6	0.5511
HX10	2401836.4	2401816.5	19.8	0.9836
HX11	2400625.4	2400439.5	186.0	0.9013
HX12	2428693.3	2427979.8	713.5	0.9412
HX13	361822.8	361798.8	24.0	0.9933
HX14	359662.4	359657.2	5.2	0.9987
HX15	229883.7	229864.0	19.7	0.9905
HX16	303042.5	303030.5	12.0	0.9941
HX17	174310.5	173992.1	318.4	0.8918
HX18	176384.6	175756.3	628.3	0.6939
HX19	4712.1	4702.1	10.0	0.9581
HX20	155928.6	155926.3	2.3	0.9942
TB1	5949.0	5392.2	556.8	0.6371
TB2	4940.8	4407.6	533.2	0.5145
C1	750.5	729.8	20.7	0.7654
C2	125877.3	125699.3	178.0	0.9140
C3	127136.3	126960.7	175.6	0.9131
C4	4396.3	4061.3	335.0	0.9090

Table 5.5. Input exergy, output exergy, and destroyed exergy (in kW), and exergy efficiency of each equipment of the integrated structure (continued)

Equipment	Inlet exergy	Outlet exergy	Exergy destruction	Exergy efficiency
C4	4396.3	4061.3	335.0	0.9090
C5	6902.9	6566.9	336.1	0.9106
C6	42791.9	42679.6	112.3	0.9067
C7	43652.7	43539.3	113.4	0.9098
C8	41131.9	41087.2	44.6	0.8811
P1	275167.2	275161.6	5.6	0.5718
FD1	904.1	814.2	34.5	0.9006
FD2	39752.0	39704.6	47.4	0.9988
T1	10903.1	6920.0	188.6	0.6347
T2	275899.2	275154.0	127.1	0.9973
T3	546302.4	545735.8	566.7	0.9990
T4	126971.9	126805.4	166.5	0.9987
T5	28837.8	28081.8	756.0	0.9738
Reactors	43441.3	41829.3	1612.0	0.9629
PV Panels	57561.6	10991.5	46570.1	0.1910
Cycle	183030.0	125770.0	57257.0	0.6872

The characteristics of the PV system designed in this study are available in Table 5.6, which includes 960 strings of 24 modules in series, 23040 in total, and nine units of inverters with 1438 kWac each. The design of the Photovoltaic panels system is validated with reference (Afrouzy & Taghavi, 2021) available in Table 5.7. Monthly average values of horizontal diffuse irradiation (DiffHor), global horizontal irradiation (GlobHor), Global incident in collector plane (GlobInc), and ambient temperature (Amb T) are demonstrated in Figure 5.11. July, followed by June, have the maximum ambient temperatures. Global horizontal irradiation also has its maximum values in these months (245.4 and 248.1 kWh/m^2 in July

and June, respectively). However, horizontal diffuse irradiation varies from a minimum of 21.88 kWh/m^2 in December to a pick of 66.28 kWh/m^2 in May. Except for February with 179.5 kWh/m^2, the value of GlobInc has a smooth variation between 200 to 230 kWh/m^2 all year round. Figure 5.12 illustrates the monthly hourly average and hourly maximum values for energy injected into the grid (HMEI) in the designed photovoltaic system, and having their maximum value at 11 a.m. Besides, 64 percent of solar energy is injected into the grid from 9 a.m. to 1 p.m. July and November have minimum and maximum average hourly solar irradiations, respectively. The average monthly efficiencies, including the array efficiency, total system efficiency, and inverter efficiency, are provided in Figure 5.13. Based on this figure, it can be deduced that the increase in the ambient temperature has a negative effect on the array and system efficiencies; however, inverter efficiency remains almost unchanged during the year by 98.6%. Array and system have their maximum averaged efficiencies in January by 19.59% and 19.30%, and their minimum in July by 17.65 and 17.40, respectively. The system's performance ratio (PR) ranges from its minimum in July by 81.3% to its maximum value of 90.2% in January. Monthly averaged power losses are presented in Figure 5.14. It can be deduced that nearly 44 % of the losses belong to the mismatch losses, followed by investors by almost 30 percent. The minimum share belongs to ohmic losses. All types of losses show the same trend in changing their values throughout the year.

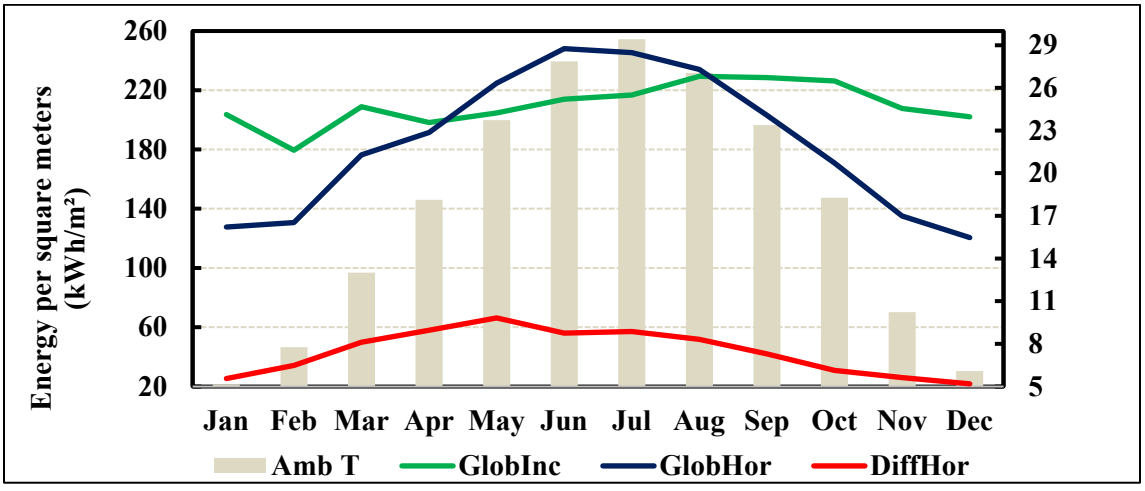

Figure 5.11. Monthly averaged temperature (Amb T), global indecent in coll. Plane (GlobInc), global horizontal irradiation (GlobHor), and Horizontal diffuse irradiation (DiffHor) in the designed photovoltaic system

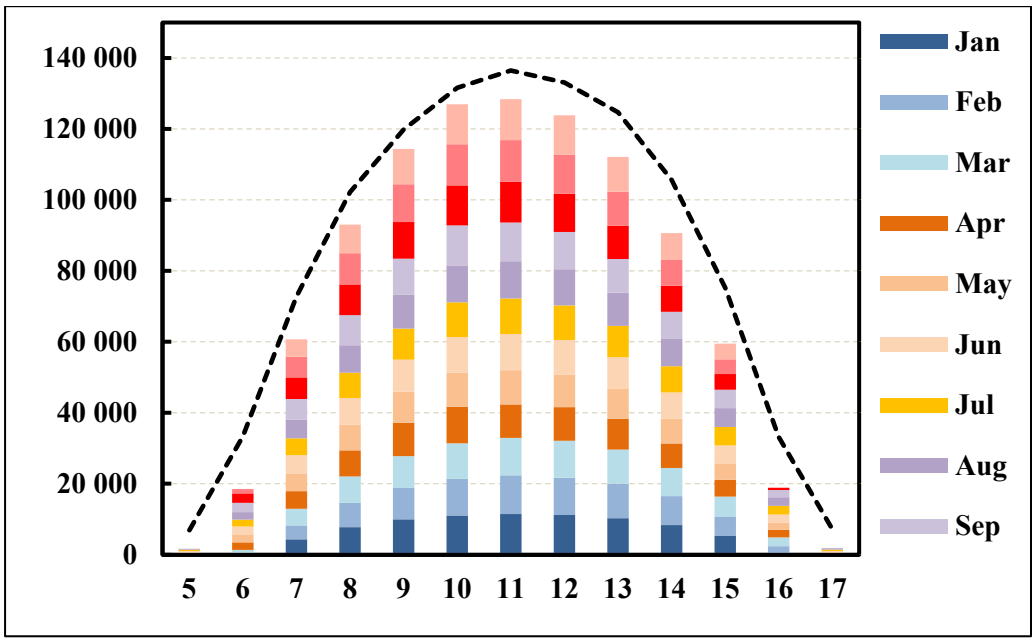

Figure 5.12. Monthly hourly average and hourly maximum values for energy injected into grid of the photovoltaic system (kWh)

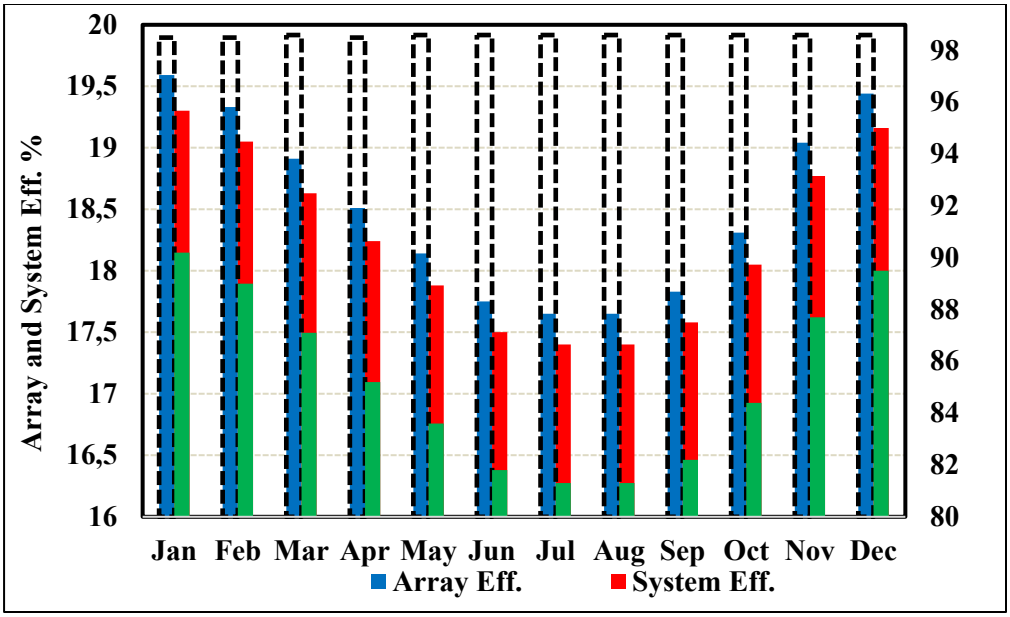

Figure 5.13. Monthly average values of Performance ratio, and efficiencies of array, system, and inventor in the PV system

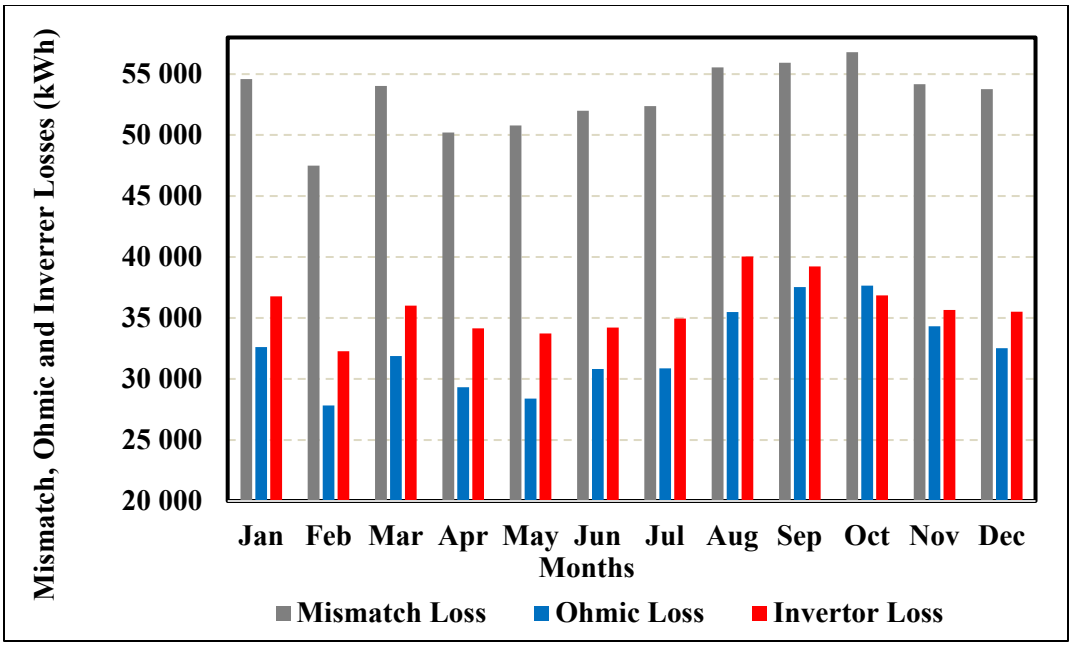

Figure 5.14. Monthly average values of mismatch, ohmic, and inventor loses

5.4.1 Sensitivity analysis

One of the most essential and most straightforward processes optimization methods is adjusting the operating conditions of different parts called operational optimization. One of the tasks that can be done to help improve optimization results is to analyze the sensitivity of essential system indicators to some critical and practical operational variables such as pressure, flow rate, and the percentage of flow components. In this study, the amount of hydrogen content in coke oven gas, inlet pressure of flue gas flow to the absorber distillation tower, COG flow rate, and maximum pressure in compression refrigeration cycle have been investigated as sensitivity analysis variables to assess their influence on the performance of the designed process. This method can be used as a practical basis for further optimizing the energy system.

5.4.1.1 Effect of the hydrogen content in coke oven gas

Figures 5.15 a,b,c,d demonstrate the effect of changing the hydrogen content in the coke oven gas on the various parameters in the integrated structure. Based on the results,

increasing the coke oven gas's hydrogen content increases the energy required to separate hydrogen from the coke oven gas. Thus, the power consumption increases, and the amount of methane leaving the distillation tower decreases. The results also showed that increasing the hydrogen flow rate to the methanol production cycle increases the amount of methanol produced and the heat dissipation in this cycle. Dissipated heat is utilized to produce more hot water. Therefore, the exergy growth of the products decreases with increasing the exergy content of the input flows. As a result, by increasing the amount of hydrogen entering the methanol production cycle from 45% mol to 85% mol, the total structure energy efficiency, LPCOG cycle exergy efficiency, and hybrid cycle exergy efficiency are reduced up to 61.92%, 56.62%, And 64.99%, respectively. There is also a contrast between the increase in power consumption in the LPCOG cycle and the decrease in the rate of methane. In this regard, the power consumption growth rate in the LPCOG cycle is greater than the rate of decline in produced methane. Therefore, by increasing the amount of hydrogen content in the inlet gas from 54 mol% to 85 mol%, the system's energy consumption for hydrogen separation and liquefaction increases to 59586 kWh/Nm^3. The results also showed that with increasing methanol production or decreasing LNG production rates, the return-on-investment time increases, and the product's prime cost declines, respectively.

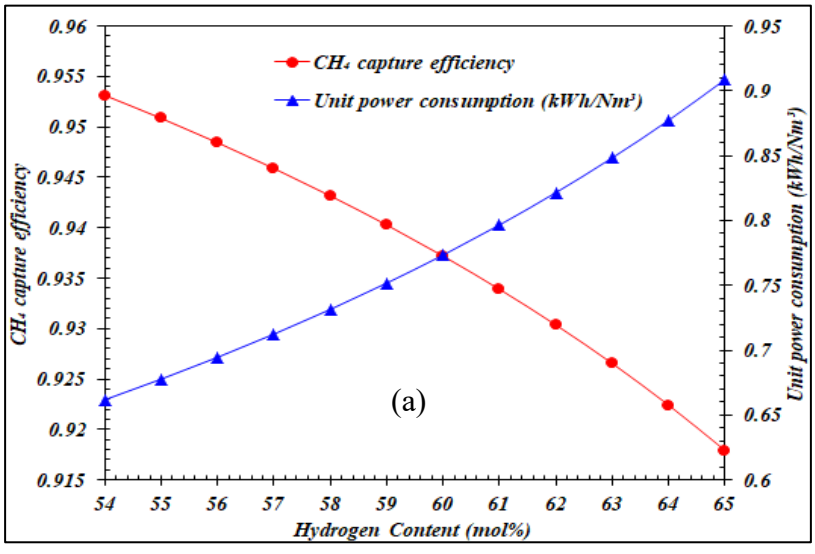

(a) The effect of changing the hydrogen content in COG

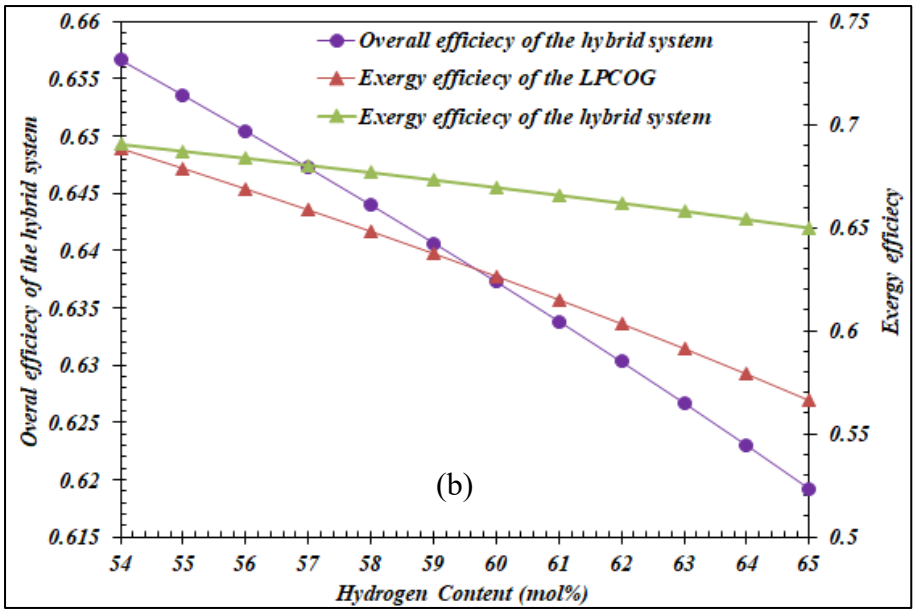

(b) The effect of changing the hydrogen content in COG

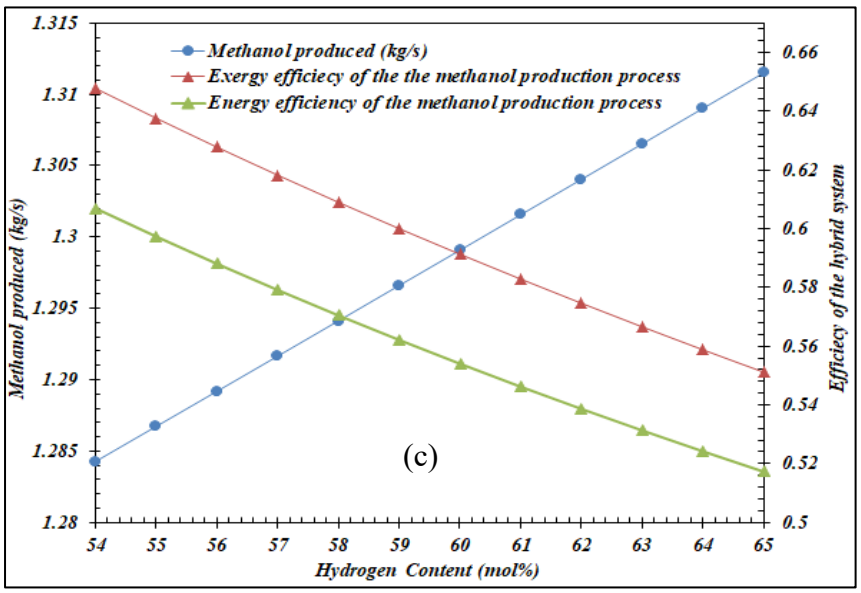

(c) The effect of changing the hydrogen content in COG

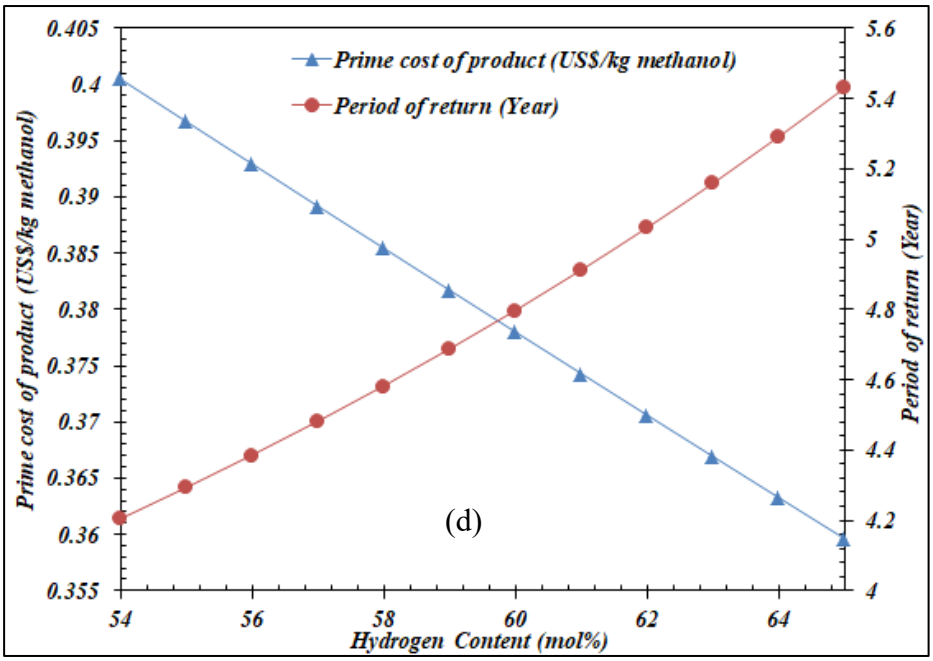

Figure 5.15. (a-d) The effect of changing the hydrogen content in the coke oven gas on the various parameters in the integrated structure

5.4.1.2 Effect of the inlet flow pressure of the flue gas to the absorber tower

Figures 5.16 a,b,c,d illustrates the influence of changes in the inlet flue gas pressure to the absorber tower in the CO_2 separation unit cycle. The amount of carbon dioxide output decreases by increasing the inlet flue gas flow pressure to the absorber tower in the carbon dioxide separation cycle. As a result, the efficiency of carbon dioxide emissions is reduced. The results show that by increasing the flow pressure of the inlet flow to the absorber tower from 0.9 bar to 1.1 bar, the specific heat consumption and net power consumption increase to 3.9665 MJ/kgCO_2 and 13336 kW, respectively. As the amount of carbon dioxide flow rate entering the methanol production cycle decreases, the methanol production rate decreases, and the levelized cost of product increases. Considering the LNG production rate remained constant, by reducing the production rate of methanol, the net price, the total system thermal efficiency, and rate of return (ROR) in the hybrid structure decreases.

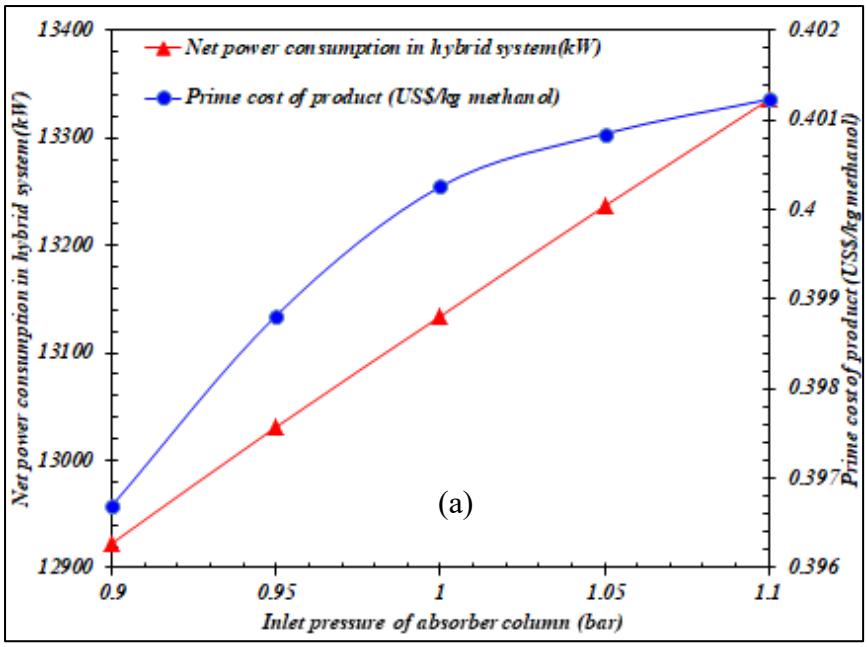

(a) The influence of changes in the inlet flue gas pressure

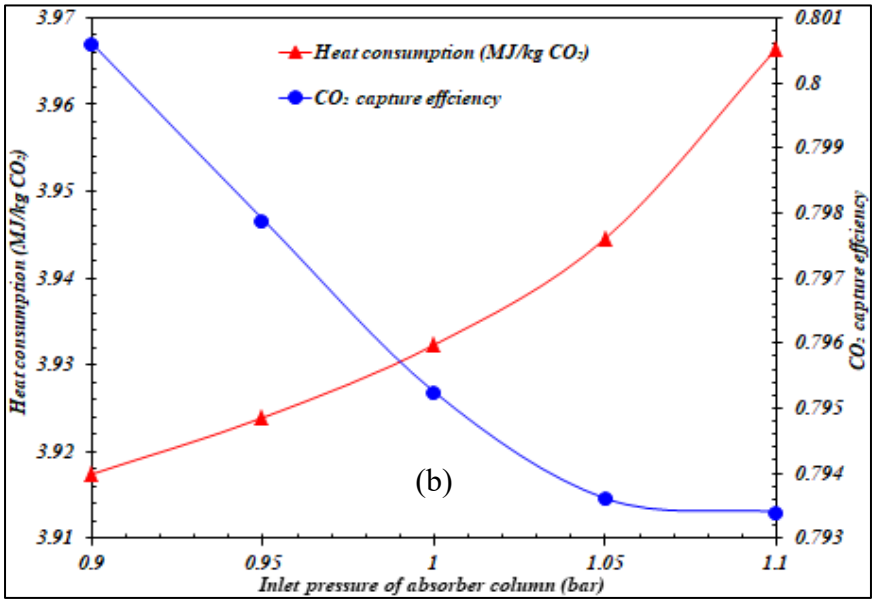

(b) The influence of changes in the inlet flue gas pressure

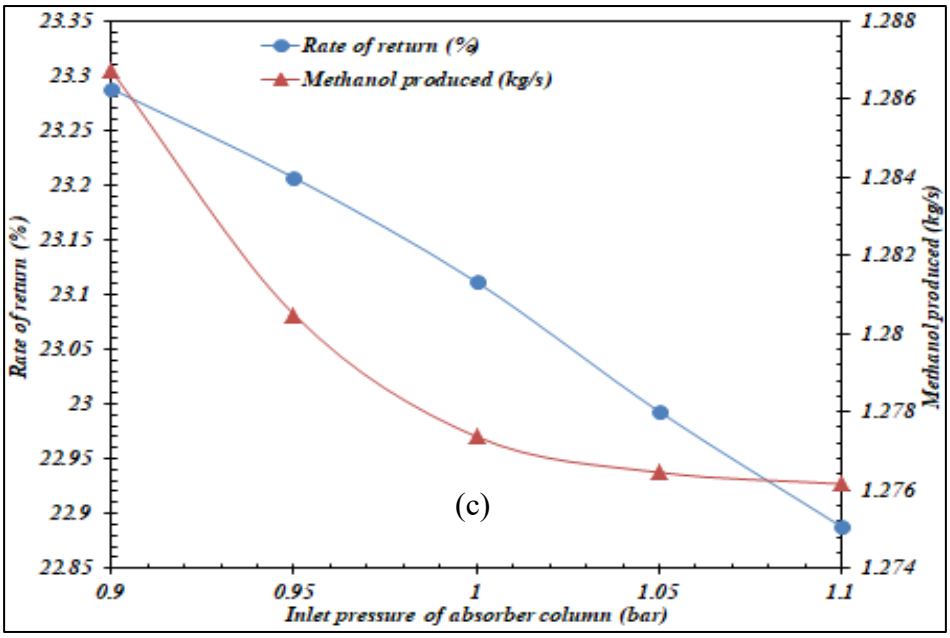

(c) The influence of changes in the inlet flue gas pressure

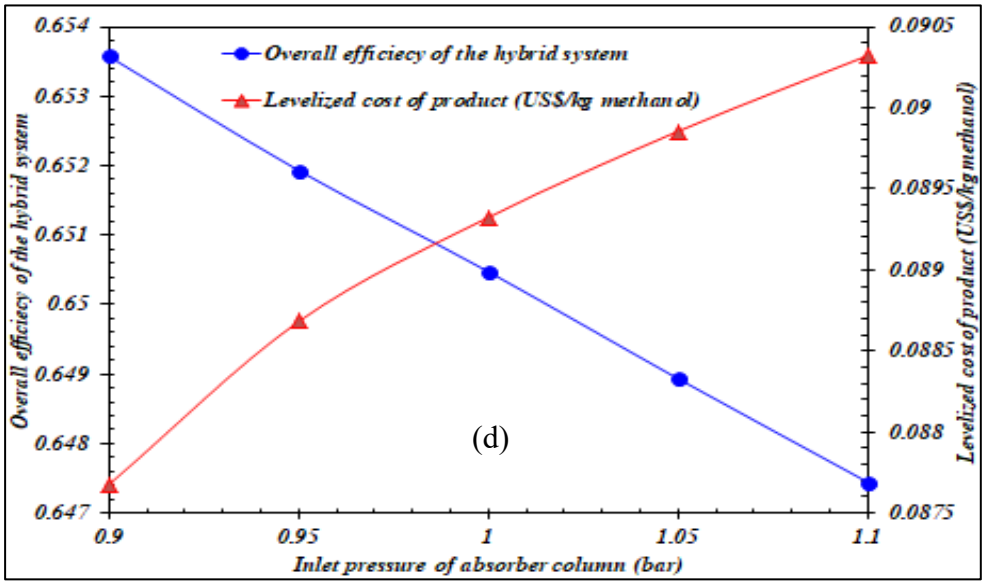

Figure 5.16. (a-d) The influence of changes in the inlet flue gas pressure to the absorber tower in the CO_2 separation unit cycle

5.4.1.3 Effect of COG flow rate

Figures 5.17 a,b,c,d show the effect of changing the COG flow rate in the integrated structure on the main output parameters. As the mass flow rate of coke oven gas increases, the power consumption required by the LPCOG cycle increases. The interaction between increasing the amount of methanol and LNG produced and increasing the power consumption of the integrated structure has led to a decrease in power consumption and increased thermal efficiency of the entire integrated structure. As the rate of coke oven gas increases from 901.6 kmol/h to 991.6 kmol/h, the cost of the product, system irreversibility, and rate of return increase to 0.4022 US$/kg methanol, 58195 kW, and 23.62%, respectively. Also, the exergy efficiency of the methanol production cycle, the exergy efficiency of the LPCOG cycle, and the specific energy consumption of the process reduces to 62.12%, 67.82%, and 62.12%, respectively.

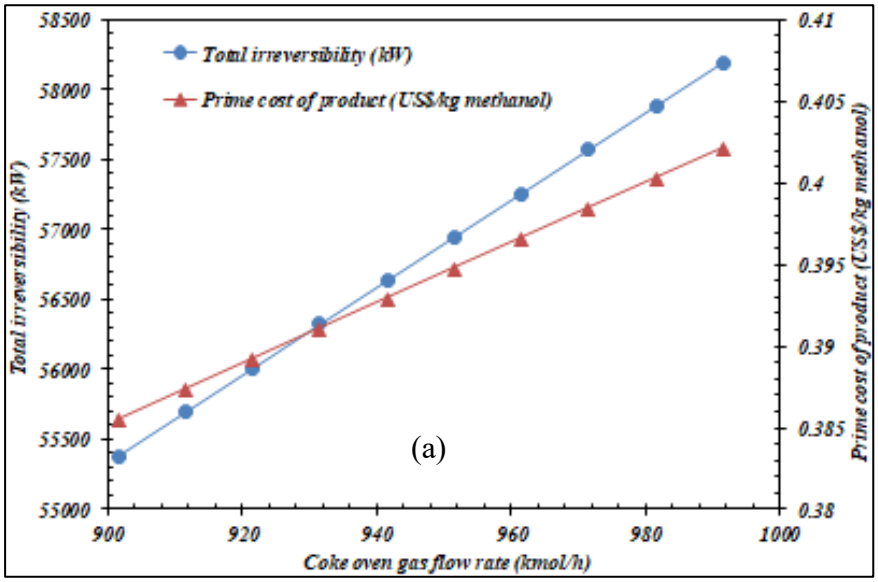

(a) The effect of changing the COG flow rate

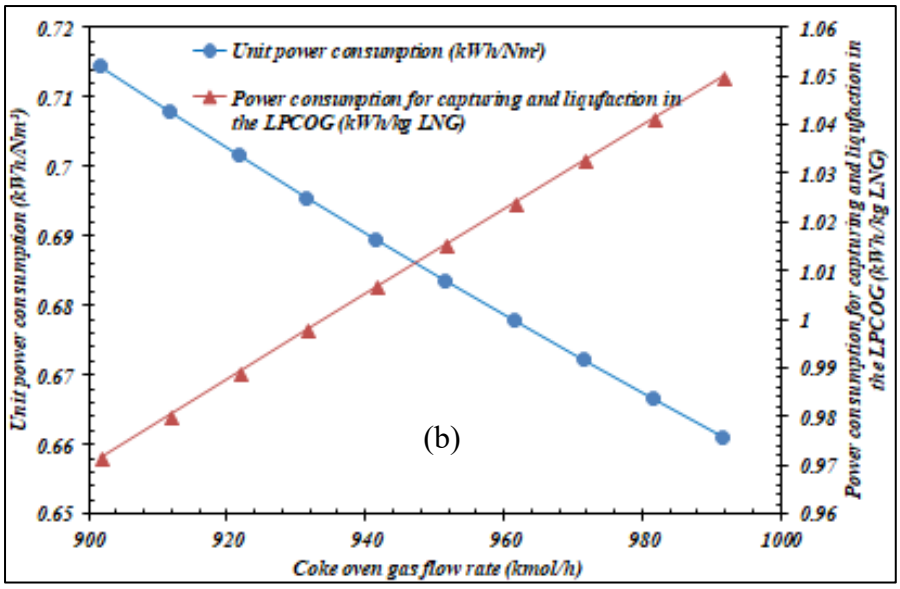

(b) The effect of changing the COG flow rate

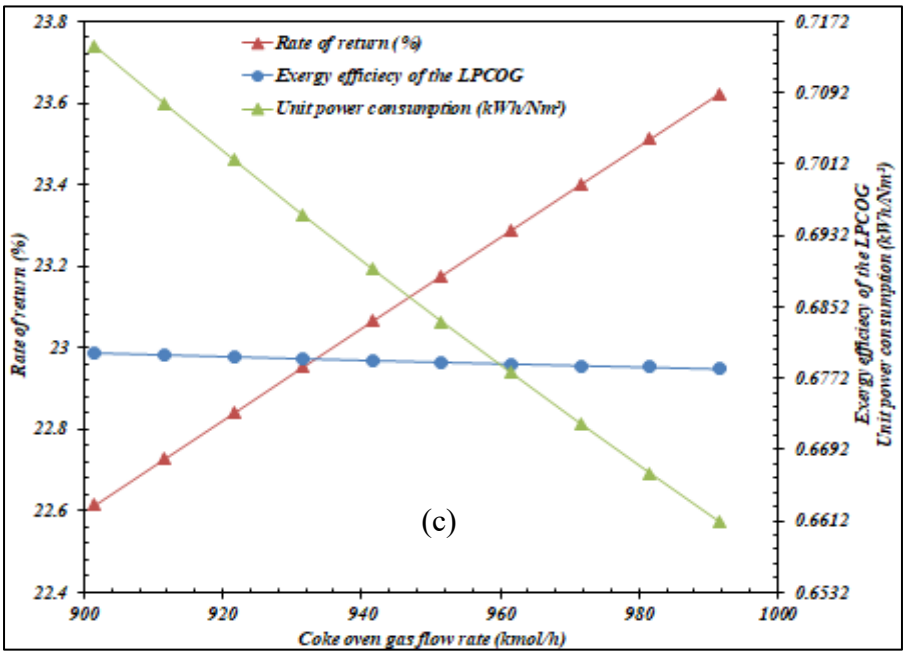

(c) The effect of changing the COG flow rate

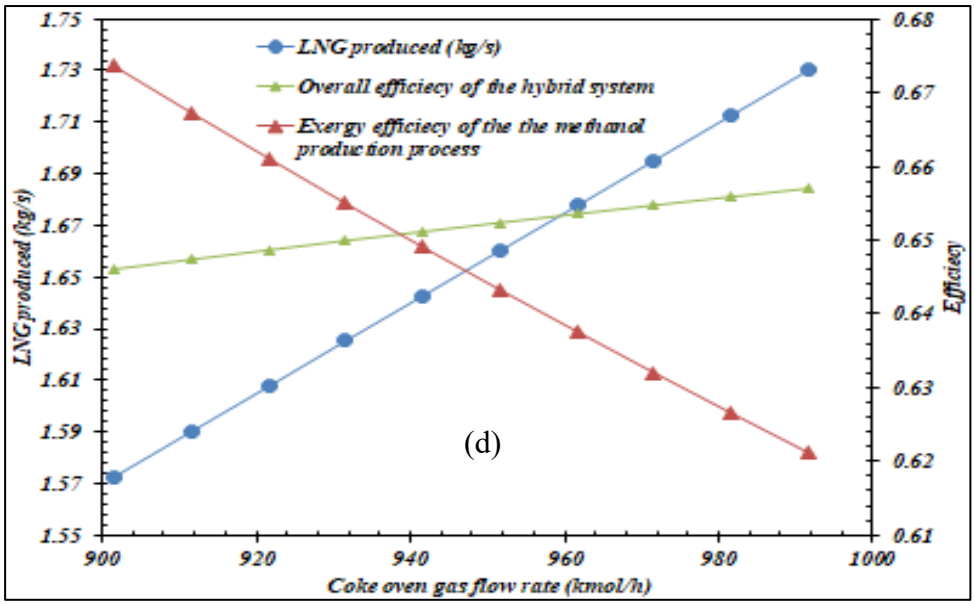

Figure 5.17. (a-d) The effect of changing the COG flow rate in the integrated structure on the main output parameters

5.4.1.4 Maximum pressure effect of the nitrogen compression refrigeration cycle

The effect of changes in maximum pressure of nitrogen compression refrigeration cycle on the main parameters of the integrated structure is shown in Figures 5.18 a,b,c,d. The results show that with increasing the maximum pressure of the nitrogen compression refrigeration cycle, the power consumption of the integrated structure and consequently the specific power consumption increase. By increasing the maximum pressure from 30 to 80 bar, the energy efficiency and exergy efficiency of the whole hybrid structure decrease to 91.27% and 64.41%, respectively. Increasing the power consumption of the developed structure leads to an increase in cycle irreversibility and levelized cost of the product. It also reduces the rate of return. The results showed that by increasing the maximum pressure of the nitrogen compression refrigeration cycle from 30 to 80 bar, the irreversible and levelized cost of the product grow to 69,651 kW and 0.09995 US$/kg methanol.

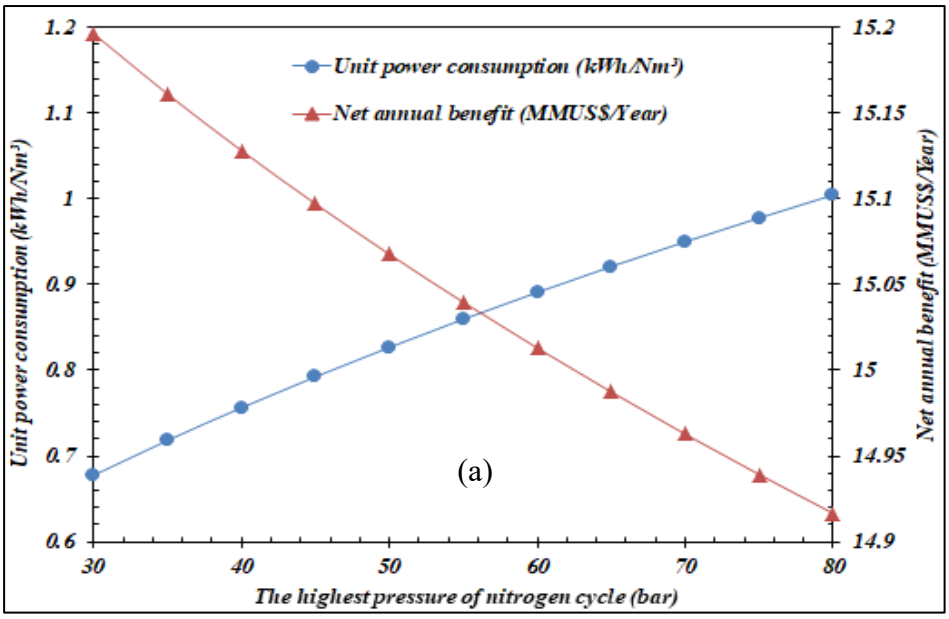

(a) The effect of changes in maximum nitrogen pressure

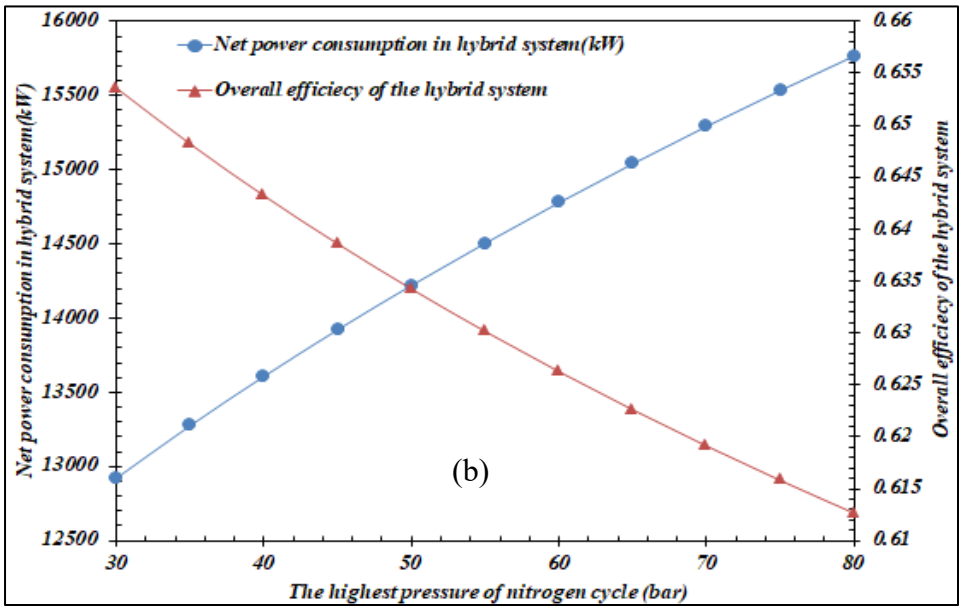

(b) The effect of changes in maximum nitrogen pressure

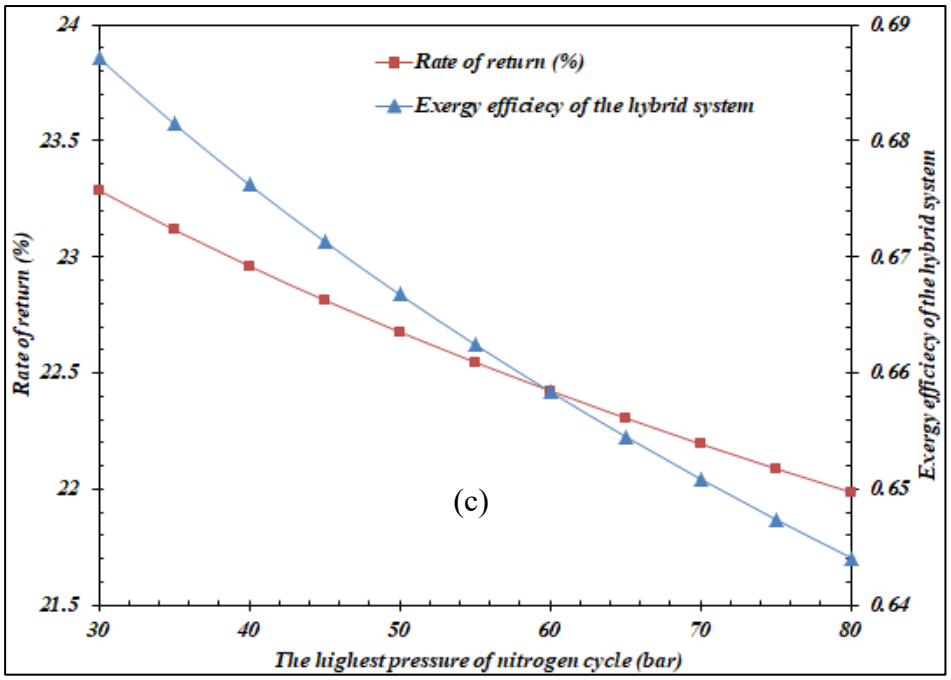

(c) The effect of changes in maximum nitrogen pressure

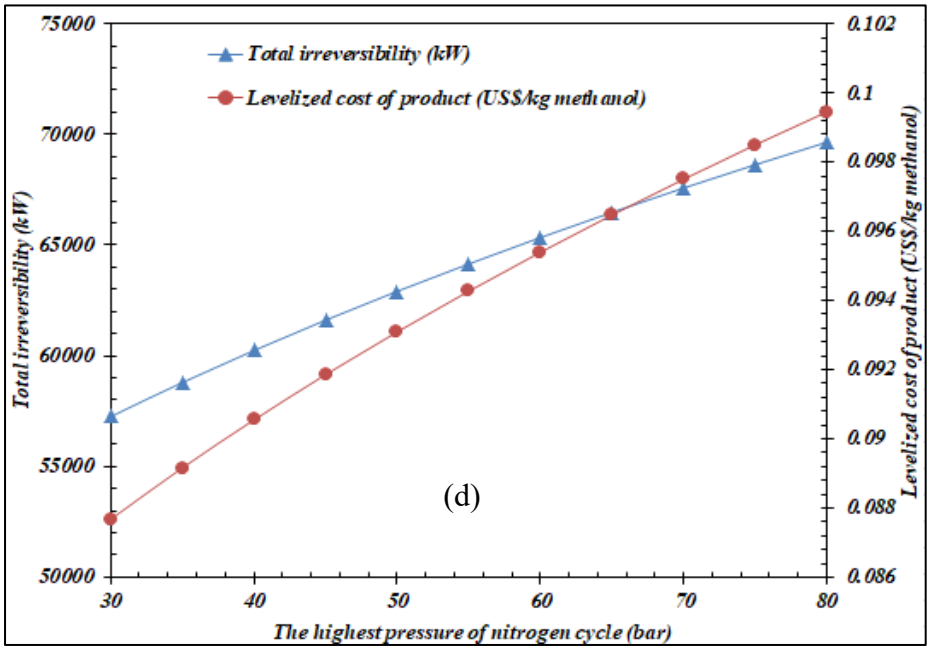

Figure 5.18. (a-d) The effect of changes in maximum pressure of nitrogen compression refrigeration cycle

5.4.1.5 Effect of feed and products prices (resulted from economic analysis)

The results showed that by increasing the price of coke oven gas from 31 US $/ton to 220 US$/ton, the payback period and the price of the product increase to 8.907 years and 0.6122 US$/kg methanol, respectively .The results show that the economic plan is justified with a return on investment of fewer than five years if the price of coke oven gas is less than 138.2 US$/ton. Also, with the increase in the price of coke oven gas, the annual operating cost increases, and the annual net profit decreases, respectively. Figures 5.19 a,b,c,d show the effect of LNG price changes from 6 to 14 US$/MillionBTU on the parameters of return on investment and annual net profit. The results show that the payback period decreases to 2.155 years by this increase, and the yearly net profit increases to 30.27 MMBTU/year. The results showed that the LNG price must be higher than 6 US$/MillionBTU for a justification of the plan for a return on investment of fewer than five years. Also, with the increase of methanol price in the market from 200 to 700 US$/ton, the return on investment will decrease to 2.495 years, and the annual net profit will increase to 26.125 MMUS$/year. In order to justify the current integrated structure for a return on investment of fewer than five years, the marketable selling price of methanol must be more than 330 US$/ton.

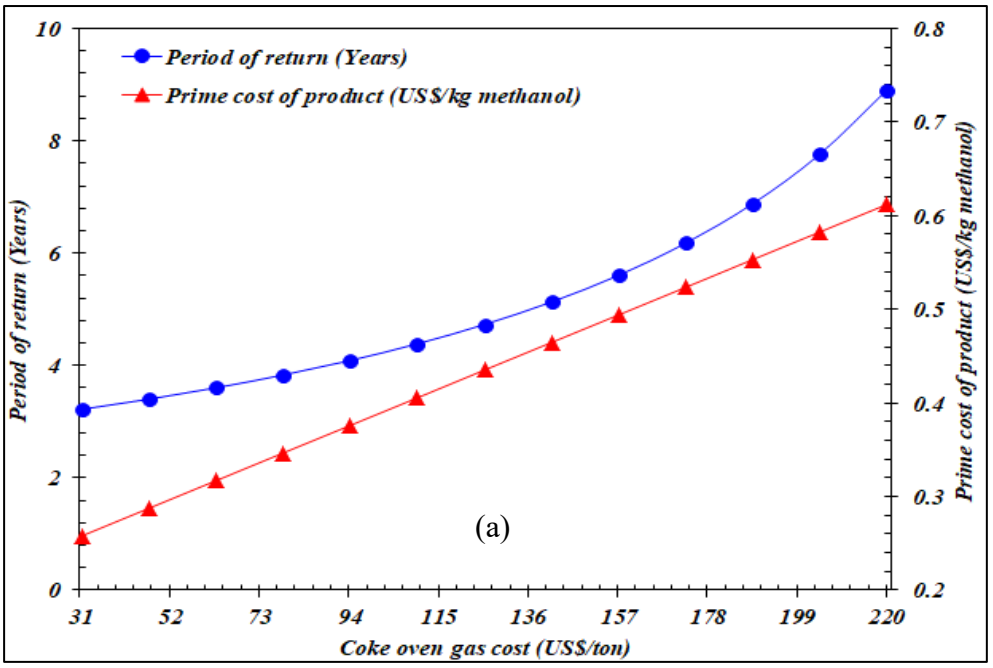

(a) The effect of LNG price changes

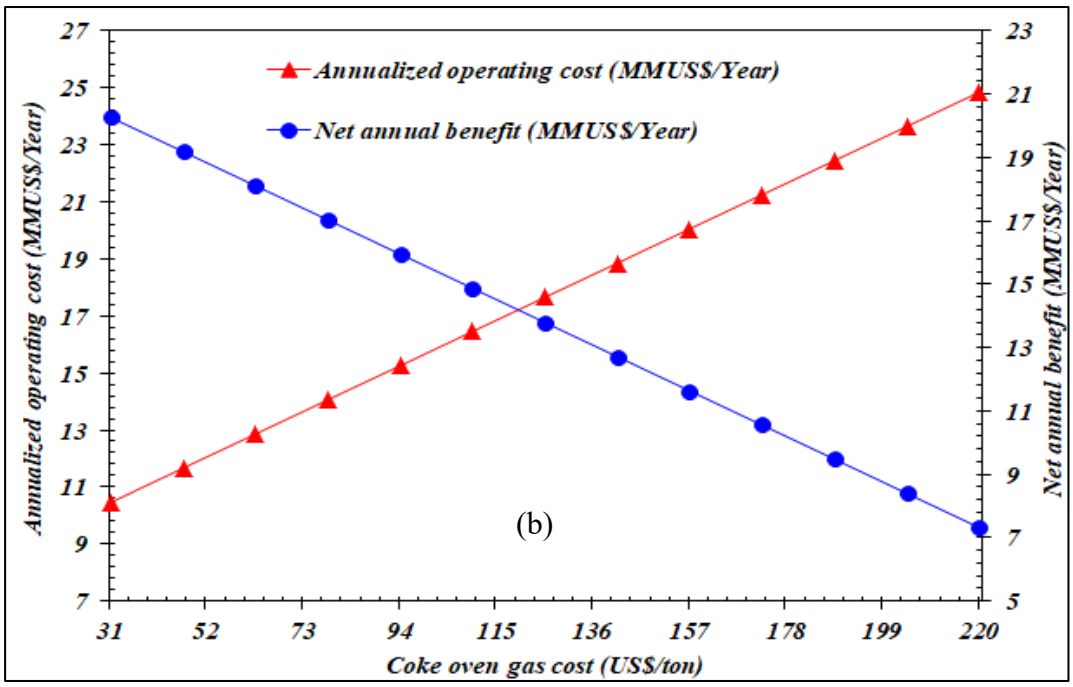

(b) The effect of LNG price changes

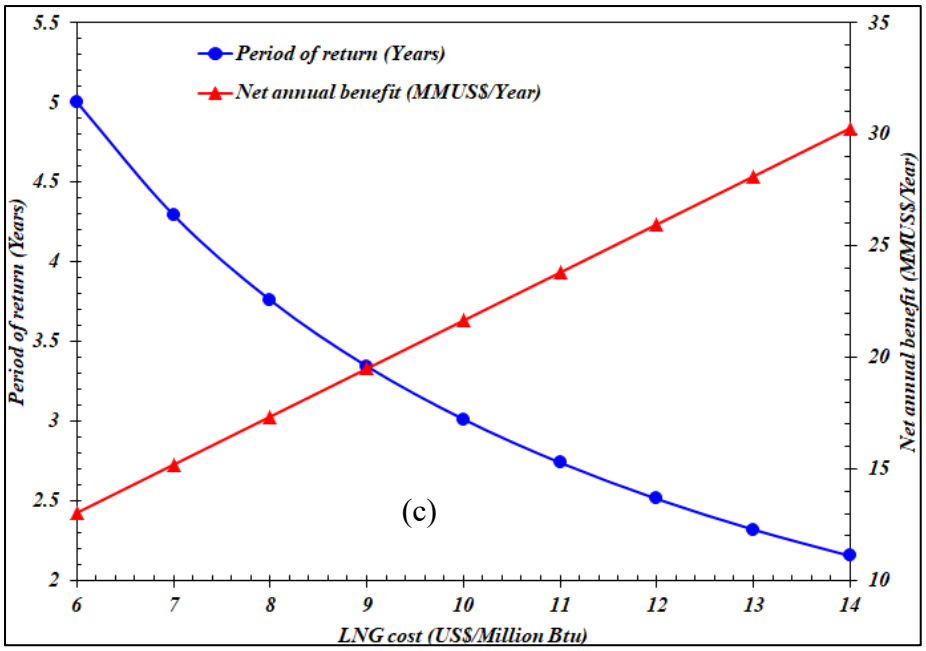

(c) The effect of LNG price changes

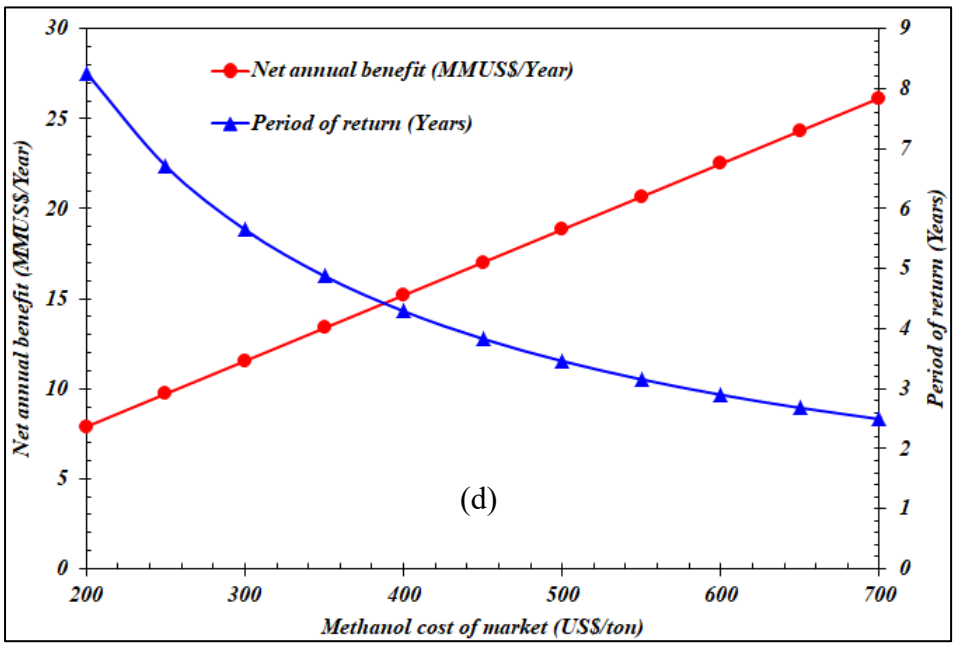

Figure 5.19. (a-d) The effect of LNG price changes in the integrated structure on the main output parameters

Table 5.6. Photovoltaic panel system characteristics

specification	Value
Cell electrical performance at standard test condition (STC)	
Maximum power (Pmax)	585 W +/- 3%
Maximum power voltage (Vmpp)	44.22 V
Maximum power current (Impp)	13.230 A
Open circuit voltage (Voc)	53.42 V
Short circuit current (Isc)	13.910 A
Max array voltage IEC	1500 V
Temperature coefficient of Voc	-156 mV/˚C
Temperature coefficient of Isc	6.7 mA/˚C
Electrical performance at 800 W/m^2, NOCT, AM1.5	
Maximum power (Pmax)	468.8 W
Maximum power voltage (Vmpp)	44.5 V
Maximum power current (Impp)	10.55 A
Open circuit voltage (Voc)	53.0 V
Short circuit current (Isc)	11.13 A
Nominal operating cell temperature (NOCT)	25 ^{0}C
Number per module	78×2
Length×Width×Depth	2411×1134×35.0 mm
Module/system (960 strings of 24 modules in series, 23040 total)	
Field type	Fixed Tilted Plane
Plane tilt/azimuth	33˚/0˚
Pnom	585 Wp
Pnom array	13.48 MWp
Area	62993 m²
Inverters (1438 kWac)	9 units, 12942 kWac total
modules area	62993 m²

Table 5.7. Validation of the designed photovoltaic panels system (Afrouzy & Taghavi, 2021)

Items	Unit	Present Study	Afrouzy et al.	Error%
Ambient temperature ºC	^{0}C	27.29	28.62	4.65
Maximum monthly average horizontal global radiation	kWh/m^2	200.6	208.1	3.60
The annual mean value of PR	%	0.843	81%	4.07
The annual mean of module quality loss	MWh	360.176	363.3	0.86
The mean annual ohmic wiring loss	MWh	517.6	527.2	1.82

5.4.2 Optimization

A multi-objective optimization strategy has two or more objective functions that must be minimized or maximized, and like a single-objective optimization, it usually has a number of constraints that the optimal solutions must satisfy (Ahmadi & Ahmadi, 2016); (Ahmadi et al., 2015). In general, a multi-objective optimization problem is defined as follows:

$$Min\{f_1(X), f_2(X), \dots, f_K(X)\} \quad (5.56)$$

$$h_i(X) = 0\ , i = 1,2, \dots, p \quad (5.57)$$

$$g_i(X) \leq 0\ , j = 1,2, \dots, m \quad (5.58)$$

Where , $\mathrm{X} = [\mathrm{x}_1, \mathrm{x}_1, \dots, \mathrm{x}_\mathrm{n}]^\mathrm{T}$is the vectors of the design variables, *f* represents the objective function, and g and h also represent the constraints of the optimization problem that must be satisfied.

In this study, the thermodynamic-economic objective functions are the efficiency of the whole hybrid developed system and the prime cost of the product (PC). Table 5.8 represents

the characteristics of the objective functions and decision variables used in the integrated structure.

$$Max\ \eta_{efficiency} = f_1(X) \tag{5.59}$$

$$Min\ PC = f_2(X) \tag{5.60}$$

One of the powerful tools to solve a multi-objective optimization problem is the use of genetic algorithms. The studied multi-objective genetic algorithm in this paper is the NSGAII algorithm. To choose the optimal point for the developed structure, a decision must be made. Among several decision-making methods, TOPSIS and LINMAP methods have been used. In the LINMAP method, the optimal endpoint is the point on the Pareto front that has the shortest distance to the ideal point. The ideal point is the point that has the best position and has a non-ideal point on the opposite side. A point outside the Pareto area that is an impossible area. In the TOPSIS method, the optimal end point is the point with the lowest CL value, which is defined in the following equation:

$$C_L = \frac{d_{i-}}{d_{i+} + d_{i-}} \tag{5.61}$$

Where d_{i-} and d_{i+} are the distances of each point from the non-ideal and ideal points, respectively. Figure 5.20 shows the Pareto front end of the entire developed system and the cost of the product. The final results of the two-objective optimization are available in Table 5.9. The results showed that the optimal value of the target functions of the efficiency of the whole hybrid system and the cost of the product are 65.83% and 0.3611 US$/kg methanol, respectively.

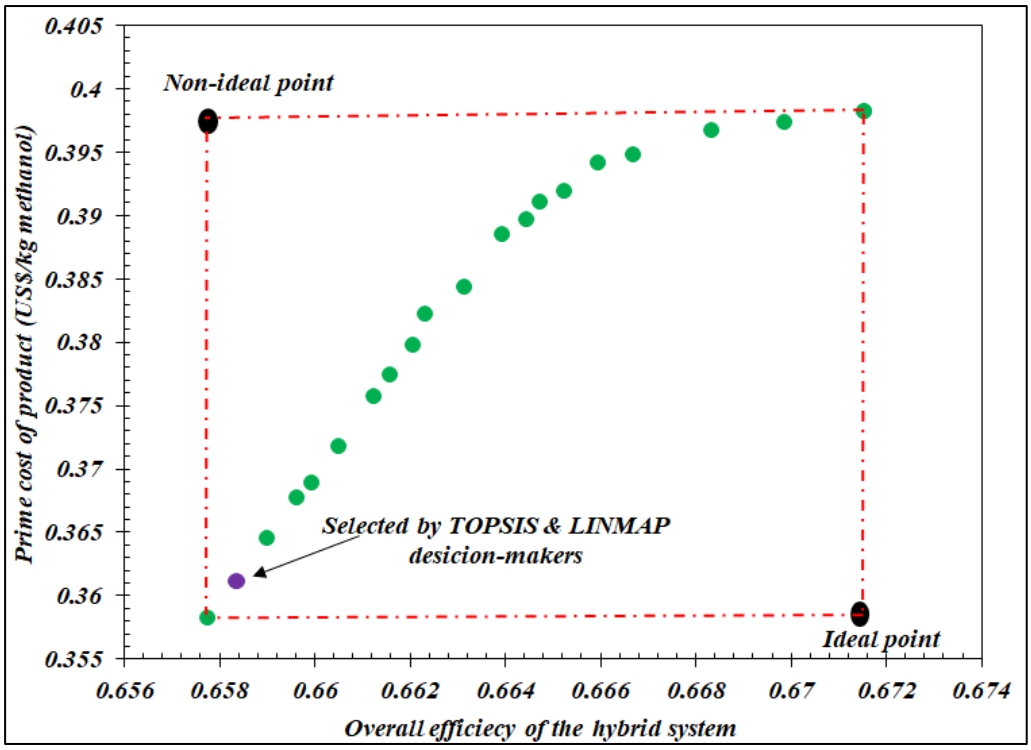

Figure 5.20. The Pareto front end of the entire integrated structure

Table 5.8. The characteristics of the objective functions and decision variables used in the integrated structure

Variables
Pressure (bar)
X1: Inlet pressure of absorber column (bar)
X2: Hydrogen Content (mol%)
X3: Coke oven gas flow rate (kmol/h)
X4: The highest pressure of nitrogen cycle (bar)
Constraints
Nitrogen content produced in LNG < 0.1 mol%
Minimum temperature approach (HX17 and HX18)> 3 ˚C
Compressor pressure ratio > 1
Reboiler temperature in stripper column >130 ˚C
Reboiler temperature in methanol distillation > 185 ˚C
Methanol mole fraction > 99.85%
Objective Function
Objective Function 1
Overall efficiency of the hybrid system
Objective Function 2
Prime cost of product (US$/kg methanol)

Table 5.9. The final results of the two-objective optimization applied

Inputs and outputs of optimization			
	Lower Bound	Upper Bound	Result
X1 (bar)	0.9	1.2	1.089
X2 (mol%)	54	65	54.21
X3 (kmol/h)	900	1000	999.7
X4 (bar)	20	80	38.50
Overall efficiency of the hybrid system		0.6583	
Prime cost of product (US$/kg methanol)		0.3611	

5.5 Conclusion

To now, for the long-term storage of energy and making it easily transportable to remote areas, multiple integrated systems with the implementation of renewable energy have been proposed. Hydrogen-containing Industrial by-products along with carbon dioxide from industrial exhaust gases can be utilized as feed for the production of liquid methanol. This paper implements a nitrogen compression refrigeration cycle to provide the required cooling to separate hydrogen and methane from coke oven gas. Subsequently, purified methane is cooled to -166 ^{0}C to produce 368 kmol/h LNG. The carbon dioxide leaving the CO_2 capture unit and the purified hydrogen enter the methanol production unit, producing 144.7 kmol/h of methanol. The heat dissipation of the integrated structure is used to supply the required energy in different sections and finally supply 9193 kgmol/h of hot water at 90 ^{0}C as a utility. The results of the energy, exergy, and sensitivity analyses are presented below:

1- The results of integrated structure simulation in HYSYS software and Matlab programming show that the energy efficiency of the methanol production cycle, the specific energy consumption of carbon dioxide separation unit, and power consumption for purification and liquefaction unit are 59.73%, 3.917 MJ/kgCO_2 and 0.6778 kWh/Nm^3. The required 12.92 MW power in the integrated structure is supplied by solar panels designed

based on meteorological data of Zarand city in Iran. Pinch analysis has also been applied to integrate the nitrogen compression refrigeration cycle with coke oven gas. The closer the hot and cold diagrams in multi-flow heat exchangers are, the lower the power consumption of the refrigeration cycle and the higher the efficiency of the whole system.

2- From the exergy analysis, it is deduced that the maximum share of exergy destruction belongs to photovoltaic panels, heat exchangers, and distillation towers (81.33%, 5.66%, and 3.15%, respectively). Each piece of equipment's exergy destruction share and exergy efficiency should be examined separately for this analysis. It is concluded that equipment such as heat exchangers, distillation towers, and reactors, which have a high share of exergy destruction, have higher exergy efficiencies. On the other hand, equipment that has a lower exergy efficiency than other equipment, such as compressors and gas turbines, has a lower exergy destruction share. Therefore, based on the exergy analysis instructions, it is not necessary to further modify the design of the developed structure. The exergy efficiency of the methanol production cycle, hydrogen and LNG production cycle, carbon dioxide separation unit, and the whole integrated structure are calculated to be 63.76%, 67.68%, 52.16%, and 68.72%, respectively.

3- The sensitivity analysis signifies that the key parameters for parametric optimization are the hydrogen content of the coke oven gas, the inlet gas pressure to the absorber tower, the coke oven gas flow rate, and the maximum pressure of the compression refrigeration cycle. The results show that by reducing the maximum pressure of the compression refrigeration cycle from 80 to 30 bar, the SEC of the hydrogen and LNG cogeneration cycle decreases from 1.0064 to 0.6777 kWh/Nm^3, respectively, and the irreversibility of the integrated structure reduces from 69.65 MW to 57.25 MW. Moreover, by reducing the hydrogen content in the coke oven gas stream from 65% mol to 54% mol, the payback period decreases from 5.43 years to 4.502 years, and the exergy efficiency enhances from 64.99% to 69.05%.

4- To improve the developed integrated structure, advanced environmental and exoeconomic analyzes can be employed to improve environmental factors and exergy efficiencies. Natural gas and isolated hydrogen can also be used in heavy hydrocarbon fuels production.

CONCLUSION

This study proposes three innovative integrated structures for energy storage in the form of fuel. The first design aims to produce liquid hydrogen from gaseous hydrogen, which can be supplied by electrolyzers in renewable power plants or purified hydrogen as the side product of several industrial processes. The second and third articles focus on methanol production by reacting carbon dioxide and hydrogen in thermally integrated processes.

Regarding hydrogen liquefaction, there are several significant challenges associated with this technology, namely high costs, inefficiency, substantial losses, and the absence of innovative solutions. Various efforts have been undertaken to enhance efficiency, minimize overall expenses, and simplify the design of hydrogen liquefaction processes. One approach involves employing a multi-component refrigerant cycle, which reduces energy consumption but introduces additional maintenance costs due to the complexity of controlling the cycle. Additionally, maintaining the stability of the refrigerant components becomes challenging in the event of leakage within a multi-component refrigerant cycle. The first article in Chapter 2 presents an integrated framework for hydrogen liquefaction, combining an ejector-compression refrigeration cycle, a cascade multi-component refrigerant cycle, and the Kalina power generation cycle. The developed structure is evaluated comprehensively through thermodynamic, pinch, exergy, and sensitivity analyses. The COP of the hydrogen liquefaction structure and the ejector-compression refrigeration cycle are 0.1030 and 0.8682, respectively. The Kalina power generation cycle consumes the excess heat of the hydrogen liquefaction process. Integrating the refrigeration system with the main configuration core is done in the form of composite and grand composite curves. Refrigerant composition percentages and refrigeration cycle operating pressures are employed to best match the cold and hot curves. The results demonstrate that the thermal efficiency of the Kalina cycle and SEC of the integrated structure are 0.1228 and 7.405 kWh/kg LH_2, respectively. Effective parameters are determined to select a suitable integrated structure in the developed hydrogen liquefaction system. The sensitivity analysis results show that the pressure increase of stream 130 from 400 to 700 kPa increases exergy efficiency and COP of the ejector-compression

refrigeration cycle by 0.6641 and 0.8924, respectively. Also, when this pressure increases, the exergy efficiency of the integrated structure will increase by 0.2364, and the exergy destruction will decrease by 453.8 MW. Moreover, by enhancing the pressure pumped in the Kalina cycle from 10 to 26 bar, the Kalina cycle thermal efficiency and its total exergy efficiency increase by 0.1268 and 0.2357, respectively. In general, the main novelties and achievements of this design can be written as follows:

- 14.2 % increase in COP of ejector-compression refrigeration cycle
- 3.7 % decrease in SEC comparing to the scenario without ejector precooling cycle
- Waste energy recovery in Kalina power cycle
- The utilization of ejector-compression refrigeration cycle in precooling stage

In the second and third articles, a novel process is developed and optimized to cogenerate 4741 kg/h of methanol, 297.7 kW of electricity, and 35.73 tons/h of hot water, including a hydrogen purification system, an absorption–compression refrigeration cycle (ACRC), a Organic Rankine Cycle (ORC), and parabolic solar troughs. The economic evaluation is made for the process and return period, and thermodynamic efficiencies are optimized using multi-objective optimization methods. The heat produced in the methanol reactor is recovered in the ORC and ACRC. Parabolic solar troughs provide thermal power to the methanol distillation tower. Thermal efficiencies of the integrated structure and the liquid methanol production cycle are 78.14% and 60.91%, respectively. The process's total exergy efficiency and irreversibility are 89.45% and 16.89 MW, respectively. Solar thermal collectors take the largest share of exergy destruction (34%), followed by heat exchangers (30%) and mixers (19%). The side products of this process include low-pressure and high-pressure fuel gases and aromatic compounds. The ORC absorbed the wasted heat in the methanol reactor to produce 475 kW of power, and the ACRC supplied 24.97 kW of cooling for the hydrogen purification cycle. The thermal efficiencies of the integrated structure, the liquid methanol production cycle, and the ORC were 78.14%, 19.64%, and 60.91%, respectively. The COP of the ACRC was calculated to be 78.14%. The results proved that 98.08% of the hydrogen was extracted from the crude feed in the purification cycle. The

exergy analysis showed that the integrated structure's exergy efficiency and destruction were 89.45% and 16.89 MW, with 6.51 MW being considered the total exergy loss. Based on economic analysis, the return period, net annual benefit, and prime cost of methanol are 6.63 years, 9.34 MMUS$/year, and 0.15 US$/kg, respectively. The optimized process showcases a remarkable 38.16% reduction in the return period compared to the base case, as indicated by the TOPSIS and LINMAP methods. In these two papers, the main novelties and achievements of this design can be written as follows:

- 70 kWh/ton reduction in the required refrigeration for precooling
- Up to 13.1% increase in the COP of ACRC
- 38% reduction in the period of return post optimization
- 7% increase in the total thermal efficiency post optimization
- External power is supplied by renewable energy
- Novel design and thermal integration for waste heat recovery

The fourth article implements a nitrogen compression refrigeration cycle to provide the required cooling to separate hydrogen and methane from coke oven gas. Subsequently, purified methane is cooled to -166 ^{0}C to produce 368 kmol/h LNG. The carbon dioxide leaves the CO_2 capture unit, and the purified hydrogen enters the methanol production unit, producing 144.7 kmol/h of methanol. The heat dissipation of the integrated structure is used to supply the required energy in different sections and finally supply 9193 kgmol/h of hot water at 90 ^{0}C as a utility. The results of integrated structure simulation in HYSYS software and Matlab programming show that the energy efficiency of the methanol production cycle, the specific energy consumption of the carbon dioxide separation unit, and the power consumption for purification and liquefaction unit are 59.73%, 3.917 MJ/kgCO_2, and 0.6778 kWh/Nm^3. The required 12.92 MW power in the integrated structure is supplied by solar panels designed based on meteorological data from Zarand, a city in Iran. Pinch analysis has also been applied to integrate the nitrogen compression refrigeration cycle with coke oven gas. The closer the hot and cold diagrams in multi-flow heat exchangers are, the lower the power consumption of the refrigeration cycle and the higher the efficiency of the whole

system. From the exergy analysis, it is deduced that the maximum share of exergy destruction belongs to photovoltaic panels, heat exchangers, and distillation towers (81.33%, 5.66%, and 3.15%, respectively). The exergy efficiency of the methanol production cycle, hydrogen and LNG production cycle, carbon dioxide separation unit, and the whole integrated structure are calculated to be 63.76%, 67.68%, 52.16%, and 68.72%, respectively. Moreover, by reducing the hydrogen content in the coke oven gas stream from 65% mol to 54% mol, the payback period decreases from 5.43 years to 4.502 years, and the exergy efficiency enhances from 64.99% to 69.05%. The main novelties and achievements of this design can be written as follows:

- 18.05% reduction in heat consumption in the CO2 absorption process
- 9.0% decrease in the prime cost of product post optimization
- 130.9 kmol/h carbon dioxide emission reduction
- External power is supplied by renewable energy
- Novel design and thermal integration for waste heat recovery

ANNEX I

THE THERMODYNAMIC PROPERTIES OF IMPORTANT STREAMS AND EQUIPMENT IN CHAPTER 2

Table-A I. 1. The exergy efficiency and exergy destruction of each equipment

	Inlet exergy	Outlet exergy	Exergy destruction	Exergy efficiency
HE1	6818945	6801059	17885.44	0.3962
HE2	10222539	10163376	59162.82	0.5145
HE3	7584841	7579738	5103.25	0.9325
HE4	3976110	3973842	2267.56	0.9229
HE5	28927147	28886697	40449.79	0.9441
HE6	516045.7	515928.6	117.17	0.9259
HE7	524074.5	524052.1	22.43	0.9822
HE8	1663715	1663640	75.46	0.8603
HE9	1688159	1687831	327.37	0.7063
HE10	5291588	5288459	3128.66	0.8263
HE11	5439858	5432557	7301.39	0.6395
HE12	2424612	2421728	2884.01	0.7579
HE13	2479169	2475836	3333.42	0.7050
HE14	2268215	2268051	164.04	0.9705
HE15	2298252	2298051	201.37	0.9643
HE16	1186589	1172255	14333.28	0.4113
HE17	1224850	1211422	13428.46	0.4194
HE18	7975133	7973655	1477.59	0.9754
HE19	1604535	1603907	628.23	0.5439
HE20	10765573	10763752	1821.23	0.8763
HE21	7685671	7685069	601.96	0.3884
HE22	10959025	10957801	1223.18	0.9023
HE23	12305313	12304961	352.10	0.7857

Table-A I.1. The exergy efficiency and exergy destruction of each equipment (continued)

	Inlet exergy	Outlet exergy	Exergy destruction	Exergy efficiency
HE24	7680055	7679689	365.91	0.9999
HE25	7687636	7685861	1775.33	0.9997
HE26	6124866	6123610	1256.41	0.7239
HE27	6113019	6112706	313.35	0.9999
T1	542191.5	66456.68	5160.86	0.3999
T2	1635249	1631058	4191.33	0.6608
T3	5378661	5338222	40438.41	0.3562
T4	2495205	2468357	26848.43	0.2541
T5	2373618	2359578	14040.29	0.2556
T6	1168292	1140008	28284.32	0.1590
T7	2868596	2867419	1176.65	0.2491
T8	5821518	5814575	6943.29	0.8987
C1	477657.5	474811.4	2846.09	0.8324
C2	488079.2	485545.7	2533.47	0.8294
C3	1616081	1614176	1904.83	0.8185
C4	1628519	1625929	2589.28	0.8260
C5	5131942	5115085	16857.20	0.8528
C6	5218353	5200813	17539.34	0.8553
C7	2327487	2317576	9910.95	0.8571
C8	2372532	2362902	9629.79	0.8559
C9	2210667	2204242	6425.15	0.8454
C10	2240169	2233771	6397.81	0.8457
C11	1075846	1067897	7948.97	0.8975
C12	1117541	1109848	7692.69	0.8960
C13	7689907	7687636	2270.86	0.7777
C14	6202379	6200872	1507.60	0.8679

Table-A I.1. The exergy efficiency and exergy destruction of each equipment (continued)

	Inlet exergy	Outlet exergy	Exergy destruction	Exergy efficiency
C15	6114566	6113019	1546.39	0.8982
C16	4883231	4881579	1652.50	0.8108
P1	7229044	7228829	214.81	0.8557
Ejc1	18142.74	17042.21	1100.53	0.9393
Ejc2	42251.66	41127.25	1124.41	0.9733
CR1	2784335	2750219	34116.32	0.9877
CR2	2774066	2770879	3187.02	0.9988
V1	1480927	1480737	189.81	0.6430
V2	4845030	4845027	2.91	0.5411
V3	1222785	1222352	433.18	0.6520
V4	4111859	4111297	561.93	0.7675
V5	1464895	1462405	2490.20	0.7125
Total	3440000	2980000	455000	0.2359

Table-A I. 2. The thermodynamic properties of important streams in the integrated system

Stream	Temp. (˚C)	Pressure (kPa)	Enthalpy (kJ/kmol)	Entropy (kJ/kmol ˚C)	Molar Flow (kmol/h)
1	298.16	2100	-1.41	97.74	39895.8
2	173.16	2100	-3571.2	82.21	39895.8
3	78.56	2100	-6335.4	58.98	39895.8
7	53.06	2100	-5721.6	18.73	39895.8
11	28.16	2100	-5293.3	-46.05	39895.8
12	18.16	2100	-5499.6	-54.96	39895.8
13	17.65	130	-5534.9	-54.6	39895.8
15	17.65	130	-5534.9	-54.6	39895.8
16	51.32	1400	-5163.5	25.37	44966.5
17	63.46	1400	-4905.8	29.89	44966.5
18	297.16	1400	-24.58	62.19	44966.5
19	362.54	2100	1335.59	62.95	44966.5
24	298.16	3000	-7.41	55.91	44966.5
25	297.16	200	-286297	53.44	11842.6
26	355.16	200	-281775	67.34	11842.6
27	65.36	3000	-4888.1	23.99	44966.5
28	176.22	938	-2973.4	76.87	44175.7
29	148.74	499	-3639.1	78.02	44175.7
30	75.16	499	-5431.3	61.38	44175.7
31	297.16	499	-24.08	94.87	44175.7
32	332.17	650	831.4	95.39	44175.7
33	298.16	650	0.44	92.75	44175.7

Table-A I.2. The thermodynamic properties of important streams in the integrated system (continued)

Stream	Temp.	Pressure	Enthalpy	Entropy	Molar Flow
34	297.16	200	-286297	53.44	15226.8
39	333.16	200	-283496	62.34	19127.4
40	69.06	1161	-5600.9	52.08	140288
41	44.3	215	-6175.3	55.56	140288
42	70.98	215	-5524.8	67.07	140288
43	297.16	215	-24.27	101.88	140288
72	396.67	279	2409.57	106.77	61987.7
73	298.16	279	0.18	99.79	61987.7
74	297.16	200	-286297	53.44	19819.7
79	293.16	10	-117.71	122.4	36696.2
80	614.42	60	7491.71	125.02	36696.2
86	297.16	200	-286297	53.44	35348.3
87	393.16	200	-278761	75.4	35348.3
88	385.98	200	-279336	73.92	253426
89	297.17	200	-286296	53.44	253426
90	280.33	2300	-108820	72.04	89419.5
91	373.16	2300	-89095	130.28	89419.5
96	361.46	2270	-174323	82.97	29843.5
97	318.63	450	-174323	83.98	29843.5
102	280.33	2300	-108820	72.04	91163.1
103	280.33	2300	-108820	72.04	1743.64
104	353.16	2290	-93655	117.71	1743.64
105	298.16	1075	-120038	90.45	13724.5
106	298.16	1075	-120038	90.45	11080
107	298.16	1075	-120038	90.45	2644.47
108	273.53	1075	-122936	80.31	11080
109	268.53	410	-120038	91.32	2644.47

Table-A I.2. The thermodynamic properties of important streams in the integrated system (continued)

Stream	Temp.	Pressure	Enthalpy	Entropy	Molar Flow
110	268.53	410	-107897	136.53	2644.47
111	234.34	117.15	-116601	108.97	19728.5
112	234.34	117.15	-108463	143.7	11081.7
113	234.33	117.1	-127032	64.46	8648.44
114	232.87	110	-127032	64.46	8648.44
115	234.5	110	-108441	144.3	8648.44
116	291.47	117.15	-104522	158.71	11081.7
117	341.97	410	-100814	160.35	11081.7
118	325.63	410	-102178	156.26	13726.1
119	298.16	410	-104369	149.24	13726.1
120	339.92	1075	-101689	150.43	13724.5
121	236.67	1670.4	38740.2	98.82	16024
122	236.67	1670.4	38740.2	98.82	12825.1
123	203.57	1670.4	36121.3	86.94	12825.1
124	171.46	116.15	41154	117.77	23564
125	236.67	1670.4	38740.2	98.82	3198.85
126	198.57	430	38740.2	100.46	3198.85
127	230.81	430	49239.7	152.85	3198.85
128	171.46	116.15	47206.1	153.07	12823.7
129	240.95	430	49658.7	154.63	12823.7
130	238.94	430	49575.1	154.28	16022.5
131	328.2	1670.4	52986.3	155.85	16024
132	298.16	1670.4	51499.7	151.11	16024
133	171.46	116.15	33927.8	75.62	10740.3
134	170.5	110	33927.7	75.62	10738.9
135	170.5	110	47177.5	153.34	49.52

ANNEX II

ANNEX IIISPECIFICATIONS OF EQUIPMENT AND STREAMS IN CHAPTER 5

Table-A II. 1. The specifications of equipment employed in the integrated structure

Pump						
Parameter	Adiabatic efficiency	Power	ΔP	P ratio	Pressure head	Capacity
Unit	%	kW	kPa	-	m	m^3/h
P1	75.00	13.15	330	3.357	30.53	107.6
Compressor						
Parameter	Adiabatic efficiency	Power	ΔP	P ratio	Operating mode	Outlet pressure
Unit	%	kW	kPa	-	-	kPa
C1	75.00	88.38	3.860	1.045	Centrifugal	90.07
C2	85.00	2070	629.0	7.228	Centrifugal	730.0
C3	85.00	2019	4270	6.849	Centrifugal	5000
C4	85.00	3681	840.0	5.000	Centrifugal	600.0
C5	85.00	3758	2400	5.000	Centrifugal	3000
C6	85.00	1202	800.0	5.000	Centrifugal	1000
C7	85.00	1257	4000	5.000	Centrifugal	5000
C8	85.00	375.4	100.0	2.000	Centrifugal	200.0
Turbine						
Parameter	Adiabatic efficiency	Power	ΔP	P ratio	Polytrophic efficiency	Outlet pressure
Unit	%	kW	kPa	-	%	°C
TB1	80.00	977.6	2400	0.2000	75.75	600.0
TB2	80.00	565.1	480.0	0.2000	78.31	120.0

Table-A II.1. The specifications of equipment employed in the integrated structure (continued)

Heat Exchanger				
Parameter	LMTD	Heat duty	UA	Min. approach
Unit	°C	kW	kJ/h.°C	°C
HX2	7.114	1922	972535	5.744
HX3	22.42	3837	616142	21.69
HX4	9.368	1136	436492	5.463
HX5	55.00	249.7	16343	8.444
HX6	10.15	3765	1335337	5.000
HX7	25.29	397.7	56621	3.039
HX8	3.521	1827	1867795	1.000
HX12	11.60	12119	3761112	1.000
HX13	8.707	3608	1491872	8.421
HX14	6.338	3837	2179402	4.261
HX15	6.810	2074	1096286	5.008
HX16	7.885	2042	932559	6.865
HX17	5.000	2942	770291	5.000
HX18	3.866	2053	583471	3.866
HX20	3.020	3942	469965	1.000
Parameter	ΔP	Heat duty	ΔT	Outlet temperature
Unit	kPa	kW	°C	°C
HX1	20.00	4445 (Cooler)	41.82	33.22
HX9	0	2663 (Heater)	170.0	195.0
HX10	0	3344 (Cooler)	24.61	182.1
HX11	0	6104 (Cooler)	47.55	134.6
HX19	0	156.3 (Cooler)	8.000	156.0

Table-A II.1. The specifications of equipment employed in the integrated structure (continued)

Column					
Parameter	Stages	Tray Volume	Diameter	Tray/Packed Space	Internal Type
Unit	-	m3	m	m	Valve
T1	10	0.8835	1.500	0.6096	2
T2	48	0.8836	1.500	0.6096	Valve
T3	23	0.8836	1.500	0.6096	Valve
T4	4	0.9719	1.500	0.5500	Sieve
Parameter	Stages	Reboiler Heating Required		Condenser Cooling Required	Inlet Stage
Unit	-	kW		kW	-
T5	51	3344		16.19	25
Reactors					
Parameter	Total Volume	Length		Diameter	Number of Tubes
Unit	m^3	m		m	-
Reactor	14.25	7.000		0.0400	1621

Table-A II. 2. The main characteristics of streams in the integrated structure

Stream	Temp.	Pressure	Mass flow	Molar enthalpy	Molar entropy	Exergy
unit	˚C	bar	kg/h	kJ/kmol	kJ/kmol.˚C	kW
A1	178.0	87.8	63297.0	-64428.8	13.3	1657.0
A2	42.0	250.0	111784.6	-284489.3	-158.9	5451.5
A3	40.2	86.2	59264.1	-50143.2	5.0	662.1
A4	83.1	250.0	115817.5	-281464.3	-149.9	6257.8
A5	45.3	90.1	59264.1	-49990.2	5.1	729.8
A6	51.8	140.0	118587.6	-293429.0	-196.7	275154.0
A7	51.9	470.0	118587.6	-293419.3	-196.7	275161.6
A8	87.0	440.0	118587.6	-290580.8	-188.4	275641.6
A9	50.5	87.8	55194.0	-36132.5	3.1	618.0
A10	89.5	220.0	6398.7	-348169.5	-4.9	904.1
A11	43.0	200.0	789.5	-284598.3	-158.7	49.8
A12	43.0	200.0	21.4	-284598.3	-158.7	1.4
A13	43.0	200.0	768.0	-284598.3	-158.7	48.5
A14	43.0	200.0	5609.3	-386091.0	-1.3	764.4
A15	124.7	235.0	112979.4	-282281.1	-178.1	276316.7
A16	108.7	215.0	112979.4	-283742.2	-181.8	275853.3
A17	75.0	195.0	112979.4	-286659.6	-189.8	275132.9
A18	33.2	175.0	112979.4	-290039.1	-200.1	274714.7
A19	25.0	175.0	1000.0	-285678.8	-162.7	48.1
A20	33.2	175.0	113979.4	-289988.5	-199.6	275169.4
A21	102.9	223.0	118403.4	-288888.4	-182.9	268515.0
A22	116.0	360.0	118403.4	-287476.1	-179.1	268914.3
S1	35.0	101.0	8699.4	-32216.2	157.1	123807.3
S2	263.0	730.0	8699.4	-24466.9	159.3	125699.3
S3	35.0	730.0	8699.4	-32230.8	140.6	125117.3

Table-A II.2. The main characteristics of streams in the integrated structure (continued)

Stream	Temp.	Pressure	Mass flow	Molar enthalpy	Molar entropy	Exergy
unit	˚C	bar	kg/h	kJ/kmol	kJ/kmol.˚C	kW
S4	256.9	5000.0	8699.4	-24672.5	142.8	126960.7
S5	35.0	5000.0	8699.4	-32318.5	124.2	126398.7
S6	-71.0	5000.0	8699.4	-35789.8	110.4	126572.0
S7	-181.9	5000.0	8699.4	-42599.4	60.8	128700.6
S8	-191.0	120.0	8699.4	-42599.4	79.5	127210.6
S9	-191.9	100.0	2660.0	-12437.0	94.3	41555.5
S10	-74.9	100.0	2660.0	-9116.7	119.6	40858.6
S11	30.0	100.0	2660.0	-6120.2	131.7	40756.5
S12	108.8	200.0	2660.0	-3844.1	132.6	41087.2
S13	26.0	200.0	2660.0	-6234.4	125.6	41039.8
S14	-156.0	600.0	61447.7	-5422.9	105.3	4940.8
S15	-193.9	120.0	61447.7	-6350.3	108.2	3842.5
S16	-109.0	120.0	61447.7	-3880.0	129.4	1485.0
S17	30.0	120.0	61447.7	138.1	147.2	714.6
S18	233.4	600.0	61447.7	6180.4	149.0	4061.3
S19	35.0	600.0	61447.7	258.3	134.2	3144.8
S20	242.3	3000.0	61447.7	6426.0	136.0	6566.9
S21	35.0	3000.0	61447.7	129.0	120.4	5568.3
S22	-71.0	3000.0	61447.7	-3178.3	107.2	5949.0
S23	-135.7	600.0	61447.7	-4782.7	110.3	4414.6
S24	-148.0	600.0	61447.7	-5166.3	107.4	4712.1
F1	29.5	200.0	8269.9	-74911.0	137.6	41589.0
F2	220.5	1000.0	8269.9	-68934.8	139.4	42679.6
F3	40.8	1000.0	8269.9	-74578.0	125.2	42395.7
F4	238.4	5000.0	8269.9	-68332.7	127.1	43539.3

Table-A II. 2. The main characteristics of streams in the integrated structure (continued)

Stream	Temp.	Pressure	Mass flow	Molar enthalpy	Molar entropy	Exergy
unit	˚C	bar	kg/h	kJ/kmol	kJ/kmol.˚C	kW
F5	200.0	5000.0	8269.9	-69573.3	124.6	43441.3
F6	200.0	3000.0	8269.8	-138840.3	146.2	40776.5
F7	44.0	3000.0	8269.8	-170206.8	69.6	39752.0
F8	43.5	2000.0	1288.7	-11264.2	118.4	12232.7
F9	43.5	2000.0	6981.1	-261002.3	43.8	27471.9
F10	93.0	2000.0	6981.1	-255796.7	59.1	27521.8
F11	180.3	1000.0	2348.9	-273634.5	87.5	517.8
F12	46.5	1000.0	2348.9	-284615.9	58.9	429.3
F13	138.5	1000.0	4632.2	-196807.9	130.6	27563.9
O1	26.0	100.0	10027.2	20859.9	108.8	104184.4
O2	258.0	100.0	10027.2	144663.5	383.3	104746.7
O3	26.0	100.0	16947.0	20859.9	108.8	176081.8
O4	250.0	100.0	16947.0	93000.5	285.6	176631.9
O5	26.0	100.0	36399.0	20859.9	108.8	378190.5
O6	130.0	100.0	36399.0	50899.3	194.6	378462.6
O7	26.0	100.0	43443.1	20859.9	108.8	451379.7
O8	195.0	100.0	43443.1	72738.5	244.7	452204.2
O9	26.0	100.0	2314.3	20859.9	108.8	24045.8
O10	230.0	100.0	2314.3	85444.1	270.9	24108.7
O11	26.0	100.0	11512.0	20859.9	108.8	119611.3
O12	215.0	100.0	11512.0	79918.2	259.7	119881.7
O13	25.0	100.0	30574.8	20601.4	108.0	317676.9
O14	195.0	100.0	30574.8	72738.5	244.7	318257.2
O15	26.0	100.0	34432.8	20859.9	108.8	357761.6

Table-A II. 2. The main characteristics of streams in the integrated structure (continued)

Stream	Temp.	Pressure	Mass flow	Molar enthalpy	Molar entropy	Exergy
unit	˚C	bar	kg/h	kJ/kmol	kJ/kmol.˚C	kW
O16	225.0	100.0	34432.8	83588.7	267.2	358654.0
O17	26.0	100.0	33983.7	20859.9	108.8	353095.5
O18	238.0	100.0	33983.7	88440.7	276.8	354089.0
O19	25.0	100.0	165885.1	-285599.5	55.4	29952.0
O20	206.6	100.0	230686.7	76863.1	253.4	2401836.4
O21	182.0	100.0	230686.7	68185.6	234.9	2400625.4
O22	134.5	100.0	230686.7	52347.7	198.1	2398741.3
O23	26.0	100.0	230686.7	20859.9	108.8	2396868.9
O24	26.0	100.0	11052.9	20859.9	108.8	114841.4
LNG	-166.2	110.0	6039.4	-89769.8	74.0	85250.0
Methanol	26.0	1000.0	4632.2	-242267.4	14.5	27128.7

BIBLIOGRAPHY

Aasadnia, M., Mehrpooya, M., & Ghorbani, B. (2021). A novel integrated structure for hydrogen purification using the cryogenic method. *Journal of Cleaner Production, 278*, 123872.

Abdin, Z., Tang, C., Liu, Y., & Catchpole, K. (2021). Large-scale stationary hydrogen storage via liquid organic hydrogen carriers. *Iscience*, 102966.

Abdin, Z., Zafaranloo, A., Rafiee, A., Mérida, W., Lipiński, W., & Khalilpour, K. R. (2020). Hydrogen as an energy vector. *Renewable and Sustainable Energy Reviews, 120*, 109620.

Abe, J. O., Popoola, A. P. I., Ajenifuja, E., & Popoola, O. M. (2019). Hydrogen energy, economy and storage: Review and recommendation. *International Journal of Hydrogen Energy, 44*(29), 15072-15086. doi: https://doi.org/10.1016/j.ijhydene.2019.04.068.

Adamson, K.-A., & Pearson, P. (2000). Hydrogen and methanol: a comparison of safety, economics, efficiencies and emissions. *Journal of Power Sources, 86*(1-2), 548-555.

Afrouzy, Z. A., & Taghavi, M. (2021). Thermo-economic analysis of a novel integrated structure for liquefied natural gas production using photovoltaic panels. *Journal of Thermal Analysis and Calorimetry, 145*(3), 1509-1536.

Ahmadi, M. H., Ahmadi, M.-A., Maleki, A., Pourfayaz, F., Bidi, M., & Açıkkalp, E. (2017). Exergetic sustainability evaluation and multi-objective optimization of performance of an irreversible nanoscale Stirling refrigeration cycle operating with Maxwell–Boltzmann gas. *Renewable and Sustainable Energy Reviews, 78*, 80-92.

Ahmadi, M. H., & Ahmadi, M. A. (2016). Multi objective optimization of performance of three-heat-source irreversible refrigerators based algorithm NSGAII. *Renewable and Sustainable Energy Reviews, 60*, 784-794.

Ahmadi, M. H., Ahmadi, M. A., Bayat, R., Ashouri, M., & Feidt, M. (2015). Thermo-economic optimization of Stirling heat pump by using non-dominated sorting genetic algorithm. *Energy Conversion and Management, 91*, 315-322.

Ahmadi, M. H., Mohammadi, A. H., & Dehghani, S. (2013). Evaluation of the maximized power of a regenerative endoreversible Stirling cycle using the thermodynamic analysis. *Energy Conversion and Management, 76*, 561-570. doi: https://doi.org/10.1016/j.enconman.2013.07.082.

Ahmadi, M. H., Sayyaadi, H., Mohammadi, A. H., & Barranco-Jimenez, M. A. (2013). Thermo-economic multi-objective optimization of solar dish-Stirling engine by implementing evolutionary algorithm. *Energy Conversion and Management, 73*, 370-380. doi: https://doi.org/10.1016/j.enconman.2013.05.031.

Aitani, A. M. (1996). Processes to enhance refinery-hydrogen production. *International Journal of Hydrogen Energy, 21*(4), 267-271. doi: https://doi.org/10.1016/0360-3199(95)00082-8.

Al-Mahmoud, H. A., Ibrahim, N. I., Al-Sulaiman, F. A., & Zubair, S. M. (2020). Thermodynamic performance evaluation of a hybrid ejector cooling and humidification-dehumidification desalination system. *Energy Conversion and Management, 225*, 113450.

Al-Nimr, M. d. A., Tashtoush, B., & Hasan, A. (2020). A novel hybrid solar ejector cooling system with thermoelectric generators. *Energy, 198*, 117318. doi: https://doi.org/10.1016/j.energy.2020.117318.

Alexis, G. (2004). Estimation of ejector's main cross sections in steam-ejector refrigeration system. *Applied Thermal Engineering, 24*(17-18), 2657-2663.

Alimoradiyan, H., & Ratlamwala, T. A. (2018). Energy, Exergy, and Exergoenvironmental Assessments of Solar-Assisted Absorption Cooling Systems and Conventional Air-Conditioning System: A Comparative Study. Dans *Exergetic, Energetic and Environmental Dimensions* (pp. 435-455). Elsevier.

Amirante, R., Cassone, E., Distaso, E., & Tamburrano, P. (2017). Overview on recent developments in energy storage: Mechanical, electrochemical and hydrogen technologies. *Energy conversion and management, 132*, 372-387. doi: https://doi.org/10.1016/j.enconman.2016.11.046.

Ardalan, H., Eslami, A., & Nariman-Zadeh, N. (2009). Piles shaft capacity from CPT and CPTu data by polynomial neural networks and genetic algorithms. *Computers and Geotechnics, 36*(4), 616-625. doi: https://doi.org/10.1016/j.compgeo.2008.09.003.

Arnaiz del Pozo, C., Cloete, S., & Jiménez Álvaro, Á. (2022). Techno-economic assessment of long-term methanol production from natural gas and renewables. *Energy Conversion and Management, 266*, 115785. doi: https://doi.org/10.1016/j.enconman.2022.115785.

Asadnia, M., & Mehrpooya, M. (2017). A novel hydrogen liquefaction process configuration with combined mixed refrigerant systems. *International Journal of Hydrogen Energy, 42*(23), 15564-15585.

Ayompe, L., Duffy, A., McCormack, S., & Conlon, M. (2011). Measured performance of a 1.72 kW rooftop grid connected photovoltaic system in Ireland. *Energy Conversion and Management, 52*(2), 816-825.

Bermúdez, J., Arenillas, A., & Menéndez, J. (2012). Equilibrium prediction of CO2 reforming of coke oven gas: suitability for methanol production. *Chemical engineering science, 82*, 95-103.

Bermúdez, J., Ferrera-Lorenzo, N., Luque, S., Arenillas, A., & Menéndez, J. (2013). New process for producing methanol from coke oven gas by means of CO2 reforming. Comparison with conventional process. *Fuel processing technology, 115*, 215-221.

Berstad, D. O., Wilhelmsen, Ø., Skjervold, V. T., & Nekså, P. (2017). Cryogenic CO2 condensation and membrane separation of syngas for large-scale LH2 production. Dans *Cryogenics 2017: Proceedings of the 14th IIR International Conference, Dresden, Germany, Mai 15-19, 2017*. IIR.

Bertau, M., Offermanns, H., Plass, L., Schmidt, F., & Wernicke, H.-J. (2014). *Methanol: the basic chemical and energy feedstock of the future* (Vol. 1). Springer.

Bilal, B. O., Sambou, V., Ndiaye, P., Kébé, C., & Ndongo, M. (2013). Multi-objective design of PV-wind-batteries hybrid systems by minimizing the annualized cost system and the loss of power supply probability (LPSP). Dans *2013 IEEE International Conference on Industrial Technology (ICIT)* (pp. 861-868). IEEE.

Bonfim-Rocha, L., Gimenes, M. L., Bernardo de Faria, S. H., Silva, R. O., & Esteller, L. J. (2018). Multi-objective design of a new sustainable scenario for bio-methanol production in Brazil. *Journal of cleaner production, 187*, 1043-1056. doi: https://doi.org/10.1016/j.jclepro.2018.03.267.

Boyano, A., Blanco-Marigorta, A. M., Morosuk, T., & Tsatsaronis, G. (2011). Exergoenvironmental analysis of a steam methane reforming process for hydrogen production. *Energy, 36*(4), 2202-2214. doi: https://doi.org/10.1016/j.energy.2010.05.020.

Cao, Y., Mihardjo, L. W., Farhang, B., Ghaebi, H., & Parikhani, T. (2020). Development, assessment and comparison of three high-temperature geothermal-driven configurations for power and hydrogen generation: Energy, exergy thermoeconomic and optimization. *International Journal of Hydrogen Energy, 45*(58), 34163-34184.

Chamousis, R. (2009). Hydrogen: Fuel of the future. *The Scientific Research Society, for the opportunity to present this research*.

Chang, H.-M., Kim, B. H., & Choi, B. (2020). Hydrogen liquefaction process with Brayton refrigeration cycle to utilize the cold energy of LNG. *Cryogenics, 108*, 103093.

Chauhan, R. K., & Chauhan, K. (2019). *Distributed Energy Resources in Microgrids: Integration, Challenges and Optimization*. Academic Press.

Chen, L., Jiang, Q., Song, Z., & Posarac, D. (2011). Optimization of methanol yield from a Lurgi reactor. *Chemical engineering & technology, 34*(5), 817-822.

Chen, Y., Han, W., & Jin, H. (2016). Analysis of an absorption/absorption–compression refrigeration system for heat sources with large temperature change. *Energy Conversion and Management, 113*, 153-164.

Chen, Y., Han, W., & Jin, H. (2017). Proposal and analysis of a novel heat-driven absorption–compression refrigeration system at low temperatures. *Applied energy, 185*, 2106-2116.

Cheng, X., Shi, Z., Glass, N., Zhang, L., Zhang, J., Song, D., . . . Shen, J. (2007). A review of PEM hydrogen fuel cell contamination: Impacts, mechanisms, and mitigation. *Journal of Power Sources, 165*(2), 739-756.

Chiou, H.-H., Lee, C.-J., Wen, B.-S., Lin, J.-X., Chen, C.-L., & Yu, B.-Y. (2023). Evaluation of alternative processes of methanol production from CO2: Design, optimization, control, techno-economic, and environmental analysis. *Fuel, 343*, 127856.

Cho, S., Park, J., Noh, W., Lee, I., & Moon, I. (2021). Developed hydrogen liquefaction process using liquefied natural gas cold energy: Design, energy optimization, and techno-economic feasibility. *International Journal of Energy Research*.

Christopher, K., & Dimitrios, R. (2012). A review on exergy comparison of hydrogen production methods from renewable energy sources. *Energy & Environmental Science, 5*(5), 6640-6651. doi: 10.1039/C2EE01098D.

Cormos, C.-C. (2011). Evaluation of power generation schemes based on hydrogen-fuelled combined cycle with carbon capture and storage (CCS). *International Journal of Hydrogen Energy, 36*(5), 3726-3738. doi: https://doi.org/10.1016/j.ijhydene.2010.12.042.

Couper, J. R., Penney, W. R., Fair, J. R., & Walas, S. M. (2005). *Chemical process equipment: selection and design*. Gulf professional publishing.

Daggash, H. A., Patzschke, C. F., Heuberger, C. F., Zhu, L., Hellgardt, K., Fennell, P. S., Mac Dowell, N. (2018). Closing the carbon cycle to maximise climate change mitigation: power-to-methanol vs. power-to-direct air capture. *Sustainable Energy & Fuels, 2*(6), 1153-1169.

Dawood, F., Anda, M., & Shafiullah, G. (2020). Hydrogen production for energy: An overview. *International Journal of Hydrogen Energy, 45*(7), 3847-3869.

Dehghani Madvar, M., Alhuyi Nazari, M., Tabe Arjmand, J., Aslani, A., Ghasempour, R., & Ahmadi, M. H. (2018). Analysis of stakeholder roles and the challenges of solar energy utilization in Iran. *International Journal of Low-Carbon Technologies, 13*(4), 438-451.

Dehghani, Z., Rahimpour, M. R., & Shariati, A. (2021). Simulation and multi-objective optimization of a radial flow gas-cooled membrane reactor, considering reduction of CO2 emissions in methanol synthesis. *Journal of Environmental Chemical Engineering, 9*(2), 104910. doi: https://doi.org/10.1016/j.jece.2020.104910.

Deng, L., & Adams II, T. A. (2020). Techno-economic analysis of coke oven gas and blast furnace gas to methanol process with carbon dioxide capture and utilization. *Energy Conversion and Management, 204*, 112315.

Du, Y., Jiang, N., Zhang, Y., Wang, X., Zhao, P., Wang, J., & Dai, Y. (2021). Multi-objective optimization of an innovative power-cooling integrated system based on gas turbine cycle with compressor inlet air precooling, Kalina cycle and ejector refrigeration cycle. *Energy Conversion and Management, 244*, 114473.

Du, Z., Liu, C., Zhai, J., Guo, X., Xiong, Y., Su, W., & He, G. (2021). A review of hydrogen purification technologies for fuel cell vehicles. *Catalysts, 11*(3), 393.

Dufour, J., Serrano, D. P., Gálvez, J. L., Moreno, J., & González, A. (2011). Hydrogen Production from Fossil Fuels: Life Cycle Assessment of Technologies with Low Greenhouse Gas Emissions. *Energy & fuels, 25*(5), 2194-2202. doi: 10.1021/ef200124d. Repéré à https://doi.org/10.1021/ef200124d

Dunn, S. (2002). Hydrogen futures: toward a sustainable energy system. *International Journal of Hydrogen Energy, 27*(3), 235-264. doi: https://doi.org/10.1016/S0360-3199(01)00131-8.

Ebrahimi-Moghadam, A., Farzaneh-Gord, M., Moghadam, A. J., Abu-Hamdeh, N. H., Lasemi, M. A., Arabkoohsar, A., & Alimoradi, A. (2021). Design and multi-criteria optimisation of a trigeneration district energy system based on gas turbine, Kalina, and ejector cycles: Exergoeconomic and exergoenvironmental evaluation. *Energy Conversion and Management, 227*, 113581.

Ebrahimi, A., Ghorbani, B., & Ziabasharhagh, M. (2020). Pinch and sensitivity analyses of hydrogen liquefaction process in a hybridized system of biomass gasification plant, and cryogenic air separation cycle. *Journal of cleaner production, 258*, 120548.

Ebrahimi, A., Meratizaman, M., Akbarpour Reyhani, H., Pourali, O., & Amidpour, M. (2015). Energetic, exergetic and economic assessment of oxygen production from two columns cryogenic air separation unit. *Energy, 90*, 1298-1316. doi: https://doi.org/10.1016/j.energy.2015.06.083.

Ebrahimi, A., & Ziabasharhagh, M. (2017). Optimal design and integration of a cryogenic Air Separation Unit (ASU) with Liquefied Natural Gas (LNG) as heat sink, thermodynamic and economic analyses. *Energy, 126*, 868-885.

Edeskuty, F. (1964). Liquid hydrogen as a coolant/propellant for nuclear rockets. Dans *Technology and uses of liquid hydrogen* (pp. 181-194). Elsevier.

Felderhoff, M., Weidenthaler, C., von Helmolt, R., & Eberle, U. (2007). Hydrogen storage: the remaining scientific and technological challenges. *Physical Chemistry Chemical Physics, 9*(21), 2643-2653.

Gervasi, J., Dubois, L., & Thomas, D. (2014). Simulation of the post-combustion CO2 capture with Aspen HysysTM software: study of different configurations of an absorption-regeneration process for the application to cement flue gases. *Energy Procedia, 63*, 1018-1028.

Ghaebi, H., Parikhani, T., & Rostamzadeh, H. (2017). Energy, exergy and thermoeconomic analysis of a novel combined cooling and power system using low-temperature heat source and LNG cold energy recovery. *Energy Conversion and Management, 150*, 678-692.

Ghahraloud, H., & Farsi, M. (2017). Modeling and optimization of methanol oxidation over metal oxide catalyst in an industrial fixed bed reactor. *Journal of the Taiwan Institute of Chemical Engineers, 81*, 95-103. doi: https://doi.org/10.1016/j.jtice.2017.10.003.

Ghorbani, B., & Amidpour, M. (2021). Energy, exergy, and sensitivity analyses of a new integrated system for generation of liquid methanol, liquefied natural gas, and crude helium using organic Rankine cycle, and solar collectors. *Journal of Thermal Analysis and Calorimetry*, 1-24.

Ghorbani, B., Ebrahimi, A., Moradi, M., & Ziabasharhagh, M. (2020). Energy, exergy and sensitivity analyses of a novel hybrid structure for generation of Bio-Liquefied natural Gas, desalinated water and power using solar photovoltaic and geothermal source. *Energy Conversion and Management, 222*, 113215.

Ghorbani, B., Ebrahimi, A., Moradi, M., & Ziabasharhagh, M. (2021). Continuous production of cryogenic energy at low-temperature using two-stage ejector cooling system, Kalina power cycle, cold energy storage unit, and photovoltaic system. *Energy Conversion and Management, 227*, 113541.

Ghorbani, B., Javadi, Z., Zendehboudi, S., & Amidpour, M. (2020). Energy, exergy, and economic analyses of a new integrated system for generation of power and liquid fuels using liquefied natural gas regasification and solar collectors. *Energy Conversion and Management, 219*, 112915. doi: https://doi.org/10.1016/j.enconman.2020.112915.

Ghorbani, B., Mehrpooya, M., & Bahnamiri, F. K. (2021). An integrated structure of bio-methane/bio-methanol cogeneration composed of biogas upgrading process and alkaline electrolysis unit coupled with parabolic trough solar collectors system. *Sustainable Energy Technologies and Assessments, 46*, 101304.

Ghorbani, B., Zendehboudi, S., & Afrouzi, Z. A. (2023). Multi-objective optimization of an innovative integrated system for production and storage of hydrogen with net-zero carbon emissions. *Energy Conversion and Management, 276*, 116506.

Ghorbani, B., Zendehboudi, S., & Khatami Jouybari, A. (2022). Thermo-economic optimization of a hydrogen storage structure using liquid natural gas regasification and molten carbonate fuel cell. *Journal of Energy Storage, 52*, 104722. doi: https://doi.org/10.1016/j.est.2022.104722.

Ghorbani, B., Zendehboudi, S., Monajati Saharkhiz, M. H., Afrouzi, Z. A., Mohammadzadeh, O., & Elkamel, A. (2023). Multi-objective Optimization of a Novel Hybrid Structure for Co-generation of Ammonium Bicarbonate, Formic Acid, and Methanol with Net-Zero Carbon Emissions. *Energy & Fuels*. doi: 10.1021/acs.energyfuels.3c01756.

Ghorbani, B., Zendehboudi, S., Saady, N. M. C., & Dusseault, M. B. (2023). Hydrogen storage in North America: Status, prospects, and challenges. *Journal of Environmental Chemical Engineering, 11*(3), 109957. doi: https://doi.org/10.1016/j.jece.2023.109957.

Goel, A., & Manik, G. (2021). Chapter 14 - Solar thermal system—an insight into parabolic trough solar collector and its modeling. Dans A. T. Azar & N. A. Kamal (Éds.), *Renewable Energy Systems* (pp. 309-337). Academic Press. doi: https://doi.org/10.1016/B978-0-12-820004-9.00021-8.

Golchoobian, H., Saedodin, S., & Ghorbani, B. (2021). Exergetic and economic evaluation of a novel integrated system for trigeneration of power, refrigeration and freshwater using energy recovery in natural gas pressure reduction stations. *Journal of Thermal Analysis and Calorimetry, 145*. doi: 10.1007/s10973-021-10607-7

Gumber, S., & Gurumoorthy, A. V. P. (2018). Chapter 25 - Methanol Economy Versus Hydrogen Economy. Dans A. Basile & F. Dalena (Éds.), *Methanol* (pp. 661-674). Elsevier. doi: https://doi.org/10.1016/B978-0-444-63903-5.00025-X.

Hamdy, S., Morosuk, T., & Tsatsaronis, G. (2017). Cryogenics-based energy storage: Evaluation of cold exergy recovery cycles. *Energy, 138*, 1069-1080.

Hamedi, H., Karimi, I. A., & Gundersen, T. (2018). Optimal cryogenic processes for nitrogen rejection from natural gas. *Computers & Chemical Engineering, 112*, 101-111.

Hammad, A., & Dincer, I. (2018). Analysis and assessment of an advanced hydrogen liquefaction system. *International Journal of Hydrogen Energy, 43*(2), 1139-1151.

Han, S., Kim, S., Kim, Y. T., Kwak, G., & Kim, J. (2019). Optimization-based assessment framework for carbon utilization strategies: Energy production from coke oven gas. *Energy Conversion and Management, 187*, 1-14.

Hao, Y., Huang, Y., Gong, M., Li, W., Feng, J., & Yi, Q. (2015). A polygeneration from a dual-gas partial catalytic oxidation coupling with an oxygen-permeable membrane reactor. *Energy Conversion and Management, 106*, 466-478.

Haydary, J. (2019). *Chemical process design and simulation: Aspen Plus and Aspen Hysys applications*. John Wiley & Sons.

Hewedy, N., Hamed, M. H., Abou-Taleb, F. S., & Ghonim, T. A. (2008). Optimal performance and geometry of supersonic ejector. *Journal of fluids engineering, 130*(4).

Hosseini, S. S., Mehrpooya, M., Alsagri, A. S., & Alrobaian, A. A. (2019). Introducing, evaluation and exergetic performance assessment of a novel hybrid system composed of MCFC, methanol synthesis process, and a combined power cycle. *Energy Conversion and Management, 197*, 111878.

Ishaq, H., & Dincer, I. (2020). Evaluation of a wind energy based system for co-generation of hydrogen and methanol production. *International Journal of Hydrogen Energy, 45*(32), 15869-15877.

Ishioka, M., Okada, T., & Matsubara, K. (1992). Formation and characteristics of vapor grown carbon fibers prepared in Linz-Donawitz converter gas. *Carbon, 30*(7), 975-979.

Jokar, M. A., Ahmadi, M. H., Sharifpur, M., Meyer, J. P., Pourfayaz, F., & Ming, T. (2017). Thermodynamic evaluation and multi-objective optimization of molten carbonate fuel cell-supercritical CO2 Brayton cycle hybrid system. *Energy Conversion and Management, 153*, 538-556. doi: https://doi.org/10.1016/j.enconman.2017.10.027.

Kalantary, F., Ardalan, H., & Nariman-Zadeh, N. (2009). An investigation on the Su–NSPT correlation using GMDH type neural networks and genetic algorithms. *Engineering Geology, 104*(1), 144-155. doi: https://doi.org/10.1016/j.enggeo.2008.09.006.

Kalogirou, S. A. (2013). *Solar energy engineering: processes and systems*. Academic Press.

Kanoglu, M., Dincer, I., & Rosen, M. A. (2007). Geothermal energy use in hydrogen liquefaction. *International Journal of Hydrogen Energy, 32*(17), 4250-4257.

Khatami Jouybari, A., Ilinca, A., & Ghorbani, B. (2022a). New Integrated Process for the Efficient Production of Methanol, Electrical Power, and Heating. *Energies, 15*(3), 1054.

Khatami Jouybari, A., Ilinca, A., & Ghorbani, B. (2022b). Thermo-economic optimization of a new solar-driven system for efficient production of methanol and liquefied natural gas using the liquefaction process of coke oven gas and post-combustion carbon dioxide capture. *Energy Conversion and Management, 264*, 115733. doi: https://doi.org/10.1016/j.enconman.2022.115733.

Khatami Jouybari, A., Ilinca, A., Ghorbani, B., & Rooholamini, S. (2022). Thermodynamic and exergy evaluation of an innovative hydrogen liquefaction structure based on ejector-compression refrigeration unit, cascade multi-component refrigerant system, and Kalina power plant. *International Journal of Hydrogen Energy, 47*(62), 26369-26393.

Khatamijouybari, A., & Ilinca, A. (2024). Economic Appraisal and Enhanced Efficiency Optimization for Liquid Methanol Production Process. *Sustainability, 16*(5), 1993.

Khayyam, H., Jamali, A., Bab-Hadiashar, A., Esch, T., Ramakrishna, S., Jalili, M., & Naebe, M. (2020). A Novel Hybrid Machine Learning Algorithm for Limited and Big Data Modeling With Application in Industry 4.0. *IEEE Access, 8*, 111381-111393. doi: 10.1109/ACCESS.2020.2999898

Kim, S., Kim, M., Kim, Y. T., Kwak, G., & Kim, J. (2019). Techno-economic evaluation of the integrated polygeneration system of methanol, power and heat production from coke oven gas. *Energy Conversion and Management, 182*, 240-250.

Kotas, T. J. (2013). *The exergy method of thermal plant analysis*. Elsevier.

Kousksou, T., Bruel, P., Jamil, A., El Rhafiki, T., & Zeraouli, Y. (2014). Energy storage: Applications and challenges. *Solar Energy Materials and Solar Cells, 120*, 59-80.

Kramer, G. J., Huijsmans, J., & Austgen, D. (2006). Clean and green hydrogen. Dans *16th World hydrogen energy conference* (Vol. 16, pp. 13-16).

Lee, J.-K., Lee, I.-B., & Han, J. (2019). Techno-economic analysis of methanol production from joint feedstock of coke oven gas and basic oxygen furnace gas from steel-making. *Journal of Industrial and Engineering Chemistry, 75*, 77-85.

Lemmon, E., McLinden, M., & Friend, D. NIST Chemistry WebBook, NIST Standard Reference Database, 2017. *National Institute of Standards and Technology*.

Li, J., & Cheng, W. (2020). Comparative life cycle energy consumption, carbon emissions and economic costs of hydrogen production from coke oven gas and coal gasification. *International Journal of Hydrogen Energy, 45*(51), 27979-27993.

Li, J., Ma, X., Liu, H., & Zhang, X. (2018). Life cycle assessment and economic analysis of methanol production from coke oven gas compared with coal and natural gas routes. *Journal of Cleaner Production, 185*, 299-308.

Li, K., Cousins, A., Yu, H., Feron, P., Tade, M., Luo, W., & Chen, J. (2016). Systematic study of aqueous monoethanolamine-based CO2 capture process: model development and process improvement. *Energy Science & Engineering, 4*(1), 23-39.

Li, Y., Liu, H., Li, X., & Yu, H. (2021). Investigation of the effect of oxygen-containing groups on the hydrogen adsorption behavior of CSCNTs using density functional theory. *International Journal of Hydrogen Energy*.

Lin, W., Zhang, L., & Gu, A. (2014). Effects of hydrogen content on nitrogen expansion liquefaction process of coke oven gas. *Cryogenics, 61*, 149-153.

Linnhoff, B. (1993). Pinch analysis-a state-of-the-art overview. *Chemical Engineering Research and Design;(United Kingdom), 71*(A5).

Liu, X., & Yuan, Z. (2016). Life cycle environmental performance of by-product coke production in China. *Journal of Cleaner Production, 112*, 1292-1301.

Liu, Z., Liu, Z., Xin, X., & Yang, X. (2020). Proposal and assessment of a novel carbon dioxide energy storage system with electrical thermal storage and ejector condensing cycle: Energy and exergy analysis. *Applied Energy, 269*, 115067.

Lundgren, J., Ekbom, T., Hulteberg, C., Larsson, M., Grip, C.-E., Nilsson, L., & Tunå, P. (2013). Methanol production from steel-work off-gases and biomass based synthesis gas. *Applied energy, 112*, 431-439.

Malerød-Fjeld, H., Clark, D., Yuste-Tirados, I., Zanón, R., Catalán-Martinez, D., Beeaff, D., . . . Kjølseth, C. (2017). Thermo-electrochemical production of compressed hydrogen from methane with near-zero energy loss. *Nature Energy, 2*(12), 923-931. doi: 10.1038/s41560-017-0029-4.

Marion, B., Adelstein, J., Boyle, K. e., Hayden, H., Hammond, B., Fletcher, T., Mitchell, L. (2005). Performance parameters for grid-connected PV systems. Dans *Conference Record of the Thirty-first IEEE Photovoltaic Specialists Conference, 2005.* (pp. 1601-1606). IEEE.

Marshall, R., Lozowski, D., Ondrey, G., Torzewski, K., & Shelley, S. (2009). Marshall and Swift cost index. *Chem. Eng. Mag*.

Mehrpooya, M., Ghorbani, B., Mousavi, S. A., & Zaitsev, A. (2020). Proposal and assessment of a new integrated liquefied natural gas generation process with auto–Cascade refrigeration (exergy and economic analyses). *Sustainable Energy Technologies and Assessments, 40*, 100728.

Mehrpooya, M., Mousavi, S. A., Asadnia, M., Zaitsev, A., & Sanavbarov, R. (2021). Conceptual design and evaluation of an innovative hydrogen purification process applying diffusion-absorption refrigeration cycle (Exergoeconomic and exergy analyses). *Journal of Cleaner Production, 316*, 128271.

Mehrpooya, M., & Pakzad, P. (2020). Introducing a hybrid mechanical–Chemical energy storage system: Process development and energy/exergy analysis. *Energy Conversion and Management, 211*, 112784.

Michalski, J. (2017). Investment decisions in imperfect power markets with hydrogen storage and large share of intermittent electricity. *International Journal of Hydrogen Energy, 42*(19), 13368-13381. doi: https://doi.org/10.1016/j.ijhydene.2017.01.141.

Moghimi, M., Emadi, M., Ahmadi, P., & Moghadasi, H. (2018). 4E analysis and multi-objective optimization of a CCHP cycle based on gas turbine and ejector refrigeration. *Applied Thermal Engineering, 141*, 516-530.

Monnerie, N., Gan, P. G., Roeb, M., & Sattler, C. (2020). Methanol production using hydrogen from concentrated solar energy. *International Journal of Hydrogen Energy, 45*(49), 26117-26125.

Montazeri, Z., & Niknam, T. (2017). Energy carriers management based on energy consumption. Dans *2017 IEEE 4th International Conference on Knowledge-Based Engineering and Innovation (KBEI)* (pp. 0539-0543). IEEE.

Morales-Mora, M., Pretelìn-Vergara, C., Martínez-Delgadillo, S., Iuga, C., & Nolasco-Hipolito, C. (2019). Environmental assessment of a combined heat and power plant configuration proposal with post-combustion CO2 capture for the Mexican oil and gas industry. *Clean Technologies and Environmental Policy, 21*(1), 213-226.

Mosaffa, A., Ghaffarpour, Z., & Farshi, L. G. (2019). Thermoeconomic assessment of a novel integrated CHP system incorporating solar energy based biogas-steam reformer with methanol and hydrogen production. *Solar Energy, 178*, 1-16.

Mousavi, S. A., & Mehrpooya, M. (2020). A comprehensive exergy-based evaluation on cascade absorption-compression refrigeration system for low temperature applications-exergy, exergoeconomic, and exergoenvironmental assessments. *Journal of Cleaner Production, 246*, 119005.

Muin, N. A. A., Isah, A. N., Asli, U. A., Sadikin, A. N., Norazahar, N., Kamaruddin, M. J., . . . Azman, N. R. (2020). A short review on various purification techniques suitable for biohydrogen-mixed gases. *Journal of Energy and Safety Technology (JEST), 3*(2).

Naeimi, A., Bidi, M., Ahmadi, M. H., Kumar, R., Sadeghzadeh, M., & Nazari, M. A. (2019). Design and exergy analysis of waste heat recovery system and gas engine for power generation in Tehran cement factory. *Thermal Science and Engineering Progress, 9*, 299-307.

Nami, H., Ranjbar, F., & Yari, M. (2018). Thermodynamic assessment of zero-emission power, hydrogen and methanol production using captured CO2 from S-Graz oxy-fuel cycle and renewable hydrogen. *Energy Conversion and Management, 161*, 53-65.

Nemati, A., Nami, H., Ranjbar, F., & Yari, M. (2017). A comparative thermodynamic analysis of ORC and Kalina cycles for waste heat recovery: A case study for CGAM cogeneration system. *Case Studies in Thermal Engineering, 9*, 1-13.

Ngan, M. S., & Tan, C. W. (2012). Assessment of economic viability for PV/wind/diesel hybrid energy system in southern Peninsular Malaysia. *Renewable and Sustainable Energy Reviews, 16*(1), 634-647. doi: https://doi.org/10.1016/j.rser.2011.08.028.

Ni, M. (2006). An overview of hydrogen storage technologies. *Energy exploration & exploitation, 24*(3), 197-209.

Nieminen, H., Laari, A., & Koiranen, T. (2019). CO2 hydrogenation to methanol by a liquid-phase process with alcoholic solvents: a techno-economic analysis. *Processes, 7*(7), 405.

Noroozian, A., Mohammadi, A., Bidi, M., & Ahmadi, M. H. (2017). Energy, exergy and economic analyses of a novel system to recover waste heat and water in steam power plants. *Energy Conversion and Management, 144*, 351-360.

Ortiz, F. G., Serrera, A., Galera, S., & Ollero, P. (2013). Methanol synthesis from syngas obtained by supercritical water reforming of glycerol. *Fuel, 105*, 739-751.

Ott, J., Gronemann, V., Pontzen, F., Fiedler, E., Grossmann, G., Kersebohm, D. B., Witte, C. (2000). Methanol. *Ullmann's encyclopedia of industrial chemistry*.

Perez-Arriaga, I. J., & Batlle, C. (2012). Impacts of intermittent renewables on electricity generation system operation. *Economics of Energy & Environmental Policy, 1*(2), 3-18.

Pourfayaz, F., Imani, M., Mehrpooya, M., & Shirmohammadi, R. (2019). Process development and exergy analysis of a novel hybrid fuel cell-absorption refrigeration system utilizing nanofluid as the absorbent liquid. *International Journal of Refrigeration, 97*, 31-41.

Rahimi, S., Meratizaman, M., Monadizadeh, S., & Amidpour, M. (2014). Techno-economic analysis of wind turbine–PEM (polymer electrolyte membrane) fuel cell hybrid system in standalone area. *Energy, 67*, 381-396. doi: https://doi.org/10.1016/j.energy.2014.01.072.

Ramachandran, R., & Menon, R. K. (1998). An overview of industrial uses of hydrogen. *International Journal of Hydrogen Energy, 23*(7), 593-598. doi: https://doi.org/10.1016/S0360-3199(97)00112-2.

Ratlamwala, T. A. H., Dincer, I., & Gadalla, M. (2012). Thermodynamic analysis of a novel integrated geothermal based power generation-quadruple effect absorption cooling-hydrogen liquefaction system. *International Journal of Hydrogen Energy, 37*(7), 5840-5849.

Ratlamwala, T. A. H., Dincer, I., Gadalla, M., & Kanoglu, M. (2012). Thermodynamic analysis of a new renewable energy based hybrid system for hydrogen liquefaction. *International Journal of Hydrogen Energy, 37*(23), 18108-18117.

Ravikumar, D., Keoleian, G., & Miller, S. (2020). The environmental opportunity cost of using renewable energy for carbon capture and utilization for methanol production. *Applied Energy, 279*, 115770.

Razzaq, R., Li, C., & Zhang, S. (2013). Coke oven gas: availability, properties, purification, and utilization in China. *Fuel, 113*, 287-299.

Reyhani, H. A., Meratizaman, M., Ebrahimi, A., Pourali, O., & Amidpour, M. (2016). Thermodynamic and economic optimization of SOFC-GT and its cogeneration opportunities using generated syngas from heavy fuel oil gasification. *Energy, 107*, 141-164. doi: https://doi.org/10.1016/j.energy.2016.04.010.

Rezaie Azizabadi, H., Ziabasharhagh, M., & Mafi, M. (2021). Applicability of the common equations of state for modeling hydrogen liquefaction processes in Aspen HYSYS. *Gas Processing Journal, 9*(1), 11-28.

Rooholamini, S., Ghorbani, B., & Ebrahimi, A. (2021). Introducing a novel hybrid system for cogeneration of liquefied natural gas and hot water using ejector-compression cascade refrigeration system (energy, exergy, pinch and sensitivity analyses). *Applied Thermal Engineering, 196*, 117283.

Rustagi, N. (2019). Current Status of Hydrogen Liquefaction Costs Originators: Elizabeth Connelly, Michael Penev, Amgad Elgowainy, Chad Hunter Peer Reviewed By: Al Burgunder, Andrew Martinez, 2 Satish Tamhankar 3.

Sadaghiani, M. S., & Mehrpooya, M. (2017). Introducing and energy analysis of a novel cryogenic hydrogen liquefaction process configuration. *International Journal of Hydrogen Energy, 42*(9), 6033-6050.

Sadeghi, S., & Ahmadi, P. (2021). Thermo-economic optimization of a high-performance CCHP system integrated with compressed air energy storage (CAES) and carbon dioxide ejector cooling system. *Sustainable Energy Technologies and Assessments, 45*, 101112.

Sadeghi, S., Ghandehariun, S., & Naterer, G. F. (2020). Exergoeconomic and multi-objective optimization of a solar thermochemical hydrogen production plant with heat recovery. *Energy Conversion and Management, 225*, 113441.

Safari, F., & Dincer, I. (2020). A review and comparative evaluation of thermochemical water splitting cycles for hydrogen production. *Energy Conversion and Management, 205*, 112182. doi: https://doi.org/10.1016/j.enconman.2019.112182.

Saltelli, A., Ratto, M., Tarantola, S., & Campolongo, F. (2005). Sensitivity analysis for chemical models. *Chemical reviews, 105*(7), 2811-2828.

Sameti, M., & Haghighat, F. (2019). Optimization of 4th generation distributed district heating system: Design and planning of combined heat and power. *Renewable energy, 130*, 371-387.

Sarbu, I., & Sebarchievici, C. (2017). Chapter 7 - Solar Thermal-Driven Cooling Systems. Dans I. Sarbu & C. Sebarchievici (Éds.), *Solar Heating and Cooling Systems* (pp. 241-313). Academic Press. doi: https://doi.org/10.1016/B978-0-12-811662-3.00007-4.

Sarkar, J. (2012). Ejector enhanced vapor compression refrigeration and heat pump systems—A review. *Renewable and Sustainable Energy Reviews, 16*(9), 6647-6659.

Schlosser, F., Arpagaus, C., & Walmsley, T. (2019). Heat pump integration by Pinch analysis for industrial applications: a review. *Chem. Eng. Trans, 76*.

Schmalensee, R. (2010). Renewable electricity generation in the United States. In *Harnessing renewable energy in electric power systems* (pp. 209-232). Routledge.

Schorn, F., Breuer, J. L., Samsun, R. C., Schnorbus, T., Heuser, B., Peters, R., & Stolten, D. (2021). Methanol as a renewable energy carrier: An assessment of production and transportation costs for selected global locations. *Advances in Applied Energy, 3*, 100050. doi: https://doi.org/10.1016/j.adapen.2021.100050.

Seyam, S., Dincer, I., & Agelin-Chaab, M. (2020a). Analysis of a clean hydrogen liquefaction plant integrated with a geothermal system. *Journal of Cleaner Production, 243*, 118562.

Seyam, S., Dincer, I., & Agelin-Chaab, M. (2020b). Development of a clean power plant integrated with a solar farm for a sustainable community. *Energy Conversion and Management, 225*, 113434.

Shahbaz, M., AlNouss, A., Ghiat, I., McKay, G., Mackey, H., Elkhalifa, S., & Al-Ansari, T. (2021). A comprehensive review of biomass based thermochemical conversion technologies integrated with CO2 capture and utilisation within BECCS networks. *Resources, Conservation and Recycling, 173*, 105734. doi: https://doi.org/10.1016/j.resconrec.2021.105734.

Sheffield, J. W., Martin, K. B., & Folkson, R. (2014). 5 - Electricity and hydrogen as energy vectors for transportation vehicles. Dans R. Folkson (Éd.), *Alternative Fuels and Advanced Vehicle Technologies for Improved Environmental Performance* (pp. 117-137). Woodhead Publishing. doi: https://doi.org/10.1533/9780857097422.1.117.

Sherif, S., Zeytinoglu, N., & Veziroğlu, T. (1997). Liquid hydrogen: potential, problems, and a proposed research program. *International Journal of Hydrogen Energy, 22*(7), 683-688.

Shirmohammadi, R., Aslani, A., Ghasempour, R., & Romeo, L. M. (2020). CO2 utilization via integration of an industrial post-combustion capture process with a urea plant: Process modelling and sensitivity analysis. *Processes, 8*(9), 1144.

Shirmohammadi, R., Aslani, A., Ghasempour, R., Romeo, L. M., & Petrakopoulou, F. (2021). Process design and thermoeconomic evaluation of a CO2 liquefaction process driven by waste exhaust heat recovery for an industrial CO2 capture and utilization plant. *Journal of Thermal Analysis and Calorimetry, 145*(3), 1585-1597. doi: 10.1007/s10973-021-10833-z.

Shirmohammadi, R., Aslani, A., Ghasempour, R., Romeo, L. M., & Petrakopoulou, F. (2022). Exergoenvironmental analysis and thermoeconomic optimization of an industrial post-combustion CO_2 capture and utilization installation. *Journal of CO_2 utilization, 59*, 101927. doi: https://doi.org/10.1016/j.jcou.2022.101927.

Sollai, S., Porcu, A., Tola, V., Ferrara, F., & Pettinau, A. (2023). Renewable methanol production from green hydrogen and captured CO2: A techno-economic assessment. *Journal of CO2 Utilization, 68*, 102345.

Stiles, A. B. (1977). Methanol, past, present, and speculation on the future. *AIChE Journal, 23*(3), 362-375.

Taghavi, M., Salarian, H., & Ghorbani, B. (2021). Thermodynamic and exergy evaluation of a novel integrated hydrogen liquefaction structure using liquid air cold energy recovery, solid oxide fuel cell and photovoltaic panels. *Journal of Cleaner Production*, 128821.

Taghdisian, H., Pishvaie, M. R., & Farhadi, F. (2015). Multi-objective optimization approach for green design of methanol plant based on CO2-efficeincy indicator. *Journal of cleaner production, 103*, 640-650. doi: https://doi.org/10.1016/j.jclepro.2014.05.032.

Taljan, G., Fowler, M., Cañizares, C., & Verbič, G. (2008). Hydrogen storage for mixed wind–nuclear power plants in the context of a Hydrogen Economy. *International Journal of Hydrogen Energy, 33*(17), 4463-4475.

Tamalouzt, S., Benyahia, N., Rekioua, T., Rekioua, D., & Abdessemed, R. (2016). Performances analysis of WT-DFIG with PV and fuel cell hybrid power sources system associated with hydrogen storage hybrid energy system. *International Journal of Hydrogen Energy, 41*(45), 21006-21021.

Tan, H., Sun, N., Zhao, Q., & Li, Y. (2017). An ejector-enhanced re-liquefaction process (EERP) for liquid ethylene vessels. *International Journal of Energy Research, 41*(5), 658-672.

Tan, H., Zhao, Q., Sun, N., & Li, Y. (2016). Enhancement of energy performance in a boil-off gas re-liquefaction system of LNG carriers using ejectors. *Energy Conversion and Management, 126*, 875-888.

Timmerberg, S., Kaltschmitt, M., & Finkbeiner, M. (2020). Hydrogen and hydrogen-derived fuels through methane decomposition of natural gas–GHG emissions and costs. *Energy Conversion and Management: X, 7*, 100043.

Toghyani, S., Kasaeian, A., & Ahmadi, M. H. (2014). Multi-objective optimization of Stirling engine using non-ideal adiabatic method. *Energy Conversion and Management, 80*, 54-62. doi: https://doi.org/10.1016/j.enconman.2014.01.022.

Uribe-Soto, W., Portha, J.-F., Commenge, J.-M., & Falk, L. (2017). A review of thermochemical processes and technologies to use steelworks off-gases. *Renewable and Sustainable Energy Reviews, 74*, 809-823.

Ursua, A., Gandia, L. M., & Sanchis, P. (2012). Hydrogen Production From Water Electrolysis: Current Status and Future Trends. *Proceedings of the IEEE, 100*(2), 410-426. doi: 10.1109/JPROC.2011.2156750

Van-Dal, É. S., & Bouallou, C. (2013). Design and simulation of a methanol production plant from CO2 hydrogenation. *Journal of Cleaner Production, 57*, 38-45.

Wang, D., Shen, Y., Chen, Y., Liu, L., & Zhao, Y. (2019). Microwave-assistant preparation of N/S co-doped hierarchical porous carbons for hydrogen adsorption. *Chemical Engineering Journal, 367*, 260-268.

Wang, N., Zhang, S., Fei, Z., Zhang, W., Shao, L., & Sardari, F. (2020). Thermodynamic performance analysis a power and cooling generation system based on geothermal flash, organic Rankine cycles, and ejector refrigeration cycle; application of zeotropic mixtures. *Sustainable Energy Technologies and Assessments, 40*, 100749.

Wang, Y., Kowal, J., Leuthold, M., & Sauer, D. U. (2012). Storage system of renewable energy generated hydrogen for chemical industry. *Energy Procedia, 29*, 657-667.

Wiesberg, I. L., Brigagão, G. V., Ofélia de Queiroz, F. A., & de Medeiros, J. L. (2019). Carbon dioxide management via exergy-based sustainability assessment: Carbon Capture and Storage versus conversion to methanol. *Renewable and Sustainable Energy Reviews, 112*, 720-732.

Wu, Y., He, F., Zhou, J., Wu, C., Liu, F., Tao, Y., & Xu, C. (2021). Optimal site selection for distributed wind power coupled hydrogen storage project using a geographical information system based multi-criteria decision-making approach: A case in China. *Journal of Cleaner Production, 299*, 126905. doi: https://doi.org/10.1016/j.jclepro.2021.126905.

Xiang, D., Xiang, J., Sun, Z., & Cao, Y. (2017). The integrated coke-oven gas and pulverized coke gasification for methanol production with highly efficient hydrogen utilization. *Energy, 140*, 78-91.

Xu, J., & Lin, W. (2021a). Integrated hydrogen liquefaction processes with LNG production by two-stage helium reverse Brayton cycles taking industrial by-products as feedstock gas. *Energy, 227*, 120443.

Xu, J., & Lin, W. (2021b). Research on systems for producing liquid hydrogen and LNG from hydrogen-methane mixtures with hydrogen expansion refrigeration. *International Journal of Hydrogen Energy, 46*(57), 29243-29260.

Xu, J., Lin, W., & Xu, S. (2018). Hydrogen and LNG production from coke oven gas with multi-stage helium expansion refrigeration. *International Journal of Hydrogen Energy, 43*(28), 12680-12687.

Yang, H., Wei, Z., & Chengzhi, L. (2009). Optimal design and techno-economic analysis of a hybrid solar–wind power generation system. *Applied energy, 86*(2), 163-169. doi: https://doi.org/10.1016/j.apenergy.2008.03.008.

Yang, H., Zhou, W., Lu, L., & Fang, Z. (2008). Optimal sizing method for stand-alone hybrid solar–wind system with LPSP technology by using genetic algorithm. *Solar Energy, 82*(4), 354-367.

Yi, Q., Gong, M.-H., Huang, Y., Feng, J., Hao, Y.-H., Zhang, J.-L., & Li, W.-Y. (2016). Process development of coke oven gas to methanol integrated with CO2 recycle for satisfactory techno-economic performance. *Energy, 112*, 618-628.

Yilmaz, C. (2018). A case study: Exergoeconomic analysis and genetic algorithm optimization of performance of a hydrogen liquefaction cycle assisted by geothermal absorption precooling cycle. *Renewable energy, 128*, 68-80.

Yin, L., & Ju, Y. (2020). Process optimization and analysis of a novel hydrogen liquefaction cycle. *International Journal of Refrigeration, 110*, 219-230.

Yousef, B. A., Rezk, H., Abdelkareem, M. A., Olabi, A. G., & Nassef, A. M. (2020). Fuzzy modeling and particle swarm optimization for determining the optimal operating parameters to enhance the bio-methanol production from sugar cane bagasse. *International Journal of Energy Research, 44*(11), 8964-8973.

Yousefizadeh Dibazar, S., Salehi, G., & Davarpanah, A. (2020). Comparison of exergy and advanced exergy analysis in three different organic Rankine cycles. *Processes, 8*(5), 586.

Yuksel, Y. E., Ozturk, M., & Dincer, I. (2018). Analysis and performance assessment of a combined geothermal power-based hydrogen production and liquefaction system. *International Journal of Hydrogen Energy, 43*(22), 10268-10280.

Zare, V., & Mahmoudi, S. (2015). A thermodynamic comparison between organic Rankine and Kalina cycles for waste heat recovery from the Gas Turbine-Modular Helium Reactor. *Energy, 79*, 398-406.

Zare, V., & Takleh, H. R. (2020). Novel geothermal driven CCHP systems integrating ejector transcritical CO2 and Rankine cycles: Thermodynamic modeling and parametric study. *Energy Conversion and Management, 205*, 112396.

Zhang, F., Zhao, P., Niu, M., & Maddy, J. (2016). The survey of key technologies in hydrogen energy storage. *International Journal of Hydrogen Energy, 41*(33), 14535-14552.

Zhang, L., & Xiang, J. (2014). The performance of a grid-tied microgrid with hydrogen storage and a hydrogen fuel cell stack. *Energy Conversion and Management, 87*, 421-427. doi: https://doi.org/10.1016/j.enconman.2014.07.045.

Zhang, Y., Xiao, J., & Shen, L. (2009). Simulation of methanol production from biomass gasification in interconnected fluidized beds. *Industrial & engineering chemistry research, 48*(11), 5351-5359.

Zhao, Y., Zhao, Y., Yi, Q., Li, T., Wang, J., Bao, W., & Chang, L. (2021). Highly flexible and energy-efficient process for converting coke-oven gas and pulverized coke into methanol and ammonia using chemical looping technology. *Energy Conversion and Management, 248*, 114796.

Zhen, X., & Wang, Y. (2015). An overview of methanol as an internal combustion engine fuel. *Renewable and Sustainable Energy Reviews, 52*, 477-493.

Züttel, A. (2004). Hydrogen storage methods. *Naturwissenschaften, 91*, 157-172.

Züttel, A. (2007). Hydrogen storage and distribution systems. *Mitigation and Adaptation Strategies for Global Change, 12*(3), 343-365. doi: 10.1007/s11027-006-9076-z.